Analyzing Extracellular Vesicles as Potential Biomarkers of Stroke Using Polymer Microfluidic Devices

By
Harshani Nayomi Kumari Wijerathne

Submitted to the graduate degree program in Department in Chemistry and the Graduate Faculty of the University of Kansas in partial fulfillment of the requirements for the degree of Doctor of Philosophy

Chair: Prof. Steven A. Soper

Prof. Susan Lunte

Prof. Robert Dunn

Prof. David Benson

Prof. Liza Friis

Date Defended: 17 July 2019

The Dissertation Committee for Harshani Nayomi Kumari Wijerathne certifies that this is the approved version of the following dissertation:

Analyzing Extracellular Vesicles as Potential Biomarkers of Stroke Using Polymer Microfluidic Devices

_____

Chairperson- Prof. Steven Soper

Date Approved: 22nd July 2019

Acknowledgments

There have been a lot of kind individuals who helped my thesis dissertation throughout the duration of my time here. I would like to express my sincere gratitude to all of them.

First and foremost, I would like to express my sincere gratitude to Prof. Steven Soper for his enormous support and invaluable kindness during my dissertation work. I'm really thankful to Prof. Steven Soper for giving me the opportunity to join his research group in January 2018. I would not have succeeded in the research work without his patience and guidance throughout my time at his lab.

It was an honor for me to have such a prestigious set of individuals in my committee; Prof. Steven Soper, Prof. Susan Lunte, Prof. Robert Dunn, Prof. David Benson and Prof. Liza Friss, I would like to thank all of you and greatly appreciate your time, corrections and support.

I want to especially thank Dr. Maggie Witek for her guidance and for closely working with me. Her positive attitude, broad knowledge, and hands-on experience not only encourages everyone in the group, but also has impacted me in many positive ways. Dr. Maggie helped me a lot when I was new to the lab and her kindness always helped me in performing research work. I would like to deliver my sincere gratitude to Dr. Matt Jackson for his valuable advices and for performing all the simulation studies included in this thesis. He also helped and trained me when I first came to the lab in 2018. I also like to thank Dr. Kumuditha Rathnayake for helping me with my research work and training me when I was new to the lab. I also want to thank all the Soper group members, Dr. Camila Campos, Dr.Nickolas Larkey, Dr. Lulu Zheng, Charuni, Sachindra, Uditha, Thilanga, Chathurika, Wenting, Zheng, Swarna, Virginia, Ian , Lindsey and Dhanushki.

I also want to thank Dr. Prem Thapa from Microscopy and Analytical Imaging Lab at the University of Kanas for helping me with the TEM images.

I also want to thank Prof. Mario Rivera for his guidance and support during my time in his lab. And all group members from Rivera group who helped me to successfully conduct my research work. I should also mention the generous financial support from the Ph.D. Program in Chemistry, The University of Kansas, for offering me a teaching position to cover my expenses.

I also want to thank the Sri Lankan community at Lawrence who were always there with me during past five years.

Last but not least, I would like to express my gratitude to my loving husband Nishantha, who gave me tremendous support in various ways. He is always there with me and gave me strength during all the hard times I had. I would not have succeeded in my life without his kindness and love. I have no words to thank my father, my mother and my two sisters Kanchana and Dinusha for their tremendous support all through out these years. My parents are always there to support me and thank you for the courage and love you give to me. I also want to thank my mother-in-law, father-in-law, brothers-in-law and sisters-in-law for their kindness and support during my studies. All these would not be possible if not for you all.

Abstract

A major drawback of currently available stroke diagnosis methods, such as computed tomography (CT) and magnetic resonance (MRI), is that they cannot provide timely diagnosis within the narrow therapeutic time window of 4.5 h from stroke onset afforded by recombinant tissue plasminogen activator treatment. Upon initiation of a stroke event, CD15+ neutrophils and CD8+ T cells are recruited and activated in response to the inflammatory stroke event and can release into blood extracellular vesicles (EVs) containing mRNA markers with altered expression profiles indicative of tissue damage. Our previous studies demonstrated that certain leukocyte subpopulations and gene expression profiling of these isolated subpopulations could be used to diagnose acute ischemic stroke (AIS) within 3 h. Here, our research goal was to develop a novel approach for the measurement of mRNA transcripts in EVs rather than cells as a possible diagnostic for AIS. To facilitate the development of the AIS diagnostic based on EVs, we developed a microfluidic device with a high-density array of antibody-modified micropillars for the affinity selection of CD8+ or CD15+ EVs with an analysis time less than the 4.5 h recombinant tissue plasminogen activator effective therapeutic time window.

We successfully developed a microfluidic device with a high-density array of antibody-modified micropillars for the affinity selection of CD8+ EVs, which could process 200 µL of plasma in <10 min with a recovery >90%. Initial validation of these devices was performed using a model cell line Molt-3, which contained CD8+ T-cells. With the aid of fluorescence microscopy, we demonstrated that EVs can be affinity selected using the microfluidic device with higher specificity compared to other EV isolation techniques, such as ultrancentrifugation or PEG-precipitation that can improve the quality of the mRNA expression data. Transmission Electron Microscopy (TEM) and Nano Particle Tracking Analysis (NTA) revealed that the microfluidic device was capable of capturing and releasing enriched EVs with a short analysis time (<25 min). Gene expression analysis performed via droplet digital PCR revealed that for

AIS, the genes we selected (*PLBD1*, *MMP9*, *VCAN*, *FOS*, *CA4*) produce similar expression between the CD8+ T cells and EVs originating from these cells. The analysis of clinical samples, which used a 7-bed microfluidic device with 10 µm pillars and an interpillar spacing of 10 µm provided a higher dynamic range compared to a 3-bed device that used larger pillars (~90 µm) as well as significantly reduced processing time.

In a blinded study performed for healthy and AIS patient samples, we were able to correctly identify 4/5 stroke patient samples and 4/5 healthy control samples. Although results reported here are very encouraging, more extensive studies are needed with a larger cohort of patient samples and healthy controls to clearly determine receiver operating characteristics for the use of EVs as a source of mRNA for AIS diagnosis.

The research work I conducted on identification of mutations stabilizing Bacterioferritin associated ferredoxin is included in Appendix.

Table of Content

Chapter 1: Introduction

Chapter 5: Conclusions and Future Directions

Appendix

List of Figures

List of tables

Chapter 1: Introduction

1.1 Stroke and stroke statistics

Stroke is considered as a brain attack with brain dysfunction resulting from an underlying vascular cause.[1] According to the American Stroke Association in 2018, stroke was a leading cause of serious long-term disability in the United States. In the United States, stroke is the 4th cause of death that kills nearly 1 million people every year. Based on additional statistics from the American Stroke Association, someone in the US has a stroke every 40 seconds and strokes account for 1 of every 19 deaths. They also stated that 795,000 people experience a new or re-current stroke, where approximately 610,000 of these are first attacks and about 185,000 are recurrent strokes.[2] In 2010, medical treatment for stroke cost nearly $54 billion and it is expected that it would exceed $1 trillion by 2050.[3] The map in Figure 1 illustrates the deaths caused by stroke in US (35+ 200-2006, by county) and it clearly shows the "Stroke Belt", an area in the Southeastern US and Mississippi Valley with a high rate of stroke mortality.[4]

The problem of stroke is not limited to the United State alone; in 2015, stroke was responsible for 11.8% of total deaths worldwide, which makes stroke the second leading global cause of death behind heart disease. Although the overall risk of stroke has dropped by about 25% during the last decade,[5] disability caused by strokes have become one of the major health problems worldwide. Thus, stroke is one of the major health issues not only in the United States, but also worldwide. Therefore, there is a need to improve healthcare facilities for stroke rehabilitation and the early detection of stroke conditions to predict the recurrence of the disease and for the primary prevention of stroke.

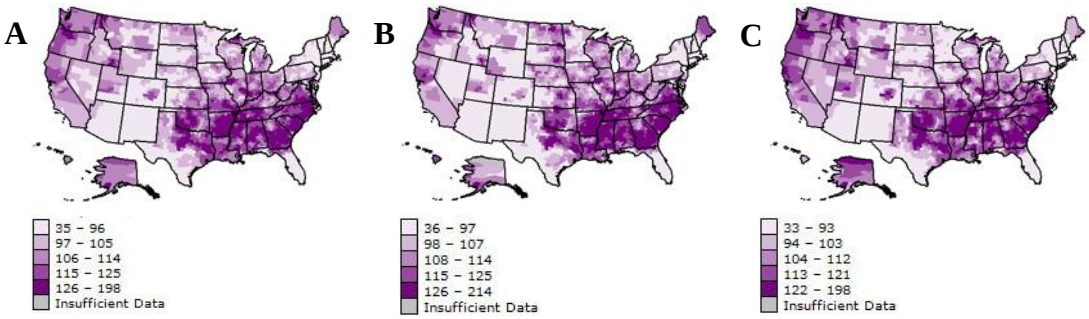

Figure 1.1: Age-adjusted average (Annual) deaths per 100,000 (A) 35+, 2000-2006, by county. (B) Men 35+, 2000-2006, by county (C) Women 35+, 2000-2006, by county. (Reproduced from reference 4).

1.2 Stroke types

The American Stroke Association has identified two major types of stroke, namely ischemic stroke (clots) and hemorrhagic stroke (bleeds). The functional changes caused by both of these subtypes are different depending on the kind of the lesion that represents the area of damaged brain tissue. Thus, it is important that the underlying mechanism involved in these stroke types are understood so that the type, diagnosis, and prognosis of stroke can be delineated.

1.2.1 Acute ischemic stroke (AIS)

AIS is the most common type of stroke, which accounts for approximately 87 percent of all strokes. AIS occurs when a clot or a mass clogs a blood vessel that supplies blood to the brain (Figure 1.2 A). This will obstruct the blood flow to the brain cells and when this happens brain cells become deprived of oxygen.[6] During an ischemic stroke, brain damage and neuronal death happens due the failure of energy producing compounds such as adenosine triphosphate (ATP), which in turn results in reduced glucose production and limits oxygen to the brain. As a result of this, cellular homeostasis is not supported. Due to the lack of energy, functioning of the ion gradient is also affected by the loss of ions such as potassium resulting in neuronal swelling. Some other complex mechanisms are also involved in brain tissue triggering ischemic stroke, such as release of glutamate and aspartate neurotransmitters in the brain, dysfunction of the calcium

channel and production of reactive oxygen species that can activate proteases and lipases that can potentially damage cellular and extracellular elements. As a final result of these processes immediate death of a section of the brain parenchyma (core) or partial injury (penumbra) with the potential recovery with treatments can take place.[7-8] The brain damage caused by AIS is determined by many factors such as the duration, severity, and the location of the ischemic stroke. The main cause for AIS is fatty deposits on the vessel walls that are called atherosclerosis. These fatty deposits cause two types of obstructions called cerebral thrombosis and cerebral embolism (See Table 1.1). Cerebral thrombosis is a thrombus or a blood clot that will develop by the fatty plaque within the blood vessel while cerebral embolism is a blood clot that forms at another location in the blood circulatory system. These are usually formed in heart and large arteries of the upper chest and neck. These blood clots can break loose and enter the bloodstream and move to the brain's vessels until it reaches a vessel that is too small to let it pass creating an obstruction for the blood flow. Irregular heartbeat, which is called atrial fibrillation, is one of main reasons of embolism that causes these clots to form in the heart and move to the brain.[9]

Table 1.1: Subtypes of stroke

Stroke			
Ischemic (87%)		Hemorrhagic (16%)	
Embolic (31.5%)	Thrombotic (51.5%)	Intracerebral (10%)	Subarachnoid (6%)

Figure 1.2: (A) Representation of a blood clot in a blood vessel that supplies blood to the brain. (B) Symptoms of stroke (FAST- **F**ace, **A**rms, **S**peech, **T**ime). (Reproduced from references 6 and 11)

Symptoms for AIS includes trouble with speaking and understanding and the person having the stroke may experience confusion, and slur of their words. Also, they will develop sudden numbness, weakness or paralysis in their face, legs or arms, which normally takes place in only one side of the body and one side of the mouth will drop when they try to smile. They will also have blurred or blackened vision in one or sometimes both eyes. A sudden, severe headache together with vomiting and altered consciousness is another sign of stroke. Regardless of the type of stroke the person is experiencing you may notice the following signs ("FAST"): **F**ace, if you ask the person to smile, one side of the face will drop; **A**rms, when you ask the person to raise both arms, one arm will drift down or he'll be unable to raise one arm; **S**peech, the person will be unable to repeat a simple phrase or their speech will be slurred or strange; and **T**ime if you see any of these signs it's time to call 911 immediately or seek immediate medical attention.[10-11]

1.2.2 Hemorrhagic stroke

Approximately 13% of all the strokes are hemorrhagic strokes. This stroke type is caused when a weakened blood vessel ruptures causing leakage of blood to the surrounding brain. Then, blood can accumulate and compress the surrounding brain tissue.[6] Pressure caused by the blood can damage the brain cells, and these damaged areas are unable to function properly. There are two major types of hemorrhagic stroke namely, intracerebral hemorrhage and subarachnoid hemorrhage. In first type, the bleeding takes place inside of the brain, which is also the main type of hemorrhagic stroke. Risk factors for intracerebral hemorrhage include hypertension, which is the most common cause, cerebral cavernous malfunctions that occurs when blood vessels do not form correctly in the brain, and arteriovenous malfunctions (AVM), which is a genetic condition where blood vessels form incorrectly resulting in an abnormally tangled web. AVMs typically occur in the brain and spine, but if they are present in the brain vessels can rupture that leads to bleeding into the brain. [12-13] However, this is a rare disorder.

In subarachnoid hemorrhage the bleeding will occur between the brain and the membranes that cover it. Risk factors for subarachnoid hemorrhage are AVMs, bleeding orders, head injury and trauma, blood-thinning medication and a bulge in blood vessel wall which is called as aneurysm.

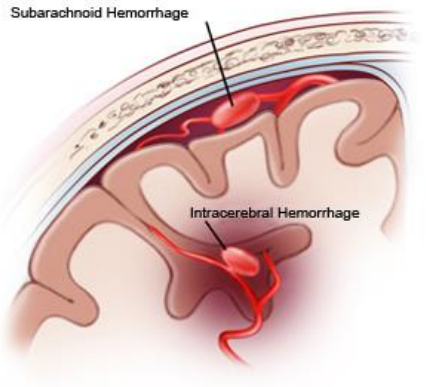

Figure 1.3: Representation of hemorrhagic stroke; Subarachnoid hemorrhage and intracerebral hemorrhage. (Reproduced from reference 12)

Symptoms of a hemorrhagic stroke may change, but the common signs are sudden severe headache, loss of balance and inability to coordinate, vision changes, unable to move, numbness in an arm or leg, seizures, loss of consciousness, confusion or loss of alertness, nausea and vomiting, confusion or loss of alertness. Some additional symptoms of either type of hemorrhagic stroke includes, paralysis in any part of the body, inability to look at light, pain in the neck area, difficulty in swallowing, hand tremors and fluctuation in heartbeat and breathing more frequently.[12]

1.3 Stroke mimics

Stroke mimics (SMs) are non-stroke conditions (false positives) that have similar symptoms as stroke and are often diagnosed as stroke. SMs are expressed as diseases caused by neurologic symptoms that resemble a stroke, and the frequency can differ from 1.2 % - 25%.[14-15]. Most of the stroke mimics don't do any significant brain damage. Complex migraine is a one of the most common stroke mimics which can result in hemiparalysis. Vision loss, aphasia, or vertigo are

some of the symptoms of migraine.[16-17] Seizures are another stroke mimic and often cause neuronal dysfunction that may be noticeable as weakness, aphasia, confusion or sensory signs and it also affects vision and speech. Some other stroke mimics are demyelinating disease, meningitis, glucose level variations, that is metabolic disorders (hypoglycemia), tumors, non-cerebrovascular diseases such as epilepsy and dementia.[16, 18-19] Conditions that are frequently misdiagnosed as stroke are summarized in table 1.2 below.[16]

Table 1.2: Common stroke mimics

Condition	**Misdiagnosed as stroke (%)**
Brain tumor	7-15
Labyrinthitis	5-6
Metabolic disorder	3-13
Migraine	11-47
Psychiatric disorder	1-40
Seizures	11-40
Syncope	5-22
Transient global amnesia	3-10
Sepsis	14-17
Other	11-37

More information about the misdiagnosis of stroke by current stroke diagnosis techniques will be discussed in the following sections. Transient ischemic attacks (TIA), which are also called mini-strokes, is a neurologic dysfunction caused as a result of loss of blood flow to the brain or spinal cord without acute infarction and since the blockage period in TIA is short there is no permanent damage caused. However in people who had a TIA, the occurrence of a following stroke is about 11% over the next 7 days and it's 24-29% over the following 5 years.[20-21] Because the presence of TIA can lead to recurrent stroke conditions, differentiating between stroke or TIA versus stroke mimics is necessary.

1.4 Stroke assessment scales

Stroke type needs to be diagnosed quickly and precisely so that treatment can be performed quickly as the longer the treatment for stroke is delayed, the lesser the effectiveness of it. Thus, the phrase "Time lost is brain lost". In many cases, due to the lack of knowledge of stroke symptoms very few patients with stroke come to the hospitals on time to receive proper treatments. Quick and accurate diagnosis of stroke subtypes and excluding stroke mimics is highly important to provide proper treatment for stroke patients.

Stroke scales are normally utilized to get an idea on the severity of the stroke. Depending on the type of information that has been collected from the patients these stroke scales are divided in to sub-categories as following: i) Global outcome scales (modified Rankin scale, Glasgow outcome scale) that provides information on the neurologic disability; ii) Physical deficit scales (National Institutes of Health Stroke Scale (NIHSS)), which are based on the scores given by neurologic examination; and iii) Activities of daily living scales (Barthel index) that is based on the functional outcome and recovery useful in studies of rehabilitation.[22-25]The diagnostic accuracy of these scales is ~80%, however the clinical specificity and sensitivity can vary.[22-24] Table 1.3 below explains the scale used by the National Institute of Health Stroke Scale (NIHSS), which is considered to be the most widely used scale with a numerical scale that can be completed within 5-8 min and yields a score from 0-42 (higher the score, more severe the stroke). This scale can be easily used by both neurologists and non-neurologists.

Scales alone cannot be used to decide a treatment method for the stroke conditions. Most of these scales are used only to understand the severity of the stroke, but it's important to understand that these scales cannot be used in distinguishing stroke subtypes. These are mostly helpful when used together with the brain imaging techniques and biomarkers for diagnosing stroke conditions.[26]

Table 1.3: National Institutes of Health Stroke Scale (NIHSS)

Item	Response score
1a. Level of consciousness	0= alert 1=not alert 2=obtunded 3=unresponsive
1b. Level of consciousness questions	0=answers both questions correctly 1= answers one question correctly 2= answers neither correctly
1b. Level of consciousness commands	0=performs both tasks correctly 1= performs one task correctly 2= performs neither task correctly
2. Graze	0=normal 1=partial gaze palsy 2=total gaze palsy
3.Visual fields	0=no visual loss 1=partial hemianopsia 2=complete hemianopsia 3=bilateral hemianopsia
4. Facial palsy	0=normal 1=minor paralysis 2=partial paralysis 3=complete paralysis
5. Motor arm (a) Left (b) Right	0=no drift 1=drifts before 5s 2=falls before 10 s 3=no effort against gravity 4=no movement
6. Motor leg (a) Left (b) Right	0=no drift 1=drifts before 5s 2=falls before 10 s 3=no effort against gravity 4=no movement
7.Ataxia	0=Absent 1=1 limb 2=2 limbs
8. Sensory	0=normal 1=mild loss 2=severe loss
9.Language	0=normal 1=mild aphasia 2=severe aphasia

	3=mute or global aphasia
10. Dysarthria	0=normal 1=mild 2=severe
11. Extinction/inattention	0=normal 1=mild 2=severe

1.5 Stroke diagnosis methods: Advantages and disadvantages

Diagnosing the subtype of stroke quickly and precisely is important to decide the proper treatment for patients. The most commonly used stroke diagnosis method available today is neuroimaging techniques. Imaging methods basically serve two main purposes, first is to rule out the stroke mimics and second is to assess the location and to decide the damage caused by the stroke. Currently available neuroimaging techniques and some of the advantages and the disadvantages are briefly discussed below.

1.5.1 Computed tomography (CT)

A CT of the brain is a noninvasive diagnostic method that uses X-rays to produce horizontal, or axial images of the brain. CT scanning combines special x-ray equipment with sophisticated computers. During a CT scan the X-ray beam will move in a circle around the body allowing different views of the brain. This X-ray information is then sent to a computer that will interpret the X-ray data and displays it in a two-dimensional (2D) image. The imaging here is based on the same principle as regular X-rays. The X-rays are absorbed differently by different parts of the body. Bones will absorb most of the X-rays, so the skull will appear white in color in the image. Water in the cerebral ventricles or fluid-filled cavities in the middle of the brain absorbs less of X-rays thus those areas appear in black. The brain has intermediate density, hence appear in grey. Most ischemic strokes are less dense than normal brain thus appear darker. There are

several types of CT available, those are non-contrast head CT (NCCT), CT angiogram of the head and neck (CTA), and the perfusion CT (PCT).[27]

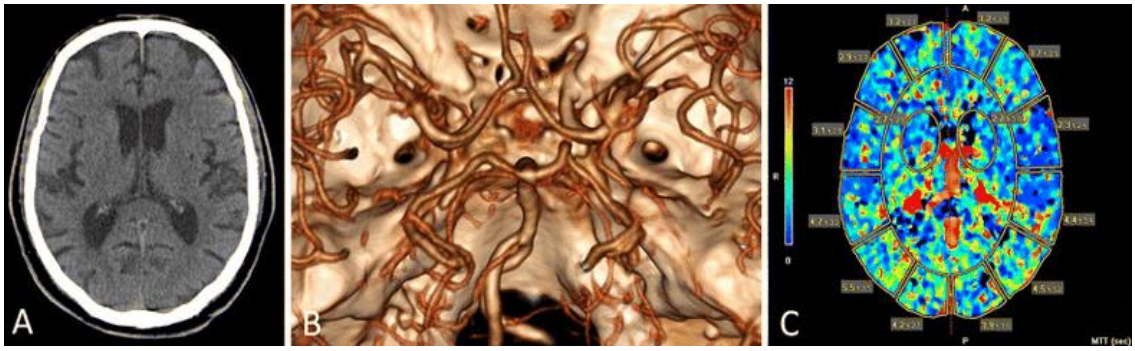

Figure 1.4: Demonstration of multimodal computed tomographic (CT) acquisition, including (**a**) non contrast CT. (**b**) CT angiography. (**c**) CT perfusion. The patient is a 91-year-old man who presented with acute onset of slurred speech (Reproduced from reference 27).

1.5.1.2 Non contrast computed tomography (NCCT)

NCCT is widely used to identify the early signs of stroke conditions and to rule out hemorrhagic stroke and other lesions, such as a tumor. Its wide availability and the speed of image acquisition makes it effective for initial evaluation of suspected stroke patients.[28] Some advantages of NCCT include rapid access, availability of emergency department CT scanner 24 hours a day in many centers[29], and evidence that its use is cost effective.[30]

However, there are some drawbacks of CT scans for stroke diagnosis. CT scans do not detect chronic hemorrhage including micro-bleeds. Also, NCCT performs poorly in detecting acute infarctions, particularly in posterior fossa due to beam hardening artifacts and insufficient contrast resolution. Acute posterior ischemia stroke accounts for approximately 20% of ischemic stroke. [31] In a study, they have shown that sensitivity for detecting acute stroke on NCCT varied from 57% to 71%.[32] Early signs of acute infarctions are subtle, especially for the smaller arterial blockings and in the hyper acute stage of ischemic stroke, which will result in limited sensitivity and reduced inter-observer reliability.[33-34] Furthermore, a study reported that within 6 h hours after onset of stroke symptoms, inter-observer agreement (median of 30 CT scans and six raters)

of all early infarction signs was 61% ± 21 and the inter-observer agreement (kappa statistics) ranged from 0.14 to 0.78 for any early infarction signs. In the same study, it was reported that the mean sensitivity and the specificity for detection of early infarction signs with CT were 66% (range 20-87%) and 87% (range 56%-100%), respectively.[35] According to the literature, the sensitivity of standard non-contrast CT for ischemic stroke increases after about 24 h.[36]

Figure 1.5: NCCT images of an Ischemic stroke Ischemic stroke not yet visible after 2 h (Reproduced from reference 37).

As shown in Figure 1.5, in some patients it's difficult to detect the affected area early and when its visible in the image it's too late to start the treatments. This NCCT was taken 2 hours after stroke symptoms and no signs of ischemic stroke was visible.[37]

Another major disadvantage of NCCT is that the images that are taken will depend on the position of the patient inside the CT scanner. Based on a study performed to evaluate physician accuracy in cranial computed tomography scan interpretation for determining the eligibility thrombolytic treatment, they reported that from a sample of 38 emergency physicians, 29 neurologists and 36 general radiologists, physicians did not uniformly attain a level of sensitivity for detection of intracerebral hemorrhage adequate to permit safe selection of patients for proper treatment. The summarized results obtained from this study are shown in Table 1.4.[38] Based on

the results we can see that the physicians have trouble differentiating between hemorrhage from calcification, and differentiating between ischemic stroke from old infarctions.

Table 1.4: Percent correct by Scan Category

		Emergency Physicians			Neurologists			General Radiologists		
Type of Scan	No. of Scans	% Correct	No. of Readings	Range Correct by Scan, %	% Correct	No. of Readings	Range Correct by Scan, %	% Correct	No. of Readings	Range Correct by Scan, %
Normal	10	83	109	57-100	90	81	77-100	89	98	70-100
Imposter (calcification)	4	77	39	44-100	78	32	43-100	71	49	39-92
Imposter (old infarction)	4	43	42	27-80	59	32	42-100	70	33	20-88
Hemorrhage (easy)	8	94	98	85-100	100	69	100	100	78	100
Hemorrhage (difficult)	10	57	124	25-93	78	99	40-100	80	128	43-93
Acute infarction (easy)	4	82	45	66-100	100	34	100	93	29	80-100
Acute infarction (intermediate)	8	46	97	14-97	77	70	42-100	85	95	33-100
Acute infarction (difficult)	8	13	15	0	44	18	0-100	50	30	0-100
Total	**56***	67	**569**	. . .†	83	**435**	. . .	83	**540**	. . .

*There were 54 scans in the initial pool, and 2 were added when 2 problem scans were replaced.
†Ellipses indicate data not applicable.

As explained in the previous section, stroke mimics is another major drawback in neuroimaging techniques. Stroke mimics accounts for 19-30% of suspected stroke presentations. The differentiation of stroke mimics from cases of AIS is challenging, given a narrow time window for the administration of intravenous thrombolysis. Figure 1.6 below illustrates a summary of common stroke mimics identified in a systematic review and meta-analysis of case series.[39] This study involved 8839 patients and based on the results they concluded that expertise in the differential diagnoses of stroke is required to manage the patients at the point of referral.[40]

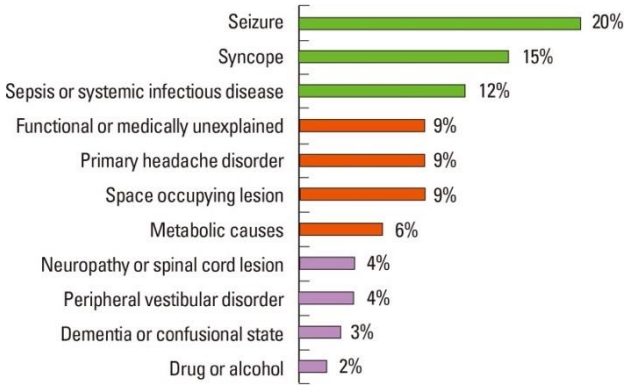

Figure 1.6: Summary of common stroke mimics identified in a systematic review (Reproduced from reference 39).

Use of high radiation doses is another major drawback of all the CT imaging techniques.

1.5.1.1 Computed tomography angiography (CTA)

In CTA, an iodinated contrast agent is injected intravenously and time-optimized scanning is activated.[41] This method is widely used to examine the blood vessels in the brain and neck. Literature demonstrates some unique benefits of CTA for AIS diagnosis. CTA may facilitate improved pre-procedure planning and allow for quick treatment decisions. Compared to CT images, CTA images provide higher resolution. In some patient's stroke that cannot be detected by NCCT, it can be seen in CTA images.[42]

There are some drawbacks of CTA as well. The iodinated contrast agent that is given before the test can potentially initiate an allergic response or toxic in some people. Thus, if the patient is >60 years of age or if they have kidney disease, diabetes, lupus, or multiple myeloma, blood test needs to be performed beforehand to make sure that the contrast agent is safe. From a practical standpoint, some insurance plans do not cover CTA, and because this test can be very expensive, it limits its use broadly. Moreover, CTA imaging depends on correct timing, technical planning, and sufficient cardiac output.[41] If these conditions are not met, CTA will yield poor images with insufficient diagnostic information.

1.5.1.2 Computed tomography perfusion (CTP)

CTP requires a rapid injection of intravenous contrast agent and repeated imaging of the brain, based on the total amount (Cerebral Blood volume CBV) and the speed that blood flows (Mean Transient time MTT) to different areas of the brain. CPT can help in evaluating the potential areas of salvageable tissue in ischemic penumbra;[34, 43] penumbra is defined as the area of the scan that has reduced blood flow but an increased blood volume.

A recent study suggested that CTP studies increase the diagnostic accuracy during for early stage stroke detection and it can lead to an increased diagnostic yield compared to CT scans (80% vs. 50%, respectively).[44] The drawbacks of CTP are: The use of CTP requires a higher level of expertise and resources compared to normal CT scans and evaluating the images needs a high

level of skill.[44] Additionally, CTP images are spatially limited to 2-4 consecutive sections with coverage of 20-40 mm thickness; this could underestimate the full extent of brain perfusion.[41] Due to this limitation, CTP is unable to detect small lacunar vessels, but it has shown ~95% accuracy in delineation of supratentorial strokes.[45-46] Regardless of these drawbacks, CTP remains a worthwhile technique to acquire physiologic information that cannot be obtained through NCCT and CTA.

1.5.2 Magnetic resonance imaging (MRI)

MRI provides improved sensitivity compared to CT scans and with the advantage of avoiding exposure to ionizing radiation and iodinated contrast agents. MRI is a non-invasive test and during the test the machine creates a magnetic field, which will alter the water molecules in the brain cells. A radio signal is turned on in bursts, and the energy is absorbed differently by different atoms in the body. Then, the absorbed energy is reflected by the body where it's detected by the MRI scanner and theses reflections are converted into a picture of the brain via a computer. Important MRI techniques used in stroke diagnosis are gradient echo (GRE), fluid-attenuated inversion recovery imaging (FLARI), MR angiography (MRI), diffusion-weighted imaging (DWI) and perfusion weighted imaging (PWI).

1.5.2.1 Gradient echo (GRE), Fluid-attenuated inversion recovery imaging (FLARI)

GRE is sensitive for detecting acute hemorrhage and micro-bleeds that cannot be detected by NCCT. FLAIR imaging can detect subtle subarachnoid hemorrhages, which can also be undetectable through CT imaging.[28, 34]

1.5.2.2 Magnetic resonance angiography (MRI)

MRA is particularly used for evaluating large, proximal arteries. The sensitivity and the specificity of MRA in detection of cervical and intracranial stenosis is reported to be in the range of 70% to 100%.[5] Time-of-flight MRA (TOF-MRA) is another method that is used to assess intracranial vasculature. There are many studies that have been conducted to compare MRA and

CTA for visualization of occlusion and stenosis of major cerebral vessels. One study showed that CTA had higher sensitivity for both stenosis and occlusion of major vessels (98% and 100%, respectively) than MRA (70% and 87%, respectively).[47] But there are other studies that demonstrated MRA as a good imaging method to detect occlusion in major vessels.[48-50]

1.5.2.3 MR diffusion

Diffusion weighted imaging depends on the motion of water. The net effect of water that is moving from extra- to intra-cellular space is an overall reduction in water mobility due to intracellular structural and molecular components acting as barriers of free motion. This is captured as hyper-intensity on DWI and hypo-intensity on apparent diffusion coefficient (ADC) maps.[31] DWI is considered to be the most reliable method for the early detection of cerebral ischemia and for detection of many stroke mimics with a reported sensitivity and specificity of 81-100% and 86-100%, respectively.[51-56] Regardless of these advantages, it is possible that DWI produce false positive and false negative results. Non-ischemic lesions including demyelinating diseases can cause neurologic symptoms and reduced perfusion, and lead to mistakenly detected infarcts. But, if DWI is used together with conventional MR imaging like FLAIR it's possible to differentiate these conditions from infarcts.[55]

If all the MRI techniques are considered together, the major disadvantage is that MRIs are not often available under emergency conditions. In a study conducted on availability and quality of the MRI equipment in U.S emergency departments, the authors reported that in U.S only 13% of hospitals have 24/7 MRI services with on-site technologist and only 26% of the hospitals have 24/7 on-call technologist. More results from this study are shown in Table 1.5.[29]

Table 1.6: Imaging equipment among some of U.S hospitals with emergency departments

	n	**% (95% CI)**
CT available (n=260)	249	96% (93,98)
CT hours (n=249)		
24/7 (on-site technologist)	235	94% (91,97)
24/7 (on-call technologist)	12	5% (3,8)
7 days/week (< 24 hours/day)	2	1% (0,3)
CT resolution, slices (n=246)		
1	35	14% (10,19)
2-4	33	13% (9,18)
5-16	81	33% (27,39)
>16	97	39% (33,46)
MRI available (n=260)		
On-site	171	66% (60,72)
Mobile	52	20% (15,25)
MRI hours (n=223)		
24/7 (on-site technologist)	29	13 % (9,17)
24/7 (on-call technologist)	59	26% (21,32)
6-7 days/week (< 24 hours/day)	30	13 % (9,18)
5 days a week	50	22 % (17,28)
< 5 days a week	55	25 % (19,30)

Considering all of the imaging techniques as the currently available stroke diagnosis methods, the advantages and limitations of each method are summarized in Table 1.6 [57]. As can be seen, due to limitations of these methods patients with stroke are unable to reach for proper treatment during the 4.5 h time window for effective treatment of AIS using recombinant tissue plasminogen activator. Hence, there is still a need to look for new biomarkers that are capable of detecting stroke conditions within a short time interval. Currently, there is not an FDA-approved molecular diagnostic test for both stroke types.

Table 1.7: Advantages and limitation of currently available neuroimaging technologies

Imaging Characteristics	CT	MRI
Availability in the acute setting (0–6 hours)	++	−
Rapid image acquisition	++	+
Lack of vulnerability to motion artifacts	+	−
Accessibility for patients with monitors and/or ventilators	++	−
Feasibility and safety for patients with metallic implants (pacemakers, implantable defibrillators)	++	−
Low cost	+	−
Lack of ionizing radiation	−	++
Renal toxicity associated with contrast administration	+	+
Time for post-processing angiography and perfusion imaging	−	−
Sensitivity to lacunar and posterior fossa infarcts	−	++
Differentiation between acute and chronic ischemia	−	++
Ability to assess causes of (Intracerebral hemorrhage) ICH or (Subarachnoid hemorrhage) SAH while in the scanner	+	+
Detection of chronic hemorrhage including micro-bleeds	−	+

1.6 Therapeutics for stroke

After a stroke, there is a low or limited blood supply to the area of the brain where the stroke took place. Thus, neurons in these areas are at greater risk with elapsing time and the final result would be neuronal cell death. This is why the time between stroke symptoms, diagnosis, and the therapeutic treatment is considered to require a short time window. In the next section, therapeutic approaches available for both ischemic and hemorrhagic strokes are explained in detail.

1.6.1 Therapeutic approaches for ischemic stroke

1.6.1.1 recombinant tissue plasminogen activator (rt-PA)

Recombinant Tissue Plasminogen Activator (rt-PA) is the only FDA (Food and Drug Administration) approved drug that is currently available for AIS. Although the proportion of patients with ischemic stroke who are treated with rt-TPA has increased since it was first approved in 1996, the treatment rate is still low and only about 3.4-5.2% of all patients having

stroke in the U.S receive rt-PA.[58] Reasons for this low rate may be due to delays in the emergency medical services, medical contradictions, coupled with the narrow therapeutic time window of rt-PA.[59]

Tissue plasminogen activator is a serine protease that consists of ~527 amino acids with 3 or 4 glycosylation sites and it has 17 disulfide bonds.[60] Vascular endothelial cells are considered as the main source of plasma tPA that is involved in the breakdown of blood clots (fibrinolysis), which is the major physiological function of tPA in blood. Standard dose of tPA approved by FDA is 0.9 mg/kg of body weight.[61] The major concern in using rt-PA is that it maintains a narrow therapeutic window of 3-4 h from the onset of stroke symptoms. Some studies have been conducted on increasing the effective time window, but the results have shown that increasing the time length from 4-6 h made the rt-PA treatment less beneficial compared treatment within 3 h.[62-63]

While best known role of tPA is its function in fibrinolysis, tPA has also been shown to regulate many non-fibrinolytic functions in the central nervous system. tPA can be synthesized and released by most of the brain cells and when they are released, they can bind to the same cells via different receptors. Interaction with these receptors will result in various effects, that can be either beneficial or harmful.[64] Under certain circumstances using tPA in delayed times after stroke onset, tPA can induce brain hemorrhage and injury.[65-66] Many complex mechanisms have been proposed for hemorrhagic transformation (HT) including tPA-mediated N-methyl-D-aspartate excitotoxicity and tPA-mediated microglial inflammation.[67-68]

Research performed using experimental models have also suggest the involvement of extracellular protease family of MMPs. These studies suggested that MMPs can degrade basal lamina and blood-brain barrier substrates, which will eventually lead to edema and vascular rupture.[66, 69-70] Some of the potential benefits of rt-PA are that it shows a critical role in inhibiting neuronal apoptosis and promote the functional recovery in later phase stroke.[71-72]

1.6.1.2 Mechanical thrombectomy

Mechanical treatment, an endovascular procedure, which is also called as mechanical thrombectomy, is another option to remove a clot in eligible patients with a large vessel occlusion (LVO). This method can restore vascular patency of the vessels with a success rate between 41% and 54%, which is an alternative method to restore blood flow to the brain.[73-74] According to guidelines provided, mechanical thrombectomy should be done within 6 h of acute stroke symptoms and this can be performed only after the patient receives tPA. Here, the doctor will thread a catheter through a blocked artery in the brain. The stent will open and grab the clot, which will allow the doctor to remove the stent with the trapped clot as illustrated in Figure 1.7.[75]

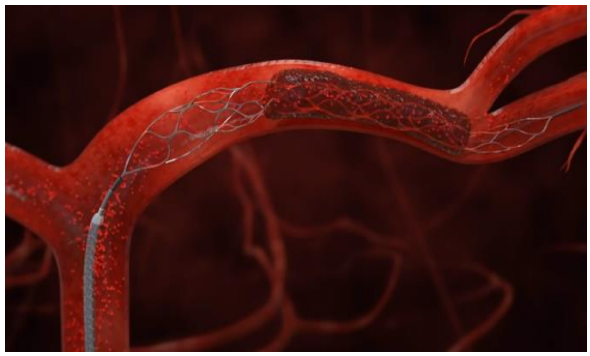

Figure 1.7: Mechanical removal of the blood clot using a stent retriever (Reproduced from reference 75).

1.6.2 Treatments for Hemorrhagic stroke

The only possible treatment for hemorrhagic stroke is a mechanical treatment to stop the blood flow. A catheter is threaded up through a major artery in an arm or leg, which will be guided into the brain, allowing the surgeon to use cameras to visualize the bleeding. When the catheter is guided to the place of bleeding, it will deposit a mechanical agent like a coil to prevent further rupture of the vessel as shown in Figure 1.8. This is an endovascular procedure in which the doctor will gain access through the vascular system, which makes it less invasive.[76-77]

Figure 1.8: A catheter is guided to the place of bleeding, it will deposit a mechanical agent like a coil to prevent further rupture of the vessel (Reproduced from reference 76).

1.7 Importance of blood brain barrier (BBB) in stroke

It's important to properly understand the role of the BBB in order to develop effective diagnostic markers for brain diseases such as stroke. BBB's primary goal is to create a restrictive barrier between the central nervous system (CNS) and the rest of the body to prevent the entry of unwanted blood borne factors. BBB's micro-vessels are made of endothelial cells that are linked by tight junctions. The neighboring glial cells including astrocytes and microglial are also important to BBB function.[78] All these components together are known as the neurovascular unit (NVU). The cellular composition of the BBB is illustrated in Figure 1.9.[79]

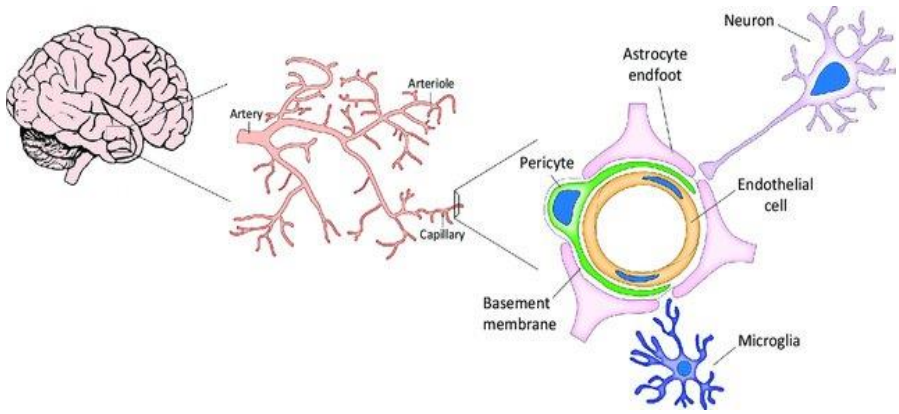

Figure 1.9: Cellular constituents of the blood-brain barrier (BBB). Cerebral endothelial cells form tight junctions which restrict the paracellular pathway. Pericytes are distributed discontinuously along the length of the cerebral capillaries and partially surround the endothelium. Both the cerebral endothelial cells and the pericytes are surrounded by a basal lamina. Astroglial end feet form a complex network surrounding the capillaries and provide the cellular link to the neurons. Microglia are CNS-resident immune cells. (Reproduced from reference 79)

BBB plays an important role in the immune system of the brain. The tight junctions (TJ) between the endothelial cells that restrict the blood borne substances from entering the brain can be affected by brain injuries including stroke. Under stroke conditions, the BBB TJ integrity is decreased, which results in increased paracellular permeability. This will cause ionic dysregulation, inflammation, oxidative and nitrosative stress, enzymatic activity, and angiogenesis.[80]

Breakdown of the BBB also allows for the passage of biomarkers from the neurons and the glial cells into the circulating blood.[81] Evidence is present that suggests leukocytes can move through the BBB to the blood circulation in human 48-72 h after a stroke event and it is hypothesized that the accumulation of these leukocytes is a reason for tissue damage and that will prevent the blood flow after restoration.[82] Timing of these events that take place during a ischemic stroke event is illustrated in Figure 1.10.[83]

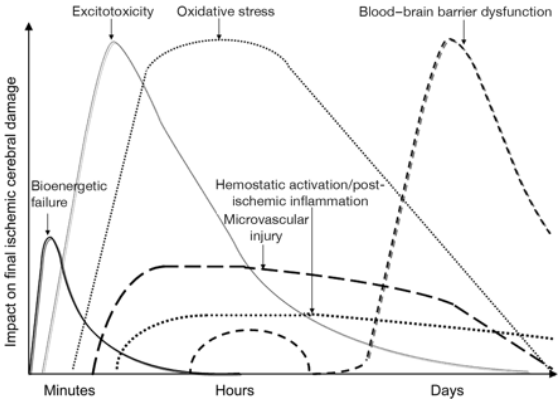

Figure 1.10: Timing of events after stroke (Reproduced from reference 83).

Moreover, biomarkers like matrix metalloproteinase-9 (MMP-9) play a biphasic role in stroke by disrupting the BBB during the initial phases of the stroke event and promote vascular growth during recovery phases. Exact mechanisms and roles of different cells in stroke are still unclear. But, better examination of the BBB would provide ways to develop novel therapeutic approaches.

1.8 Currently available biomarkers for stroke, why we need to look for new biomarkers?

A biomarker can define a broad category of medical signs with objective indications of medical state observed by the patient, that can be measured accurately and reproducibly.[84] Examples of biomarkers are genes, cells, enzymes, hormones or any change in biological function in response to a disease state. There can be an upregulation or a down regulation of these biomarkers during a disease state. As discussed in the previous sections, current diagnostic techniques for stroke involve neuroimaging techniques, which have many drawbacks.

Thus, it's important to look for new peripheral-blood-based biomarkers for stroke diagnosis that allow for easy accessibility of the biomarker, appear in blood early following the stroke event, and allow for high clinical sensitivity and specificity for diagnosing the two types of stroke. However, looking for new biomarkers and developing a new diagnostic test for stroke is challenging for several reasons, including the complexity of stroke conditions and the presence

of the BBB, which may delay the appearance of some biomarkers into peripheral blood. Hence a rapid and simple diagnostic test will be extremely useful for pre-hospital screening before treatment and provide a higher percentage of eligible patients receiving rt-PA therapy.

There are many factors that need to be considered when selecting a biomarker for stroke. The major challenge is the late release following the stroke event and the inability of most of these biomarkers to move through the BBB. Due to these challenges, currently there is no molecular diagnostic test available for stroke and no biomarker has shown to be either clinically sensitive and specific to diagnose any of the stroke types. [85]

In the field of clinical studies, the sensitivity and the specificity are different from the analytical sensitivity and specificity. The clinical sensitivity provides information on the positivity of the clinical test, whereas the clinical specificity provides information about the negativity of the test.

$$Clinical\ sensitivity = \frac{True\ positives}{True\ positives + Flase\ negatives} \quad \text{(Eq. 1)}$$

$$Clinical\ specificity = \frac{True\ Negatives}{True\ negatives + False\ Negatives} \quad \text{(Eq. 2)}$$

According to the literature, ideal biomarkers or a panel of biomarkers should be able to answer the following questions; firstly, does the patient have a stroke (must be able to differentiate stroke from stroke mimics), secondly what type of a stroke is it, ischemic stroke or hemorrhagic stroke, and finally is there a need for thrombolytic treatment and is there a risk of recurrence?[85] Answers to these questions can be found by an ideal biomarker that will release to the blood stream quickly in detectable quantities using the appropriate analytical technique.

A conceptual design that as modeled to illustrate the relation of a biomarker to a clinical end point is shown in Figure 1.11. The model also shows that biomarkers may be useful in the assessment of safety and efficacy.[86]

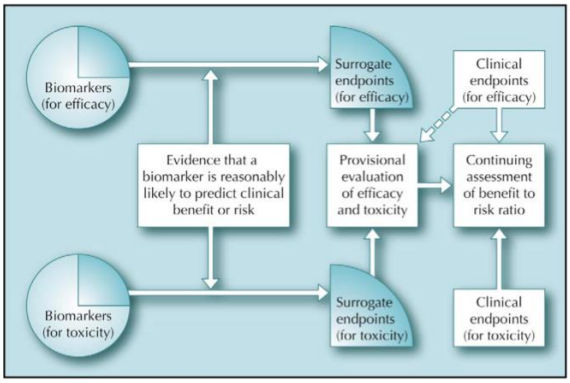

Figure 1.11: Conceptual model of the relationship of biomarkers, surrogate endpoints, and the process of evaluating therapeutic interventions. (Reproduced from reference 86)

A selected biomarker based on these concepts considered to have following properties shown in Table 1.7 to be considered as an ideal biomarker and the five key features are 1) a biomarker adds independent clinical information 2) it should account for a large proportion of the risk associated with a given disease or condition 3) it should be reproducible 4) if it is to be used as a diagnostic test, it should be sensitive and 5) test should be readily available.[86]

Table 1.8: Ideal properties of biologic markers (biomarkers)

Properties and uses	**Ideal properties**
Physical properties	Stable, not susceptible to generation of artefacts or loss during processing or storage, independence od diet or dysmetabolism
Analytical properties	Extremely sensitive, Specific, Reproducible
Clinical and scientific validity properties	Biomarker levels reflect degree of brain injury, Biomarker levels reflect degree of clinical severity, Changes in biomarker levels corresponds closely to changes in patient's clinical status or prognosis, Lack of influence of disease symptoms or signs on the marker
Practical properties	Minimal invasiveness or patient discomfort, Low per-usage cost, Wide availability at treatment centers in all desired geographic location
Uses	Drug development, favoring early evaluation of efficiency and safety of new drug, Potential tool for predicting individual responses for the clinical response, If the biomarker level is influenced by the drug dose, it's use in preclinical trials might improve the dose range definition

1.9 Current biomarkers for strokes; Advantages and Disadvantages

Biomarkers that are available for stroke can be categorized into: 1) Imaging markers that measure the changes in the nervous system via brain imaging; 2) molecular biomarkers; and 3) pharmacodynamic biomarkers (biomarkers that are indicative of certain pharmacological responses useful in drug development)[87]

At present, no single biomarker with discriminative characteristics is robust enough to be clinically used in the diagnosis and management of patients with stroke. Biomarker candidates for stroke may be rationally identified to reflect components of the ischemic cascade as illustrated in Figure 1.12.[88]

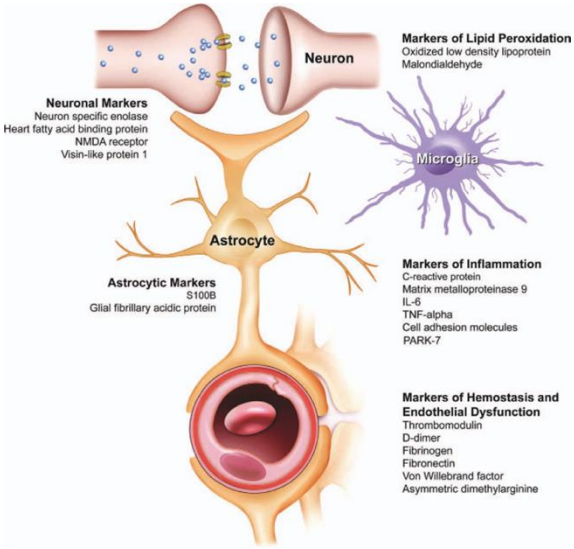

Figure 1.12: Potential biomarkers of stroke may be categorized by their role in the ischemic cascade. Representative markers for each category (neuronal injury, glial activation, lipid peroxidation, inflammatory, and hemostasis/endothelial dysfunction) are illustrated. IL 5 interleukin; NMDA 5 N-methyl-D-aspartate; PARK 5 Parkinson disease protein; TNF 5 tumor necrosis factor. (Reproduced from reference 88).

In the next sections, possible molecular biomarkers found in bodily fluids like blood, plasma, serum and CSF for stroke are discussed briefly. During any brain disease several biomarkers can be released into the CSF and then enter the blood stream, however all these markers

may not be specific to stroke conditions. Sub groups of these markers (Figure 1.12) will be explained in briefly in the next section.

1.9.1 Markers of glial activation, inflammation and oxidative stress

After a stroke event due to the damage that will happen to the BBB, proteins that are released from neurons and glia will enter into the blood stream.[89] These proteins and their levels in blood could be measured and potentially could be used in diagnosing stroke conditions. Glial activation, neuronal injury, oxidative stress, and release of inflammatory mediators are some of the early events that take place just after a ischemic stroke event.[89] S100B, glial fibrillary acidic protein and myelin basic protein are considered to be the markers that are relatively specific to glial function and studies have shown that these markers could be used for predicting risk of hemorrhagic transformation, prognosis, infarct volume and early stroke diagnosis.[90-93] C-reactive protein (CRP) , matrix metalloproteinase 9 (MMP9), interleukin 6 (IL6), adhesion molecules, and tumor necrosis factor alpha (TNF-alpha) are the nonspecific inflammatory markers that are released due to the neuro-inflammatory cascade that have been studied for prognosis and diagnosis for ischemic stroke.[94-99] But due to the limited specificity, these are not used clinically useful for stroke diagnosis.[100] Among these markers S100B is considered to be a major candidate for stroke diagnosis in the research field, but latency in release and lack of specificity to stroke conditions limits its use in clinical applcations.[101]

Oxidative stress and lipid peroxidation can also take place as a result of neuro-inflammation as some early events in neuronal injury. Some of the biomarkers related to these are redox sensitive molecular chaperone, lipid oxidation products like malondialdehyde and oxidized low-density lipoprotein.[102-104] However many of these oxidative stress markers are not specific to the brain, therefore it is better to use lipids that are highly enriched in the brain as potential markers. As an example, the F_4-neuroprostane, which is a byproduct of free radical-induced oxidation of

docosahexaenoic acid, is a fatty acid that is highly enriched in CNS. Thus, this could be a good potential candidate as a stroke biomarker.[105]

1.9.2 Markers of Neuronal Injury

After the initial events of glial activation and inflammation that occurs with a stroke event, glutamate excitotoxicity and oxidative stress can result and increase in neuronal injury and eventually result in neuronal death.[88] One of the extensively studied markers of neuronal injury is neuron specific enolase (NSE). As shown in Figure 1.13, the release patterns of NSE after a stroke event was studied and the authors observed an increment in NSE levels in ischemic stroke patients' serum samples after 48 h of the stroke event, which is out from the 4.5 h therapeutic window for effective treatment, which is a disadvantage of this marker as a potential biomarker for AIS.[106]

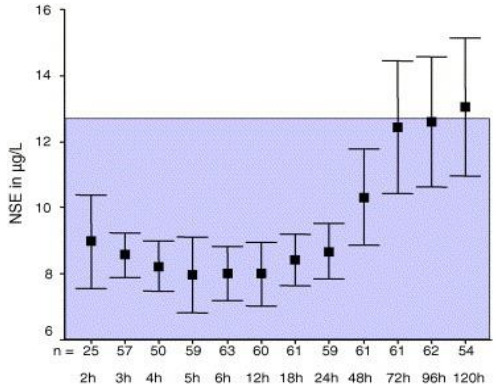

Figure 1.13: Release of NSE in acute stroke. Data shown as means ± 95% CI. Shaded areas indicate the respective reference range (12.5 µg/L) (Reproduced from reference 106).

Some other neuron specific markers are N-methyl-D-aspartate receptor (NMDA-R), visinlike protein I, and heart fatty acid binding protein.[107-108]

1.9.3 Markers of hemostasis and endothelial dysfunction

During cerebral ischemia, hypoxic endothelial cells will upregulate cell adhesion molecules and sub-endothelial matrix proteins will be released into blood. Platelets adhere to the vessel wall by binding of the platelet surface receptors to endothelial von Willebrand factor (vWF)

and adhesion of platelets to collagen, which can result in reduction of blood flow and delayed injury. Some of the classic hemostatic markers that are identified as potential biomarkers of stroke are thrombomodulin, D-dimer, fibrinogen, fibronectin, and vWF.[94, 96, 109-111]

Few studies have been conducted with plasminogen activator inhibitor-I (PAI-I), D-dimer, and thrombin-activatable fibrinolysis inhibitor (TAFI), where researchers identified patients having risk of hemorrhagic transformation after tPA administration.[112] Asymmetrical dimethylarginine, which is also a marker of dysfunction, has been studied as a potential marker for subclinical cerebrovascular injury.[113]

1.9.4 Miscellaneous markers

There are many other biochemical measurements that do not belong to the categories that have been explained above but have been shown to be potential biomarkers for stroke in the literature. Brain natriuretic peptides (BNP) became elevated after AIS and subarachnoid hemorrhage. BNP is also used as a marker for diagnosing congestive heart failures. However, it's still unclear whether the increased levels of BNP are of cardiac or brain origin.[26, 114-115] Lipoprotein-associated phospholipase A2 is an enzyme that has the function of hydrolyzing oxidized phospholipids. This enzyme has also been studied as a biomarker for ischemic stroke.[116-117] Free hemoglobin has also been suggested as a potential marker for stroke because it has shown increased levels in ischemic stroke patients compared to healthy controls.[118] Calcium levels are also increased after 72 and 96 h of a stroke event, however more experiments need to be performed to determine the sensitivity and specificity of using calcium levels as a biomarker for stroke diagnosis.[119] Table 1.8 below summarizes the currently used biomarkers for stroke and their function.

Table 1.9: Currently used biomarkers for stroke and their function

Biomarker	Description and function	Ref	Disadvantages
<u>Markers of Glial Activation</u> 1. S100B 2. Glial fibrillary acidic protein 3. Myelin basic protein	Calcium binding protein which is expressed in astrocytes and oligodendrocytes Expressed by astrocytes (intermediate filament protein) Myelin sheath protein	[90] [120] [121]	limited specificity, latency in release
<u>Markers of Inflammation</u> 1. C-reactive protein 2. IL-6 3. TNF-alpha 4. Adhesion molecules	Acute phase protein Inflammatory cytokine Inflammatory cytokine Immunoglobulin super family members	[95] [122] [123] [124]	latency in release, lack of specificity to stroke conditions
<u>Markers of oxidative stress</u> 1. PARK-7 2. Malondialdehyde 3. Oxidized low density lipo-protein	Redox-sensitive molecular chaperone Lipid peroxidation product Lipid peroxidation product	[125] [126] [104]	these oxidative stress markers are not specific to the brain
<u>Markers of neuronal injury</u> 1. Neuron specific enolase 2. Heart fatty acid binding protein 3. NMDA receptor	Neuronal glycolytic enzyme Involved in intracellular fatty acid transport (Cytosolic protein) Excitotoxic receptor	[106] [127] [107]	Late response to stroke conditions
<u>Markers of Hemostasis and Endothelial dysfunction</u> 1. Thrombomodulin 2. D-dimer 3. Von Willebrand factor	Endothelial cell glycoprotein (anticoagulation properties) Fibrin degradation product Glycoprotein involved in platelet adhesion stabilization	[109] [128] [129]	lack of specificity to stroke conditions
<u>Miscellaneous markers</u> 1. Natriuretic peptides (ANP, BNP) 2. Lipoprotein associated phospholipase A2 3. Calcium 4. Free hemoglobin	Vasoactive peptide hormones Hydrolytic enzyme Physiologic ion Erythrocyte protein	[26] [117] [119] [118]	Lack of specificity to stroke conditions, Late response to stroke conditions

1.10 Gene expression profiling in peripheral blood as biomarkers of stroke

Gene expression profiling in peripheral blood for diagnosing many diseases has been a developing area of research. Gene expression profiling measures which genes are being expressed in a cell at any given moment. This method can measure the activity of thousands of genes at a time and even the entire genome can be measured at one time.[130]

Alterations in the gene expression, that is upregulation and/or downregulation of gene activity and monitoring the changes in mRNA expression levels of cells can be studied in response to many diseases and this information can be used as biomarkers for disease management.

Developing biomarkers based on mRNA expression in body fluids, especially in blood, has become an emerging and exciting area of research. mRNA biomarkers offer numerous advantages over protein-based biomarkers, which were discussed in previous sections. mRNA is induced more quickly in response to disease when compared to protein expression. In addition, mRNA expression analysis can offer high throughput because thousands of genes can be analyzed at the same time.[131]

1.11 Peripheral blood mononuclear cell (PBMC) mRNA markers

Moore *et al.* were the first to investigate and publish gene expression profiling in circulating peripheral blood mononuclear cells containing monocytes and lymphocytes were used from stroke patients using microarrays.[132] They showed that after an ischemic stroke, within 72 h there was a predominant up regulatory response in PMBCs. They were able to identify 22 genes for stroke diagnosis with 78% clinical sensitivity and 80% clinical specificity.[132] In another study performed by Tang *et al*., (based on microarray studies), they found that 17 genes were upregulated during an ischemic stroke event.[133]

In another study a panel of 30 genes were identified for intracerebral hemorrhage (ICH) using reverse transcription PCR (RT PCR) and the investigators were able to obtain >85% accuracy for ICH diagnosis.[134] Furthermore, they identified that two genes, amphiphysin (*AMPH*)

and *IL1R2* were expressed differently in hemorrhagic and ischemic stroke patients, which showed that gene profiling could be potentially used for differentiating between the two types of stroke.[134]

These studies show the utility of gene expression profiling for stroke diagnosis. Due to the emerging advances in gene profiling methods, use of gene expression profiling for stroke diagnosis has become one of the most valuable research areas.

1.12 microRNA (miR) markers

microRNA (miR) are recognized as important post-transcriptional regulators of gene expression. miR, through a variety of mechanisms like mRNA degradation and regulation of translation, control the expression for ~30% of all transcripts. Although miRNA was discovered about 10 years ago, many researches have conducted research to identify and characterize their functions.

In a recent study, microarrays were utilized for the first time to study the whole blood miRNA changes specific to acute stroke.[135] Microarray is a tool that is used to detect the expression of thousands of genes at the same time. DNA microarrays are microscope slides with thousands of tiny spots in defined positions, with each spot containing a known DNA sequence or gene. These DNA molecules attached to each slide act as probes to detect gene expression, that are also called as transcriptome, or the set of mRNA transcripts expressed by a group of genes. In their study, they found that miR-122, miR-148a, let-7i, miR487b were decreased in patients with acute stroke while miR-363 and miR-487b were increased in stroke patients. This study provided an important extension on the potential application utilizing mRNA and miR for stroke diagnosis.

1.13 Application of mRNA markers in circulating leukocytes

In a recent study performed by Adamski *et al.,* high throughput RT-PCR (HT RT-qPCR) was used to verify the results of microarray studies. They used circulating leukocytes, which contain multiple cellular subsets with highly specific functions.[136]

As the innate immune response is known to be the major system involved in AIS, it could be hypothesized that the cells of the innate immune response, that is circulating granulocyte (neutrophils) would be the main leukocyte subsets showing altered gene expression.[7, 137-138]

The investigators performed density gradient centrifugation with Histopaque 1077 and 1119 to separate blood mononuclear cells (PMBCs) and granulocytes from whole blood. Then, the granulocyte fraction was purified to CD15+ and the PMBC were used to isolate positive fractions of CD14+, CD4+, CD20+ and CD8+ leukocyte subsets. RNA was extracted from these cells and 40 transcripts identified in previous studies were selected for analysis, which are shown in table 1.9.

Table 1.10: Stroke related transcript panels identified in microarray gene expression studies

Transcript And Study	**Up or down-regulation**	**Transcript And Study**	**Up or down-regulation**
PBMCs		**Whole Blood**	
MOORE et al 20051		**TANG et al, 20062**	
CD163	UP	*Hox 1.11*	UP
PLBD1	UP	*CKAP4*	UP
ADM	UP	*S100A9*	UP
KIAA0146	UP	*MMP9*	UP
APLP2	UP	*S100P*	UP
NPL	UP	*F5-1*	UP
FOS	UP	*FPR1*	UP
TLR2	UP	*S100A12*	UP
NAIP	UP	*RNASE2*	UP
CD36	UP	*ARG1*	DOWN
DUSP1	UP	*CA4*	UP
ENTPD1	UP	*LY96*	UP
VCAN	UP	*SLC16A6*	UP
CYBB	UP	*HIST2H2AA3*	UP
IL13RA1	UP	*ETS2*	UP
LTA4H	UP	*BCL6*	UP
ETS2	UP	*PYGL*	UP

CD14-1	UP	*NPL*	UP
CD14-2		UP	
BST1	UP	**BARR et al, 20103**	
CD93	UP	*ARG1*	DOWN
PILRA	UP	*CA4*	UP
FCGR1A	UP	*CCR7*	UP
VCAN		UP	
IQGAP1		UP	
LY96		UP	
MMP9		UP	
ORM1		UP	
S100A12		UP	

Based on the HT-RT qPCR results, they found that individual genes were significantly upregulated in ischemic stroke patients in 4 leucocyte populations. In CD15+ granulocytes, 14 genes were upregulated while in CD8+ T-lymphocytes 16 genes were upregulated. Two and 1 gene were upregulated in γδ TCR+ cells and CD4+ T lymphocytes, respectively. Figure 1.14 below illustrates the gene alterations in AIS patients.

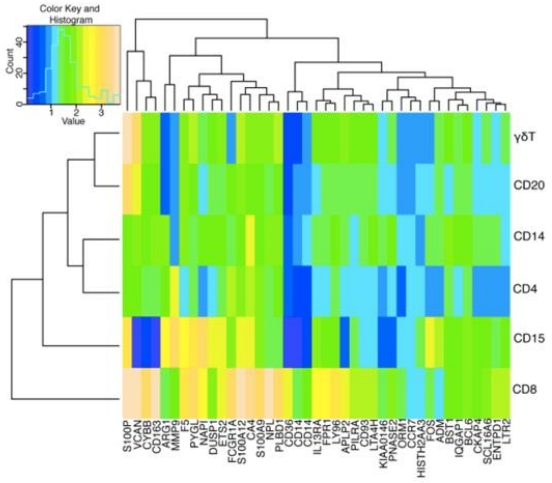

Figure 1.14: Hierarchical cluster analysis and heatmap of fold changes in expression of 41 genes, in 6 leukocyte subsets, between IS (n=18) and control subjects (n=15). (Reproduced from reference 136).

Furthermore, in hierarchical cluster analysis 43 cluster of transcripts were identified specific to six subsets that showed a significant discrimination between stroke and healthy controls. All these subsets are listed in Table 1.10.

Table 1.11: Gene expression clusters significantly characteristic for IS identified in hierarchical cluster analyses in 4 leukocyte subsets.

Transcripts	P value, of cluster, stroke versus control	Adjusted p value*	Adjusted p value**
CD15- Cluster 1 *IQGAP1, SLC16A6, NPL, CD93, PYGL, PLBD1*	9.4e-6	8.84e-5	4.41e-4
CD15- Cluster 2 ADM, CKAP4, FOS, BST1	2.94e-5	1.73e-4	1.38e-3
CD15- Cluster 3 ENTPD1, IL13RA1, LTA4H, S100P	9.7e-5	3.80e-4	4.56e-3
CD15- Cluster 5 *DUSP1, HIST2H2AA3, BCL6, PILRA, FCGR1A, TLR2*	7.70e-5	3.29e-4	3.62e-3
CD15- Cluster 7 LY96, S100A9, FPR1, S100A12, RNASE2, CCR7	0.0012	3.01e-3	5.73e-3
CD15- Cluster 8 CA4, MMP9, NAIP	6.14e-7	9.62e-6	2.88e-5
CD14- Cluster 4 *PLBD1, BST1, LTA4H, CYBB, SCL16, BCL6, VCAN, FCGR1A*	0.00019	6.38e-4	8.93e-3
CD4- Cluster 3 IQGAP1, NPL, FOS, PLBD1, BST1, VCAN	0.000146	5.28e-4	6.86e-3
CD8- Cluster 1 *IL13, APLP2, ENTPD1, ETS2, PYGL, DUSP1, KIAA, ADM, S100P, CD36,*	3.64e-7	8.55e-6	1.71e-5
CD8- Cluster 3 CYBB, BST1, CD93, NPL, IQGAP1	0.00021	6.58e-4	9.87e-3
CD8- Cluster 4 FOS, VCAN, PLBD1, MMP9, CA4	1.42e-5	1.11e-4	6.67e-4
CD8- Cluster 5 BCL6, SLC16, LTA4H, CKAP4, FPR1, FCGR1A	2.58e-5	1.73e-4	1.21e-3
γδT- Cluster 1 *IQGAP1, NPL, FOS, DUSP1, CD93, CKAP4, PLBD1, BST1, VCAN*	7.52e-6	8.84e-5	3.53e-4
γδT- Cluster 4	5.19e-5	2.44e-4	2.44e-3

ETS2, IL13, ENTPD1, PYGL, ADM, KIAA, APLP2, MMP9, CA4			

Wilcoxon rank sum tests were used for the analyses, *- (False discovery rate) FDR, **Bonferroni correction (Made for inflated Type I error (the higher the chance for a false positive, rejecting the null hypothesis when you should not))

They also validated a 3 gene expression cluster for stroke diagnosis from CD15+ granulocytes (CA4, MMP9, NAIP). Figure 1.15 shows the validation studies performed on these genes and based on the results, the overall accuracy of the 3-gene cluster classified stroke with a clinical sensitivity of 89% and a clinical specificity of 67%. Based on the results (clinical sensitivity of 89% and a clinical specificity of 67%.) we can see that the upregulation of these gene subsets could be potentially used as to identify the ischemic stroke conditions.

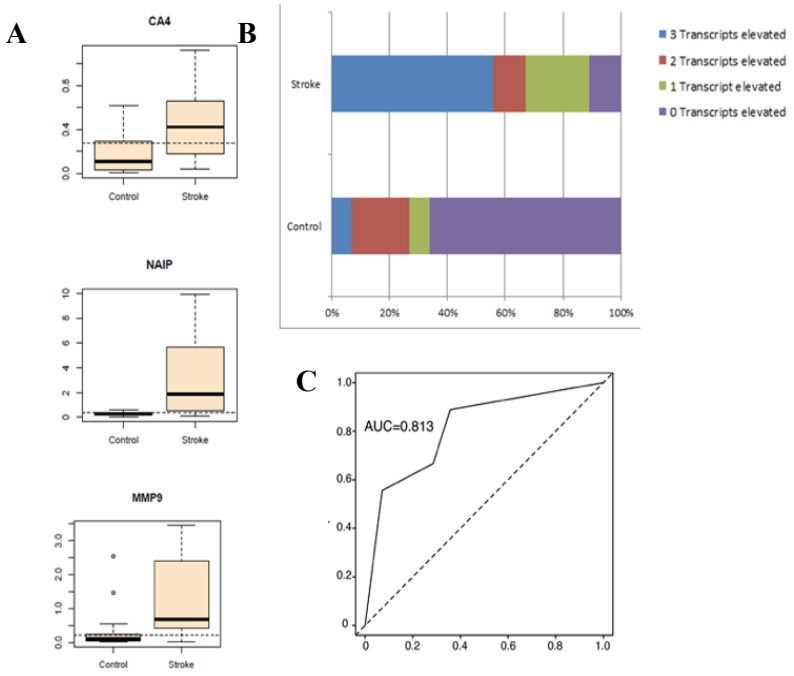

Figure 1.15: (A) Boxplots demonstrating the threshold values for defining elevated expression of each of the transcripts (CA4, NAIP, MMP9). (B) Bar graphs depicting the number of transcripts elevated in the stroke patients and the control subjects. (C) ROC analysis for Cluster 1 for stroke classification revealed that the AUC was 0.813. Elevation of 3 or more transcripts gave the greatest sensitivity and specificity**.** (Reproduced from reference 136)

1.14 Microfluidic device for cell selection with potential applications in clinical applications

Previous studies have been performed on developing a microfluidic device for the selection of leukocyte subsets directly from peripheral blood.[139] The device developed by Pullagurla *et al.*, uses antibodies, which are covalently attached to the surface of the microfluidic that enables the affinity selection of leukocyte subsets with high efficiency. The device consists of a series of sinusoidal channels containing anti CD4 and anti CD66b mAbs that targets specific types of cells. This device was designed so that it can simultaneously capture multiple cell types in blood. In this study, T cells and neutrophils from whole blood were captured and as shown in Figure 1.16 C, CD66b-positive neutrophils expressed higher levels of S100A9 gene that was considered to be overexpressed in a stroke event.[140]

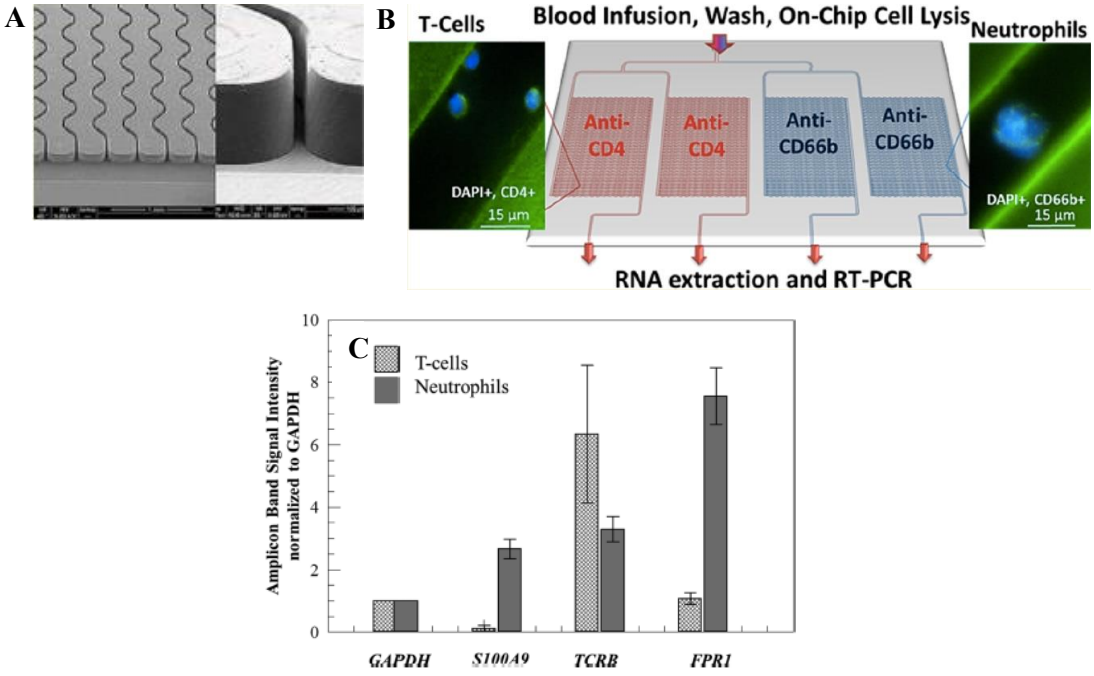

Figure 1.16: A Lab-on-a-Chip device for the selection of leukocyte subsets directly from the peripheral blood. (A) SEMs of a cell selection chip containing high-aspect ratio channels with a sinusoidal architecture. (B) Parallel arrangement of cell selection microchips for the simultaneous isolation of T cells (using anti-CD4 antibodies) and neutrophils (using anti-CD66b antibodies). (C) Gene expression profiling of selected genes from T cells and neutrophils. The mRNA transcripts were harvested from selected cells and subjected to RT-qPCR. (Reproduced from reference 140)

For clinical applications, isolation of leukocyte subsets using microfluidics and analyzing the molecular content via PCR methods offer many advantages over other gene profiling techniques such as micro array. As discussed in previous sections time is the most critical factor in stroke diagnosis. Microarray techniques requires approximately 11 h to obtain the necessary data. Also, special instruments are required with experienced personnel to acquire the necessary data, which is not conducive to POCT.[141] But, microfluidic platforms can be developed for POCT easily because they deliver fast analysis times and ease of use with minimum equipment.

1.15 Challenges in using circulating leukocytes as a source mRNA for stroke diagnosis

According to the previous studies, using blood samples from stroke patient's mRNA changes in the leukocytes were observed in ~5 h after a stroke event. Only 66% of the patients showed a significant change in the gene expression differences after 2.4 h, 87% of the patients showed significant differences after 5h, and 100% of the patients showed differences in gene expression after 24 h.[133] These results reveal that, we must at least wait 5 h before collecting blood for gene expression analysis since 87% of the patients showed a significant difference 5 h after an ischemic stroke event. But then it can be late for efficient therapeutic treatments. Therefore, we need to look for new sources of mRNA markers that show a quicker response to ischemic stroke conditions.

1.16 Extracellular vesicles as a potential source of mRNA markers for stroke diagnosis

The cellular release of various types of molecules have been studied for some time and based on the results, it is clear that cells release vesicles of varying sizes through both the endosomal pathway and by budding from the plasma membrane. These vesicles are known by different names including exosomes, microvesicles, apoptitic bodies and collectively termed as extracellular vesicles (EVs). These subtypes of EVs are based on their biogenesis and release pathway.[142] Most of the cells in the blood including leukocytes, platelets, red blood cells and endothelial cells release EVs.[143]

1.17 EV subtypes

1.17.1 Microvesicles

Microvesicles (MVs) are heterogeneous, membrane bound vesicles shed from the surface of a myriad of cell types including embryonic stem cells, neurons and astrocytes.[144] MVs can range from 100 nm to 1 μm in size. In recent years, investigations have been done to analyze their important roles in altering the extracellular environment, intracellular signaling and facilitating cell invasion through cell-independent matrix proteolysis.[144] MVs transfer a valuable cargo of bioactive molecules such as proteins, mRNA, and miRNA that is transferred between cells.[145] MVs can be found in a variety of bodily fluids such as blood, urine and saliva, which has increased the interest in research on MVs that reveal their functions in both healthy and diseased tissues.[146] Mechanism of MV release is illustrated in Figure 1.17.[144, 147] MVs are membrane (lipid bilayer) enclosed heterogeneous structures. On the surface of MVs there are surface markers such as CD63, CD81, CD9 and inside an EV there are lipids, proteins and different types of RNA.

Almost all of the eukaryotic cell types release MVs under both physiological and disease conditions.[148] The function of MVs are determined by the vesicle cargo content, which will depend on the cell type from which they are shed. Cargo contained inside MVs participate in a variety of biological functions and some of them are listed in Figure 1.18.[149]

MV biogenesis takes place through direct outward blebbing and pinching of the plasma membrane releasing the MVs into extracellular space.[150-151] Membrane blebbing is accompanied by other localized changes in plasma membrane protein and lipid components that will result in changes in the membrane curvature and rigidity.[152] Although MVs have been studied as novel means of cell-cell communication the mechanisms of their formation and release is still not understood completely.[149]

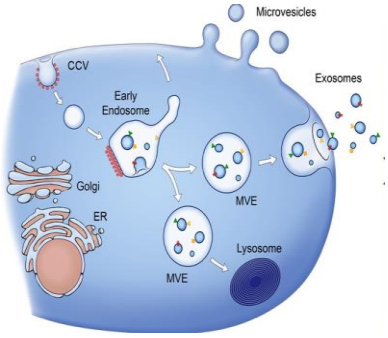

Figure 1.17: MV biogenesis through direct outward blebbing and pinching of the plasma membrane releasing the MVs into extracellular space (Reproduced from references 144).

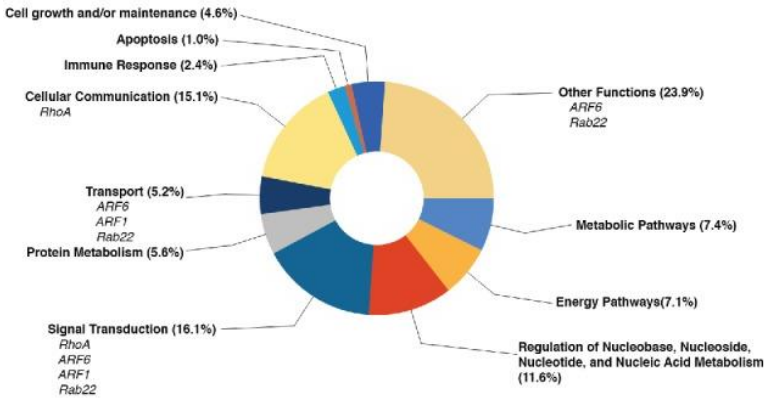

Figure 1.18: Common biological functions of MV protein cargo (Reproduced from reference 149).

a. Biological roles of MVs (Blood cell derived MVs, coagulation, inflammation and immunity)

MVs can be utilized in both pro-inflammatory and anti-inflammatory effects by transferring of cytokines and chemokine receptors to the recipient cells, and induce the cells to release cytokines.[153-154] MVs could also regulate the inflammatory responses in cytokine independent mechanisms, such as apoptotic induction of immune cells via vesicle associated FasL (FasL is a ligand involved in the regulation of cell death) signaling.[155] Because inflammation itself stimulates coagulation, it has been shown that the roles of blood cell-derived microvesicles in coagulation, immunity, and inflammation are interconnected.[156] Coordination of these physical functions that are controlled by MVs has an important role in development of cardiovascular disease.[157] Other

than blood cell-derived MVs, there are tumor cell-derived MVs that transfer growth factor receptors, increase cell motility, induce angiogenesis, and develop drug resistance.[158]

Stem cell microvesicles is another type of MVs that are important in crosstalk between stem and injured cells. MVs shed from damaged cells may facilitate the differentiation-dependent repair associated with the stem cell-based therapies.

1.17.2 Exosomes

Exosomes are the smallest of the EV family, which has the size ranging from 30 -150 nm and are released to the extracellular environment after the fusion of late endosomes/multivesicular bodies (MVB) with the plasma membrane.

Few cellular steps need to be completed in order to release exosomes. Those steps include formation of intraluminal vesicles (ILVs) in MVBs, transport of MVBs to the plasma membrane, and fusion of MVBs with the plasma membrane. Many molecules as shown in Figure 1.19, are involved in the exosome release process but its challenging to distinguish them experimentally. A simplified diagram showing the mechanism for exosome release is shown in Figure 1.19.[159]

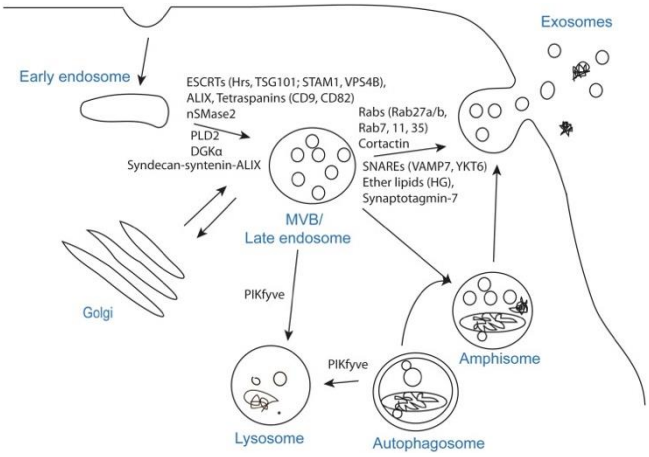

Figure 1.19: Molecules involved in exosome release (Reproduced from reference 159).

a. Exosome biogenesis

Exosome biogenesis starts within the endosomal system, early endosomes mature into late endosomes or MVBs, and during this process endosomal membrane invaginates to form intraluminal vesicles (ILVs) in the lumen of the organelles.[160] Endosomal sorting complexes required

for transport (ESCRT) machinery is shown to be important in this process, which consists of four protein complexes ESCRT 0, I, II, III and the associated AAA (ATPase associated with various cellular activities) Vps4 complex.[161] Some studies have suggested that MVB biogenesis can occur without ESCRTs. For example, it has been shown that even by silencing of key subunits of all ESCRT-complexes, ILVs are still formed in MVBs.[162] Expression of the tetraspanins, CD9 and CD82, have been shown to enhance exosome release of β-catenin from HEK293 cells.[163] Another tetraspanin that has been shown to be involved in exosome biogenesis is Tspan8.[163-164] Other than proteins, lipids are also important in vesicular transport. Both proteins and lipids are important in processes such as membrane deformation, fission and fusion and these processes are important for vesicular transport.[152] Figure 1.20 below shows a structure of an exosome.[165]

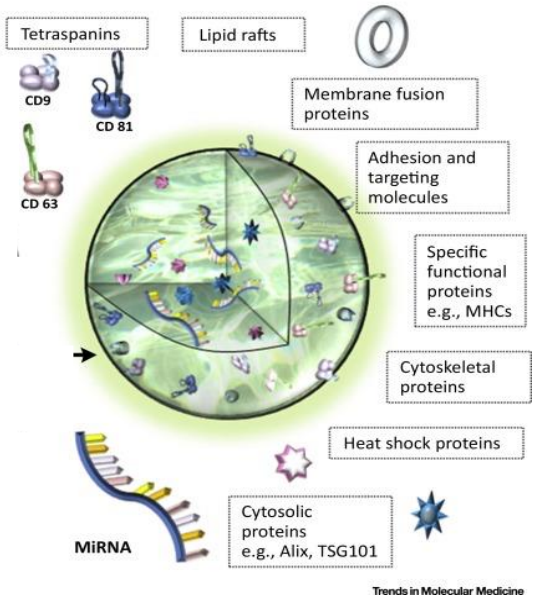

Figure 1.20: Structure of an exosome (Reproduced from reference 165).

b. Packaging of cargo into exosomes

Exosomes contain different proteins, lipids and nucleic acids. The composition of exosomes are cell type dependent and can be influenced by different cellular conditions or treatments.[159] Although several studies have detailed the exosome cargo, less is known about whether and how the cargo is selected and subsequently packaged into vesicles. Certain miRs are enriched in exosomes relative to the cells from which the exosomes originate, which indicates that miR can be

preferentially packaged into exosomes.[166] miRs also have been shown to be selectively enriched in exosomes. Exosomal mRNA shows enrichment in 3' UTR (untranslated regions) fragments, and these could play a role for mRNA sorting into vesicles.[167-169] Lipids are also shown to be important for packaging of specific proteins into exosomes. Some studies have shown that exosomes are enriched in cholesterol, sphingomyelin, and glycosphingolipids compared to their parent cells.[170] This suggests that exosomal membranes may contain lipid rafts and membrane subdomains that are enriched in cholesterol and glycosphingolipids, which are important in signaling.

1.17.3 Apoptotic bodies

Apoptotic bodies, another type of EVs, are released as a product of apoptotic cell disassembly. Both exosomes and microvesicles are released from healthy cells however dying cells can also release a variety of EVs, and apoptotic cell-derived EVs as shown in Figure 1.21.[171] These can range from 500 -1000 nm in size.

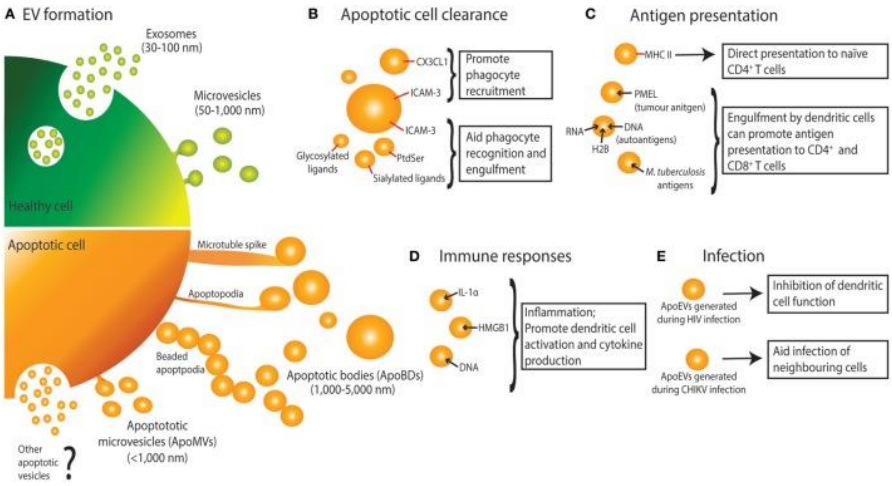

Figure 1.21: (A) Formation of apoptotic bodies (B) Apoptotic bodies release signals to attract phagocytotic cells and to promote uptake by phagocytes (C) Antigen representation of apoptotic bodies (D) Immune responses of apoptotic bodies (E) Infection inhibition by cell activation (Reproduced from reference 171)

a. Generation of EVs during apoptosis

During apoptosis, cells undergo a series of morphological changes that result in the dismantling of dying cells.[172] Disassembly of cells can be categorized into three steps. The first step is the apoptotic membrane blebbing, the second step is thin membrane protrusion formation, and the final step is the generation of apoptotic bodies.[172-173] Other than apoptotic bodies, cells can also release smaller EVs like apoptotic macrovesicles, which have a size <1 μm possibly through membrane budding.[174-175]

b. Functions of apoptotic bodies

It has been shown that apoptotic bodies coordinate many intercellular signals to help their detection and removal. These signals are important to ensure the immunologically silent characteristic of apoptosis.[173] Also, apoptotic bodies can help in the clearance of apoptotic materials. For this, phagocytotic cells need to be directed to the site of cell death. According to the literature, apoptotic cells can release factors known as "find-me" signals so that they can attract phagocytes. There is also evidence supporting that apoptotic body-associated signals are also released from apoptotic cells.

Other than attracting phagocytes, formation of apoptotic bodies by cell fragmentation has been suggested to improve release of apoptotic material from cells. This might be due to the smaller size of apoptotic bodies, which makes it easy to be engulfed by phagocytes. Evidence has shown that dendritic cells can easily and readily engulf smaller apoptotic bodies than whole apoptotic cells.[176]

Like other types of EVs, apoptotic EVs can also regulate antigen presentation in many disease conditions, such as antimicrobial immune responses, autoimmunity and organ/transplant rejection. Furthermore, apoptotic bodies can protect many different biomolecules that can directly control immune cells through vesicle-associated cytokines that can drive inflammation and dictate responses of immune cells.

1.18 Why are EVs good biomarkers for stroke?

As discussed in the previous sections, there is a need to find new biomarkers for stroke and here, we propose EVs as a new biomarker for stroke. When a stroke event takes place, EVs that originate from leukocytes responding to tissue damage inside the brain could be a good source of mRNA markers for stroke diagnosis.

mRNA biomarkers have been suggested for diagnosing AIS by harvesting mRNAs from certain leukocyte subsets that are responding to inflammation in a blood vessel within the brain cavity, such as CD8-expressing T cells.[136] Thus, CD8-expressing leukocyte-derived EVs could be used as a source of AIS mRNA biomarkers due to the success of using CD8+ T-cells,[136] which are responding to inflammation in brain blood vessels. EVs will be a more abundant source of mRNA, which can be then be used for the expression profiling at an earlier time because time is the most critical factor in stroke diagnosis and treatment.

1.19 The molecular composition of EVs

Understanding the molecular composition of EVs and their functions is important to study those as potential biomarkers for various diseases. EV cargo mainly contains various types of proteins and RNA. In next sections, EV cargo and their importance is discussed briefly.

1.19.1 Proteins and protein-associated functions of EVs

Most commonly found proteins in EVs are cytoskeletal, cytosolic, heat shock, and plasma membrane proteins. EVs also contain proteins that show post-translational modifications specifically reflecting the vesicle localization, cellular origin, and mechanism of secretion.[177] Characterization of EV protein content is widely conducted by immunoblotting, immuno-gold labelling combined with electron microscopy, and antibody-coupled bead flow cytometry analysis. Proteins in EV sub-populations that are used as markers (even though not necessarily specific to EV type) include tetraspanins such as CD9, CD63, CD81 and CD82, 14-3-3 proteins, major histocompatibility complex (MHC) molecules and cytosolic proteins such as specific stress proteins

(heat shock protein , HSPs), Tsg101, and the Endosomal Sorting Complex Required for Transport (ESCRT-3) binding protein Alix.[178] Previously, tetraspanins CD9, CD63, and CD81 were considered to be only specific for exosomes, but now it has been shown that these proteins are also present in apoptotic bodies and microvesicles.[77, 179] The common proteins of different types of EVs can be related to their biogenesis and to membrane curvature as shown on Figure 1.22.[180] Curvature-induced packaging of membrane constituents and the direct interactions can result in the formation of lateral microdomains with special composition (tetraspanin-enriched microdomains, membrane rafts) as shown in Figure 1.22.

The variable protein content in EVs may determine their functionality in different ways. The surface exposed receptors on EVs are responsible for biodistribution and for binding of EVs to target cells or to the extracellular matrix. EVs can trigger intracellular signaling pathways via a simple interaction with surface receptors or ligands of target cells. Furthermore, EVs can induce changes in the cell phenotype by transferring to the target cell active receptors such as CCR5, EGFRvIII or MET.[181-183]

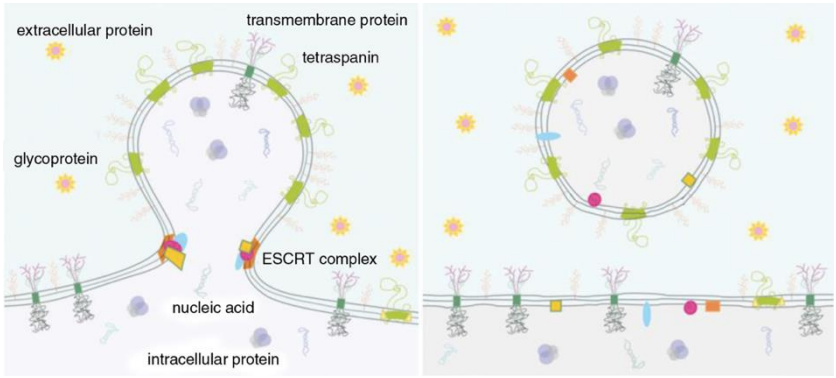

Figure 1.22: Curvature sorting mechanism of EVs (Reproduced from reference 181).

Biodistribution and targeting of EVs also have been studied recently. Studies have shown that half-life of purified exogenous EVs that have been artificially introduced to circulation is very short. One study showed that biotinylated rabbit EVs were cleared in rabbit circulation in about 10 min.[184] In another study, researchers have shown that EVs from splenocyte supernatants, red blood cell-derived EVs, and EVs from B16 melanoma cells showed a clearance of

~90% after 30 min.[185-187] Human platelet concentrate-derived EVs have been found to be in circulation with a half-life of 5.5 h.[188]

In addition to mediating the exchange of intercellular information, EVs have been shown to carry important mediators like cytokines. Interleukin 1 beta (IL-β) is one of the best-known examples of the involvement of EVs in cytokine transport. When IL-1β containing EVs are secreted, their cargo is released into the extracellular space upon binding of ATP to P2X7R on the EVs. Some other EV associated cytokines are interleukin 1α, Interleukin 18, Interleukin 32, Interleukin 6 and Interleukin 8.[180]

1.19.2 RNA composition

EV RNA can be found in many different forms. There are RNAs that are contained in EVs bound in protein complexes, and some RNAs can exist in freely circulating forms. The presence of functional RNA in EVs was first detected and described for murine stem cell derived EVs.[189] Although the cellular mRNA has a size range of about 400 to 12,000 nucleotides, EV RNA show a size of <700 nucleotides.[168, 190] EVs also contain intact mRNA, mRNA fragments, long non-coding RNA, miRNA, and fragments of tRNA.[168, 191-192] Previous studies have also shown that the absence of ribosomal 18S and 28S in EVs.[179, 192-194] However, some studies show the presence of rRNA(~87%) and some studies have shown the presence of rRNA fragments based on next-generation sequencing studies.[195-196] Studies have also shown the intraluminal localization of RNAs in EVs by RNase A treatment.[179, 197]

According to other studies, EVs show enrichment of 3' UTR mRNA fragments than intact mRNA molecules. Because 3' UTR regions contain multiple sites that can bind regulatory miRNA, there's the possibility that EVs may compete with cellular RNA for binding of miRNA or RNA-binding protein in recipient cells.[168]

Micro RNA also is secreted by EVs, which are about ~21 nt in size. miRNA is transcribed as hairpin precursors, cleaved by Dicer, bound by Argonaute proteins, and then loaded to miRNA

induced silencing complexes for mRNA target regulation. The loading of miRNA into EVs are mostly controlled by heterogeneous nuclear ribonuclear protein A2B1.[198] Some studies have shown that a sequence present within the 3' UTR in many mRNAs enriched in EVs can act as a "zipcode" sequence that targets mRNA into EVs. This specific sequence is a 25 nt sequence with a short CTGCC core domain in a stem-loop structure.[169] Studies have also shown that the addition of non-templated nucleotides to the 3' end of miRNA may help miRNA packaging into EVs.[199]

There are many biological functions of EV mRNA. mRNA containing EVs enhance the cell survival and repair of tissues under stress conditions.[200] mRNA found in human mesenchymal stem cell-derived EVs are involved in cell differentiation, transcription, cell proliferation and immune regulation.[201]

Previous studies have also revealed that the EV mRNA content is determined by the physiological state of the cell and stress conditions. In a study researchers have shown a significant difference in the mRNA content between the EVs derived from mast cells grown under normal conditions and under oxidative stress conditions.[202] Moreover EVs that are derived from large adipocytes have been shown to transfer specific mRNAs that are important in fatty acid esterification and lipid droplet biogenesis.[203]

Some research has revealed that disposal of some miRNA in EVs to be a quick way of regulating gene expression during lymphocyte activation and as a mechanism of tumor suppressor miRNA removal in cancer.[204-205] Also, miRNA transferred by EVs have immunological relevance. Some miRNAs from T-cell antigen-presenting cells (APCs) that is mediated by CD63+ EVs shown to be occurring during the immune synapse formation and these miRNAs modulate the gene expression in recipient cells.[166] There are some studies that showed the relevance of miRNA transfer in several physiological conditions, for instance miRNA in EVs may function as a neuron-to-astrocyte communication pathway in central nervous system.[206]

1.19.3 DNA Content of EVs

Unlike RNA content of EVs the presence of DNA in EVs less explored. However there are some studies showing the presence of oncogenic DNA in apoptotic bodies.[207] Few studies have shown the presence of mitochondrial DNA (mtDNA), single stranded DNA, double stranded DNA, and oncogene amplifications in EVs.[208-212] Transport of mtDNA can take place by EVs, thus EVs could be an another method of entering altered mtDNA into other cells.[209] In addition some studies have shown that different EV subgroups carry different DNA cargos.[213] Although these studies reveal that EVs carry DNA the physiological significance of DNA cargo in EVs is still unknown.

1.20 Diagnostic potential of EVs

Due to the valuable cargo of EVs as explained in previous sections, EVs are considered to be promising biomarkers for many diseases. Because EVs originate directly from parent cells, the content of the EVs are similar to the cells from which they originated. Furthermore, EVs are found in many bodily fluids in high abundance (healthy serum is estimated to contain approximately $3x10^6$ exosomes per microliter).[214] In addition, EVs have the potential to be used as drug therapy entities that can deliver pharmacologic cargo to a specific target.

In many diagnostic processes blood samples are being used because it is known that blood contains many biomarkers. In line with this, analysis of EVs in the peripheral blood is likely to provide an indicator of the systematic health status of people, which could be used in clinical settings.

Another advantage of using EVs as a biomarker over many other soluble molecules in the blood like hormones and cytokines is the inherent protection of the EV cargo, such as proteins and RNAs, from degradation thus keeping these cargos intact and functional. If not, these could rapidly degraded in blood.[167, 214] This has proven to be particularly significant for the use of mRNA since most of the RNA in blood exists as cargo of EVs.[215] Relatively long half-life of

EVs in blood is another major advantage of using EVs as a biomarker.[214] Hence, EVs can be transported from any location of the body to the blood stream making it easily accessible for liquid biopsy. Additionally, EV size distribution, phenotype, or cargo content can change during various disease states. Analysis of cell-specific and disease-specific EV profiles of their cargo will provide a fingerprint for disease diagnosis.

1.21 Currently used EV isolation methods

In order to analyze the EV cargo, first EVs of interest must be isolated in high purity and high yields from bodily fluids. With the increasing research studies conducted on EVs there are many techniques that have been developed to isolate EVs and each method has its own advantages and disadvantages. Some of the currently used EV isolation methods are discussed below.

1.21.1 Ultracentrifugation

Ultracentrifugation is the classical method used for EV isolation, which is based on separation of particles according to their buoyant density. First, the particles with high buoyant density like cells, cell debris, apoptotic bodies, and aggregates are sedimented. To decrease the level of contamination, this step is divided into sub steps: Centrifugation at 300-400g for 10 min to sediment cells; 2000g to sediment cell debris; and then centrifuge at 10,000g to remove the aggregates of biopolymers, apoptotic bodies, and other structures with a density higher than EVs. The resulting supernatant with EVs are ultracentrifuged at >100,000g for 2 h, which will yield an EV pellet .[216-217] Figure 1.23 below illustrates the steps involved in ultracentrifugation of FBS to remove EVs prior applying to the cell culture media.[218]

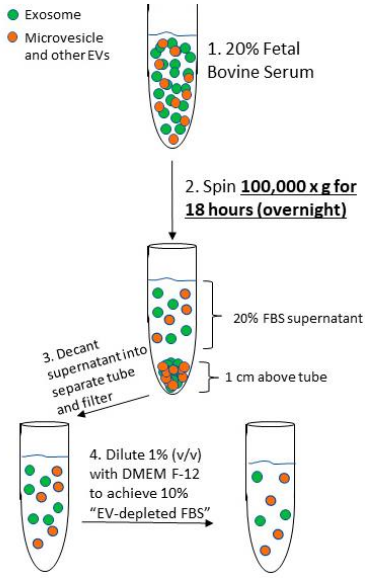

Figure 1.23: Ultracentrifugation to isolate EVs based on density of particles (Reproduced from reference 219).

Efficiency of EV isolation by ultracentrifugation depends on many factors like acceleration, type of rotor, and viscosity of the sample. Thus, these parameters need to be considered when optimizing the protocol to obtain less contaminated EVs. Long time duration and need of expensive equipment limits the use of ultracentrifugation in a clinical setting for diagnostic purposes. Moreover, ultracentrifugation cannot differentiate between subtypes of EVs that are specific to disease conditions.

1.21.2 Density gradient Ultracentrifugation

This technique uses two methods for formation of the gradient, a continuous density gradient or a stepwise gradient based on sucrose. High spin speeds for long times result in concentration of exosome-like vesicles in a band with closer densities (approximately 1.1-1.9 g/mL). Because different EV types can have similar densities, the isolation of EVs by density gradient does not provide a pure fraction of exosomes depleted of other EV types.[219]

1.21.3 Precipitation reagents

Different types of commercial kits have been developed with precipitation reagents that can be used to isolate EVs. These reagents, such as polyethylene glycol reduce the solubility by

lowering the hydration of EVs and lead to precipitation. These commercial kits can be used to separate EVs using lower spin speeds with higher yields compared to ultracentrifugation. But the disadvantages of these kits are low purity due to co-precipitation of proteins with EVs. This is because upon addition of the precipitation reagents, solubility of proteins is also decreased. [220] Another disadvantage associated with some of these kits is that long incubation times of up to 12 h are required.[221]

1.21.4 Size-based isolation of EVs

EVs can be separated from cells and large debris by using nano-sized membrane filters. Using these filters large debris including large vesicles, sub-cellular fractions, protein aggregates, protein-nucleic acid aggregates, and plasma proteins can be removed. Membrane filters with pore sizes 0.2, 0.22 and 0.45 μm, which are made of polyvinylidene fluoride, are widely used for removal of large particles.[222] Although these techniques can separate EV from complex samples, they cannot isolate EVs specifically. Combination of ultracentrifugation along with filtration has been shown to increase the purity of isolated EVs.[223]

1.21.5 Affinity-based isolation of EVs

All the methods that have been explained above isolate all types of EVs present in the sample. These methods cannot be used to isolate EVs that are only related to diseases. Thus, to isolate EVs that are specific to a disease state, many new isolation techniques utilize antibodies directed against certain antigens found in the membrane of the EV including microfluidic devices, immunomagnetic beads, photosensitizer beads have been reported.[222, 224] Various microfluidic devices have been developed to selectively isolate EVs. Simplicity of these techniques make those well suited for point-of-care (POC) diagnostics. Figure 1.24 (a) illustrates a microfluidic device that uses magnetic beads, which are about 3 μm in diameter and coated with anti-EGER to capture EVs from 100 μL of serum and has shown a capture efficiency of ~93%. This

device is an integrated device that can perform EV isolation to RNA analysis by qPCR in a single chip.[225]

In another study, after capturing EVs using anti-CD64-magnetic beads, electric field-induced release and measurement was used for disrupting exosomes and monitoring RNA and protein biomarkers.[226]

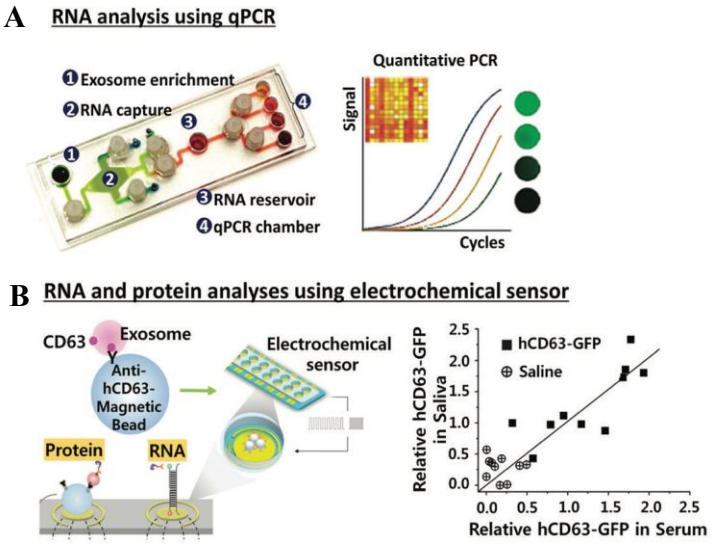

Figure 1.24: Microfluidic device with magnetic beads used for isolation of EVs. (a) RNA analysis using qPCR. (b) RNA and protein analysis using an electrochemical sensor. (Reproduced from reference 226, 227).

There are many devices that have been developed without using magnetic beads, where the surface of the device was modified with antibodies to capture EVs. Figure 1.25 A describes a device that consists of circular capture chambers to isolate EVs and then fluorescence assays were utilized to quantify the captured EVs.[227] In another study, an integrated nanostructured coating was used to reduce nonspecific interactions and this device was used to identify ovarian cancer patients from healthy controls (Figure 1.25 B).[228]

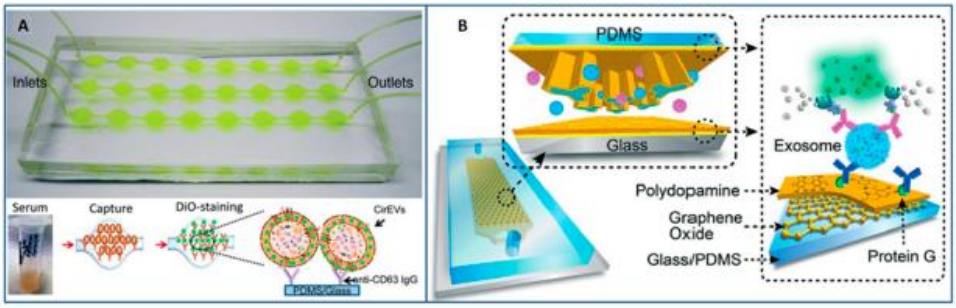

Figure 1.25: Microfluidic devices modified with Ab to capture EVs (a) Microfluidic device with circular capture chambers. (b) Microfluidic device with pillars to capture the EVs (Reproduced from references 228 and 229).

However, many of these microfluidic devices use general affinity-enrichment of bulk EVs by targeting the tetraspanins such as CD9, CD63, and CD81.[227, 229-230] This is a shortcoming because they cannot be used for isolating and analyzing a subset of EVs that are specific to diseased conditions.

Another drawback of microfluidic devices is the low sample processing speeds they possess, which requires long analysis times that can be a challenge when developing assays in which time is a critical factor. For example, a recent EV affinity isolation microfluidic device was reported, which used 3-dimensional herringbone nanopatterns, and operated at a volume flow rate of 0.5 µL min^{-1}, which would require 400 min (6.7 h) to process a volume of 200 µL of plasma.[13] Some advantages and disadvantages of the currently available EVs isolation techniques briery discussed in Table 1.11 below.[219]

Table 1.12: Advantages and disadvantages of EV isolation methods

Method	Time	Advantages	Disadvantages
Ultracentrifugation, differential centrifugation: 300 ×g, 10000 ×g, 100000–200000 ×g (1.5 h)	140–600 min	Cost (in the case of ultracentrifugation) isolation from large volumes absence of additional chemicals	Equipment, complexity, non-exosomal impurities, low reproducibility, low RNA yield, damage of exosomes; efficiency is affected by the type of rotor, force, sample viscosity; only six samples can be concurrently processed in one ultracentrifuge
Density gradient ultracentrifugation, sucrose or iodixanol density gradient, differential centrifugation	250 min–2 days	Pure preparations; no contamination with viral particles after iodixanol centrifugation; absence of additional chemicals	Complexity, loss of sample, ultracentrifugation; fails to separate large vesicles with similar sedimentation rates; contamination with viral particles after sucrose density gradient procedure
Ultrafiltration, nanomembrane or filters with a pore diameter of 0.8–0.1 μm	130 min	Simple procedure allowing for concurrent processing of many samples; pure preparations; additional chemicals; no limitations on sample volume	Filter plugging, loss of sample, contamination (proteins); deformation of vesicles; small quantity of exosomal proteins
Size-exclusive chromatography (SEC), columns filled with polymers with heterogeneous pores	1 ml/min + column washing	Reproducibility and purity; preserves vesicle integrity; use of the buffers with a high ionic strength enhances elimination of nonspecific impurities; high sensitivity, no losses, scalability, large amount of exosomal proteins; prevents EV aggregation; insensitive to high viscosity of samples; no additional chemicals	Limitations on sample volume and number of separated peaks (necessary difference of the components in molecular weight, ≥10%); specialized equipment; complexity; coisolation of large protein aggregates and lipoproteins; processing no more than one sample in each procedure; cost
Precipitation with polymers, polyethylene glycol caused EV precipitation	65 min	Cost and simplicity of procedure; preservation of EV integrity; no need in additional equipment; pH close to physiological range; high ion concentrations	Contamination and retention of the polymer

Commercial kits for polymer precipitation (ExoQuick, TEI, and Norgen), polymer precipitates EVs	45–65 min (sometimes overnight)	Simple procedure; preservation of EV integrity; no need in additional equipment; pH close to physiological range; high ion concentrations	Cost (especially for diluted samples, such as urine); poor reproducibility; impurities and retention of polymer; low content of exosomal proteins
Use of antibodies to EV receptors, in particular, tetraspanins (CD9, CD63, CD81), TSG101, EpCAM	about 240 min	Purity and high selectivity	High selectivity, cost, availability of antibodies; difficulties with detachment of molecules and analysis of intact vesicles (eluting buffers can damage EV functional activity); nonspecific binding
Microfluidic technologies	1–14 μl/min	Rapidness, purity, efficiency	Complexity of devices and need in additional equipment; cost

As discussed here, most of these isolation methods cannot be used in a clinical setting due to their complexity and long analysis time. Hence, efficient methods need to be developed to isolate and subsequently analyze EVs with high recovery and purity to be able to use them as diagnostic markers, which requires the analysis of their molecular cargo.

1.22 Methods of analyzing EVs

Once EVs are isolated by one of the methods described above the isolated EVs need to be analyzed by downstream assays, such as sizing of the EVs. For this purpose, a combination of different optical and non-optical techniques is used. Some of these methods are summarized below.

1.22.1 Size and morphological information

a. Transmission electron microscopy (TEM)

TEM provides structural information of EVs. Here EV suspensions are applied and fixed on grids for imaging. Figure 1.26 A shows TEM images of MDA-MB 231 EVs. TEM images are used to assess the size, morphology, and the presence of surface markers on EVs. But, the concentration of EVs cannot be determined by TEM.[223]

b. Atomic Force Microscopy (AFM)

AFM provides information about the surface characteristics of EVs and have been used to study the morphology of EVs. As TEM, AFM cannot be used for determining EV concentration.[230]

c**. Nanoparticle tracking analysis (NTA)**

A laser beam scattered by particles in solution and the mean velocity of the particles is determined based on the Strokes-Einstein equation. Based on the Brownian motion of particles in suspension, the software will provide the size distribution and the concentration of particles in the samples. However, prior to NTA it is required to remove the particles with similar sizes to EVs from the samples. NTA is the most widely used method for EV quantification. Figure 1.26 B shows a size distribution obtained for EVs.[228]

d. Dynamic light scattering (DLS)

DLS is used to determine the size distribution and zeta potential of EVs (Figure 1.26 C and d). This method is also based on the Brownian motion of particles. Particles in solution are illuminated with a laser and the light scattered by the particles at a specific angle is detected and intensity changes are then analyzed to find the size distribution of EVs in the sample.[222]

e. Zeta potential measurements

Zeta potential shows the stability of particles in a solution, which is determined by the velocity during electrophoresis where charged particles migrate towards the electrode under an applied electric field and the speed at which the particle is proportional to the field strength and the zeta potential. DLS provides the average size of relatively mono-dispersed population of isolated

EVs. Although no size difference was observed between EVs from cancer cells and EVs from normal cells, higher zeta potential values were observed for EVs derived from cancer cells.

f. Western blotting

This method is widely used to show the presence of EV proteins including surface markers like CD9, CD63, and CD81.[231] Isolated EVs need to be lysed first and then proteins are separated and analyzed. Although western blotting cannot be used alone to show the presence of EVs, it's useful in identifying proteins in already-isolated EVs. Figure 1.26 E shows a western blot analysis of proteins from EVs isolated from a microfluidic device.[232]

g. Bradford assay

This method can be used to quantify the total protein content of purified EVs. But care should be taken to remove any other protein contaminants present in the sample before performing the assay. Figure 1.26 F shows a result from a Bradford assay where the protein content of EVs isolated from non-small-cell lung cancer patients and from healthy donors is compared. Higher protein content was found in EVs from cancer patients and they also showed that larger number of EVs are present in-patient samples compared to healthy controls .[232]

h. Flow cytometry

Flow cytometry (FC) can be used for both qualitative and quantitative characterization of EVs. Standard FC can detect vesicles above 200 nm in size. Thus, EVs are typically fixed onto beads that are labeled with fluorophore-conjugated antibodies and then analyzed by FC. This will provide information about the surface markers proteins but does not provide quantitative information. Figure 1.26 G shows a flow cytometry analysis of surface markers of EVs.[233]

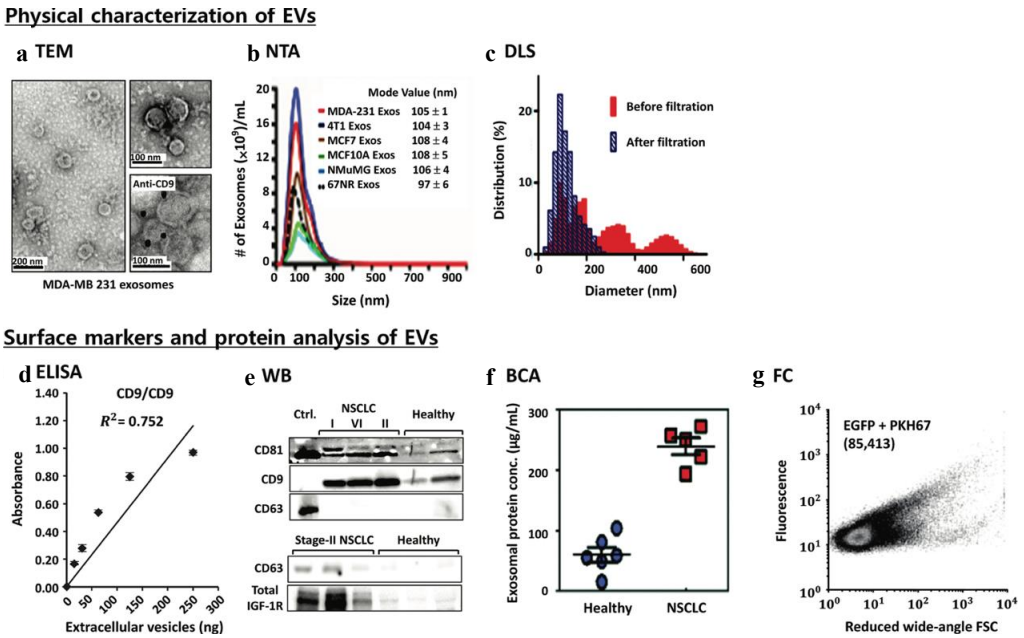

Figure 1.26: Currently used methods for EV characterization (a) Transmission electron microcopy. (b) Nano particles tracking analysis. (c) Dynamic light scattering. (d) ELISA. (e) Western blotting. (f) Bradford assay. (g) Flow cytometry (Reproduced from references 222,223, 228, 232, 233).

1.23 Molecular Analysis of the EV cargo

To be able to be used as diagnostic markers in most cases, the molecular content of the EVs need to be analyzed after isolation and characterization. Some of the currently used methods for molecular analysis of EVs are described below.

a. Fluorescence imaging

A recent study demonstrated the use of fluorescence imaging for analyzing EVs. To monitor EVs derived from cancer cells a lipophilic dye for capturing a lipid bilayer of EVs or a fluorescent probe fused with EV specific protein markers was used in this study. Figure 1.27 a illustrates fluorescence images of cells producing EVs GFP labelled EVs and their uptake by the recipient cells.[234]

b. Molecular Profiling

Because EVs contain proteins and RNA consisting primarily of short sequences (20-200 nt), molecular profiling of these entities has been widely used to examine their relationship with their

cellular origin.[222, 225] Quantitative reverse transcription PCR, miRNA analysis, bioanalyzers, and mass spectrometry are some of the currently used methods for profiling EV cargo. Figure 1.27 b shows the molecular profiling of protein markers performed to detect ovarian cancer patients. Using nano plasmonic exosome assay (nPLEX assay, they screened exosomes across different ovarian cancer cell lines and showed that exosomes derived from ovarian cancer cells could be identified by the expression of CD 24 and EpCAM.[222]

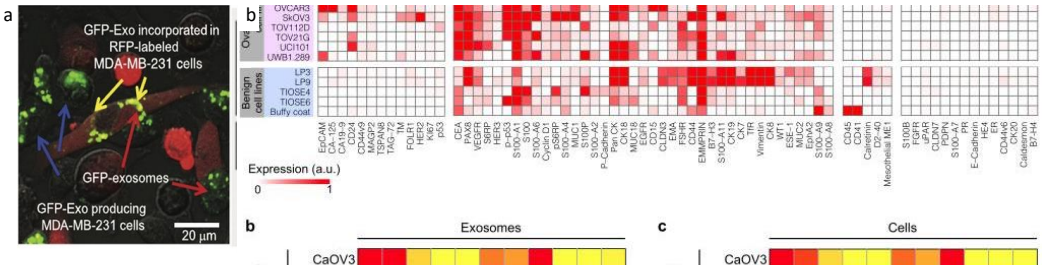

Figure 1.27: a) Fluorescence images of cells producing GFP-labelled EVs and their uptake by recipient cells. (b) Molecular profiling of protein markers. (Reproduced from references 237, 223)

1.24 Summary of thesis chapters

1.24.1 Chapter 2: Design and development of microfluidic devices fabricated in thermo-plastics for the selective capture of extracellular vesicles and biological cells as a source of stroke biomarkers

This chapter describes the development and characterization of a microfluidic device with micropillars that can be surface modified to capture EVs. The modeling of the device and the surface modification of the device's surface for affinity selection of EVs is explained in detail. Using a model cell line Molt-3, we showed that the EVs can be affinity selected by the device with high specificity. In addition, we demonstrated the release of EVs from the surface with high release efficiency. Lastly, using the model cell line, we showed that EV mRNA extracted from isolated EVs could be used for gene expression analysis for stroke detection.

1.24.2 Chapter 3: Microfluidic device platforms for affinity selection of CD8+ EVs and CD8+ T-cells from blood and plasma samples

The methodology developed in chapter 2 was utilized to analyze plasma samples and blood samples from healthy donors to check the applicability of our method to be used in a clinical setting. This chapter describes the use of microfluidic devices for affinity selecting both CD8+ EVs and CD8+ T-cells from plasma and blood, respectively. Following isolation, the mRNA extracted from both EVs and T-cells were analyzed using droplet digital PCR for gene expression analysis.

1.24.3 Chapter 4: Clinical application of microfluidic devices for stroke diagnosis

Because stroke diagnosis has to be done rapidly within a short time window of 4.5 h, the biomarkers need to be isolated within a short time with high recovery. In this chapter, a high capacity microfluidic device is described that can capture EVs within a short processing time enabling quick isolation and analysis of EV mRNA markers for stroke diagnosis. The developed microfluidic device was then used to analyze both healthy and stroke patient plasma samples (blinded study) and we demonstrated that the method developed can be successfully used for stroke diagnosis.

1.24.4 Chapter 5: Conclusions and Future directions

Additional gene panels and more clinical samples need to be analyzed to determine with better confidence the clinical sensitivity and specificity of the developed method. Moreover, animal model studies need to be performed to determine the actual time of appearance of EVs after a stroke event. Integrating the system to release the EVs from the device and enumerate them before gene expression analysis is another goal of this project. Finally, the system will be used in a clinical setting to isolate, release, enumerate and analyze EV mRNA to be used as stroke biomarkers for stroke detection.

1.25 References

1. Hill, M. D., What Kind of Stroke Is It? *Clinical Chemistry* **2008,** *54* (12), 1943-1944.
2. Dreyer, R.; Murugiah, K.; Nuti, S. V.; Dharmarajan, K.; Chen, S. I.; Chen, R.; Wayda, B.; Ranasinghe, I., Most important outcomes research papers on stroke and transient ischemic attack. *Circulation: Cardiovascular Quality and Outcomes* **2014,** *7* (1), 191-204.
3. Heidenreich, P. A.; Trogdon, J. G.; Khavjou, O. A.; Butler, J.; Dracup, K.; Ezekowitz, M. D.; Finkelstein, E. A.; Hong, Y.; Johnston, S. C.; Khera, A., Forecasting the future of cardiovascular disease in the United States: a policy statement from the American Heart Association. *Circulation* **2011,** *123* (8), 933-944.
4. The Internet Stroke Center. http://www.strokecenter.org/patients/about-stroke/stroke-statistics/.
5. Jauch, E. C.; Saver, J. L.; Adams Jr, H. P.; Bruno, A.; Connors, J.; Demaerschalk, B. M.; Khatri, P.; McMullan Jr, P. W.; Qureshi, A. I.; Rosenfield, K., Guidelines for the early management of patients with acute ischemic stroke: a guideline for healthcare professionals from the American Heart Association/American Stroke Association. *Stroke* **2013,** *44* (3), 870-947.
6. Association, A. S. Ischemic Stroke (Clots). https://www.strokeassociation.org/en/about-stroke/types-of-stroke/ischemic-stroke-clots (accessed 04/23).
7. Dirnagl, U.; Iadecola, C.; Moskowitz, M. A., Pathobiology of ischaemic stroke: an integrated view. *Trends in neurosciences* **1999,** *22* (9), 391-397.
8. Fisher, M.; Garcia, J. H., Evolving stroke and the ischemic penumbra. *Neurology* **1996,** *47* (4), 884-888.
9. Members, W. G.; Lloyd-Jones, D.; Adams, R. J.; Brown, T. M.; Carnethon, M.; Dai, S.; De Simone, G.; Ferguson, T. B.; Ford, E.; Furie, K., Executive summary: heart disease and stroke statistics—2010 update: a report from the American Heart Association. *Circulation* **2010,** *121* (7), 948-954.
10. Musuka, T. D.; Wilton, S. B.; Traboulsi, M.; Hill, M. D., Diagnosis and management of acute ischemic stroke: speed is critical. *CMAJ* **2015,** *187* (12), 887-893.
11. When strok strikes, act fast. https://www.myhealth.london.nhs.uk/services/urgent-care-london-walk-centres/when-stroke-strikes-act-fast/ (accessed 05/31).
12. "What is a Hemorrhagic stroke." Retrieved 05/31, 2019, from https://www.joeniekrofoundation.com/understanding/what-is-a-hemorrhagic-stroke/.
13. Zhang, P.; Zhou, X.; He, M.; Shang, Y.; Tetlow, A. L.; Godwin, A. K.; Zeng, Y., Ultrasensitive detection of circulating exosomes with a 3D-nanopatterned microfluidic chip. *Nature Biomedical Engineering* **2019**, 1.
14. Artto, V.; Putaala, J.; Strbian, D.; Meretoja, A.; Piironen, K.; Liebkind, R.; Silvennoinen, H.; Atula, S.; Häppölä, O.; Group, H. S. T. R., Stroke mimics and intravenous thrombolysis. *Annals of emergency medicine* **2012,** *59* (1), 27-32.
15. Hemmen, T. M.; Meyer, B. C.; McClean, T. L.; Lyden, P. D., Identification of nonischemic stroke mimics among 411 code strokes at the University of California, San Diego, Stroke Center. *Journal of Stroke and Cerebrovascular Diseases* **2008,** *17* (1), 23-25.
16. Nau, K. C.; Crocco, T.; Biola, J.; Larrabee, H., Is it stroke, or something else? Rapid response to stroke is crucial, but the rush to treat can endanger patients with conditions that mimic stroke. Here's how to more readily spot the difference. *Journal of family practice* **2010,** *59* (1), 26-32.
17. Brunser, A. M.; Illanes, S.; Lavados, P. M.; Muñoz, P.; Cárcamo, D.; Hoppe, A.; Olavarria, V. V.; Delgado, I.; Díaz, V., Exclusion criteria for intravenous thrombolysis in

stroke mimics: an observational study. *Journal of Stroke and Cerebrovascular Diseases* **2013,** *22* (7), 1140-1145.
18. Guillan, M.; Alonso-Canovas, A.; Gonzalez-Valcarcel, J.; Barragan, N. G.; Caldentey, J. G.; Hernandez-Medrano, I.; DeFelipe-Mimbrera, A.; Sanchez-Gonzalez, V.; Terecoasa, E.; De Leciñana, M. A., Stroke mimics treated with thrombolysis: further evidence on safety and distinctive clinical features. *Cerebrovascular diseases* **2012,** *34* (2), 115-120.
19. McKeith, I. G., Consensus guidelines for the clinical and pathologic diagnosis of dementia with Lewy bodies (DLB): report of the Consortium on DLB International Workshop. *Journal of Alzheimer's Disease* **2006,** *9* (s3), 417-423.
20. Khadilkar, S., Neurology: the scenario in India. *J Assoc Physicians India* **2012,** *60*, 42-4.
21. Khare, S., Risk factors of transient ischemic attack: An overview. *Journal of mid-life health* **2016,** *7* (1), 2.
22. Lyden, P.; Claesson, L.; Havstad, S.; Ashwood, T.; Lu, M., Factor analysis of the National Institutes of Health Stroke Scale in patients with large strokes. *Archives of neurology* **2004,** *61* (11), 1677-1680.
23. Lyden, P. D.; Lu, M.; Levine, S.; Brott, T. G.; Broderick, J., A modified national institutes of health stroke scale for use in stroke clinical trials. *Stroke* **2001,** *32* (6), 1310-1317.
24. Kasner, S. E., Clinical interpretation and use of stroke scales. *The Lancet Neurology* **2006,** *5* (7), 603-612.
25. Cavanagh, S. J.; Gordon, V. L., Grading scales used in the management of aneurysmal subarachnoid hemorrhage: a critical review. *Journal of Neuroscience Nursing* **2002,** *34* (6), 288-296.
26. Makikallio, A.; Makikallio, T.; Korpelainen, J.; Vuolteenaho, O.; Tapanainen, J.; Ylitalo, K.; Sotaniemi, K.; Huikuri, H.; Myllyla, V., Natriuretic peptides and mortality after stroke. *Stroke* **2005,** *36* (5), 1016-1020.
27. Nour, M.; Liebeskind, D. S., Brain imaging in stroke: insight beyond diagnosis. *Neurotherapeutics* **2011,** *8* (3), 330-339.
28. Adams Jr, H. P.; Adams, R. J.; Brott, T.; Del Zoppo, G. J.; Furlan, A.; Goldstein, L. B.; Grubb, R. L.; Higashida, R.; Kidwell, C.; Kwiatkowski, T. G., Guidelines for the early management of patients with ischemic stroke: a scientific statement from the Stroke Council of the American Stroke Association. *stroke* **2003,** *34* (4), 1056-1083.
29. Ginde, A. A.; Foianini, A.; Renner, D. M.; Valley, M.; Camargo, J., Carlos A, Availability and quality of computed tomography and magnetic resonance imaging equipment in US emergency departments. *Academic emergency medicine* **2008,** *15* (8), 780-783.
30. Wardlaw, J. M.; Seymour, J.; Cairns, J.; Keir, S.; Lewis, S.; Sandercock, P., Immediate computed tomography scanning of acute stroke is cost-effective and improves quality of life. *Stroke* **2004,** *35* (11), 2477-2483.
31. Morgan, C. D.; Stephens, M.; Zuckerman, S. L.; Waitara, M. S.; Morone, P. J.; Dewan, M. C.; Mocco, J., Physiologic imaging in acute stroke: Patient selection. *Interventional Neuroradiology* **2015,** *21* (4), 499-510.
32. Lev, M. H.; Farkas, J.; Gemmete, J. J.; Hossain, S. T.; Hunter, G. J.; Koroshetz, W. J.; Gonzalez, R. G., Acute stroke: improved nonenhanced CT detection—benefits of soft-copy interpretation by using variable window width and center level settings. *Radiology* **1999,** *213* (1), 150-155.
33. Adams Jr, H. P.; Del Zoppo, G.; Alberts, M. J.; Bhatt, D. L.; Brass, L.; Furlan, A.; Grubb, R. L.; Higashida, R. T.; Jauch, E. C.; Kidwell, C., Guidelines for the early management of adults with ischemic stroke: a guideline from the American Heart Association/American Stroke Association Stroke Council, Clinical Cardiology Council, Cardiovascular Radiology and Intervention Council, and the Atherosclerotic Peripheral Vascular Disease and Quality of

Care Outcomes in Research Interdisciplinary Working Groups: the American Academy of Neurology affirms the value of this guideline as an educational tool for neurologists. *Circulation* **2007,** *115* (20), e478-e534.
34. Srinivasan, A.; Goyal, M.; Azri, F. A.; Lum, C., State-of-the-art imaging of acute stroke. *Radiographics* **2006,** *26* (suppl_1), S75-S95.
35. Wardlaw, J. M.; Mielke, O., Early signs of brain infarction at CT: observer reliability and outcome after thrombolytic treatment—systematic review. *Radiology* **2005,** *235* (2), 444-453.
36. Oliveira-Filho, J.; Koroshetz, W., Neuroimaging of acute ischemic stroke. *UpToDate. Waltham, MA: UpToDate. Retrieved January* **2010**.
37. Janković, S.; Pavičić Ivelja, M.; Kolić, K.; Buča, A.; Dolić, K.; Lovrić Kojundžić, S.; Čaljkušić, K.; Bilić, I.; Ćapkun, V., CT Perfusion and Noncontrast CT in Acute Ischemic Stroke Diagnosing–Is there Influence on early Thrombolytic Therapy Outcome? *Collegium antropologicum* **2010,** *34* (4), 1391-1396.
38. Schriger, D. L.; Kalafut, M.; Starkman, S.; Krueger, M.; Saver, J. L., Cranial computed tomography interpretation in acute stroke: physician accuracy in determining eligibility for thrombolytic therapy. *Jama* **1998,** *279* (16), 1293-1297.
39. Kim, B. J.; Kang, H. G.; Kim, H.-J.; Ahn, S.-H.; Kim, N. Y.; Warach, S.; Kang, D.-W., Magnetic resonance imaging in acute ischemic stroke treatment. *Journal of stroke* **2014,** *16* (3), 131.
40. Gibson, L.; Whiteley, W., The differential diagnosis of suspected stroke: a systematic review. 2013.
41. Amar, A. P., Brain and vascular imaging of acute stroke. *World neurosurgery* **2011,** *76* (6), S3-S8.
42. Lerario, M. P.; Segal, A. Z., PEER REVIEWER.
43. Lev, M. H.; Segal, A. Z.; Farkas, J.; Hossain, S. T.; Putman, C.; Hunter, G. J.; Budzik, R.; Harris, G. J.; Buonanno, F. S.; Ezzeddine, M. A., Utility of perfusion-weighted CT imaging in acute middle cerebral artery stroke treated with intra-arterial thrombolysis. *Stroke* **2001,** *32* (9), 2021-2028.
44. Campbell, B. C.; Weir, L.; Desmond, P. M.; Tu, H. T.; Hand, P. J.; Yan, B.; Donnan, G. A.; Parsons, M. W.; Davis, S. M., CT perfusion improves diagnostic accuracy and confidence in acute ischaemic stroke. *J Neurol Neurosurg Psychiatry* **2013,** *84* (6), 613-618.
45. Leiva-Salinas, C.; Provenzale, J. M.; Wintermark, M., Responses to the 10 most frequently asked questions about perfusion CT. *American Journal of Roentgenology* **2011,** *196* (1), 53-60.
46. Wintermark, M.; Fischbein, N. J.; Smith, W. S.; Ko, N. U.; Quist, M.; Dillon, W. P., Accuracy of dynamic perfusion CT with deconvolution in detecting acute hemispheric stroke. *American journal of neuroradiology* **2005,** *26* (1), 104-112.
47. Bash, S.; Villablanca, J. P.; Jahan, R.; Duckwiler, G.; Tillis, M.; Kidwell, C.; Saver, J.; Sayre, J., Intracranial vascular stenosis and occlusive disease: evaluation with CT angiography, MR angiography, and digital subtraction angiography. *American Journal of Neuroradiology* **2005,** *26* (5), 1012-1021.
48. Gillard, J. H.; Oliverio, P. J.; Barker, P. B.; Oppenheimer, S. M.; Bryan, R. N., MR angiography in acute cerebral ischemia of the anterior circulation: a preliminary report. *American journal of neuroradiology* **1997,** *18* (2), 343-350.
49. Staroselskaya, I. A.; Chaves, C.; Silver, B.; Linfante, I.; Edelman, R. R.; Caplan, L.; Warach, S.; Baird, A. E., Relationship between magnetic resonance arterial patency and perfusion-diffusion mismatch in acute ischemic stroke and its potential clinical use. *Archives of neurology* **2001,** *58* (7), 1069-1074.

50. Fujita, N.; Hirabuki, N.; Fujii, K.; Hashimoto, T.; Miura, T.; Sato, T.; Kozuka, T., MR imaging of middle cerebral artery stenosis and occlusion: value of MR angiography. *American journal of neuroradiology* **1994,** *15* (2), 335-341.
51. Chalela, J. A.; Kidwell, C. S.; Nentwich, L. M.; Luby, M.; Butman, J. A.; Demchuk, A. M.; Hill, M. D.; Patronas, N.; Latour, L.; Warach, S., Magnetic resonance imaging and computed tomography in emergency assessment of patients with suspected acute stroke: a prospective comparison. *The Lancet* **2007,** *369* (9558), 293-298.
52. Gonzalez, R. G.; Schaefer, P. W.; Buonanno, F. S.; Schwamm, L. H.; Budzik, R. F.; Rordorf, G.; Wang, B.; Sorensen, A. G.; Koroshetz, W. J., Diffusion-weighted MR imaging: diagnostic accuracy in patients imaged within 6 hours of stroke symptom onset. *Radiology* **1999,** *210* (1), 155-162.
53. Mullins, M. E.; Schaefer, P. W.; Sorensen, A. G.; Halpern, E. F.; Ay, H.; He, J.; Koroshetz, W. J.; Gonzalez, R. G., CT and conventional and diffusion-weighted MR imaging in acute stroke: study in 691 patients at presentation to the emergency department. *Radiology* **2002,** *224* (2), 353-360.
54. Yoo, A. J.; González, R. G., Clinical applications of diffusion MR imaging for acute ischemic stroke. *Neuroimaging Clinics* **2011,** *21* (1), 51-69.
55. Fung, S. H.; Roccatagliata, L.; Gonzalez, R. G.; Schaefer, P. W., MR diffusion imaging in ischemic stroke. *Neuroimaging Clinics* **2011,** *21* (2), 345-377.
56. Saur, D.; Kucinski, T.; Grzyska, U.; Eckert, B.; Eggers, C.; Niesen, W.; Schoder, V.; Zeumer, H.; Weiller, C.; Röther, J., Sensitivity and interrater agreement of CT and diffusion-weighted MR imaging in hyperacute stroke. *American journal of neuroradiology* **2003,** *24* (5), 878-885.
57. Wintermark, M.; Sanelli, P. C.; Albers, G. W.; Bello, J.; Derdeyn, C.; Hetts, S. W.; Johnson, M. H.; Kidwell, C.; Lev, M. H.; Liebeskind, D. S., Imaging recommendations for acute stroke and transient ischemic attack patients: a joint statement by the American Society of Neuroradiology, the American College of Radiology, and the Society of NeuroInterventional Surgery. *American Journal of Neuroradiology* **2013,** *34* (11), E117-E127.
58. Adeoye, O.; Hornung, R.; Khatri, P.; Kleindorfer, D., Recombinant tissue-type plasminogen activator use for ischemic stroke in the United States: a doubling of treatment rates over the course of 5 years. *Stroke* **2011,** *42* (7), 1952-1955.
59. Investigators, C. A. S. P. R., Prioritizing interventions to improve rates of thrombolysis for ischemic stroke. *Neurology* **2005,** *64* (4), 654-659.
60. Chevilley, A.; Lesept, F.; Lenoir, S.; Ali, C.; Parcq, J.; Vivien, D., Impacts of tissue-type plasminogen activator (tPA) on neuronal survival. *Frontiers in cellular neuroscience* **2015,** *9*, 415.
61. Joshi, M., Advances in nanomedicine for treatment of stroke. *International Journal of Nanomedicine and Nanosurgery* **2016**.
62. Hacke, W.; Kaste, M.; Fieschi, C.; Toni, D.; Lesaffre, E.; Von Kummer, R.; Boysen, G.; Bluhmki, E.; Höxter, G.; Mahagne, M.-H., Intravenous thrombolysis with recombinant tissue plasminogen activator for acute hemispheric stroke: the European Cooperative Acute Stroke Study (ECASS). *Jama* **1995,** *274* (13), 1017-1025.
63. Clark, W. M.; Wissman, S.; Albers, G. W.; Jhamandas, J. H.; Madden, K. P.; Hamilton, S.; Investigators, A. S., Recombinant tissue-type plasminogen activator (alteplase) for ischemic stroke 3 to 5 hours after symptom onset: the ATLANTIS study: a randomized controlled trial. *Jama* **1999,** *282* (21), 2019-2026.
64. Liu, S.; Feng, X.; Jin, R.; Li, G., Tissue plasminogen activator-based nanothrombolysis for ischemic stroke. *Expert opinion on drug delivery* **2018,** *15* (2), 173-184.

65. Wardlaw, J.; Sandercock, P.; Berge, E., Thrombolytic therapy with recombinant tissue plasminogen activator for acute ischemic stroke: where do we go from here? A cumulative meta-analysis. *Stroke* **2003,** *34* (6), 1437-1442.
66. Kidwell, C. S.; Latour, L.; Saver, J. L.; Alger, J. R.; Starkman, S.; Duckwiler, G.; Jahan, R.; Vinuela, F.; Kang, D.-W.; Warach, S., Thrombolytic toxicity: blood brain barrier disruption in human ischemic stroke. *Cerebrovascular diseases* **2008,** *25* (4), 338-343.
67. Fernández-Monreal, M.; López-Atalaya, J. P.; Benchenane, K.; Cacquevel, M.; Dulin, F.; Le Caer, J.-P.; Rossier, J.; Jarrige, A.-C.; MacKenzie, E. T.; Colloc'h, N., Arginine 260 of the amino-terminal domain of NR1 subunit is critical for tissue-type plasminogen activator-mediated enhancement of N-methyl-D-aspartate receptor signaling. *Journal of Biological Chemistry* **2004,** *279* (49), 50850-50856.
68. Siao, C.-J.; Tsirka, S. E., Tissue plasminogen activator mediates microglial activation via its finger domain through annexin II. *Journal of Neuroscience* **2002,** *22* (9), 3352-3358.
69. Rosenberg, G. A., Matrix metalloproteinases in neuroinflammation. *Glia* **2002,** *39* (3), 279-291.
70. Lo, E. H.; Dalkara, T.; Moskowitz, M. A., Neurological diseases: Mechanisms, challenges and opportunities in stroke. *Nature reviews neuroscience* **2003,** *4* (5), 399.
71. Haile, W. B.; Wu, J.; Echeverry, R.; Wu, F.; An, J.; Yepes, M., Tissue-type plasminogen activator has a neuroprotective effect in the ischemic brain mediated by neuronal TNF-α. *Journal of Cerebral Blood Flow & Metabolism* **2012,** *32* (1), 57-69.
72. Lemarchand, E.; Maubert, E.; Haelewyn, B.; Ali, C.; Rubio, M.; Vivien, D., Stressed neurons protect themselves by a tissue-type plasminogen activator-mediated EGFR-dependent mechanism. *Cell death and differentiation* **2016,** *23* (1), 123.
73. Berlis, A.; Lutsep, H.; Barnwell, S.; Norbash, A.; Wechsler, L.; Jungreis, C. A.; Woolfenden, A.; Redekop, G.; Hartmann, M.; Schumacher, M., Mechanical thrombolysis in acute ischemic stroke with endovascular photoacoustic recanalization. *Stroke* **2004,** *35* (5), 1112-1116.
74. Smith, W. S.; Sung, G.; Starkman, S.; Saver, J. L.; Kidwell, C. S.; Gobin, Y. P.; Lutsep, H. L.; Nesbit, G. M.; Grobelny, T.; Rymer, M. M., Safety and efficacy of mechanical embolectomy in acute ischemic stroke: results of the MERCI trial. *Stroke* **2005,** *36* (7), 1432-1438.
75. Guidelines urge new approach to treating worst strokes. https://www.heart.org/en/news/2018/05/01/guidelines-urge-new-approach-to-treating-worst-strokes.
76. "Stroke Information." from http://www.strokecarenow.com/stroke-information/.
77. Tauro, B. J.; Greening, D. W.; Mathias, R. A.; Mathivanan, S.; Ji, H.; Simpson, R. J., Two distinct populations of exosomes are released from LIM1863 colon carcinoma cell-derived organoids. *Molecular & Cellular Proteomics* **2013,** *12* (3), 587-598.
78. Chodobski, A.; Zink, B. J.; Szmydynger-Chodobska, J., Blood–brain barrier pathophysiology in traumatic brain injury. *Translational stroke research* **2011,** *2* (4), 492-516.
79. Rustenhoven, J.; Jansson, D.; Smyth, L. C.; Dragunow, M., Brain pericytes as mediators of neuroinflammation. *Trends in pharmacological sciences* **2017,** *38* (3), 291-304.
80. Sandoval, K. E.; Witt, K. A., Blood-brain barrier tight junction permeability and ischemic stroke. *Neurobiology of disease* **2008,** *32* (2), 200-219.
81. C. Papadopoulos, S. S., DC Davies, BA Bell, M, Emerging molecular mechanisms of brain tumour oedema. *British journal of neurosurgery* **2001,** *15* (2), 101-108.
82. TSAO, N.; HSU, H.-P.; WU, C.-M.; LIU, C.-C.; LEI, H.-Y., Tumour necrosis factor-α causes an increase in blood-brain barrier permeability during sepsis. *Journal of medical microbiology* **2001,** *50* (9), 812-821.

83. Brouns, R.; De Deyn, P., The complexity of neurobiological processes in acute ischemic stroke. *Clinical neurology and neurosurgery* **2009,** *111* (6), 483-495.
84. Strimbu, K.; Tavel, J. A., What are biomarkers? *Current Opinion in HIV and AIDS* **2010,** *5* (6), 463.
85. Pullagurla, S. R.; Baird, A. E.; Adamski, M. G.; Soper, S. A., Current and future bioanalytical approaches for stroke assessment. *Bioanalysis* **2015,** *7* (8), 1017-1035.
86. Group, B. D. W.; Atkinson Jr, A. J.; Colburn, W. A.; DeGruttola, V. G.; DeMets, D. L.; Downing, G. J.; Hoth, D. F.; Oates, J. A.; Peck, C. C.; Schooley, R. T., Biomarkers and surrogate endpoints: preferred definitions and conceptual framework. *Clinical pharmacology & therapeutics* **2001,** *69* (3), 89-95.
87. Craig-Schapiro, R.; Fagan, A. M.; Holtzman, D. M., Biomarkers of Alzheimer's disease. *Neurobiology of disease* **2009,** *35* (2), 128-140.
88. Kernagis, D. N.; Laskowitz, D. T., Evolving role of biomarkers in acute cerebrovascular disease. *Annals of neurology* **2012,** *71* (3), 289-303.
89. Jin, R.; Yang, G.; Li, G., Molecular insights and therapeutic targets for blood–brain barrier disruption in ischemic stroke: critical role of matrix metalloproteinases and tissue-type plasminogen activator. *Neurobiology of disease* **2010,** *38* (3), 376-385.
90. Foerch, C.; Wunderlich, M. T.; Dvorak, F.; Humpich, M.; Kahles, T.; Goertler, M.; Alvarez-Sabín, J.; Wallesch, C. W.; Molina, C. A.; Steinmetz, H., Elevated serum S100B levels indicate a higher risk of hemorrhagic transformation after thrombolytic therapy in acute stroke. *Stroke* **2007,** *38* (9), 2491-2495.
91. Foerch, C.; Otto, B.; Singer, O. C.; Neumann-Haefelin, T.; Yan, B.; Berkefeld, J.; Steinmetz, H.; Sitzer, M., Serum S100B predicts a malignant course of infarction in patients with acute middle cerebral artery occlusion. *Stroke* **2004,** *35* (9), 2160-2164.
92. Wunderlich, M. T.; Wallesch, C.-W.; Goertler, M., Release of neurobiochemical markers of brain damage is related to the neurovascular status on admission and the site of arterial occlusion in acute ischemic stroke. *Journal of the neurological sciences* **2004,** *227* (1), 49-53.
93. Missler, U.; Wiesmann, M.; Friedrich, C.; Kaps, M., S-100 protein and neuron-specific enolase concentrations in blood as indicators of infarction volume and prognosis in acute ischemic stroke. *Stroke* **1997,** *28* (10), 1956-1960.
94. Welsh, P.; Barber, M.; Langhorne, P.; Rumley, A.; Lowe, G. D.; Stott, D. J., Associations of inflammatory and haemostatic biomarkers with poor outcome in acute ischaemic stroke. *Cerebrovascular diseases* **2009,** *27* (3), 247-253.
95. Winbeck, K.; Poppert, H.; Etgen, T.; Conrad, B.; Sander, D., Prognostic relevance of early serial C-reactive protein measurements after first ischemic stroke. *Stroke* **2002,** *33* (10), 2459-2464.
96. Castellanos, M.; Leira, R.; Serena, J.; Blanco, M.; Pedraza, S.; Castillo, J.; Dávalos, A., Plasma cellular-fibronectin concentration predicts hemorrhagic transformation after thrombolytic therapy in acute ischemic stroke. *Stroke* **2004,** *35* (7), 1671-1676.
97. Montaner, J.; Molina, C. A.; Monasterio, J.; Abilleira, S.; Arenillas, J. F.; Ribó, M.; Quintana, M.; Alvarez-Sabín, J., Matrix metalloproteinase-9 pretreatment level predicts intracranial hemorrhagic complications after thrombolysis in human stroke. *Circulation* **2003,** *107* (4), 598-603.
98. Tuttolomondo, A.; Di Sciacca, R.; Di Raimondo, D.; Serio, A.; D'Aguanno, G.; La Placa, S.; Pecoraro, R.; Arnao, V.; Marino, L.; Monaco, S., Plasma levels of inflammatory and thrombotic/fibrinolytic markers in acute ischemic strokes: relationship with TOAST subtype, outcome and infarct site. *Journal of neuroimmunology* **2009,** *215* (1-2), 84-89.
99. DeGraba, T. J.; Sirén, A.-L.; Penix, L.; McCarron, R. M.; Hargraves, R.; Sood, S.; Pettigrew, K. D.; Hallenbeck, J. M., Increased endothelial expression of intercellular adhesion

molecule-1 in symptomatic versus asymptomatic human carotid atherosclerotic plaque. *Stroke* **1998,** *29* (7), 1405-1410.
100. Chamorro, A. n.; Hallenbeck, J., The harms and benefits of inflammatory and immune responses in vascular disease. *Stroke* **2006,** *37* (2), 291-293.
101. Anderson, R. E.; Hansson, L.-O.; Nilsson, O.; Dijlai-Merzoug, R.; Settergren, G., High serum S100B levels for trauma patients without head injuries. *Neurosurgery* **2001,** *48* (6), 1255-1260.
102. Allard, L.; Burkhard, P. R.; Lescuyer, P.; Burgess, J. A.; Walter, N.; Hochstrasser, D. F.; Sanchez, J.-C., PARK7 and nucleoside diphosphate kinase A as plasma markers for the early diagnosis of stroke. *Clinical chemistry* **2005,** *51* (11), 2043-2051.
103. Cano, C. P.; Bermúdez, V. P.; Atencio, H. E.; Medina, M. T.; Anilsa, A.; Souki, A.; Molina, O. M.; Restrepo, H.; Vargas, M. E.; Núñez, M., Increased serum malondialdehyde and decreased nitric oxide within 24 hours of thrombotic stroke onset. *American journal of therapeutics* **2003,** *10* (6), 473-476.
104. Uno, M.; Kitazato, K.; Nishi, K.; Itabe, H.; Nagahiro, S., Raised plasma oxidised LDL in acute cerebral infarction. *Journal of Neurology, Neurosurgery & Psychiatry* **2003,** *74* (3), 312-316.
105. Roberts, L. J.; Montine, T. J.; Markesbery, W. R.; Tapper, A. R.; Hardy, P.; Chemtob, S.; Dettbarn, W. D.; Morrow, J. D., Formation of isoprostane-like compounds (neuroprostanes) in vivo from docosahexaenoic acid. *Journal of Biological Chemistry* **1998,** *273* (22), 13605-13612.
106. Wunderlich, M. T.; Lins, H.; Skalej, M.; Wallesch, C.-W.; Goertler, M., Neuron-specific enolase and tau protein as neurobiochemical markers of neuronal damage are related to early clinical course and long-term outcome in acute ischemic stroke. *Clinical neurology and neurosurgery* **2006,** *108* (6), 558-563.
107. Dambinova, S. A.; Khounteev, G. A.; Izykenova, G. A.; Zavolokov, I. G.; Ilyukhina, A. Y.; Skoromets, A. A., Blood test detecting autoantibodies to N-methyl-D-aspartate neuroreceptors for evaluation of patients with transient ischemic attack and stroke. *Clinical chemistry* **2003,** *49* (10), 1752-1762.
108. Laterza, O. F.; Modur, V. R.; Crimmins, D. L.; Olander, J. V.; Landt, Y.; Lee, J.-M.; Ladenson, J. H., Identification of novel brain biomarkers. *Clinical chemistry* **2006,** *52* (9), 1713-1721.
109. Olivot, J.-M.; Labreuche, J.; Aiach, M.; Amarenco, P., Soluble thrombomodulin and brain infarction: case-control and prospective study. *Stroke* **2004,** *35* (8), 1946-1951.
110. Barber, M.; Langhorne, P.; Rumley, A.; Lowe, G. D.; Stott, D. J., Hemostatic function and progressing ischemic stroke: D-dimer predicts early clinical progression. *Stroke* **2004,** *35* (6), 1421-1425.
111. Del Zoppo, G. J.; Levy, D. E.; Wasiewski, W. W.; Pancioli, A. M.; Demchuk, A. M.; Trammel, J.; Demaerschalk, B. M.; Kaste, M.; Albers, G. W.; Ringelstein, E. B., Hyperfibrinogenemia and functional outcome from acute ischemic stroke. *Stroke* **2009,** *40* (5), 1687-1691.
112. Ribo, M.; Montaner, J.; Molina, C. A.; Arenillas, J. F.; Santamarina, E.; Quintana, M.; Alvarez-Sabín, J., Admission fibrinolytic profile is associated with symptomatic hemorrhagic transformation in stroke patients treated with tissue plasminogen activator. *Stroke* **2004,** *35* (9), 2123-2127.
113. Pikula, A.; Böger, R. H.; Beiser, A. S.; Maas, R.; DeCarli, C.; Schwedhelm, E.; Himali, J. J.; Schulze, F.; Au, R.; Kelly-Hayes, M., Association of plasma ADMA levels with MRI markers of vascular brain injury: Framingham offspring study. *Stroke* **2009,** *40* (9), 2959-2964.

114. Wang, T. J.; Larson, M. G.; Levy, D.; Benjamin, E. J.; Leip, E. P.; Omland, T.; Wolf, P. A.; Vasan, R. S., Plasma natriuretic peptide levels and the risk of cardiovascular events and death. *New England Journal of Medicine* **2004,** *350* (7), 655-663.
115. McGirt, M. J.; Blessing, R.; Nimjee, S. M.; Friedman, A. H.; Alexander, M. J.; Laskowitz, D. T.; Lynch, J. R., Correlation of serum brain natriuretic peptide with hyponatremia and delayed ischemic neurological deficits after subarachnoid hemorrhage. *Neurosurgery* **2004,** *54* (6), 1369-1374.
116. Gorelick, P. B., Lipoprotein-associated phospholipase A2 and risk of stroke. *The American journal of cardiology* **2008,** *101* (12), S34-S40.
117. Cucchiara, B. L.; Messe, S. R.; Sansing, L.; MacKenzie, L.; Taylor, R. A.; Pacelli, J.; Shah, Q.; Kasner, S. E., Lipoprotein-associated phospholipase A2 and C-reactive protein for risk-stratification of patients with TIA. *Stroke* **2009,** *40* (7), 2332-2336.
118. Huang, P.; Lo, L.-H.; Chen, Y.-C.; Lin, R.-T.; Shiea, J.; Liu, C.-K., Serum free hemoglobin as a novel potential biomarker for acute ischemic stroke. *Journal of neurology* **2009,** *256* (4), 625.
119. Ovbiagele, B.; Starkman, S.; Teal, P.; Lyden, P.; Kaste, M.; Davis, S. M.; Hacke, W.; Fierus, M.; Saver, J. L., Serum calcium as prognosticator in ischemic stroke. *Stroke* **2008,** *39* (8), 2231-2236.
120. Foerch, C.; Curdt, I.; Yan, B.; Dvorak, F.; Hermans, M.; Berkefeld, J.; Raabe, A.; Neumann-Haefelin, T.; Steinmetz, H.; Sitzer, M., Serum glial fibrillary acidic protein as a biomarker for intracerebral haemorrhage in patients with acute stroke. *Journal of Neurology, Neurosurgery & Psychiatry* **2006,** *77* (2), 181-184.
121. Jauch, E. C.; Lindsell, C.; Broderick, J.; Fagan, S. C.; Tilley, B. C.; Levine, S. R., Association of serial biochemical markers with acute ischemic stroke: the National Institute of Neurological Disorders and Stroke recombinant tissue plasminogen activator Stroke Study. *Stroke* **2006,** *37* (10), 2508-2513.
122. Waje-Andreassen, U.; Kråkenes, J.; Ulvestad, E.; Thomassen, L.; Myhr, K. M.; Aarseth, J.; Vedeler, C., IL-6: an early marker for outcome in acute ischemic stroke. *Acta Neurologica Scandinavica* **2005,** *111* (6), 360-365.
123. Zaremba, J.; Losy, J., Early TNF-α levels correlate with ischaemic stroke severity. *Acta Neurologica Scandinavica* **2001,** *104* (5), 288-295.
124. Mocco, J.; Choudhri, T. F.; Mack, W. J.; Laufer, I.; Lee, J.; Kiss, S.; Poisik, A.; Quest, D. O.; Solomon, R. A.; Connolly, E. S., Elevation of soluble intercellular adhesion molecule-1 levels in symptomatic and asymptomatic carotid atherosclerosis. *Neurosurgery* **2001,** *48* (4), 718-722.
125. Jensen, M. B.; Chacon, M. R.; Sattin, J. A.; Levine, R. L.; Vemuganti, R., Potential biomarkers for the diagnosis of stroke. *Expert review of cardiovascular therapy* **2009,** *7* (4), 389-393.
126. Lorente, L.; Martín, M. M.; Pérez-Cejas, A.; Abreu-González, P.; Ramos, L.; Argueso, M.; Cáceres, J. J.; Solé-Violán, J.; Jiménez, A., Association between total antioxidant capacity and mortality in ischemic stroke patients. *Annals of intensive care* **2016,** *6* (1), 39.
127. Zimmermann-Ivol, C. G.; Burkhard, P. R.; Le Floch-Rohr, J.; Allard, L.; Hochstrasser, D. F.; Sanchez, J.-C., Fatty acid binding protein as a serum marker for the early diagnosis of stroke: a pilot study. *Molecular & Cellular Proteomics* **2004,** *3* (1), 66-72.
128. Barber, M.; Langhorne, P.; Rumley, A.; Lowe, G. D.; Stott, D. J., D-dimer predicts early clinical progression in ischemic stroke: confirmation using routine clinical assays. *Stroke* **2006,** *37* (4), 1113-1115.
129. Sato, M.; Suzuki, A.; Nagata, K.; Uchiyama, S., Increased von Willebrand factor in acute stroke patients with atrial fibrillation. *Journal of Stroke and Cerebrovascular Diseases* **2006,** *15* (1), 1-7.

130. Metsis, A.; Andersson, U.; Baurén, G.; Ernfors, P.; Lönnerberg, P.; Montelius, A.; Oldin, M.; Pihlak, A.; Linnarsson, S., Whole-genome expression profiling through fragment display and combinatorial gene identification. *Nucleic acids research* **2004,** *32* (16), e127-e127.
131. Pajer, K.; Andrus, B.; Gardner, W.; Lourie, A.; Strange, B.; Campo, J.; Bridge, J.; Blizinsky, K.; Dennis, K.; Vedell, P., Discovery of blood transcriptomic markers for depression in animal models and pilot validation in subjects with early-onset major depression. *Translational psychiatry* **2012,** *2* (4), e101.
132. Moore, D. F.; Li, H.; Jeffries, N.; Wright, V.; Cooper Jr, R. A.; Elkahloun, A.; Gelderman, M. P.; Zudaire, E.; Blevins, G.; Yu, H., Using peripheral blood mononuclear cells to determine a gene expression profile of acute ischemic stroke: a pilot investigation. *Circulation* **2005,** *111* (2), 212-221.
133. Tang, Y.; Xu, H.; Du, X. L.; Lit, L.; Walker, W.; Lu, A.; Ran, R.; Gregg, J. P.; Reilly, M.; Pancioli, A., Gene expression in blood changes rapidly in neutrophils and monocytes after ischemic stroke in humans: a microarray study. *Journal of Cerebral Blood Flow & Metabolism* **2006,** *26* (8), 1089-1102.
134. Baird, A. E.; Moore, D. F.; Goldin, E.; Johnson, K., Differential expression of molecules associated with intra-cerebral hemorrhage. Google Patents: 2010.
135. Jickling, G. C.; Ander, B. P.; Zhan, X.; Noblett, D.; Stamova, B.; Liu, D., microRNA expression in peripheral blood cells following acute ischemic stroke and their predicted gene targets. *PloS one* **2014,** *9* (6), e99283.
136. Adamski, M. G.; Li, Y.; Wagner, E.; Seales-Bailey, C.; Bennett, N.; Yu, H.; Murphy, M.; Soper, S. A.; Baird, A. E., CD15+ granulocyte and CD8+ T lymphocyte based gene expression clusters for ischemic stroke detection. *Medical Research Archives* **2017,** *5* (11).
137. Barone, F. C.; Hillegass, L.; Price, W.; White, R.; Lee, E.; Feuerstein, G.; Sarau, H.; Clark, R.; Griswold, D., Polymorphonuclear leukocyte infiltration into cerebral focal ischemic tissue: myeloperoxidase activity assay and histologic verification. *Journal of neuroscience research* **1991,** *29* (3), 336-345.
138. Herz, J.; Sabellek, P.; Lane, T. E.; Gunzer, M.; Hermann, D. M.; Doeppner, T. R., Role of neutrophils in exacerbation of brain injury after focal cerebral ischemia in hyperlipidemic mice. *Stroke* **2015,** *46* (10), 2916-2925.
139. Pullagurla, S. R.; Witek, M. A.; Jackson, J. M.; Lindell, M. A.; Hupert, M. L.; Nesterova, I. V.; Baird, A. E.; Soper, S. A., Parallel affinity-based isolation of leukocyte subsets using microfluidics: application for stroke diagnosis. *Analytical chemistry* **2014,** *86* (8), 4058-4065.
140. Baird, A. E., Blood biologic markers of stroke: improved management, reduced cost? *Current atherosclerosis reports* **2006,** *8* (4), 267-275.
141. Baird, A. E.; Soper, S. A.; Pullagurla, S. R.; Adamski, M. G., Recent and near-future advances in nucleic acid-based diagnosis of stroke. *Expert review of molecular diagnostics* **2015,** *15* (5), 665-679.
142. Zaborowski, M. P.; Balaj, L.; Breakefield, X. O.; Lai, C. P., Extracellular vesicles: composition, biological relevance, and methods of study. *Bioscience* **2015,** *65* (8), 783-797.
143. Straat, M.; Böing, A. N.; Tuip-De Boer, A.; Nieuwland, R.; Juffermans, N. P., Extracellular vesicles from red blood cell products induce a strong pro-inflammatory host response, dependent on both numbers and storage duration. *Transfusion Medicine and Hemotherapy* **2016,** *43* (4), 302-305.
144. Raposo, G.; Stoorvogel, W., Extracellular vesicles: exosomes, microvesicles, and friends. *J Cell Biol* **2013,** *200* (4), 373-383.
145. Cocucci, E.; Racchetti, G.; Meldolesi, J., Shedding microvesicles: artefacts no more. *Trends in cell biology* **2009,** *19* (2), 43-51.

146. Fleissner, F.; Goerzig, Y.; Haverich, A.; Thum, T., Microvesicles as novel biomarkers and therapeutic targets in transplantation medicine. *American Journal of Transplantation* **2012,** *12* (2), 289-297.
147. Smith, J. A.; Ng, K. S.; Mead, B. E.; Dopson, S.; Reeve, B.; Edwards, J.; Wood, M. J.; Carr, A. J.; Bure, K.; Karp, J. M., Extracellular vesicles commercial potential as byproducts of cell manufacturing for research and therapeutic use. *Bioprocess Int* **2015,** *13* (4), 20-26.
148. Gangoda, L.; Boukouris, S.; Liem, M.; Kalra, H.; Mathivanan, S., Extracellular vesicles including exosomes are mediators of signal transduction: are they protective or pathogenic? *Proteomics* **2015,** *15* (2-3), 260-271.
149. Tricarico, C.; Clancy, J.; D'Souza-Schorey, C., Biology and biogenesis of shed microvesicles. *Small GTPases* **2017,** *8* (4), 220-232.
150. Muralidharan-Chari, V.; Clancy, J. W.; Sedgwick, A.; D'Souza-Schorey, C., Microvesicles: mediators of extracellular communication during cancer progression. *J Cell Sci* **2010,** *123* (10), 1603-1611.
151. Shifrin Jr, D. A.; Beckler, M. D.; Coffey, R. J.; Tyska, M. J., Extracellular vesicles: communication, coercion, and conditioning. *Molecular biology of the cell* **2013,** *24* (9), 1253-1259.
152. McMahon, H. T.; Boucrot, E., Membrane curvature at a glance. *J Cell Sci* **2015,** *128* (6), 1065-1070.
153. Distler, J. H.; Pisetsky, D. S.; Huber, L. C.; Kalden, J. R.; Gay, S.; Distler, O., Microparticles as regulators of inflammation: novel players of cellular crosstalk in the rheumatic diseases. *Arthritis & Rheumatism* **2005,** *52* (11), 3337-3348.
154. Köppler, B.; Cohen, C.; Schlöndorff, D.; Mack, M., Differential mechanisms of microparticle transfer toB cells and monocytes: anti-inflammatory propertiesof microparticles. *European journal of immunology* **2006,** *36* (3), 648-660.
155. Jodo, S.; Xiao, S.; Hohlbaum, A.; Strehlow, D.; Marshak-Rothstein, A.; Ju, S.-T., Apoptosis-inducing Membrane Vesicles A NOVEL AGENT WITH UNIQUE PROPERTIES. *Journal of Biological Chemistry* **2001,** *276* (43), 39938-39944.
156. Ratajczak, J.; Wysoczynski, M.; Hayek, F.; Janowska-Wieczorek, A.; Ratajczak, M., Membrane-derived microvesicles: important and underappreciated mediators of cell-to-cell communication. *Leukemia* **2006,** *20* (9), 1487.
157. Tushuizen, M. E.; Diamant, M.; Sturk, A.; Nieuwland, R., Cell-derived microparticles in the pathogenesis of cardiovascular disease: friend or foe? *Arteriosclerosis, thrombosis, and vascular biology* **2011,** *31* (1), 4-9.
158. D'Souza-Schorey, C.; Clancy, J. W., Tumor-derived microvesicles: shedding light on novel microenvironment modulators and prospective cancer biomarkers. *Genes & development* **2012,** *26* (12), 1287-1299.
159. Hessvik, N. P.; Llorente, A., Current knowledge on exosome biogenesis and release. *Cellular and Molecular Life Sciences* **2018,** *75* (2), 193-208.
160. Huotari, J.; Helenius, A., Endosome maturation. *The EMBO journal* **2011,** *30* (17), 3481-3500.
161. Henne, W. M.; Stenmark, H.; Emr, S. D., Molecular mechanisms of the membrane sculpting ESCRT pathway. *Cold Spring Harbor perspectives in biology* **2013,** *5* (9), a016766.
162. Stuffers, S.; Sem Wegner, C.; Stenmark, H.; Brech, A., Multivesicular endosome biogenesis in the absence of ESCRTs. *Traffic* **2009,** *10* (7), 925-937.
163. Chairoungdua, A.; Smith, D. L.; Pochard, P.; Hull, M.; Caplan, M. J., Exosome release of β-catenin: a novel mechanism that antagonizes Wnt signaling. *The Journal of cell biology* **2010,** *190* (6), 1079-1091.
164. Nazarenko, I.; Rana, S.; Baumann, A.; McAlear, J.; Hellwig, A.; Trendelenburg, M.; Lochnit, G.; Preissner, K. T.; Zöller, M., Cell surface tetraspanin Tspan8 contributes to

molecular pathways of exosome-induced endothelial cell activation. *Cancer research* **2010,** *70* (4), 1668-1678.
165. Colao, I. L.; Corteling, R.; Bracewell, D.; Wall, I., Manufacturing exosomes: a promising therapeutic platform. *Trends in molecular medicine* **2018,** *24* (3), 242-256.
166. Mittelbrunn, M.; Gutiérrez-Vázquez, C.; Villarroya-Beltri, C.; González, S.; Sánchez-Cabo, F.; González, M. Á.; Bernad, A.; Sánchez-Madrid, F., Unidirectional transfer of microRNA-loaded exosomes from T cells to antigen-presenting cells. *Nature communications* **2011,** *2*, 282.
167. Skog, J.; Würdinger, T.; Van Rijn, S.; Meijer, D. H.; Gainche, L.; Curry Jr, W. T.; Carter, B. S.; Krichevsky, A. M.; Breakefield, X. O., Glioblastoma microvesicles transport RNA and proteins that promote tumour growth and provide diagnostic biomarkers. *Nature cell biology* **2008,** *10* (12), 1470.
168. Batagov, A. O.; Kurochkin, I. V., Exosomes secreted by human cells transport largely mRNA fragments that are enriched in the 3′-untranslated regions. *Biology direct* **2013,** *8* (1), 12.
169. Bolukbasi, M. F.; Mizrak, A.; Ozdener, G. B.; Madlener, S.; Ströbel, T.; Erkan, E. P.; Fan, J.-B.; Breakefield, X. O.; Saydam, O., miR-1289 and "Zipcode"-like sequence enrich mRNAs in microvesicles. *Molecular Therapy-Nucleic Acids* **2012,** *1*, e10.
170. Skotland, T.; Sandvig, K.; Llorente, A., Lipids in exosomes: current knowledge and the way forward. *Progress in lipid research* **2017,** *66*, 30-41.
171. Caruso, S.; Poon, I. K., Apoptotic cell-derived extracellular vesicles: More than just debris. *Frontiers in immunology* **2018,** *9*, 1486.
172. Kerr, J. F.; Wyllie, A. H.; Currie, A. R., Apoptosis: a basic biological phenomenon with wideranging implications in tissue kinetics. *British journal of cancer* **1972,** *26* (4), 239.
173. Poon, I. K.; Lucas, C. D.; Rossi, A. G.; Ravichandran, K. S., Apoptotic cell clearance: basic biology and therapeutic potential. *Nature Reviews Immunology* **2014,** *14* (3), 166.
174. Ainola, M.; Porola, P.; Takakubo, Y.; Przybyla, B.; Kouri, V.; Tolvanen, T.; Hänninen, A.; Nordström, D., Activation of plasmacytoid dendritic cells by apoptotic particles–mechanism for the loss of immunological tolerance in Sjögren's syndrome. *Clinical & Experimental Immunology* **2018,** *191* (3), 301-310.
175. Schiller, M.; Parcina, M.; Heyder, P.; Foermer, S.; Ostrop, J.; Leo, A.; Heeg, K.; Herrmann, M.; Lorenz, H.-M.; Bekeredjian-Ding, I., Induction of type I IFN is a physiological immune reaction to apoptotic cell-derived membrane microparticles. *The Journal of Immunology* **2012,** *189* (4), 1747-1756.
176. Poon, I. K.; Chiu, Y.-H.; Armstrong, A. J.; Kinchen, J. M.; Juncadella, I. J.; Bayliss, D. A.; Ravichandran, K. S., Unexpected link between an antibiotic, pannexin channels and apoptosis. *Nature* **2014,** *507* (7492), 329.
177. Gonzales, P. A.; Pisitkun, T.; Hoffert, J. D.; Tchapyjnikov, D.; Star, R. A.; Kleta, R.; Wang, N. S.; Knepper, M. A., Large-scale proteomics and phosphoproteomics of urinary exosomes. *Journal of the American Society of Nephrology* **2009,** *20* (2), 363-379.
178. Witwer, K. W.; Buzas, E. I.; Bemis, L. T.; Bora, A.; Lässer, C.; Lötvall, J.; Nolte-'t Hoen, E. N.; Piper, M. G.; Sivaraman, S.; Skog, J., Standardization of sample collection, isolation and analysis methods in extracellular vesicle research. *Journal of extracellular vesicles* **2013,** *2* (1), 20360.
179. Crescitelli, R.; Lässer, C.; Szabo, T. G.; Kittel, A.; Eldh, M.; Dianzani, I.; Buzás, E. I.; Lötvall, J., Distinct RNA profiles in subpopulations of extracellular vesicles: apoptotic bodies, microvesicles and exosomes. *Journal of extracellular vesicles* **2013,** *2* (1), 20677.
180. Yáñez-Mó, M.; Siljander, P. R.-M.; Andreu, Z.; Bedina Zavec, A.; Borràs, F. E.; Buzas, E. I.; Buzas, K.; Casal, E.; Cappello, F.; Carvalho, J., Biological properties of extracellular vesicles and their physiological functions. *Journal of extracellular vesicles* **2015,** *4* (1), 27066.

181. Mack, M.; Kleinschmidt, A.; Brühl, H.; Klier, C.; Nelson, P. J.; Cihak, J.; Plachý, J.; Stangassinger, M.; Erfle, V.; Schlöndorff, D., Transfer of the chemokine receptor CCR5 between cells by membrane-derived microparticles: a mechanism for cellular human immunodeficiency virus 1 infection. *Nature medicine* **2000,** *6* (7), 769.
182. Al-Nedawi, K.; Meehan, B.; Micallef, J.; Lhotak, V.; May, L.; Guha, A.; Rak, J., Intercellular transfer of the oncogenic receptor EGFRvIII by microvesicles derived from tumour cells. *Nature cell biology* **2008,** *10* (5), 619.
183. Peinado, H.; Alečković, M.; Lavotshkin, S.; Matei, I.; Costa-Silva, B.; Moreno-Bueno, G.; Hergueta-Redondo, M.; Williams, C.; García-Santos, G.; Ghajar, C. M., Melanoma exosomes educate bone marrow progenitor cells toward a pro-metastatic phenotype through MET. *Nature medicine* **2012,** *18* (6), 883.
184. Rand, M.; Wang, H.; Bang, K.; Packham, M.; Freedman, J., Rapid clearance of procoagulant platelet-derived microparticles from the circulation of rabbits. *Journal of Thrombosis and Haemostasis* **2006,** *4* (7), 1621-1623.
185. Saunderson, S. C.; Dunn, A. C.; Crocker, P. R.; McLellan, A. D., CD169 mediates the capture of exosomes in spleen and lymph node. *Blood* **2014,** *123* (2), 208-216.
186. Willekens, F. L.; Werre, J. M.; Kruijt, J. K.; Roerdinkholder-Stoelwinder, B.; Groenen-Döpp, Y. A.; van den Bos, A. G.; Bosman, G. J.; van Berkel, T. J., Liver Kupffer cells rapidly remove red blood cell–derived vesicles from the circulation by scavenger receptors. *Blood* **2005,** *105* (5), 2141-2145.
187. Takahashi, Y.; Nishikawa, M.; Shinotsuka, H.; Matsui, Y.; Ohara, S.; Imai, T.; Takakura, Y., Visualization and in vivo tracking of the exosomes of murine melanoma B16-BL6 cells in mice after intravenous injection. *Journal of biotechnology* **2013,** *165* (2), 77-84.
188. Rank, A.; Nieuwland, R.; Crispin, A.; Grützner, S.; Iberer, M.; Toth, B.; Pihusch, R., Clearance of platelet microparticles in vivo. *Platelets* **2011,** *22* (2), 111-116.
189. Ratajczak, J.; Miekus, K.; Kucia, M.; Zhang, J.; Reca, R.; Dvorak, P.; Ratajczak, M., Embryonic stem cell-derived microvesicles reprogram hematopoietic progenitors: evidence for horizontal transfer of mRNA and protein delivery. *Leukemia* **2006,** *20* (5), 847.
190. Chen, T. S.; Lai, R. C.; Lee, M. M.; Choo, A. B. H.; Lee, C. N.; Lim, S. K., Mesenchymal stem cell secretes microparticles enriched in pre-microRNAs. *Nucleic acids research* **2009,** *38* (1), 215-224.
191. Baj-Krzyworzeka, M.; Szatanek, R.; Węglarczyk, K.; Baran, J.; Urbanowicz, B.; Brański, P.; Ratajczak, M. Z.; Zembala, M., Tumour-derived microvesicles carry several surface determinants and mRNA of tumour cells and transfer some of these determinants to monocytes. *Cancer Immunology, Immunotherapy* **2006,** *55* (7), 808-818.
192. Huang, X.; Yuan, T.; Tschannen, M.; Sun, Z.; Jacob, H.; Du, M.; Liang, M.; Dittmar, R. L.; Liu, Y.; Liang, M., Characterization of human plasma-derived exosomal RNAs by deep sequencing. *BMC genomics* **2013,** *14* (1), 319.
193. Valadi, H.; Ekström, K.; Bossios, A.; Sjöstrand, M.; Lee, J. J.; Lötvall, J. O., Exosome-mediated transfer of mRNAs and microRNAs is a novel mechanism of genetic exchange between cells. *Nature cell biology* **2007,** *9* (6), 654.
194. Nolte-'t Hoen, E. N.; Buermans, H. P.; Waasdorp, M.; Stoorvogel, W.; Wauben, M. H.; 't Hoen, P. A., Deep sequencing of RNA from immune cell-derived vesicles uncovers the selective incorporation of small non-coding RNA biotypes with potential regulatory functions. *Nucleic acids research* **2012,** *40* (18), 9272-9285.
195. Miranda, K. C.; Bond, D. T.; Levin, J. Z.; Adiconis, X.; Sivachenko, A.; Russ, C.; Brown, D.; Nusbaum, C.; Russo, L. M., Massively parallel sequencing of human urinary exosome/microvesicle RNA reveals a predominance of non-coding RNA. *PloS one* **2014,** *9* (5), e96094.

196. Jenjaroenpun, P.; Kremenska, Y.; Nair, V. M.; Kremenskoy, M.; Joseph, B.; Kurochkin, I. V., Characterization of RNA in exosomes secreted by human breast cancer cell lines using next-generation sequencing. *PeerJ* **2013,** *1*, e201.
197. Cheng, L.; Sharples, R. A.; Scicluna, B. J.; Hill, A. F., Exosomes provide a protective and enriched source of miRNA for biomarker profiling compared to intracellular and cell-free blood. *Journal of extracellular vesicles* **2014,** *3* (1), 23743.
198. Villarroya-Beltri, C.; Gutiérrez-Vázquez, C.; Sánchez-Cabo, F.; Pérez-Hernández, D.; Vázquez, J.; Martin-Cofreces, N.; Martinez-Herrera, D. J.; Pascual-Montano, A.; Mittelbrunn, M.; Sánchez-Madrid, F., Sumoylated hnRNPA2B1 controls the sorting of miRNAs into exosomes through binding to specific motifs. *Nature communications* **2013,** *4*, 2980.
199. Koppers-Lalic, D.; Hackenberg, M.; Bijnsdorp, I. V.; van Eijndhoven, M. A.; Sadek, P.; Sie, D.; Zini, N.; Middeldorp, J. M.; Ylstra, B.; de Menezes, R. X., Nontemplated nucleotide additions distinguish the small RNA composition in cells from exosomes. *Cell reports* **2014,** *8* (6), 1649-1658.
200. Bruno, S.; Grange, C.; Collino, F.; Deregibus, M. C.; Cantaluppi, V.; Biancone, L.; Tetta, C.; Camussi, G., Microvesicles derived from mesenchymal stem cells enhance survival in a lethal model of acute kidney injury. *PloS one* **2012,** *7* (3), e33115.
201. Bruno, S.; Grange, C.; Deregibus, M. C.; Calogero, R. A.; Saviozzi, S.; Collino, F.; Morando, L.; Falda, M.; Bussolati, B.; Tetta, C., Mesenchymal stem cell-derived microvesicles protect against acute tubular injury. *Journal of the American Society of Nephrology* **2009,** *20* (5), 1053-1067.
202. Eldh, M.; Ekström, K.; Valadi, H.; Sjöstrand, M.; Olsson, B.; Jernås, M.; Lötvall, J., Exosomes communicate protective messages during oxidative stress; possible role of exosomal shuttle RNA. *PloS one* **2010,** *5* (12), e15353.
203. Müller, G.; Schneider, M.; Biemer-Daub, G.; Wied, S., Microvesicles released from rat adipocytes and harboring glycosylphosphatidylinositol-anchored proteins transfer RNA stimulating lipid synthesis. *Cellular signalling* **2011,** *23* (7), 1207-1223.
204. de Candia, P.; Torri, A.; Gorletta, T.; Fedeli, M.; Bulgheroni, E.; Cheroni, C.; Marabita, F.; Crosti, M.; Moro, M.; Pariani, E., Intracellular modulation, extracellular disposal and serum increase of MiR-150 mark lymphocyte activation. *PloS one* **2013,** *8* (9), e75348.
205. Ostenfeld, M. S.; Jeppesen, D. K.; Laurberg, J. R.; Boysen, A. T.; Bramsen, J. B.; Primdal-Bengtson, B.; Hendrix, A.; Lamy, P.; Dagnaes-Hansen, F.; Rasmussen, M. H., Cellular disposal of miR23b by RAB27-dependent exosome release is linked to acquisition of metastatic properties. *Cancer research* **2014,** *74* (20), 5758-5771.
206. Morel, L.; Regan, M.; Higashimori, H.; Ng, S. K.; Esau, C.; Vidensky, S.; Rothstein, J.; Yang, Y., Neuronal exosomal miRNA-dependent translational regulation of astroglial glutamate transporter GLT1. *Journal of Biological Chemistry* **2013,** *288* (10), 7105-7116.
207. Holmgren, L.; Szeles, A.; Rajnavölgyi, E.; Folkman, J.; Klein, G.; Ernberg, I.; Falk, K. I., Horizontal transfer of DNA by the uptake of apoptotic bodies. *Blood* **1999,** *93* (11), 3956-3963.
208. Balaj, L.; Lessard, R.; Dai, L.; Cho, Y.-J.; Pomeroy, S. L.; Breakefield, X. O.; Skog, J., Tumour microvesicles contain retrotransposon elements and amplified oncogene sequences. *Nature communications* **2011,** *2*, 180.
209. Guescini, M.; Genedani, S.; Stocchi, V.; Agnati, L. F., Astrocytes and Glioblastoma cells release exosomes carrying mtDNA. *Journal of neural transmission* **2010,** *117* (1), 1.
210. Thakur, B. K.; Zhang, H.; Becker, A.; Matei, I.; Huang, Y.; Costa-Silva, B.; Zheng, Y.; Hoshino, A.; Brazier, H.; Xiang, J., Double-stranded DNA in exosomes: a novel biomarker in cancer detection. *Cell research* **2014,** *24* (6), 766.

211. Waldenström, A.; Gennebäck, N.; Hellman, U.; Ronquist, G., Cardiomyocyte microvesicles contain DNA/RNA and convey biological messages to target cells. *PloS one* **2012,** *7* (4), e34653.
212. Lee, T. H.; Chennakrishnaiah, S.; Audemard, E.; Montermini, L.; Meehan, B.; Rak, J., Oncogenic ras-driven cancer cell vesiculation leads to emission of double-stranded DNA capable of interacting with target cells. *Biochemical and biophysical research communications* **2014,** *451* (2), 295-301.
213. Lázaro-Ibáñez, E.; Sanz-Garcia, A.; Visakorpi, T.; Escobedo-Lucea, C.; Siljander, P.; Ayuso-Sacido, Á.; Yliperttula, M., Different gDNA content in the subpopulations of prostate cancer extracellular vesicles: apoptotic bodies, microvesicles, and exosomes. *The Prostate* **2014,** *74* (14), 1379-1390.
214. Vlassov, A. V.; Magdaleno, S.; Setterquist, R.; Conrad, R., Exosomes: current knowledge of their composition, biological functions, and diagnostic and therapeutic potentials. *Biochimica et Biophysica Acta (BBA)-General Subjects* **2012,** *1820* (7), 940-948.
215. Revenfeld, A. L. S.; Bæk, R.; Nielsen, M. H.; Stensballe, A.; Varming, K.; Jørgensen, M., Diagnostic and prognostic potential of extracellular vesicles in peripheral blood. *Clinical therapeutics* **2014,** *36* (6), 830-846.
216. Théry, C.; Amigorena, S.; Raposo, G.; Clayton, A., Isolation and characterization of exosomes from cell culture supernatants and biological fluids. *Current protocols in cell biology* **2006,** *30* (1), 3.22. 1-3.22. 29.
217. Sunkara, V.; Woo, H.-K.; Cho, Y.-K., Emerging techniques in the isolation and characterization of extracellular vesicles and their roles in cancer diagnostics and prognostics. *Analyst* **2016,** *141* (2), 371-381.
218. Lehrich, B.; Liang, Y.; Khosravi, P.; Federoff, H.; Fiandaca, M., Fetal bovine serum-derived extracellular vesicles persist within vesicle-depleted culture media. *International journal of molecular sciences* **2018,** *19* (11), 3538.
219. Konoshenko, M. Y.; Lekchnov, E. A.; Vlassov, A. V.; Laktionov, P. P., Isolation of extracellular vesicles: general methodologies and latest trends. *BioMed research international* **2018,** *2018*.
220. Atha, D. H.; Ingham, K. C., Mechanism of precipitation of proteins by polyethylene glycols. Analysis in terms of excluded volume. *Journal of Biological Chemistry* **1981,** *256* (23), 12108-12117.
221. Caradec, J.; Kharmate, G.; Hosseini-Beheshti, E.; Adomat, H.; Gleave, M.; Guns, E., Reproducibility and efficiency of serum-derived exosome extraction methods. *Clinical biochemistry* **2014,** *47* (13-14), 1286-1292.
222. Im, H.; Shao, H.; Park, Y. I.; Peterson, V. M.; Castro, C. M.; Weissleder, R.; Lee, H., Label-free detection and molecular profiling of exosomes with a nano-plasmonic sensor. *Nature biotechnology* **2014,** *32* (5), 490.
223. Melo, S. A.; Sugimoto, H.; O'Connell, J. T.; Kato, N.; Villanueva, A.; Vidal, A.; Qiu, L.; Vitkin, E.; Perelman, L. T.; Melo, C. A., Cancer exosomes perform cell-independent microRNA biogenesis and promote tumorigenesis. *Cancer cell* **2014,** *26* (5), 707-721.
224. Tauro, B. J.; Greening, D. W.; Mathias, R. A.; Ji, H.; Mathivanan, S.; Scott, A. M.; Simpson, R. J., Comparison of ultracentrifugation, density gradient separation, and immunoaffinity capture methods for isolating human colon cancer cell line LIM1863-derived exosomes. *Methods* **2012,** *56* (2), 293-304.
225. Shao, H.; Chung, J.; Lee, K.; Balaj, L.; Min, C.; Carter, B. S.; Hochberg, F. H.; Breakefield, X. O.; Lee, H.; Weissleder, R., Chip-based analysis of exosomal mRNA mediating drug resistance in glioblastoma. *Nature communications* **2015,** *6*, 6999.
226. Wei, F.; Yang, J.; Wong, D. T., Detection of exosomal biomarker by electric field-induced release and measurement (EFIRM). *Biosensors and Bioelectronics* **2013,** *44*, 115-121.

227. Kanwar, S. S.; Dunlay, C. J.; Simeone, D. M.; Nagrath, S., Microfluidic device (ExoChip) for on-chip isolation, quantification and characterization of circulating exosomes. *Lab on a Chip* **2014,** *14* (11), 1891-1900.
228. Zhang, P.; He, M.; Zeng, Y., Ultrasensitive microfluidic analysis of circulating exosomes using a nanostructured graphene oxide/polydopamine coating. *Lab on a Chip* **2016,** *16* (16), 3033-3042.
229. Chen, C.; Skog, J.; Hsu, C.-H.; Lessard, R. T.; Balaj, L.; Wurdinger, T.; Carter, B. S.; Breakefield, X. O.; Toner, M.; Irimia, D., Microfluidic isolation and transcriptome analysis of serum microvesicles. *Lab on a Chip* **2010,** *10* (4), 505-511.
230. Ashcroft, B.; De Sonneville, J.; Yuana, Y.; Osanto, S.; Bertina, R.; Kuil, M.; Oosterkamp, T., Determination of the size distribution of blood microparticles directly in plasma using atomic force microscopy and microfluidics. *Biomedical microdevices* **2012,** *14* (4), 641-649.
231. Rho, J.; Chung, J.; Im, H.; Liong, M.; Shao, H.; Castro, C. M.; Weissleder, R.; Lee, H., Magnetic nanosensor for detection and profiling of erythrocyte-derived microvesicles. *ACS nano* **2013,** *7* (12), 11227-11233.
232. He, M.; Crow, J.; Roth, M.; Zeng, Y.; Godwin, A. K., Integrated immunoisolation and protein analysis of circulating exosomes using microfluidic technology. *Lab on a Chip* **2014,** *14* (19), 3773-3780.
233. Van Der Vlist, E. J.; Nolte, E. N.; Stoorvogel, W.; Arkesteijn, G. J.; Wauben, M. H., Fluorescent labeling of nano-sized vesicles released by cells and subsequent quantitative and qualitative analysis by high-resolution flow cytometry. *Nature protocols* **2012,** *7* (7), 1311.
234. Suetsugu, A.; Honma, K.; Saji, S.; Moriwaki, H.; Ochiya, T.; Hoffman, R. M., Imaging exosome transfer from breast cancer cells to stroma at metastatic sites in orthotopic nude-mouse models. *Advanced drug delivery reviews* **2013,** *65* (3), 383-390.

Chapter 2: Design and development of microfluidic devices fabricated in thermoplastics for the selective capture of extracellular vesicles and biological cells as a source of stroke biomarkers

2.1 Introduction

A major drawback of currently available stroke diagnostic methods, such as computed tomography (CT) and magnetic resonance imaging (MRI), is that they cannot provide timely diagnosis within the narrow therapeutic time window of 4.5 h from stroke onset afforded by recombinant tissue plasminogen activator treatment for AIS. In addition to the time constrain, these neuroimaging techniques have several other disadvantages including difficulty in identifying small affected areas, inability to differentiate stroke conditions from stroke mimics, need of trained personnel to operate complex instrumentation and interpret results, and unavailability of service under emergency conditions.[1-3] Hence, there is a need to look at alternative diagnostic methods for stroke including new assay strategies and the accompany biomarkers that can provide timely answers with high clinical sensitivity and specificity. In particular, an in vitro diagnostic using a liquid biopsy supplying the necessary biomarkers would be attractive.

However, looking for new biomarkers and developing a new diagnostic test for stroke is challenging due to many reasons. Complexity of the stroke conditions and the presence of the blood brain barrier are main challenges in finding new biomarkers. Additionally, biomarkers that are selected should show a quick response because there is a short time window for effective treatment of stroke conditions. Hence, a rapid and simple diagnostic test will be extremely useful for pre-hospital screening before treatment.

Biomarkers that are available for stroke can be categorized into imaging markers that measure the changes in the nervous system via brain imaging, and molecular and pharmacodynamic biomarkers (biomarkers that are indicative of certain pharmacological responses useful in

drug development).[4] All of the stroke biomarkers that are currently used have their disadvantages like latency in appearance in peripheral blood, and lack of specificity to stroke conditions.

Recently, gene expression profiling in peripheral blood has been successfully used for ischemic stroke diagnosis.[5] Based on HT-RT qPCR results, researchers found that individual genes were significantly dysregulated in ischemic stroke patients when sourced from 4 leukocyte subpopulations. In CD15+ granulocytes 14 genes were dysregulated while in CD8+ T-lymphocytes 16 genes were dysregulated. Two and one genes were upregulated in γδTCR+ cells and CD4+ T lymphocytes, respectively. Among the 14 genes upregulated, the researchers also validated a 3 gene expression cluster for stroke diagnosis from CD15+ granulocytes (*CA4*, *MMP9*, *NAIP*). Based on the results overall accuracy of the 3-gene cluster classified ischemic stroke with a sensitivity of 89% and a specificity of 67%.

However, according to previous studies using blood samples from stroke patients, mRNA changes in the appropriate leukocyte subpopulations were observed in a mean time of 2.4 h after the stroke event.[6] In this study, only 66% of the patients showed a significant change in gene expression after 2.4 h. 87% of the patients showed significant differences after 5 h, and 100% of the patients showed differences in gene expression after 24 h.[6]

In this study, we propose to use extracellular vesicles (nano-sized vesicles) released by most of the cells in to body fluids, as a new source of mRNA biomarkers for ischemic stroke diagnosis. mRNA biomarkers have been suggested for diagnosing AIS by harvesting mRNAs from certain leukocyte subpopulations that are responding to inflammation in a blood vessel within the brain cavity, such as CD8-expressing T cells. In this study, we targeted CD8-expressing leukocyte-derived EVs for mRNA profiling to determine if EVs could be used as a source of AIS biomarkers due to the success of using CD8+ T cells, which are responding to inflammation in a brain blood vessel for diagnosing AIS. EVs could be a more abundant source of mRNA, which can then be used for the expression profiling at an earlier time because time is the most

critical factor in stroke diagnosis and treatment. In addition, the packaging of mRNA into EVs will protect them from RNases to preserve their integrity to allow for expression profiling.

In order to analyze EV cargo, first EVs of interest must be isolated in high purity and high yields from body fluids. Many currently available EV isolation methods like ultracentrifugation, PEG precipitation, and filtration methods cannot be utilized in a clinical setting due to their long processing time, contamination with protein, and inability to isolate specific types of EVs.

Thus, to isolate EVs that are specific to a disease state, many new isolation techniques utilize antibodies directed against certain antigens found in the membrane of the EV including microfluidic devices, immunomagnetic beads, photosensitizer beads have been reported.[7-8] However, many of these microfluidic devices use general affinity-enrichment of bulk EVs by targeting the tetraspanins such as CD9, CD63, and CD81.[9-11] This is a shortcoming because they cannot be used for isolating and analyzing a subset of EVs that are specific to diseased conditions. Another drawback of microfluidic devices is the low sample processing speeds they possess, which requires long analysis times that can be a challenge when developing assays in which time is a critical factor. For example, a recent EV affinity isolation microfluidic device was reported, which used 3-dimensional herringbone nanopatterns, and operated at a volume flow rate of 0.5 $\mu L\ min^{-1}$, which would require 400 min (6.7 h) to process a volume of 200 µL of plasma.[12]

Herein, we report a microfluidic device with arrays of micropillars modified with mAb that can selectively isolate EVs of interest. Following isolation, the enriched EVs can be released from the device surface for downstream analysis. EV-mRNA can also be characterized and studied as a source of biomarkers for detecting stroke.

2.2 Material and Methods

2.2.1 Cell lines and growth conditions

Molt 3 T cells (ATCC, Manassas, VA- acute lymphoblastic leukemia T lymphoblast, isolated from peripheral blood of a child, 19 yo, male) were grown in Roswell Park Memorial Institute medium (RPMI) (Carlsbad, CA) supplemented with 20% fetal bovine serum (FBS) (Gibco Laboratories, Gaithersburg, MD). To remove the naturally extracellular vesicles in FBS, FBS was ultra-centrifuged at 100,000 xg for 18 h and EV depleted FBS was used in cell culture media. Cells were grown in 37 $^{\circ}$C in 5% CO_2 for 4 days before splitting the cells. Viability of the cells were calculated frequently using a LIVE/DEAD cell imaging kit (Thermo Fisher Scientific, Waltham, MA).

2.2.2 Cell line characterization- Flow cytometry

Expression level of CD8 T cells in cell line was investigated using flowcytometry with a BD accuri C6 plus flowcytometer. Calibration beads (Quantum Simply Cellular anti-mouse IgG, Bang Laboratories, Fishers, IN) was used for generating calibration curve according to manufacturer's instructions. In brief, procedure is as follows. First, the containers with the calibration bead were mixed thoroughly and then two drops of each calibration standard were place in a 2 ml tube. Then 10 μL of APC conjugated mouse IgG2B anti hCD8∝ Ab (R & D systems, Minneapolis, MN) were added each tube and 100 μL of 0.5% (w/v) bovine serum albumin in PBS was added. Then samples were incubated in dark at room temperature for 40 min. After incubation they were centrifuged at 300 g for 10 min and pellet was then resuspended in 1 mL of 0.5% (w/v) bovine serum albumin in PBS. The samples were centrifuged again for 10 min at 300 g for three times and finally the pellet was resuspended in 300 μL of 0.5% (w/v) bovine serum albumin in PBS before analyzing through the flow cytometry.

For the preparation of cells for flow cytometry, first cells were collected from Molt 3 cell line and then centrifuged at 300 g for 10 min. Then the cells were resuspended in 400 μL of 0.5%

(w/v) bovine serum albumin in PBS. The cell count in the sample was ~0.5x10^6 cells/mL. Next, the sample was divided in to two aliquots and 10 μL of APC conjugated mouse IgG2B anti hCD8∝ Ab (R & D systems, Minneapolis, MN) was added to one aliquot and 10 μL APC conjugated mouse IgG2B isotype control (R & D systems, Minneapolis, MN) was added to other portion. Then the samples were threated in the same way as for the calibration beads. Finally bead and the cell samples were analyzed with the BD accuri C6 plus flowcytometer and the data were analyzed using software provided by the manufacturer.

2.2.3 Micro fluidic device for cell isolation

2.2.3.1 Device fabrication and assembly

For isolation of CD8+ T cells from cell media the curvilinear channel device was used.[13] The molding master was fabricated in brass mold via high-precision micro milling (HPMM) using a commercial milling machine (KERN 44, KERN Micro- und Feinwerk technik GmbH & Co.KG; Murnau, Germany) as previously described.[13] In brief, the surface of a 6.3 mm thick, 120 mm diameter circular brass plate was pre-cut with a 500 μm diameter milling bit to confirm parallelism between both surfaces of the brass plate and constant height of the final structures. Next, rough milling of the microstructures was carried out using a 500 μm and 200 μm milling bits and a finishing cut was performed with a 200 μm or 100 μm diameter milling bit. Diameter of the milling bit will be determined by the smallest distance between milled structures. Micro-milling was performed at 50,000 rpm at feed rates that were dependent on the size of the milling.

After fabricating the brass mold devices were replicated into cyclic olefin copolymer ((Topas 6013) S-04, Topas Advanced Polymers, Florence KY) via hot embossing. The conditions used for hot embossing is as follows: devices were embossed at 155 °C, by applying a force of 30kN for 120 s and de-molding was performed at 122 °C. The channel dimensions were analyzed via non-contact profilometry to confirm proper dimensions of devices.

The devices were then cut using a bench top band saw. COC cover plates used for bonding is 100 μm in thickness. Both cover plates and the devices were cleaned well before assembling. First, cover plates and devices were sonicated in 10% Micro-90 for 5 min and rinsed with isopropanol and deionized (DI) water (>18 MΩ) and dried at 65 °C overnight. After cleaning the COC devices, two capillaries (ID 250 μm. 365 μm OD) were assembled as inlet and outlet and device was covered with a COC cover plate, placed in between two borosilicate glass plates. Then the COC cover plate and device were thermally fusion bonded at 137 ^{o}C for 1h (Heratherm Oven, ThermoFisher, USA). The places where capillaries connect to the devices were sealed with epoxy and dried to prevent any leakages during sample processing.

2.2.4 Micro fluidic device for extracellular vesicle isolation

2.2.4.1 Design of the micro fluidic device

Monte Carlo fluid dynamics simulation of EV isolation device was performed by a custom code programmed in Fortran 90, compiled with GFortran, and executed on a computer workstation. All the simulation studies discussed in this chapter were performed by Dr. Matthew Jackson. (Dr. Soper's Lab, The University of Kansas)

2.2.4.2 Fabrication and assembly

The EV isolation device was also fabricated using the same method explained in section 2.2.2.1 section. However, embossing protocol is different from what was used for the channel device. Polymer replicas of the mold master were produced using hot embossing into cyclic olefin copolymer (COC) using a Precision Press model P3H-15-PLX (Wabash MPI, IN). The COC plaques were dried in an oven at 65 ^{o}C overnight prior to hot embossing. The optimized hot embossing protocol used in this study is briefly described below. First 150 lb force is applied for 60 s at 155 ^{o}C (closes platens, holds for temperature equilibration), and then 900 lb force is applied for 30 s at 162 ^{o}C during this time the pressure is ramped up. After that, same force was applied for 300 s at same temperature before demolding the devices at 145 – 148 ^{o}C. The hot

embossing was followed by non-contact profilometry to confirm correct pillar dimensions using a Keyence Microscope (Keyence, Itasca, IL, USA). Only devices with proper dimensions were used for thermal fusion bonding. Cover plates used for the devices were COC which is 75 μm in thickness. Both cover plates and devices were cleaned well before assembling. First, cover plates and devices were sonicated in 10% Micro-90 for 5 min and rinsed with isopropanol (IPA) and deionized (DI) water (>18 MΩ) and dried at 65 ^{o}C overnight. After cleaning the COC devices, two capillaries (ID 150 μm. 365 μm OD) were assembled as the inlet and the outlet and device was covered with a COC cover plate, placed in between two borosilicate glass plates. Then the COC cover plate and the device were thermally fusion bonded at 137 ^{o}C for 1h (Heratherm Oven, ThermoFisher, USA). After thermal fusion bonding the devices were again checked for the pillar dimensions using the images captured by a measurer scope and using ImageJ software. Selected devices with proper pillar dimension and spacing were used for experiments. The places where capillaries connect to the devices were sealed with epoxy and dried to prevent any leakages during sample processing.

2.2.5 Modification of the microfluidic devices for affinity capture of CD8+ T cells and CD8+ Extracellular vehicles (EVs)

Modification of the microfluidic device for affinity selection was carried out as previously reported with slight modification.[14] In brief the procedure is as follows. First, assembled devices were UV/O_3 modified for 13 min (254 /185 nm, 22 mV/cm^2) to create arboxylic groups on COC polymer surface. For modifying surface of devices, devices were flooded with a 40 μM oiligonucletide solution (Integrated DNA Technologies, Coralville, IA) prepared in 20 mg/ml EDC and kept at room temperature for 2 h (or at 4 ^{o}C overnight) to attach oligonucleotide to device surface via carboxylic group. The sequence of oligo used for the reaction is 5'/5AmMC 12/TTT TTT TTC CCT TCC TCC TCA CTT CCC TTT/ ideoxyU/TT TTT TTT T/3ThioMC3D/. The molecular weight is 12428.3 g/mol and the melting temperature is T_m=61.2 °C.

The di-sulfide bond in the oligonucleotide needs to be reduced in order to attach the anti CD8 antibody. Hence, before immobilizing the antibody, the devices were washed three times with 300 mM DTT in 0.05 M carbonate buffer pH 10.8 with 10-15 min time intervals. DTT will reduce 3'-disulfide group into a reactive sulfhydryl moiety (-S-H) which can react with the $-NH_2$ group in the Ab.

To attach the antibody to the device surface through oligo first anti CD8 antibody (1 mg/ml) was prepared in nanopure water and 50x excess of (5.8 μL of 10 mg/mL diluted in 200 μL of nanopore water) SMCC (succinimidyl 4-(N-maleimidomethyl) cyclohexane-1-carboxylate) was added and kept on a rocker for 40 min. Purification of anti-CD8 antibody was carried out using Zeba™ Spin Desalting columns (Thermo scientific, IL, USA). To prepare desalting column for binding, first the Zeba™ Spin Desalting column (Sample volume range 200 -700 μl) was washed with 700 μL of PBS three times by centrifuging at 1,000 xg for 2 mins. After 40 min antibody was purified using desalting column by centrifuging at 1000 xg for 2 min to remove excess non-reacted SMCC. Then, the devices were washed with PBS pH 7.4 and purified anti body was injected quickly and kept at 4 ^{o}C overnight. After that protein stabilizing cocktail (Thermo Fisher Scientific, Waltham, MA) was injected to the devices and stored at 4 ^{o}C until they are used for experiments.

2.2.6 EV isolation on the microfluidic device

EVs isolated from Molt-3 cell line was used for initial EV isolation studies. After culturing cells for 3 days the cell media was centrifuged for 10 min at 300 xg to separate the cells. After centrifuging cells, supernatant was used for isolating EVs. First, microfluidic devices were connected to a hydrodynamic pump (New Era Pump Systems, Inc., Farmingdale, NY USA) via a syringe connector and the pre-rinse of the devices was performed with 500 μL 1 % PVP40, 0.5% BSA solution at 10 μl/min. Then cell supernatant samples (~ 500 μL) was infused to the 3-bed device at 5 μL /min. Post-isolation rinse was performed at 10 μl /min with TBS/tween20. All

the solutions used for rinsing were filtered using a 0.45 μm polypropylene housing, surfactant free cellulose acetate membrane filter (Thermo scientific, IL, USA) prior to use. Then the devices were incubated with APC conjugated mouse IgG2B anti hCD8∝ Ab (R & D systems, Minneapolis, MN) for 40 min. As controls the same procedure was carried out for a UV-modified device without anti CD8 Ab. Also, isotype control experiment was performed by incubating a device with APC conjugated mouse IgG2B anti hCD8∝ Ab. Next, devices were washed with Tween 20 in TBS to remove any excess dye-labeled Ab and then washed with PBS prior to visualizing through a florescence microscope. The devices were visualized using a 200M inverted microscope (Zeiss) with a 20x objective (0.3 NA, Plan NeoFluar), XBO 75 Xe arc lamp, single band Cy5 filter set (Omega optical), Cascade:1K EM-CCD camera (Photometric), and MAC 5000 stage (Ludl Electronic Products), all of which were computer-controlled via Micro-Manager. Finally, images were background subtracted and analyzed using Image-J software.

2.2.7 Release of enriched EVs from device surface

In order to release captured EVs on device, the device was infused with 2U/10 μl USER™ enzyme (New England Biolabs, Ipswich, MA) and incubated at 37 °C. Immediately after incubation, the released EVs were washed from the microfluidic device at 10 μL/min and collected to a pre weighed 2 mL centrifuge tube.

2.2.8 Characterization of released EVs

2.2.8.1 Transmission electron microscopy

Samples were vortexed thoroughly and then 5 μL drop of the EV samples that have been released from the microfluidic devices were placed on to a grid carbon (Carbon Type-B, 300 mesh, Copper, TED PELLA, Inc., Redding, CA) film side for 20 min. Then grid was washed in a drop of deionized water by setting the grid in each drop for a few seconds before moving to the next drop. This step is important to dilute any buffer salts that have been used in sample preparation process. If not, salt can be precipitated with uranyl acetate stain. Next, grid was placed on

2% (w/v) uranyl acetate stain which has been filtered by a 0.22 μm filter (Thermo scientific, IL, USA), for 10 seconds and blot dried it. The grids were dried for at least 15 min before viewing through the microscope. (FEI TECNAI F20 XT field emission transmission electron Microscope, 200 kV electron source - Schottky field emitter)

2.2.8.2 Nanoparticle Tracking Analysis

EVs that have been released from the microfluidic devices were analyzed via nanoparticle tracking (Nano sight NT 2.3) in order to investigate concentration of nanoparticles in samples. The samples were diluted as required and before analyzing they were vortexed thoroughly. Instrument parameters used for analysis were: camera shutter 1206, camera gain 366, capture duration 90 s. Five videos were taken for each sample and the flow cell was washed five times with PBS in between sample analysis. During the final wash with PBS the video was monitored to check if there are any particles left in the flow cell. If particles were seen in the video washing was continued until no particles are there in the flow cell.

2.2.9 LPS stimulation of T cells: Optimization of LPS concentration and stimulation time

To induce stimulation in T cells Lipopolysacchride (LPS) from E. coli (InvivoGen, San Diego, CA) was used. The stock solution of LPS was prepared in fresh phosphate buffered saline (PBS) (Gibco Laboratories, Gaithersburg, MD). Then cells (started with approximately one million cells) were stimulated with 100 ng/ ml, 10 ng/ml of LPS and cells were monitored for any morphology changes at time points up to 75 h. A control experiment was carried out without stimulating cells with LPS. At each time point cell viability of cells were calculated using a LIVE/DEAD viability/cytotoxicity kit for mammalian cells (Thermo Fisher Scientific, Waltham, MA). The optimized LPS concentration and stimulation time was used for all the stimulation experiments.

2.2.10 Sample Processing and Extraction of RNA from CD8+ T cells

Cell cultures with ~$1x10^6$ cells/mL were stimulated with LPS (concentration optimized in section 2.2.8), and a control experiment was performed without adding LPS to cell media. After 24 h cell media was centrifuged for 10 min at 300 xg to separate cells. Then the cell pellet was resuspended in PBS buffer. Before running the sample through curvilinear channel device, it was washed with 0.5% BSA/PBS solution using a hydrodynamic pump at 55 μL /min flow rate to reduce nonspecific binding. All the solutions were filtered with a 0.45 μm filter (Thermo Fisher Scientific, Waltham, MA). Sample was then processed through the device at 25 μL/min. Finally, the microfluidic device was washed with 0.5% BSA/PBS to remove any non-specifically bound cells on device. Then on-chip lysis was performed inside a hood using Zymo research science RNA kit (Zymo Research, Irvine, CA) it's protocol. In brief, lysis solution was injected into the device manually using a syringe and then incubated for 5 mins. Then, another aliquot of the lysis solution injected and flow through was collected to a 2 mL centrifuge tube. Next, equal volume of 100% ethanol (Molecular Biology Grade, Thermo Fisher Scientific, Waltham, MA) was added to tube and loaded to an RNA purification column. Then the column was centrifuged at 16,000 g for 30s. Next the column was washed with 400 μL of RNA wash buffer by centrifuging at 16,000 g for 30s. Next on column DNase digestion was carried out by incubating the column with 6 U of DNase for 15 min at room temperature. After that the column was washed twice with 400 μL of RNA pre wash buffer and 700 μL of RNA wash buffer. Finally, purified RNA was eluted with 10-15 μL nuclease free water. Then profiles of extracted RNA were analyzed using Agilent 2200 Tape Station.

2.2.11 Sample Processing and Extraction of RNA from CD8+ EVs

As described in section 2.2.9, the supernatant of the centrifuged cell media was used for isolating the EVs. Before processing the sample, microfluidic device (pillars) was washed with 0.5% BSA/1%PVP40 in PBS at 10 μL/min flow rate. Then the sample was processed at 5 μL/min

flow rate. After that the devices were washed with Tween 20 solution to remove any non-specifically attached EVs on to device surface. Then RNA was extracted from EVs using the same protocol as for the cells.

2.2.12 cDNA synthesis from purified RNA

Complementary DNA from purified RNA were synthesized via reverse transcription (RT) reaction. This was accomplished using ProtoScript II First Strand cDNA Synthesis Kit (New England BioLabs, Ipswich, MA) according to manufacturer's instructions. In brief the procedure is as follows. Up to 1 μg of template was mixed with 2 μL of $d(T)_{23}VN$, 10 μL ProtoScript II reaction mix (2X), 2 μL ProtoScript II Enzyme mix (10X) and nuclease-free water was added so that the final volume of the mixture is 20 μL. Then the mixture was incubated at 42 °C for 1 hour using a thermocycler. The enzyme was inactivated by an additional incubation step at 80 °C for 5 min. No-RT negative control reaction was performed in absence of enzyme mixture.

2.2.13 Droplet digital PCR

Synthesized cDNA was used in the droplet digital RCR reaction for gene expression analysis. Primers (Table 2.1) for the genes *MMP9, PLBD1*, *FOS, CA4* and *VCAN* was designed and purchased from Integrated DNA Technologies (IDT, Coralville, IA).

Table 2.1: Primer sequences used in gene expression analysis

Gene	Primer F 5'-3' (T_m / °C)	Primer R 5'-3' (T_m / °C)
FOS	TGC CAG GAA CAC AGT AG (51.4)	TTC AGA GAG CTG GTA GTT AG (50.7)
VCAN	TCT CAA AGA AAC AGA GTG ATA (49.9)	AGA GCC ACA GAGCAT TT (51.1)
PLBD1	GTA CTG AGA TGC TAG GTA GAT A (50.2)	CAA GGG AAA GTG ACT GAT AC (50.4)
MMP9	GGG ATT TAC ATG GCA CTG (50.8)	ACC GAG AGA AAG CCT ATT (50.2)
CA4	GAA GCC TGG AAC TTG GA (51.7)	AGC GCA CGG TGA TAA A (51.4)

Droplet digital PCR protocol was carried out using EVAGreen supermix (Bio Rad, Hercules, CA) according the manufacturer instructions. The steps are briefly explained below. For reaction setup all the samples were thawed to room temperature and the samples were mixed thoroughly by vortexing tubes to ensure homogeneity because a concentration gradient may form during –20°C storage. Then all samples and reagents were centrifuged briefly to collect contents at the bottom of the tube. Depending on the number of reactions reaction mix was prepared according to Table 2.1. All the required components were assembled except the sample. Then, equal aliquots were dispensed into each reaction tube and the sample (cDNA) was added to each reaction tube as the final step. cDNA sample was diluted as required. After that reaction mix was vortexed thoroughly and centrifuged briefly to ensure that all components are at the bottom of the reaction tube. Reaction tubes were allowed to equilibrate at room temperature for about 3 minutes.

Table 2.2: Preparation of the reaction mix with EvaGreen super mix, primers and DNA template

Component	Volume per reaction (µl)	Final Concentration
2x QX200™ ddPCR™ EvaGreen® Supermix	10	1x
Forward primer	variable	100-250 nM
Reverse primer	variable	100-250 nM
DNA template and RNase-/ DNase-free water	variable	Up to 100 ng
Total volume	20	-

Once the reaction mixture is ready, droplet generation was performed. This was done using a QX200 droplet generator (Bio Rad, Hercules, CA). First the DG8 cartridge (Bio Rad, Hercules, CA) was inserted into the holder and 20 µL of each prepared sample was transferred to sample well (middle row) in the cartridge. Then 70 µL of droplet generation oil was dispensed to fill each oil well (bottom row). Then the gasket was securely hooked over the cartridge to ensure that sufficient pressure required for droplet generation is achieved. Cartridge was then

placed in the droplet generator and once the droplet generation is complete, 40 μL of generated droplets was transferred into a 96-well PCR plate.

PCR was carried out in a Bio Rad C1000 touch thermal cycler, with following steps. 98 °C for 0.30 s followed by 40 cycles of denaturation at 98 °C for 0.15 s; annealing for 0.20 s at 52 °C and extension at 72 °C for 0.30 s. Final cooling step was carried out at 4 °C.To read droplets a Bio Rad QX-200 droplet digital PCR system was used, and data were analyzed using the QuantaSoft™ software. Droplet digital results were normalized to ng of RNA before comparing the gene profiles.

2.2.14 Polyethylene glycol precipitation

First, cell media sample was mixed in 0.5x volume of PBS. And the 0.02 x proteinaseK was added and incubated for 20 min at 37 ºC to digest protein. The volume of polyethylene glycol (PEG) added to the mixture is equal to total volume of the mixture, that is total volume of sample, volume of PBS and volume of proteinase K. After adding PEG, tube was inverted and placed in 4 ºC overnight before centrifuging the solution at 4000 g for 1 hour at 4 ºC. Collected pellet was lysed using Zymo research science RNA kit (Zymo Research, Irvine, CA) according to manufacturer protocol. Here, after adding the lysis solution the sample was vortexed thoroughly to dissolve the pellet completely before loading to the RNA purification column. After RNA purification was followed by cDNA synthesis and droplet digital PCR as explained in the previous section.[15]

2.3 Results and discussion

2.3.1 Molt-3 cell line

The Molt-3 cell line contains T lymphoblast cells. This is a hyper tetraploid human cell line and cells were grown at 37°C at 5% CO_2 atmosphere. Like most mammalian cells, T cells are also grown at pH 7.4 and maintaining this pH is critical for maintaining high cell viability. At 5% CO_2 atmosphere, CO_2 gas dissolve into cell culture media and establishes an equilibrium

with HCO_3^-. Because CO_2 is acidic, the pH of the medium will drop. Although salts and amino acids in RPMI media provides some buffering capacity, additional buffering compounds are required to maintain a proper physiological pH. Here, RPMI media was used for cell culture and contains HEPES, which is a zwitterionic organic buffer that helps to maintain the physiological pH.[16] Media was also supplemented with 1 mM glutamine, which is important in facilitating storage and transfer of nitrogen to cells in culture. Although glutamine is one of the most readily available amino acids for use as an energy source, it is quite unstable when it is dissolved in liquid media. At temperatures above 4°C glutamine non-enzymatically degrades into toxic ammonium and pyroglutamate by-products.[17] Due to this short half-life, L-glutamine solutions were stored frozen at -20 °C and added to freshly prepared media prior to use. Another important supplement used for the cell culture media is fetal bovine serum (FBS). Its major functions are providing hormone factors for cell growth and proliferation, promoting cell differentiation, supplying transport proteins, essential nutrients, trace elements, and stabilizing and detoxifying factors that are required for maintaining favorable cell growth. Among many common animal serums available, FBS is widely used in cell cultures due to its very low level of antibodies and high levels of growth factors that allows the propagation of most types of human cells.[18-19] Although FBS is necessary for cell growth, FBS contains large number of bovine extracellular vesicles (EVs), which obstruct analysis of EVs of preference. It can also be problematic in downstream analysis because these EVs are morphologically can be similar to EVs released by the cultured cells.[20-21] Hence, EV depletion of FBS is important prior applying to the media. So, first FBS was EV depleted by ultracentrifugation at 100,000g for 18 h. Long centrifugation times were selected because shorter centrifugation steps are insufficient for complete FBS EV depletion.[22-23]

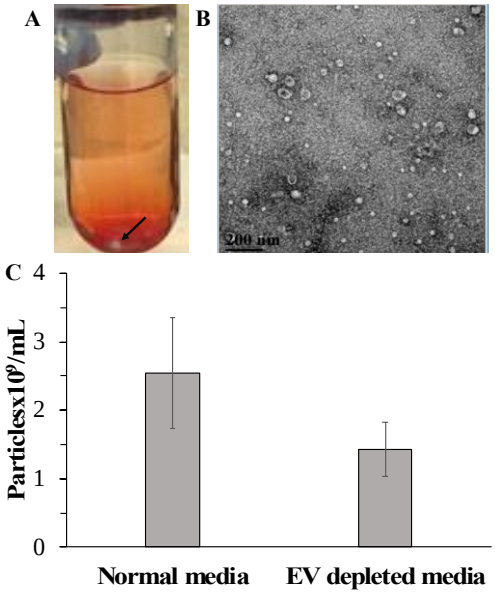

Figure 2.1: (A) EV depletion of FBS by ultra-centrifugation; the pellet shown in arrow shows the depleted EVs. (B) TEM image of depleted EVs after ultra-centrifugation. (C) Concentration of EVs in normal media and EV depleted media measured by Nanoparticle tracking (n=3).

Ultracentrifugation is based on separation of particles according to their buoyant density. Higher centrifugation speeds such as 100,000g is sufficient to precipitate smaller sized particles including extra cellular vesicles which are in the in the range of 30-200 nm. Figure 2.1 A shows the EV pellet that was obtained after centrifuging FBS for 18 h. The supernatant was then decanted carefully and stored at -20°C, which was then used in the cell culture media. The EV pellet was further analyzed via TEM and images. As shown in Figure 2.1B EVs were not seen in the images revealing that EVs had been depleted from FBS during ultra-centrifugation.

NTA was performed to calculate the number of EV in normal media and EV depleted media. As shown in Figure 2.1C there was a difference in number of EVs in EV depleted and non-depleted media. EV non-depleted media showed a significantly higher number of EVs compared to EVs in depleted media. (p value 0.0291 at 95% confidence level). Before using cells grown in EV depleted media for experiments, the cells grown in both EV depleted and non-depleted media was compared for any difference in morphology and RNA profiles.

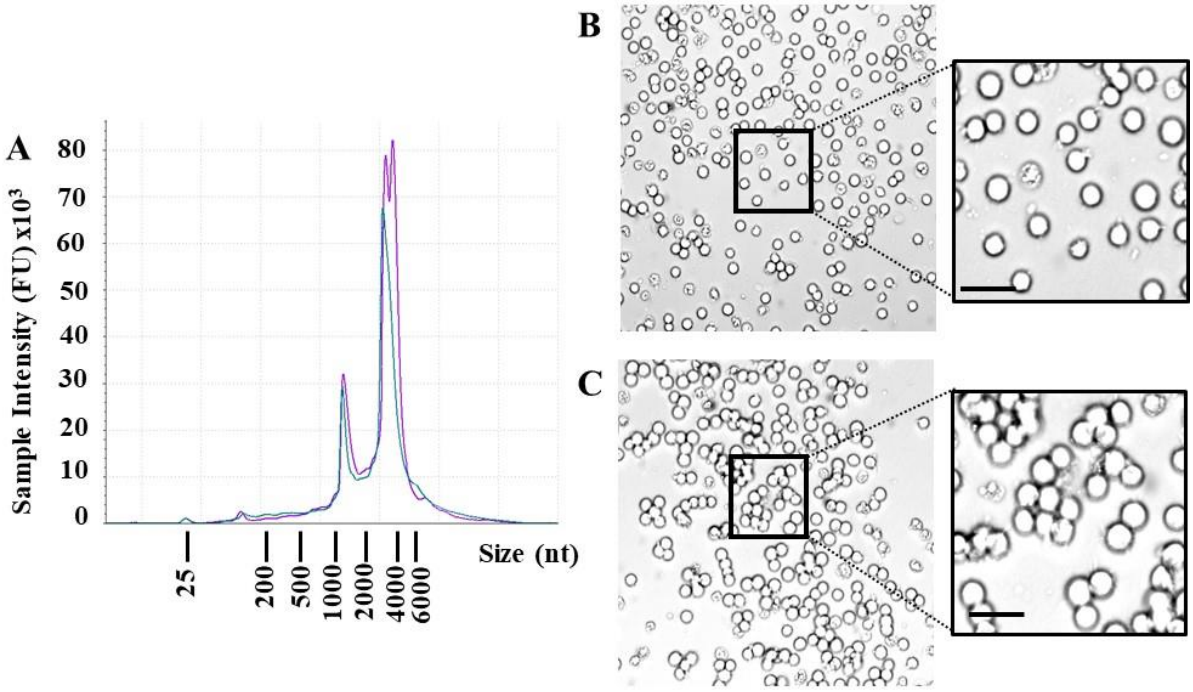

Figure 2.2: (A) Electropherogram for the separation of RNA isolated from T cells grown in EV-depleted media (green trace) and in non-depleted media (purple trace). (B) Cells grown in EV-depleted media – 20x magnification. (C) Cells grown in EV non depleted media -20x magnification, scale bar on the images is 15 μm.

Analysis of RNA profiles is important to see if there's any change in the cells growing in EV depleted media. As shown in Figure 2.2 A the RNA profiles of RNA extracted from cells grown in EV depleted and non-depleted media are similar. Moreover, the total RNA (TRNA) isolated from T cells grown in both EV-depleted and non-depleted media showed typically observed TRNA profiles for eukaryotic cells with well pronounced ribosomal RNAs larger and smaller subunits. Because the ribosomal bands (28S and 18S) are clear and the 28S band was approximately twice as intense as the 18S band, it is clear that the TRNA isolated from both cell culture conditions are intact.[24]

Furthermore, cell morphology and size of the cells were not affected by EV depletion in FBS. Figure 2.2 B and C shows cells grown in EV-depleted and non-depleted media, respectively. Size of cells in cultured in both media are in the range of 5-7 μm in diameter, which is the typical size of a T cell.

Cell cultures were maintained by addition or replacement of fresh medium and cells were sub-cultured when cell density reached between 1 and 2 x 10^6 cells/mL (every 3-4 days) and cell density of the media was maintained at 5 x 10^5 cells/mL. To confirm that cells used in the experiments are viable, a cell viability assay was performed frequently, and the calculated cell viability was always >90%, which implies that the cell line is healthy.

2.3.2 Flow cytometry characterization of Molt-3 cell line

Molt-3 cells show 13.5% level of CD8 antigen expression.[25] This cell line shows a higher expression of CD1, CD2, CD5 and CD7 antigens, which are 92.7%, 72.9%, 99.2%, and 98.9%, respectively.[18] In order to analyze the expression level of CD8 in the Molt-3 cell line, flow cytometry was performed. Based on the calibration curve generated using calibration beads, the average number of CD8 receptors on the surface of each cell was calculated to be 2484.94 and for the isotype control, the calculated value was 1219.90 (Figure 2.3 B).

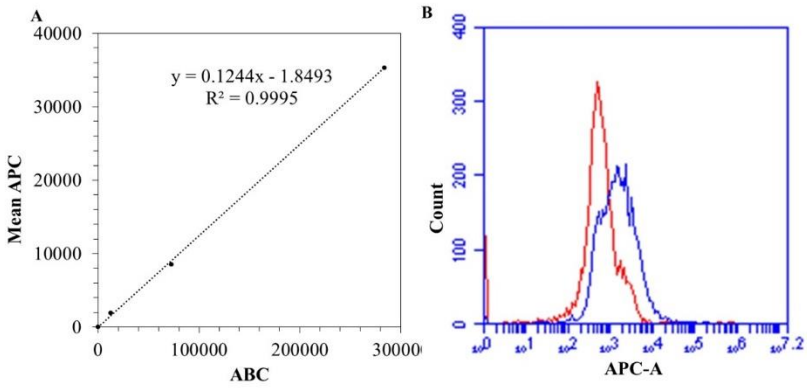

Figure 2.3: (A) Calibration curve generated with calibration beads. (B) Representative fluorescence histogram data for Molt-3 cells stained with: red trace - APC conjugated IgG2B isotype, blue trace - APC conjugated CD8 Ab.

2.3.3 Micro fluidic device for cell isolation

2.3.3.1 Design of the microfluidic device

The microfluidic device used in this study for cell isolation was developed by our lab for circulating tumor cell (CTC) isolation.[13] The design of this high throughput - circulating tumor cell (HT-CTC) chip is shown in Figure 2.4 A. This device consists of a parallel array of sinusoidal microchannels with dimensions of 25 μm in width, 150 μm in depth and a length of each channel being 30 mm. The device consists of 50 such channels and inlet and outlet channels arranged in a Z- configuration. By using the sinusoidal channel geometry we can attain a higher recovery compared to use of straight channels of same dimensions.[26-27] Higher recovery is due to the escape of cells' travel from flow streamlines associated with fully developed laminar flow and Fahraeus-Lindqvist effect which is, cell focusing to channel center, that can be overcome in sinusoidal-shaped channel designs because that result in higher probability of cell/wall interactions.[26] Optimal linear velocity that supports higher recoveries was found to be 2-2.5 mm/s. At higher velocities, short residence time of cell membrane antigens with the surface capture antibodies reduces the cell isolation capacity.[26, 28-29]

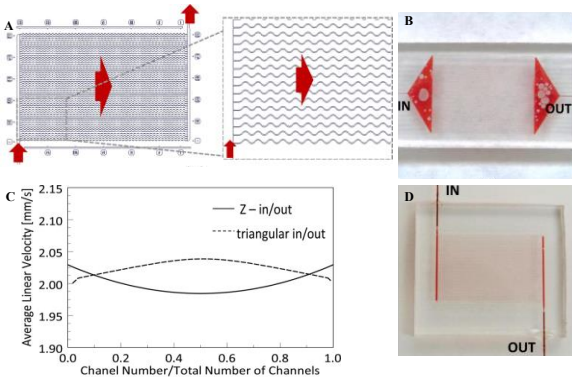

Figure 2.4: (A) Schematic representation of the design and the operation of the cell isolation device arranged in a Z-configuration. (B) Capture beds filled with blood for the triangular configuration. (C) Results of a computer simulations for the distribution of low velocities wihtin the CTC isolation bed with Z-configuration or 51 microchannels with triangular inlets and outputs. (D) Capture beds filled with blood for the Z-configuration (Reproduced from reference 13).

Previous studies performed have used triangular inlets and outlets for isolating CTC from blood (Figure 2.4 B). Critical to device efficiency, flow through the capture channels need to be uniform, remaining at a linear velocity of 2 mm/s to optimize CTC recovery.[26-28] In previous studies, using simulation studies with a numerical tractable model, where triangular inlet and outlet regions connected 51 sinusoidal channles, it has been shown that flow is uniformly distributed in the previously distributed device (with trangular inlets), where viscous drag along the inlet and outlet walls by no-slip conditions reduced flow velocity.(Figure 2.4 C). [26-27] But velocity of fluids through these triangular regions is slower, which is about ~0.2 mm/s compared to capture channels. The pressure difference within these regions will not be enough to displace air bubbles introduced during sample processing. Therefore, in this study a new architecture, which is called the Z-configuration was used. Here, fluid will enter the selection bed through a single inlet channel composed perpendicular to an array of channels and exits also through a single outlet channel, which is also perpendicular to the channels (Figure 2.4 D). Flow of the fluid throughout the device is also uniform in the Z-configuration and it has been shown that the flow through the inlet/outlet channels are higher than 2 mm/s which creates enough pressure to remove any air bubbles introduced during sample processing process.[13]

2.3.3.2 Device fabrication and assembly

Devices used in this study were manufactured as disposable units to minimize any cross-commination problems that can occur during the sample analysis if multiple clinical blood samples would be analyzed using a single device. To fulfill this requirement, it is necessary to produce microfluidic devices at low cost per unit. Micromanufacturing techniques with thermoplastic polymers is a method that satisfies this requirement, because polymers are inexpensive and there are many low-cost fabrication approaches that are available for the mass production of these devices.[30-31] Here, we used hot embossing as our device fabrication method, which is considered to be a medium-scale production tool for microfluidic devices. When requiring higher

numbers of devices at an even lower production cost compared to hot embossing, injection molding can be used.[32]

The first step in hot embossing is the production of a molding tool, which in this case was made in brass via high-precision micromilling (HPMM). Compared to other molding tool fabrication methods including X-ray-LiGA or UV-LiGA, HPMM has many advantages, such as shorter turnover times, low cost, and it is a single step fabrication method.[31, 33-34] After producing the molding tool (Figure 2.5), hot embossing was used to replicate the necessary devices into cyclic olefin copolymer (COC). COC was used due to its many advantages over other thermoplastics including low cost, low water absorption, excellent resistant to chemicals, good optical transparency in the near UV range, and ease of fabrication are some of the advantages.[35] Another benefit of using COC is its high carboxylic acid coverage that can be acquired after UV/ozone irradiation, which is essential for attaching antibodies to the device surface via an EDC coupling reaction. During hot embossing, COC thermoplastic is heated slightly above its glass transition temperature (T_g) and the mold, which is also at the same temperature, is pressed into the polymer by supplying a high force under partial vacuum for a short period of time. After that, demolding is performed by cooling the mold, which will emboss patterns from the brass molding tool into the thermoplastic. After hot embossing, the devices were analyzed via non-contact profilometry to confirm the correct dimensions of the microchannels in the devices (see Table 2.1).

Table 2.3: Dimensions of the channels of curvilinear channel device

Parameter	**Size /μm**
Channel depth	150 μm
Micro channel width	25 μm

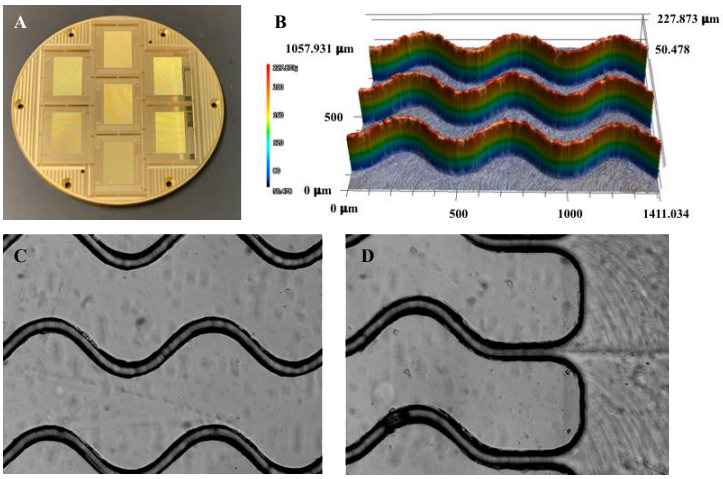

Figure 2.5: (A) Brass mold used for hot embossing devices. (B) Non-contact profilometry images of a device to determine channel dimensions. (C) Curvilinear channels images under a microscopy (10x magnification). (D) Channel configuration close to the inlet.

Once correct dimensions were confirmed via non-contact profilometry, the next step was to enclose the fluidic network with a COC cover plate (100 µm thick). For this, we used thermal fusion bonding, where device and cover plate are brought into conformal contact under a fixed pressure. To accomplish this, we placed the embossed device and cover plate between two boro-silicate glass plates and used clips to apply a fixed pressure as shown in Figure 2A. Also, two capillaries (250 µm ID) were placed in inlet and outlet channels. After assembling, the devices were slowly heated to a temperature slightly below its glass transition temperature (T_g) using an oven. These bonding conditions needed to be selected carefully to preserve structural integrity of microchannels as much as possible. For thermal fusion bonding a temperature of 132°C was used for 1 h. Figure 2.6 B shows how the final device appears after thermal fusion bonding.

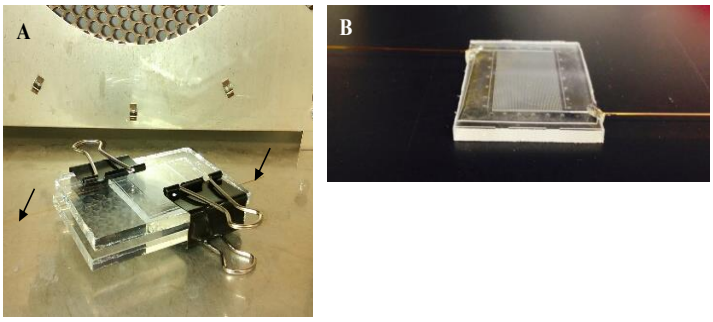

Figure 2.6: (A) Device and cover plate placed between two borosilicate plates and use of clips to apply pressure (capillaries used for inlet and outlet are shown in arrows) (B) Final device after thermal fusion bonding.

2.4 Microfluidic device for extracellular vesicle (EV) isolation

2.4.1 Device design

Because the size of EVs (30 nm – 1 μm) are smaller than that of cells (~10 μm), the dimensions of channels within the cell isolation device are not appropriate for EV isolation. It has been shown that for efficient isolation using these channels, at least one dimension of the microchannel must be close to average diameter of target that we are isolating (*i.e.*, cells, CTC, EVs) to help induce cell-wall interactons.[26] Even though the sinusoidal geometry can induce centrifugal forces to "push" cells toward the wall to induce cell-wall interactions, this would not occur for small particles, such as exosomes. Thus, only lateral diffusion would induce EV-wall interactions and to increase the number of potential wall interactions, the diffusional distance must be reduced.

Hence, for isolating EVs we designed a microfluidic device that consisted of pillar structures. This device consisted of 3-beds that are serially connected with capillary ports of 360 μm OD (Figure 2.7 A). Each bed was 2 mm wide and the length was 40.6 mm. Total length throughout the serially-connected beds was 122 mm. The entire device had 15,202 circular micropillars with each pillar being 92 μm in height, 117 μm in diameter and a spacing between pillars of 10 μm. Surface area and volume of this 3-bed device was 6.8 cm^2 and 6.5 μL respectively.

The architecture of the device was carefully designed to maximize recovery of the EVs while providing high throughput sample processing. Sample infused into the device will enter the affinity bed and EVs will diffuse laterally to interact with the monoclonal antibodies immobilized on micropillar surfaces while at the same time driven hydrodynamically through the bed. Narrow inter-pillar spacing (~10 μm) and long bed lengths decrease diffusional distances and provide sufficient residence time, respectively, so that the EV recovery is favorable.

To study the efficiency of the EV diffusion-based EV isolation process, we developed a fluid dynamics simulation to model the processes of EV diffusion amidst hydrodynamic Poiseuille flow and EV-Ab binding kinetics that could estimate EV recovery (Figure 2.7 B), the results of which were used to help in the design of the fluidic device. While COMSOL can simulate these physics, accurate estimation of EV recovery requires modeling diffusion through the entire EV isolation bed's length, which becomes numerically intractable given the large geometric size. Accordingly, a Monte Carlo model was developed to track the diffusive and convective motions of individual EVs through the EV isolation bed,[36] and simulate the probability of Ab-EV binding based on the Chang-Hammer model.[28] Individual EVs were tracked until they were either recovered or lost by exiting the device, and the results were averaged over thousands of EV events until the simulation converged to an average EV recovery.

For the device prototype used herein, simulations predict an EV recovery of 80% at 2.1 μL/min volume flow rate; linear velocity is 1.8 mm/s for 15 μm interpillar spacing). Notably, the simulated recovery at various flow rates was not dependent on inter-pillar spacing (Figure 2.7 C) because increased diffusional distances were countered by reduced linear velocities given a constant flow rate. Rather, extended bed lengths and the associated increased EV resident times with longer isolation bed lengths were critical to enable high recovery at higher linear velocity; reducing inter-pillar dimensions were more critical to constrain the device's internal volume (<40 μL) so as to be compatible with downstream molecular profiling. The Monte Carlo model used for

the simulation studies and the way simulation studies were performed are explained in detail below.

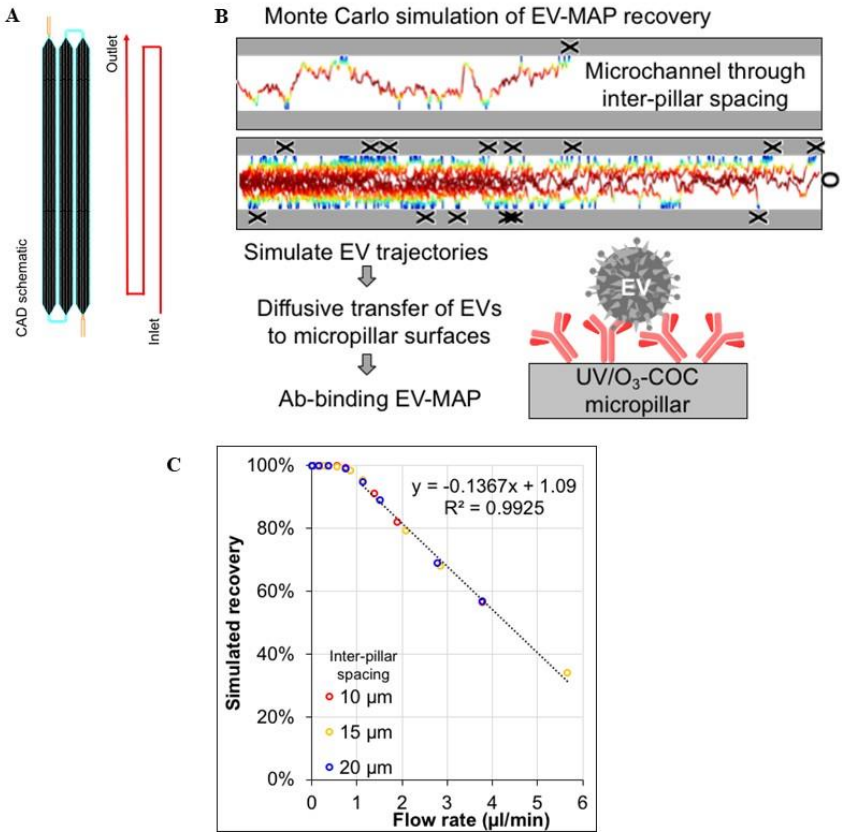

Figure 2.7: (A) Picture of CAD schematic showing the serial connection of three bed device with circular micro pillars. (B) The network of narrow microchannels enable efficient EV recovery by reducing the distances required for EVs to diffuse and interact with the Abs coated on the 3-bed device. These dynamics were simulated via a custom Monte Carlo model that incorporates diffusive and convective EV transfer and Ab-EV binding dynamics. Shown are tracks of individual EVs (not to scale) diffusing through a microchannel, where color scales with the EV velocity (blue-low, red-high) and "X" indicates a successful EV-Ab binding event whereas "O" indicates the EV was not captured. Results are averaged until the predicted EV recovery converges. (C) Monte Carlo simulation results for the 3-bed prototype used in this study. (Courtesy of Dr. Matthew Jackson)

2.4.2 Simulation studies: Diffusional dynamics modeled using the Monte Carlo simulation to predict EV recovery

The dynamics of EV affinity-selection can be split into two separate events: (1) Delivery of EVs from solution to the EV device surface; and (2) binding of the surface-bound Ab to the EV. The efficiencies of both processes dictate EV recovery. Thus, we developed a Monte Carlo fluid dynamics simulation incorporating chemical physics and fluid dynamics principles to guide the design of EV-MAP micropillar isolation beds. Previously, we have outlined renditions of these chemical physics for CTC affinity-selection[37-38] and diffusion models for the affinity-selection of membrane proteins,[39] although the diffusion model presented herein is a significant advancement compared to our previous report.

The delivery of EVs to the antibody-coated EV-MAP surface is limited by diffusion through the plasma matrix. As an EV is hydrodynamically pumped through the device, it diffuses laterally and longitudinally according to Fick's Second Law of diffusion. Over a small time, increment, Δt, the probability that an EV will diffuse a distance x_D from its initial position is given by a Gaussian distribution, $P(x)$:

$$P(x) = \frac{1}{\sigma\sqrt{2\pi}} e^{-\frac{x_D^2}{2\sigma^2}} \quad \text{(Eq. 1)}$$

This Gaussian distribution has a standard deviation given by $\sigma = \sqrt{2D\Delta t}$, where D is the EV's diffusion coefficient. Thus, smaller EVs with higher D are more likely to diffuse farther in time Δt. In additional to diffusive transfer, the EVs experience Poiseuille flow. In a microchannel with a width of W, the EV's forward velocity at position x from the channel's midline can be approximated by:

$$V(x) = 1.5\, V_{ave}(1 - \left(\frac{x}{W/2}\right)^2 \quad \text{(Eq. 2)}$$

In Eq. 2, V_{ave} is simply calculated by dividing the volumetric flow rate by the EV bed's cross-section. The consequences of the parabolic flow profile in Eq. 2 are complex. As EV diffuses closer to surfaces, EV forward motion slows, and more time is given for diffusion to occur. Consequently, the residence time of different EVs within the same device will not be the same if they take different diffusive, random paths through the Poiseuille flow profile.

Thus, we use a Monte Carlo simulation to simulate the flow path of individual EVs through EV isolation devices. Then, we can repeat this process until the averaged EV isolation converges. This model will allow us to test various EV isolation bed lengths, inter-pillar spacings (W), and average flow velocities (V_{ave}) to design EV isolation architectures with high recovery, high throughput, and high surface area-to-volume ratios.

For each EV, the Monte Carlo simulation propagates an EV's axial position (X dimension) and longitudinal position (Y dimension) over finite time steps (Δt):

$$x(t) = x(t - \Delta t) + rand(P(\sigma(D, \Delta t)) \quad \text{(Eq. 3a)}$$

$$y(t) = y(t - \Delta t) + V\big(x(t - \Delta t)\big) + rand(P(\sigma(D, \Delta t)) \quad \text{(Eq. 3b)}$$

In Eq. 3a, the EV's lateral x position changes with axial diffusion over Δt using $rand(P(\sigma(D, \Delta t))$, which is given by a pseudo-random number generator that moves the EV laterally according to a Gaussian $P(x)$ distribution with standard deviation σ. Longitudinal diffusion is considered in the same manner by Eq. 3b, but the EV has an additional term due to Poiseuille flow, namely the $V\big(x(t - \Delta t)\big)$ term described in Eq. 2.

2.4.3 Ab-binding dynamics in the Monte Carlo simulations of EV isolation recovery

As an EV diffuses to and interacts with the EV device's surface, successful binding between the surface-bound Ab and the transient EV is not guaranteed in a single encounter. In general, multiple encounters are necessary for successful EV recovery. Herein, we adapt the Chang-Hammer model[28] to describe this process.

The Chang-Hammer model thoroughly describes the binding process between surface-confined Abs and transient antigens, such as those present on the membrane of an EV. This model considers Ab-antigen binding kinetics, the transient motion of the antigen and its associated residence time in proximity to the surface-confined Ab, and the distance over which the EV rolls along the surface. Previously, we reduced the Chang-Hammer model to a few key equations,[38] and herein, we adopt those dynamics.

Firstly, as the EV rolls along the EV isolation device's surface, the forward rate constant k_o for the encounter of antigens with a surface-confined Ab is:

$k_o = 2a_i V_{eff}$ (Eq. 4)

In Eq. 4, a_i is the Ab-antigen interaction radius (2 nm), and V_{eff} is the velocity of the antigen relative to the surface, which is roughly half (0.47 times) the rolling EV's velocity due to the opposing rotational motion of the EV's surface. Furthermore, as the antigen encounters the Ab, the probability that they complex (P) is a function of both the Ab's binding kinetics, k_{in}, and the encounter duration $\tau = 8a_i/3\pi V_{eff}$:

$P = \frac{k_{in}}{k_{in}+1/\tau}$ (Eq. 5)

As the EV's linear velocity increases, τ decreases yielding less time available for the Ab and antigen to complex, and P decreases as well. Both the encounter rate, k_o, and the binding probability, P, are weighted against one another to yield an effective forward rate constant, k_f:

$k_f = k_o P$ (Eq. 6)

Lastly, the overall rate of EV adhesion, k_{ad}, combines k_f with the EV's antigen surface density, C_∞;

$k_{ad} = k_f C_\infty$ (Eq. 7)

To review, k_{ad} considers the EV's antigen expression and the velocity of the EV's antigens, both in terms of how often the antigens encounter Abs and how probable a binding event

is given the balance of antigen-Ab interaction time and the Ab's binding kinetics. To relate k_{ad} to experimental systems, consider an EV rolling along an Ab-coated surface at a linear velocity (V) for only a limited distance (L). The percent of EVs that will bind is:

$$\%_{bound} = 1 - 1/e^{\frac{k_{ad}L}{V}} \qquad \text{(Eq. 8)}$$

Two aspects of Eq. 8 that improve EV recovery are immediately apparent: (i) decrease linear velocity; and/or (ii) maximize interaction length between the EV and the surface. Unlike CTC dynamics,[38] EVs have a relatively high diffusion coefficient, and the dynamics of an EV rolling along the micropillar surface are described by a Peclet number <1. Very little can be done to enhance lateral diffusion rates and control or manipulate the length of any given EV-micropillar interaction. Further, decreasing bulk flow rate will do little to affect Eq. 8, which only describes the velocity at the surface, because surface flow velocities are limited to approximately zero by the no-slip condition. The velocity in Eq. 8 is more likely to be affected by EV diffusion rather than fluid velocity. Thus, the probability of Ab-binding is dictated by the binding dynamics of the affinity agent, and external manipulation of the EV-MAP process (decreasing fluid velocity, decreasing inter-pillar spacings) largely affect the diffusion-based delivery of EVs to the surface.

The flow profile through an EV isolation bed with length L_{bed} experienced by an EV was approximated as a straight microfluidic channel with a width W equal to the interpillar spacing and length $L = L_{bed}C$, where C is a correction factor for linked to elongation of the flow path due to the pillar's geometry. For diamond micropillars, $C = \sqrt{2} \approx 1.41$, and for circular micropillars, $C = \pi/2 \approx 1.57$.[39]

EVs were initiated at 11 positions along the pseudo-channel's midline, and the EV's position through the channel was propagated by Eq. 3. If the EV encounters the channel's surfaces ($x = \pm W/2$), the EV is propagated by multiplying $V(x)$ (Eq. 2) by the simulation's time step (Δt) and the probability of binding was calculated via Eqs. (4-8). The binding probability was

turned into an actionable decision (*i.e.*, binding or not) by using a pseudo-random number generator uniformly distributed between 0 and 1. If the random number was less than Eq. 8's binding probability, the EV was recovered. If not, the EV's position was propagated further via Eqs. 3. This series of events continued until either the EV was recovered or the EV was lost ($y = L$).

Each EV's track is a binary event, recovered or lost, and thousands of EVs are tracked until the simulated recovery converges, defined herein as a <0.01% change in average recovery when additional EVs were tracked. An additional convergence criterion was emplaced that stipulated a <10% standard deviation for five repetitive simulations. Lastly, given various V_{ave} were tested, the program's discretization of time into Δt time steps was added as a final convergence criterion: after halving the Δt increment, the averaged solution from five simulations must differ by <1%, else the simulations would be repeated after halving Δt again. An example of the average EV isolation recovery converging as addition EV tracks are included in the simulation while also converging the simulation's Δt time stepping is shown in Figure 2.8.

The accuracy of the Monte Carlo program was first tested by removing all recovery effects and letting EVs freely diffuse through solution; the analytical model of Fick's Second Law (Eq. 1) then becomes fundamentally valid. The results from the Monte Carlo simulation agreed well with a Gaussian function produced via Eq. 1. After enabling EV-MAP recovery but without Chang-Hammer dynamics, where any surface interaction was considered successful, EVs accumulated along the channel for a total recovery of 64%. The Chang-Hammer dynamics governing the probability of Ab-EV binding in Eqs. 4-8 were then activated (axial distribution not shown), and the EV isolation recovery dropped substantially to 16% for this set of simulation parameters: inter-pillar spacing of 10 μm but short bed length of 2.5 mm and average velocity of 1 mm/s, which reduces the overall time available for axial diffusion. Lastly, we compared the Monte Carlo model to our previous, less precise model for the set of experimental data in Battle, *et al.*[39] Our previous simulation, which did not take into account Chang-Hammer dynamics and did not

couple diffusion with fluid flow, generated 68% recovery for membrane proteins, while the Monte Carlo method predicted 75% recovery, which better approached the experimental values of 90 ±2%. Further improvements to the model, namely improving the Poiseuille approximation (Eq. 2) to better approximate the flow profile around circular pillars (50 µm spacing in Battle, *et al.*[39]), would include reduced flow velocities between pillar rows and increase residence time available for diffusion and overall recovery in the model. All subsequent simulations used the parameters in Table 1.2 for evaluating EV isolation recovery *in silico*.

Table 2.4: Parameters used for Chang-Hammer dynamics (Eqs. 4-8) in Monte Carlo EV-MAP model.

Property	Value	Reference
EV diameter	50-150 nm	-
Diffusion coefficient (D) in plasma	5-15 $\mu m^2/s$	-
Minimum Ab surface density (C_∞)	12.31 μm^{-2}	[40]
Antibody binding kinetics (k_{in})	2.5 x 10^4 M^{-1} s^{-1}	[41]
Ab-antigen encounter radius (a_i)	2 nm	[28, 42]

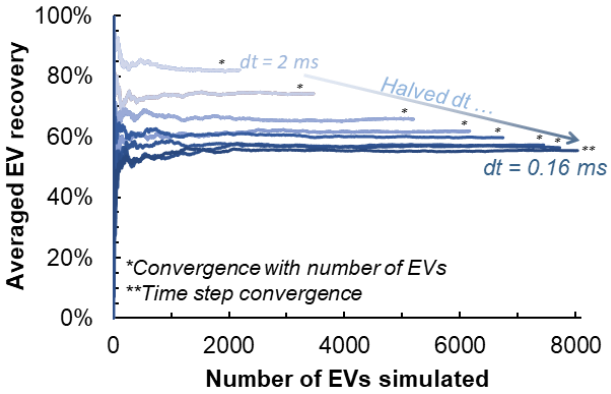

Figure 2.8: An example of convergence within the Monte Carlo simulations. More EVs are simulated until the accumulated average EV isolation recovery converges to <0.01% difference (*). Further, Δt is halved until the averaged recovery converges to <1% error change (**). Another convergence criterion is not shown, where five sequential simulations conducted with the same conditions yield <10% standard deviation. These results were obtained for an EV with D = 5 $\mu m^2/s$, initially centered in a channel with L = 25 mm and W = 10 µm, and infused with an average velocity of 1 mm/s. (Courtesy of Dr. Matthew Jackson)

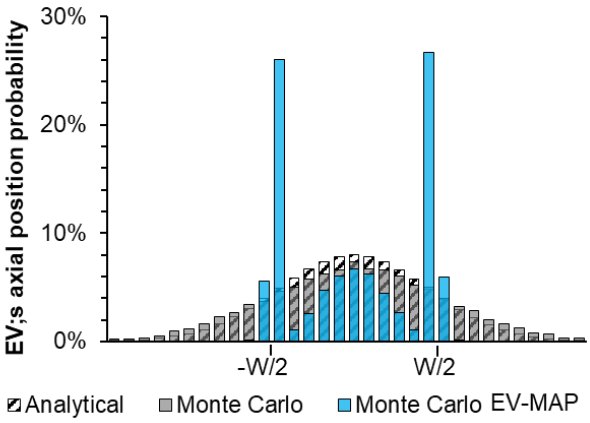

Figure 2.9: EVs diffused axially amidst Poiseuille flow, and their axial position was tracked with respect to the channel's width (*W*). Simulations agreed with the analytical solution to Fick's Second Law (hashed bars) when affinity-binding was disregarded in the Monte Carlo model (grey bars). When MAP affinity-binding was enacted (blue bars), the EV spatial distribution changes significantly, even within the channel's width, because Fick's law becomes invalid as EV concentration is no longer constant. Note that D = 5 $\mu m^2/s$, L = 2.5 mm, W = 10 µm, V_{ave} = 1. mm/s, and Chang-Hammer dynamics were neglected so that all EV-Ab interactions were successful. (Courtesy of Dr. Matthew Jackson)

2.5 Fabrication and assembly of the device

The 3-bed device was also fabricated by hot embossing using a COC thermoplastic. Figure 2.10 A shows the brass mold used for hot embossing. Figure 2.10 B and C shows SEM images of the micropillars in each bed.

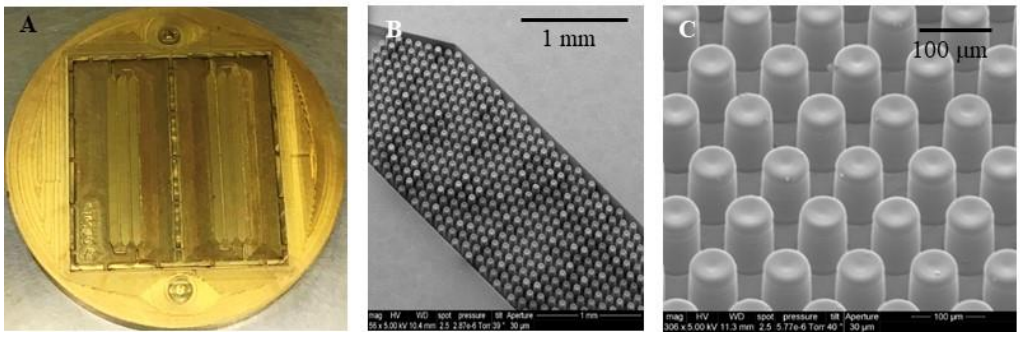

Figure 2.10: (A) Brass mold used for hot embossing. (B) SEM image of the device bed with the pillar. (C) Circular micropillars in each bed (there are over 15000 such pillars per device).

Following embossing it was necessary to confirm pillar dimensions. Thus, pillar dimensions were checked using non-contact profilometry (see Table 2.5 for the results)**.** Calculated average pillar dimensions based on the profilometric analyses are shown in Table 2.3.

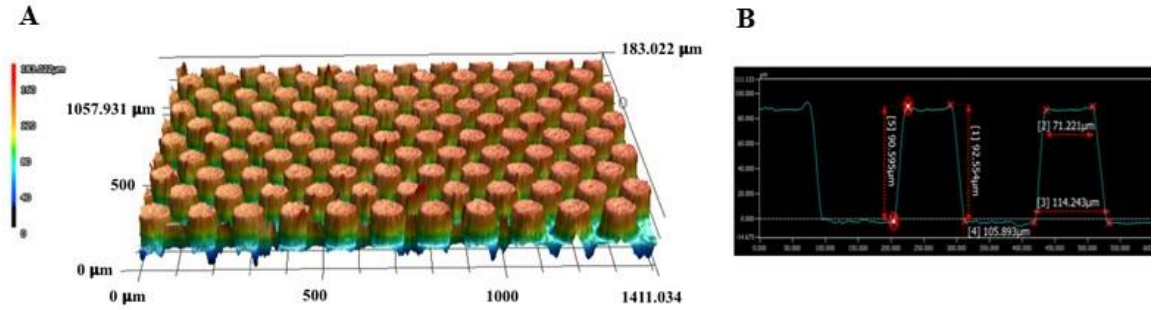

Figure 2.11: (A) A profile image of the pillars in the 3-bed device (color scale shows the height distribution). (B) Profilometry analysis of the pillars.

Table 2.5: Pillar dimensions of the 3- bed device

Dimension	Value
Pillar height/ µm	92 ± 3
Pillar diameter/ µm	109 ± 3
Inter pillar spacing/ µm	10-20

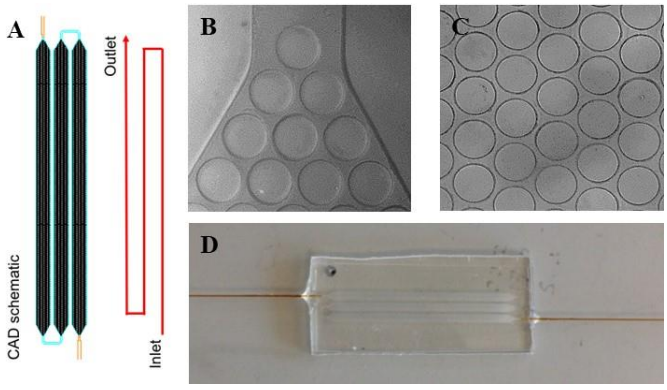

Figure 2.12: (A) Pillars of the device closer to the inlet – 10x magnification (before bonding). (B) Pillars of device in the middle of bed (before bonding)- 10x magnification. (C) Pillars after bonding - 10x magnification. (D) Final device.

Devices with correct dimensions were used in experiments for isolating EVs. Next, devices were cut and then cleaned well to remove dust particles because the presence of dust particles can cause problems in the thermal fusion bonding step. Cleaned devices were dried by keeping in an oven before thermal fusion bonding. The method used here is the same as the method we used in bonding sinusoidal devices explained previously in this chapter and used for cell isolation. But here, we used capillaries with 150 µm ID and 250 µm OD and bonding was performed at 137 °C for 1 h. After bonding, non-contact profilometry was performed again to confirm the dimensions of the pillars (Figure 2.12 C). In this step, 9 images of the device were taken at different points of the 3 bed (middle and two corners), which were later analyzed using a custom written macro in ImageJ software. Finally, inlet and outlet positions of the devices with the correct pillar dimensions are sealed with epoxy to prevent any leakages during sample processing. Figure 2.12 D shows final device after assembly, which is ready for modification for affinity selecting EVs of interest.

2.6 Modification of the microfluidic devices for affinity capture of CD8+ T cells and CD8+ EVs

Following assembly, the surfaces of the microfluidic devices must be modified to affinity select markers of interest. Use of mAb for affinity selection is advantageous due to its exquisite target specificity, which is important in isolating markers for clinical applications. However, one of the major drawbacks in many microfluidic devices developed recently is the use general affinity-enrichment of bulk EVs by targeting the tetraspanins such as CD9, CD63, and CD81.[9-11] These cannot be used for isolating and analyzing subset of EVs that are specific to disease conditions, such as in case of stroke diagnosis. Thus, we used CD8 mAb for specifically affinity selecting CD8 T cells and CD8 EVs. When using CD8 mAb for affinity selection we can specifically extract mRNA in CD8 EVs providing more accurate gene expression data for ischemic

stroke diagnosis. Both CD8 T cells and CD8 EVs contain CD8 antigen on their surface that allow the isolation through affinity selection via an anti CD8 mAb.

The first step in the antibody surface immobilization process is to generate on the surface of the device functional groups for Ab attachment. Most of the thermoplastics used for microfluidics including COC does not contain surface functional groups. Therefore, activation protocols are employed to create suitable surface functional groups. In this study, we used irradiation method to generate functional scaffolds via photo-oxidation reactions. During UV activation process UV/O_3 treatment is performed using a quartz Hg lamp, which will constantly generate and consumes O_3, which results in a steady-state concentration of strongly oxidizing atomic O. At higher energy, both UV exposure and oxidative stress will produce radicals within the polymer. Generated radicals may break or scission polymer chains into smaller fragments, which can result in intramolecular rearrangements, crosslinking of polymer chains, and/or react with water or oxidative species to form carboxyl or other O-containing groups.[43-47]

Due to formation of carboxylic groups on the polymer surface, it becomes more hydrophilic compared to its pristine form, which can be demonstrated by measuring water contact angle. Upon UV irradiation, wettability of the surface was increased and water contact angle of COC polymer decreased from 85.6 ± 2.52° to 33.68 ± 3.15°. For generating carboxylic groups, devices were UV-modified for 13 min (22 mW cm^{-2}). Once the carboxylic acid groups are formed on the device surfaces, antibodies can then be immobilized onto the device surface.

The ability to release affinity-selected biomarkers, including cells and EVs, from the device surface following isolation without changing their morphology or molecular content, is essential for molecular diagnostics and for further characterization processes. Hence, we used a single-stranded DNA (ssDNA) that bifunctional linker to link the capture antibody to the surface of the microfluidic device.[14] ssDNA used here contained a uracil (dU) residue that enables enzymatic nicking by USER™ (Uracil-Specific Excision Reagent), thus releasing any biomarker that is

affinity selected on the Ab through the ssDNA. High stability and the ability to attach to many surfaces are some of the advantages of using ssDNA linkers.[14]

The oligonucleotide was designed and modified so that it could be covalently attached to the device surface through the -COOH group (5'/5AmMC 12/TTT TTT TTC CCT TCC TCC TCA CTT CCC TTT/ ideoxyU/TT TTT TTT T/3ThioMC3D/). The 5' end of the oligonucleotide contained a NH_2 group that made it easy to covalently attach to the device surface via 1-Ethyl-3-(3dimethylaminopropyl)-carbodiimide (EDC) coupling reaction. The mechanism involving this step are shown in Figure 2.13. The time for the reaction was ~2 h at room temperature.

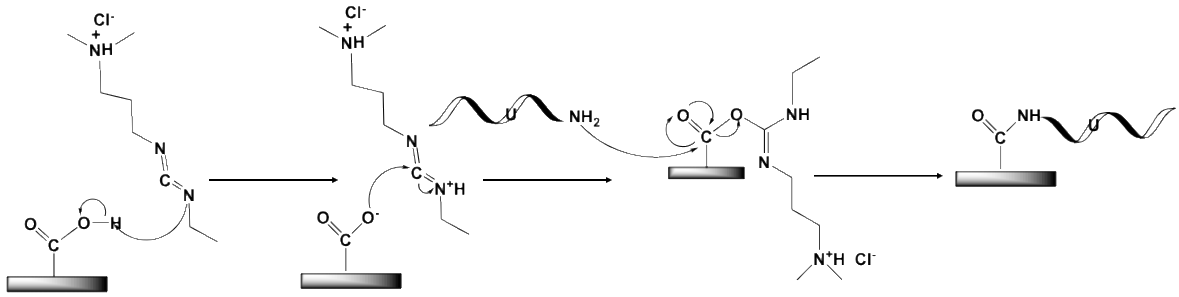

Figure 2.13: Mechanism for attachment of oligonucleotide to the device surface through EDC coupling reaction.

The next step was to react the mAb with a sulfo-NHS ester of succinimidyl *trans*-4 (maleimidylmethyl) cyclohexane-1-carboxylate (SMCC), which will yield a maleimide-labeled mAb (SMCC-mAb) through as illustrated in Figure 2.14. Sulfo-SMCC is a heterobifunctional crosslinker that contains *N*- hydroxysuccinimide (NHS) ester and maleimide groups that allow the conjugation of amine and sulfhydryl containing molecules. Thus, amine containing mAb can be conjugated with sulfo-SMCC. These NHS esters can react with primary amines at pH 7-9 forming amide bonds, while maleimides react with sulfhydryl groups at pH 6.5-7.5 and form stable thioester bonds. The NHS-ester group undergo hydrolytic degradation, whose rate increases at higher pH values. But the maleimide group is considerably more stable than the NHS-ester group. But it will also hydrolyze and will lose reaction specificity for sulfhydryl at pH values >7.5. Hence, the reaction is usually performed at pH 7.2-7.5. The cyclohexane ring in the

spacer arm in sulfo-SMCC decreases the rate of hydrolysis of the maleimide group compared to similar reagents without a ring.[48] We started with a mAb concentration of 1 mg/mL (excess) to ensure that we have enough Ab concentration after the final purification step.

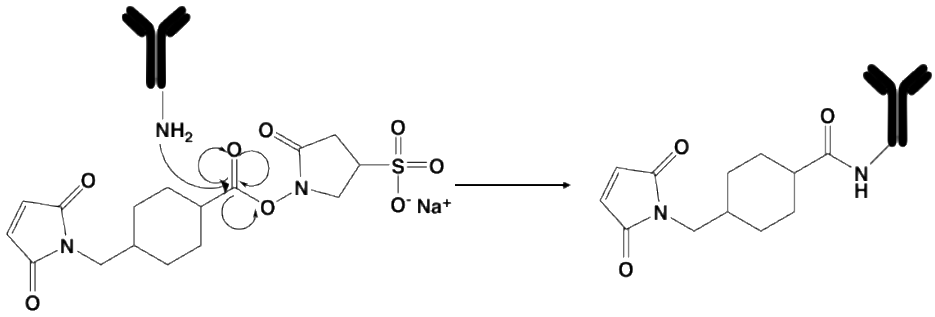

Figure 2.14: Mechanism for Ab conjugation with sulfo-SMCC.

After mAb is conjugated with SMCC, next excess (nonreacted) reagent was removed by a desalting column. In order to attach SMCC-mAb to the oligonucleotide, there should be a sulfhydryl group in 3' end of the oligonucleotide. Thus, dithiothreitol (DTT) (at pH 10) was used to reduce the disulfide bond present in the 3' end to a -SH group. Then, devices were washed with PBS (pH 7.4), and the mAb was injected into the devices. The mechanism involved in these steps is shown in Figure 2.15. Surface modified devices were kept at 4°C overnight for reaction to take place. These mAb modified devices can be stored at 4°C until samples are run by stabilizing the Ab using a stabilizing cocktail, which is important when it comes to using these devices for clinical applications.

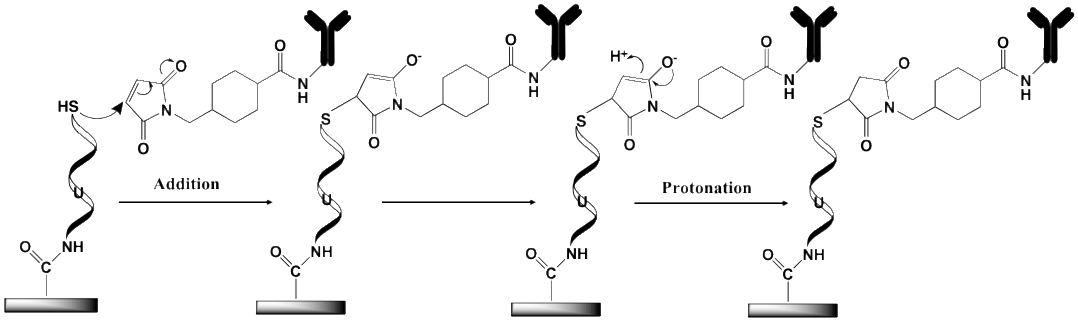

Figure 2.15: Immobilization of Ab on to the device surface via the oligonucleotide.

2.7 EV isolation using the microfluidic device

The microfluidic device that we designed and developed needed to be checked to confirm whether EVs can be actually captured on the micropillars. For initial experiments, EVs from the Molt-3 cell line was used. Cells grown in EV depleted FBS media was centrifuged for 10 min at 300 g. At this speed EVs in the media will remain in the supernatant, which was then used for EV isolation.

Non-specific binding to polymer surfaces is one of the major problems that needs to be overcome when processing clinical samples for diagnostic purposes. Non-specific binding is the binding of material to sites on the polymer surface, which will result in a false positive contribution to the result. The main reasons for non-specific binding are, molecular forces, like charge interactions, and hydrophobic interactions between the surface and other solution borne materials.

Here, a mixture of BSA and PVP was used as a blocking agent to minimize non-specific binding. BSA is considered to be a universal blocking reagent. The main reason for using BSA is that, BSA does not affect the functions of other proteins (antibodies), which is important because Abs are used in the microfluidic device.

Polyvinyl pyrrolidine (PVP) is a non-protein alternative to conventional blocking buffers. It is a water-soluble polymer, which can be used in a variety of applications owing to many advantageous characteristics. PVP has good solubility in water, shows strong affinity to various polymers, has a high hygroscopicity, and good adhesiveness to various substrates. This is commonly used with a combination of other blocking solutions. Here, 0.5% BSA/1% PVP solution was used as a blocking buffer. Devices were washed with 500 µL (~70 times device volume) of blocking buffer at 10 µL/min prior to sample processing.

Next, sample was processed through the device at 5 µL/min. Flow rate we selected was based on results obtained from the simulation studies that was explained previously. Based on Monte Carlo simulations, at this flow rate we can obtain a recovery of ~42%.

Once the sample was processed, 1% Tween 20 solution was used to prevent non-specific interactions. Tween 20 is a nonionic detergent (surfactant) that is widely used as a blocking agent. Specific binding is typically more resistant (strong) to this reagent while nonspecifically bound substrates with weak interactions can be washed out.

Fluorescence imaging is a widely used technique to visualize affinity selected markers on modified surfaces. Here, an APC conjugated CD8 antibody was used to detect if EVs were captured using our device. Allophycocyanin (APC) exhibits far-red fluorescence with high quantum yields and is excited at 594 nm and 633 nm with an absorbance maximum at 650 nm and emission wavelength of 660 nm. When APC conjugated Abs are incubated in chip, it will bind to the CD8+ EVs that have been already been isolated by the device. Thus, it's a good way of showing that CD8+ EVs have been captured by the Ab-decorated micropillars. As control experiments, we performed a negative control and an isotype control. In the negative control experiment, we did not have the CD 8 Ab.

As another control, isotype control experiments were also performed. Here, instead of CD8 mAb, isotype control was used in the modification step. Isotype controls are also primary antibodies, but they lack specificity to the target. They should match the class and type of the primary antibody that has been used.

Isotype of the primary Ab was used mainly to detect non-specific binding. Primary Ab background signal could be caused by binding of substrates to receptors on target cells/EVs by non-specific interactions with other cells/EVs or due to autofluorescence. Isotype control antibodies act as negative controls to help differentiate non-specific background signal from specific antibody signals because they have no relevant specificity to target antigen.[49]

After incubating devices with the dye-labeled Ab, devices were washed again with Tween 20 solution to get rid of any non-specifically bound Ab. Prior to imaging, devices were washed well with PBS since Tween 20 to quench the fluorescence as it is a surfactant.

Fluorescence images in Figure 2.16 show the results we obtained for CD8 Ab-modified device, isotype IgG2B modified device, and a device without Ab. All the images were background subtracted and intensity scaled based on the negative control. There was an increase in fluorescence intensity in the CD8 Ab modified device compared to the isotype control and negative control experiments. These results demonstrate that EVs can be isolated using the microfluidic device. Since an increase in the fluorescence was observed in the CD 8 mAb modified device compared to the controls, the device we designed can be used for isolating EVs and methodology we used for surface modification for affinity selection gives us the specificity that is required for analyzing clinical samples.

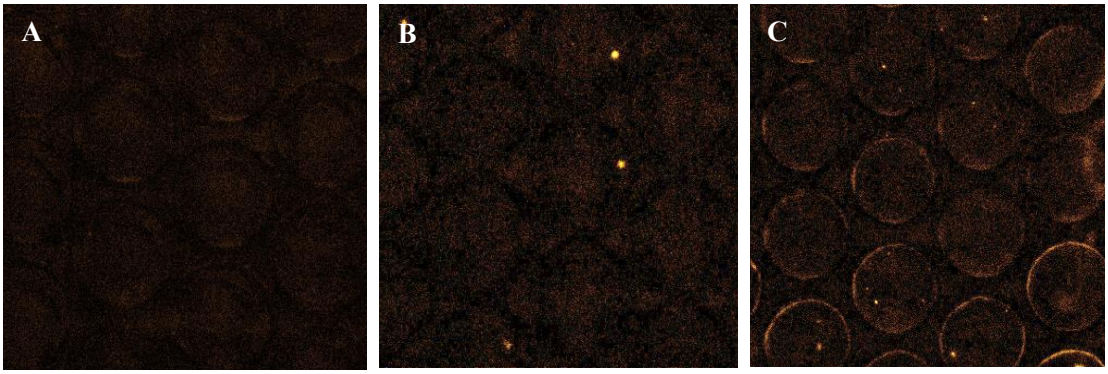

Figure 2.16: Fluorescence images after staining the EVs captured on the device surface with Cy5 labeled secondary antibody: (A) negative control without CD8 Ab (B) Isotype (IgG2B) control (C) CD8+ Ab.

2.8 Release of enriched EVs from the device's surface

Because successful isolation of EVs is possible by the microfluidic device, the next challenge is to release the enriched EVs from the device surface without affecting its morphology and its' molecular content. As a releasing method of enriched EVs, we used an enzymatic cleavage method, which has been used earlier for releasing affinity selected circulating tumor cells from an antibody capture surface.[14]

For this purpose, a ssDNA was used that contained a single uracil (dU) residue. (5'/5AmMC 12/TTT TTT TTC CCT TCC TCC TCA CTT CCC TTT/ideoxyU/TT TTT TTT

T/3ThioMC3D/). The uracil residue in the oligonucleotide enables the enzymatic cleavage using USER™ (Uracil-Specific Excision Reagent), releasing EVs that have been affinity selected by CD8 mAbs.

USER™ consists of a mixture of uracil DNA glycosylase (UDG) and DNA glycosylase-lyase endonuclease VIII. UDG in the mixture catalyzes excision of dU forming an abasic site and endonuclease VIII breaks the phosphodiester bond of the abasic site, cleaving the ssDNA linker, which will release the selected EVs from the microfluidic device's surface. The benefits of using USER is that it's active at physiological temperatures and in a variety of buffers, such as PBS. Previous studies have reported that under these release conditions the cells are not affected.[14] The mechanism of EV release is illustrated in Figure 2.17.

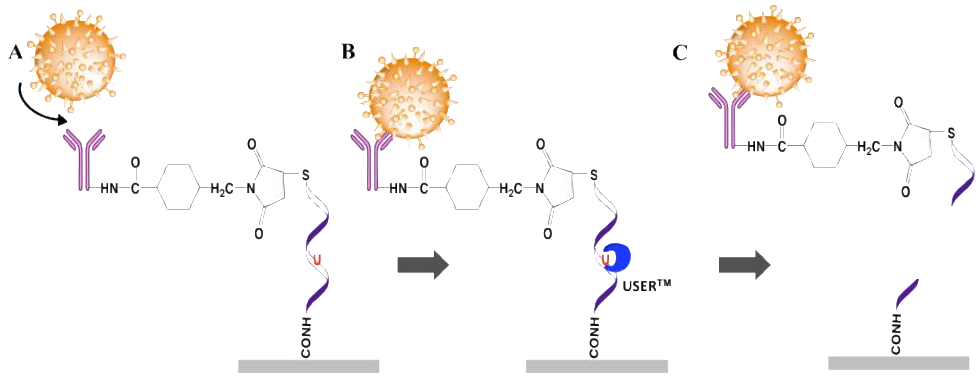

Figure 2.17: EV selection and releasing method (A) mAb immobilized on the device surface via oilgonucleotide with a uracil residue. (B) Incubation of isolated EVs and the oligonucleotide with the USER enzyme. (C) Cleavage at the uracil position results om the release of isolated EVs from the device surface.

2.9 Transmission Electron Microscopy (TEM)

Imaging released EVs is important to determine the size distribution and morphology of EVs. Yet, imaging and tracking of EVs can be challenging due to their small sizes. Electron microscopy has been considered as a standard imaging method available for visualizing nano-sized particles.[50] As such, electron microscopy typically has a resolution of approximately 0.5 nm,

which is smaller than EVs. Therefore, using electron microscopy can provide structural information about EVs. Here, we used EVs stained with uranyl acetate stain for imaging. The advantage of using uranyl acetate is that it produces the highest electron density and thus, good image contrast.

Collected EV samples were stored at -80 °C until use. Before preparing the grids, samples were vortexed thoroughly to obtain a homogeneous solution. EV samples were then mounted on a carbon coating grid for imaging and samples were air dried on the grid and then stained with uranyl acetate. As mentioned earlier, interaction of the electron beam with the sample generates contrast in the image. The most common type of staining is negative staining, where the electron beam primarily interacts with the stain. The stain surrounds the sample, but it is excluded from the volume occupied by the sample and thus, we see sharp dark edges and light color inside the EVs. During the drying process, the EVs can collapse resulting in a cup-shaped morphology, which is often considered an atypical feature of EVs.[51-52] But when quickly frozen, EVs analyzed by cryo-electron microscopy will show that EVs have a perfectly rounded shapes.[53] The TEM images in Figure 2.18 shows EVs secured from the Molt-3 cell line. Since, compared to the control sample, EVs were observed in the grids with samples released from the devices (plasma processed devices), these images reveal that EVs have been successfully isolated on our microfluidic device and those have been released successfully by USER enzyme system.

However, the size of EVs appear in TEM images could be smaller compared to the actual value of EV size due to dehydration of sample during sample preparation step.[54-55]

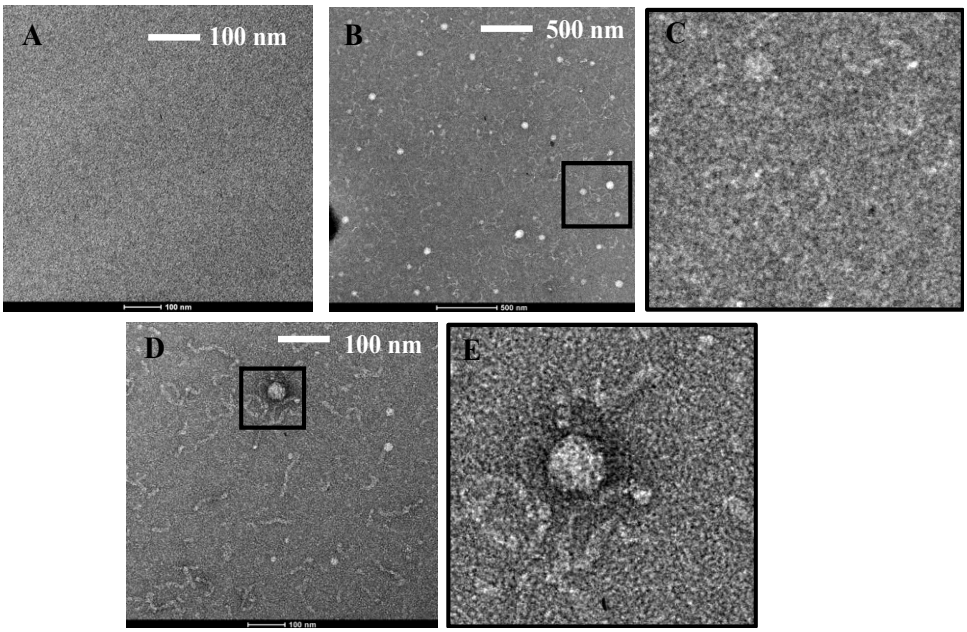

Figure 2.18: TEM images (A) Blank (Buffer and the USER enzyme) (B) and (D) EVs released from Molt 3 cell line (C) and (E) Zoomed view of EVs of figure B and figure D.

2.10 Nanoparticle Tracking Analysis (NTA)

This technique is a combination of laser light scattering microscopy and a charge-coupled device (CCD) camera that enables visualization and recording of nanoparticles in suspension (Brownian Motion). Particles will move randomly in all directions when they are dispersed in a suspension. The liquid is also called the continuous phase, which can be water or any other solvent. Phenomena of random motion is known as diffusion and expressed by the diffusion coefficient (D). Undirected migration of any given particle will be caused by energy transfer from the surrounding water molecules to the particle. In the absence of any concentration gradient within the dispersion and upon long-term observation, small particles move in any direction and will counterbalance each other with time, which will lead to a total movement of almost zero. But, during given time periods, diffusing particles move within certain volume elements. Due to Brownian motion, in NTA the time (t) between two different observation points is small, which is approximately 30 ms. During NTA analysis, the movement of nanoparticles per time interval is recorded and quantifies as the mean square displacement $\langle x \rangle^2$. Depending on the number of

dimensions, the observed mean square displacement and the diffusion coefficient can be calculated as explained below.

For one dimension: $D = \frac{\langle x^2 \rangle}{2t}$ (Eq.9a)

For two dimensions: $D = \frac{\langle x,y^2 \rangle}{4t}$ (Eq. 9b)

For three dimensions: $D = \frac{\langle x,y,z \rangle^2}{6t}$ (Eq. 9c)

For these expressions, D is the diffusion coefficient and t is the time between two different observation points. Through the Stokes-Einstein relationship, the diameter of the particle d can be calculated as a function of diffusion coefficient D at a given temperature T and a constant viscosity η of the liquid.

$D = \frac{4k_B T}{3\eta\pi d}$ (Eq.10)

where k_B is the Boltzmann's constant.

In NTA, variability of a single particle is considered in two dimensions, thus combining both the Stokes-Einstein relationship and two-dimensional mean square displacement. The following equation can be used to find particle diameter (d);

$D = \frac{4k_B T}{3\pi\eta t} . \frac{4t}{\langle x,y \rangle^2} = \frac{16k_B T}{3\pi\eta\langle x,y \rangle^2}$ (Eq. 11)

By simultaneously tracking particles, their diameters can be calculated. In NTA, the smallest detectable particle size is determined by the scattered intensity of the particle and the sensitivity of the camera used in the instrument. The refractive indices of biological nanoparticles, like EVs is around 1.37-1.45 which makes a limit of detection of 30-50 nm for NTA.[56-57]

Nanoparticle tracking analysis has several advantages over TEM for EV analysis. First advantage is the ability to accurately measure small particles with a diameter of approximately 30 nm. Sample analysis is performed in liquid form thus there's no hydration taking place during sample processing. Furthermore, sample preparation is very fast and easy which is not as complex as in TEM. Also, measurement can be completed within few minutes. Another feature that

makes NTA more attractive is that samples can be recovered in its native form after the measurements.[55] NTA is precise between particle concentrations are in the range $2x10^8$ and $2x10^9$ particles/mL. Therefore, samples were diluted whenever necessary.

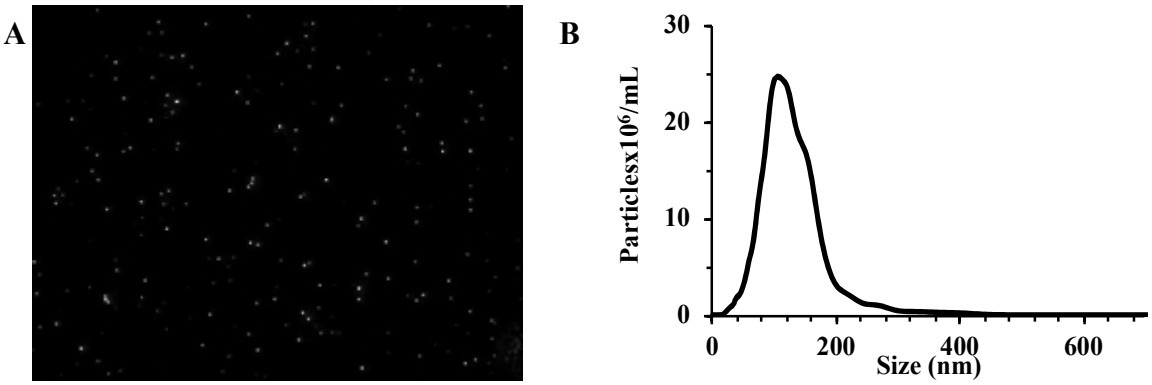

Figure 2.19: (A) Nanoparticles detected by NTA during sample analysis. (B) Size distribution and concentration of EVs isolated from Molt-3 cell line.

Blank (control sample) which consisted of USER enzyme and PBS didn't show any nanoparticle detected from NTA. Figure 2.19 A shows nanoparticles that have been captured in a video during an NTA experiment. After data analysis a size distribution curve (shown in Figure 2.19 B) can be obtained. The average number of particles that have been released from the devices were (2.94 ± 0.48) $x10^9$ particles/mL (n=3, 5 readings per sample) and the average size of EVs was (150.4 ± 22.6) nm (n=3, 5 readings per sample).

2.11 Efficiency of EV release from the microfluidic device

For counting the number of EVs captured and to provide sufficient material for mRNA expression profiling, it is important to ensure that all the EVs have been released from the device surface. Hence, release efficiency of EVs was determined experimentally. While we have used the uridine-containing ssDNA and the USER enzyme system for the release of biological cells,[25] we have not investigated the use of this release system for EVs. The release efficiency was determined by performing a first round of EV release, followed by a second round performed with the USER enzyme. Then TEM and NTA were performed for collected EV samples resulting

from each release round. Figure 2.20 A and B below show TEM images of EVs collected during the first and second release.

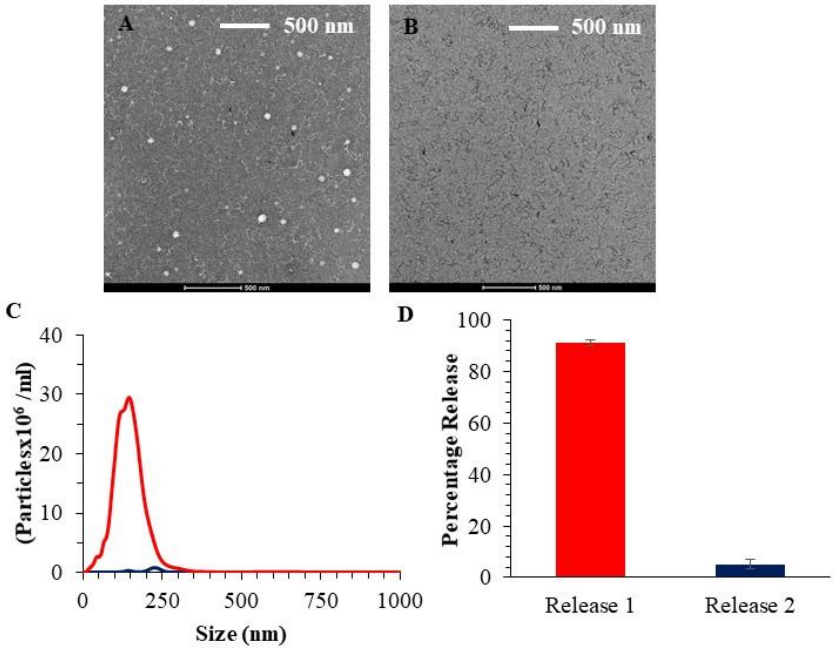

Figure 2.20: (A) TEM image of EVs released during the first release with the USER enzyme. (B) TEM image of EVs released during the second release with the USER enzyme. (C) NTA analysis showing the concentration of EVs released during first (red trace) and second release (blue) with the USER enzyme. (D) Percentage of EVs released during first (red trace) and second release (blue) with the USER enzyme.

According to the NTA results, during the first release (2.94 ± 0.48) x10^9 particles/mL were released and (1.71 ± 0.79) x10^8 particles/mL were released during the second release. After the second release proteinase K digestion was performed to see if any particle is released. But only a very little particles were released by proteinase K, which suggest that after second release almost all the EVs have been released by the USER enzyme. These values were used to calculate the EV release efficiency using the following equation.

$$Release\ Efficieny = \frac{EVs\ relased\ during\ first\ relase}{EVs\ relased\ during\ first\ relase + EVs\ relased\ during\ second\ relase} \quad \text{(Eq. 12)}$$

The release efficiency was determined to be 96.4 ±1.8% (n=3, 5 readings per samples), which shows that high release efficiencies can be obtained using enzymatic cleavage to release EVs.

2.12 Stimulation of T cells in Molt-3 cell line

Inflammatory responses taking place during ischemic strokes can be characterized by rapid activation of certain cells, including different subtypes of T cells, macrophages, and neutrophils.[58-60] Lipopolysaccharide (LPS) is a strong stimulator and can cause antigen presenting cells (macrophages and T cells) to release cytokines, such as IFN-I, TNF-α, and IL-12. Even small doses of LPS can cause strong activation of $CD8^+$ T cells.[61] Thus, the inflammatory responses induced by LPS can be related to inflammatory responses that takes place during an ischemic stroke event.

In order to stimulate cells, LPS was used. LPS is a major component of the outer membrane of gram-negative bacteria. Intact bacterial LPS are macromolecules with a molecular mass of approximately 10-20 kDa. The three major structural components of LPS are shown in Figure 2.21. Those are O-specific chain that is specific to the bacterial stereotype, a core oligosaccharide, and a lipid component that is termed as lipid A. Lipid A component of LPS determines the endotoxic and toxic activities of LPS.[62]

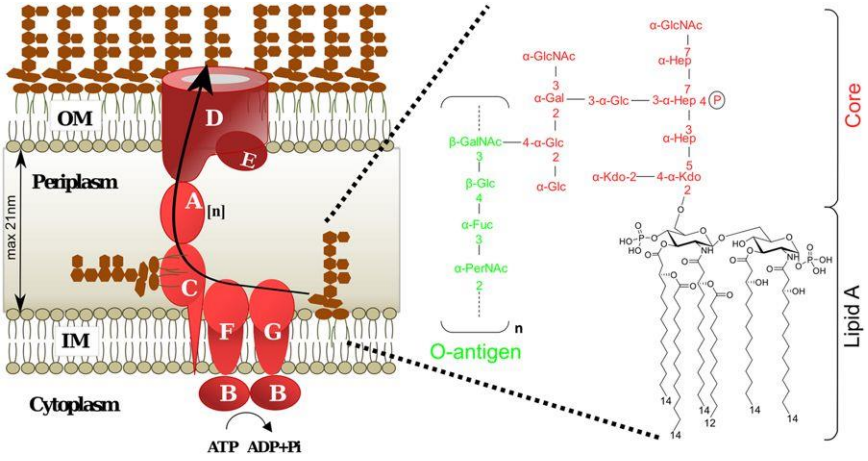

Figure 2.21: Structure of LPS; O-antigen, the core oligosaccharide, and the lipid component (Reproduced from reference Laguri, Sperandeo et al. 2017)

LPS can also trigger the production of reactive oxygen species (ROS), such as nitric oxide (NO).[63-64] Produced ROS can cause toxic effects to cells including DNA or RNA damage, oxidation of polyunsaturated fatty acid in lipids, oxidations of amino acids, and oxidative deactivation of specific enzymes by oxidation co-factors. All these effects cause cell death.[64] Moreover, LPS can increase oxidative stress, mitochondrial respiratory dysfunction, and cell death via inducing apoptosis.[65]

Thus, LPS stimulation conditions such as concentration and stimulation time need to be optimized for Molt-3 cell line so that the cells still viable after LPS stimulation. For this purpose, cell cultures were started (~$1x10^6$ cells) and the cells were stimulated with different LPS concentrations. Changes in cell media, viability of cells, and morphology of cells were monitored at different time points up to 72 h. A control experiment was performed without adding LPS to the cells. RPMI media contains phenol red indicator, which can be used to monitor pH changes. At pH 7 the color of the media is light orange and at higher pH values color changes to purple. Yellow color indicates acidic pH. At 1 ng/mL of LPS, the color of the media started to change to yellow (media has become acidic) after 48 h, while at higher LPS concentrations (100 ng/mL), the color started to change to yellow, after 12 h (Figure 2.22). This pH change might be due to cell death caused by apoptosis and release of cell components to the culture media.

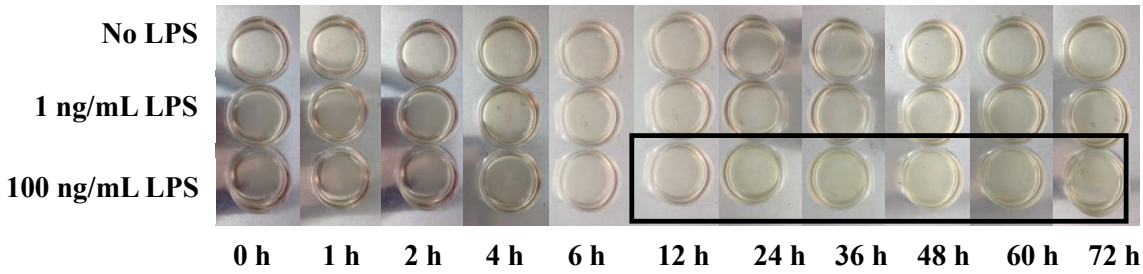

Figure 2.22: Color change in media indicating the pH change (phenol red indicator in the RPMI media was used to monitor the color change).

Figure 2.23 shows morphology changes in cells upon stimulation with LPS. In the control sample without LPS, there were no visible difference in morphology up to 75 h. However, we did observe a change in morphology in cells upon stimulating with LPS. For 1 ng/mL of LPS, we didn't observe changes in the cells for up to 60 h. However, at 72 h we observed some morphology changes in the cells and these morphology changes (cells were not round in shape) were more visible when cells were stimulated with high LPS concentrations. These morphology changes may be due to cell apoptosis caused by LPS. There are various morphological changes that can occur during apoptosis, such as cell shrinkage and pyknosis.[66] Due to cell shrinkage, the organelles become more tightly packed within the cells. Pyknosis takes place as a result of chromatin condensation.[67] As a result of these processes, small blebs are formed, and the nucleus starts to break apart and DNA breaks into small fragments as well. Finally, the cell can break into apoptotic bodies as well. These apoptotic bodies are visible in cell media stimulated with 100 ng/mL LPS at 48 h and can be seen more clearly in the sample collected at 75 h (shown in arrows in Figure 2.23 C right).

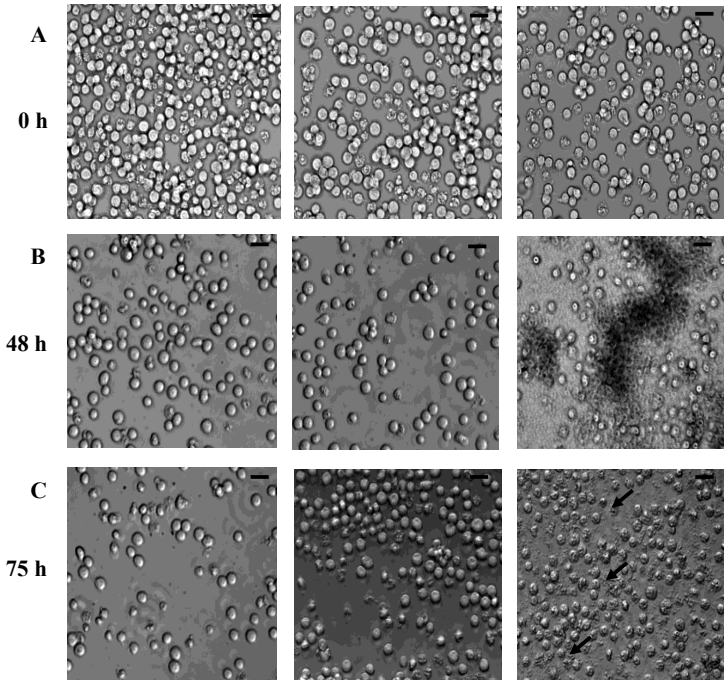

Figure 2.23*:* Morphology changes of T cells during LPS stimulation (Left: no LPS, middle:1 ng/mL of LPS, right: 100 ng/mL) (A) 0 h (B) 48 h (C) 60 h - 40x magnification; scale bar on the images is 15 μm.

Therefore, it's important that cells remain viable during these experiments to prevent formation of apoptotic bodies while at the same time, provide sufficient stimulation of the cells. Thus, cell viability was determined at each time point. For cell viability determinations, Live/dead cell assay kit was used, which contains two fluorescent dyes, calcein AM and propidium iodide. Calcein AM is a cell-permeant dye that is widely used to determine cell viability in eukaryotic cells. In live cells, the non-fluorescent calcein AM will be converted to a green-fluorescent calcein due to the acetoxymethyl ester hydrolysis by intracellular esterase present in live cells. Thus, live cells will appear as green. Because the cell membrane is damaged in dead cells, propidium iodide can go inside cells where it intercalates with DNA and results in enhanced red fluorescence. Hence, dead cells will appear as red. Calculated cell viability values are shown in Figure 2.24. In control samples without LPS and at low LPS concentration (1 ng/mL), a significant change in the cell viability was not be observed up to 72 h time period. After 72 h, the cell viability for control and for samples stimulated with 1 ng/mL of LPS were 87% and 82%, respectively.

However, at high LPS concentrations (100 ng/mL), cell viability started to drop after 24 h. At 24 h, the observed cell viability was ~85% but after 36 h, it dropped to ~76% and reached ~30% after 72 h. Thus, to stimulate the cells in a minimum stimulation time while preserving their cell viability, we selected 100 ng/mL of LPS, and the time of stimulation selected was 24 h. Another reason for selecting these conditions is that we want to induce a strong stimulation within a short time period and analyze the EVs which is similar to what happens during a stroke event.

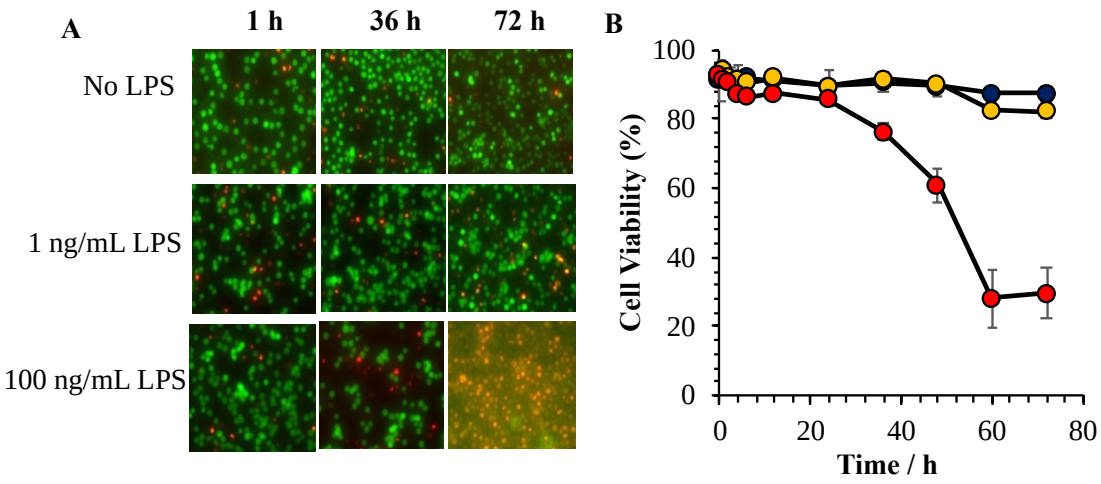

Figure 2.24: (A) Cell viability images for Molt-3 cell line upon stimulating the cells with LPS (Live cells are in green and the dead cells are in red). (B) Variation of cell viability during LPS stimulation at varying LPS concentration.

2.13 Isolation of CD8+ T cells from media

Cell cultures were started with ~1x10^6 cells/mL and stimulated with 100 ng/mL of LPS. After 24 h, cell viabilities of the control (without LPS) and the sample stimulated with LPS were 96.4 ± 0.37% and 87.3 ± 1.09%, respectively. Cell media was centrifuged to enrich cells and the obtained cell pellet was resuspended in PBS (Figure 2.25 A). Supernatant obtained from this step was used for EV isolation as well.

For isolation, the microfluidic device with sinusoidal channels (explained in section 2.3.3) was used. Prior to sample processing, devices were washed with 0.5% BSA to reduce non-specific binding. Next, the cell suspension was hydrodynamically passed through the microfluidic device using a syringe pump (Figure 2.25 B) to capture CD8+ T cells. Post washing was performed with 0.5% BSA to remove any non-specifically bound cells. Figure 2.25 C shows the CD8+ T cells that have been captured on the microfluidic device.

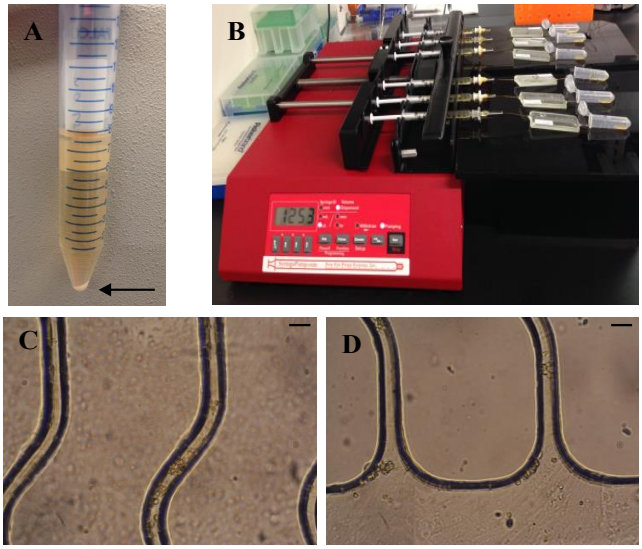

Figure 2.25: (A) Cell pellet collected after centrifuging the sample at 300 g for 10 min (shown by the arrow). (B) Syringe pump set-up used to hydrodynamically flow the samples through the devices (C) and (D) Cells captured from Molt 3 cell line: scale bar 25 μm.

2.14 Isolation of CD8+ EVs from media

As described in the previous section, when the cell media was centrifuged at 300g, EVs will remain in the supernatant. Therefore, the supernatant was used for isolation of EVs. Sample processing protocol was the same as that described in section 2.7.

2.15 On-chip lysis and extraction of RNA

Isolated T cells and EVs were in some cases lysed in order to analyze their molecular content. In this study, we were interested in analyzing the mRNA of T cells and EVs. To accomplish this, RNA was extracted from EVs and T cells using a commercially available RNA extraction kit. The kit consisted of a TRIzol reagent, which is a monophasic solution of phenol and guanidinium isothiocyanate. TRIzol works by maintaining the RNA integrity during sample homogenization at the same time disrupting and breaking down cells and denatures proteins.[68] TRIzol solution was injected into the microfluidic devices and flow through (lysate) was collected for RNA purification. Because the quality of the extracted RNA is important for analyzing its molecular

content, the quality of the extracted RNA and the concentration was analyzed by gel electrophoresis. We did not observe significance differences between the RNA profiles of LPS non-stimulated and stimulated EVs (Figure 2.26).

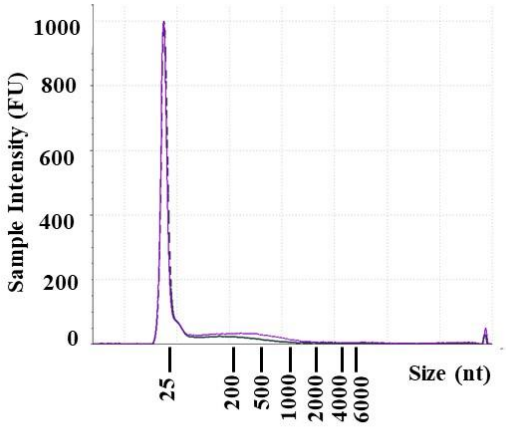

Figure 2.26: RNA profiles of LPS stimulated and non-stimulated EVs: Purple trace: Non-stimulated, Green trace: stimulated with 100 ng/mL of LPS.

2.16 Complementary DNA synthesis from purified RNA

Purified RNA needs to be converted to its complementary DNA (cDNA) for performing PCR for gene expression analysis. The cDNA synthesis kit used in this study contains reverse transcriptase enzyme and an RNase inhibitor (protects the RNA from Ribonuclease (RNase), which is an enzyme that catalyzes the breakdown of RNA into oligonucleotides and smaller molecules). The reaction mixture also contains deoxyribonucleotide triphosphate (dNTPs) and an optimized buffer, which increases the efficiency of the reaction. There is also an anchored oligo-dT primer [$d(T)_{23}VN$], which forces annealing to the beginning of polyA tail of RNA, thus preventing priming at internal sites in the polyA tail.[69] Use of oligo dT primer ensures that all cDNA copies terminate at the 3' end of the RNA and produces the longest contiguous cDNA of the appropriate mRNA template. Control reactions were performed without adding the enzyme to the reaction mixture. Any signal obtained from the negative control will indicate the presence of genomic DNA contamination in the sample.

2.17 Droplet digital PCR for gene expression analysis

For gene expression analysis, droplet digital PCR (dd PCR) was used. Although quantitative PCR (Real time qPCR) is considered the gold standard to measure cDNA levels, results acquired from qPCR can be variable.[49, 70] In qPCR, control genes (internal control) also called reference genes or housekeeping genes, are used to normalize mRNA levels between samples. A house keeping gene should be effectively expressed in cells of interest and essentially it should show minimal variability in expression between different samples under specific experimental conditions that have been used.[71] However, a major problem associated with these housekeeping genes is that the expression level of these genes can vary among cells and can vary under certain circumstances, for example disease states.[72-74] For clinical sample analysis, we need a method that will acquire mRNA expression results with high precision, high sensitivity and reproducibility, irrespective of the physiological state of the cells. Hence, droplet digital (dd PCR) was used in this study.

In droplet digital PCR, target DNA molecules in the sample are distributed in multiple reaction containers (droplets). Some droplets do not have template (mRNA) and other droplets do have the template. After amplification, droplets with template will yield positive end-points, whereas the droplets without template will yield a negative end-point. Droplet digital PCR is based on a water-oil emulsion system. Number of target molecules with positive end point is calculated based on Poisson statistics according to the equation below.

$$\lambda = -\ln(1 - p) \quad \text{(Eq. 13)}$$

In this equation, λ is the average number of target molecules per replicate reaction and p is the fraction of reactions with positive end-point. An approximation of the absolute target concentration is calculated based on λ, together with the volume of each replicate PCR and the total number of replicates (droplets) analyzed.[75] The dynamic range of target quantification largely depends on the number of replicates (number of droplets in each reaction mixture). An order of

magnitude increase in the number of droplets will yield nearly an order of magnitude increase in dynamic range. Moreover, increasing the number of droplets will also improve the precision enabling the detection of small concentration differences.[76] For the ddPCR experiment, total droplet number were always >12,000. (If we have 12,000 droplets and 430 positive endpoints the average number of target molecules per replicate reaction would be 0.035).

In droplet digital PCR, EVA green dye was used. This is constructed of two monomeric DNA-binding dyes that are linked by a flexible cationic linker. In the absence of a double stranded DNA molecule, dye forms a looped conformation that is inactive in DNA binding. But in the presence of double stranded DNA, loop confirmation shifts via an equilibrium to a random conformation, which is capable of binding DNA and thus, emitting fluorescence.

DNA samples, primers and the dye were mixed within each droplet using the droplet generator, which consisted of an oil with stabilizing surfactants. This mixture was used to generate mono-dispersed droplets at a rate of ~1,000 per second. The surfactant stabilized droplets were collected and transferred to a 96-well PCR thermal cycler and amplified to an end point. Then, the reaction plate was transferred to the droplet reader where droplets from each well were aspirated and streamed toward the detector for two color detection system, with each color serving as a negative or a positive control.[75] Figure 2.27 A below illustrates a representative result we obtained from the droplet reader.

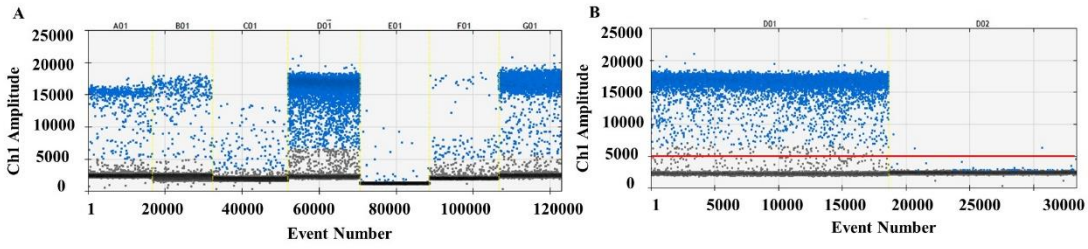

Figure 2.27*:* (A) Final result from droplet reader. (B) Creating the threshold for determining the positive droplets; red line shows the thresh hold.

Blue droplets are positive droplets in which target cDNA was present. To determine actual positive droplet results, the negative reverse transcription reaction was used. As shown in Figure 2.27 B, a threshold was created (red line) and then, the number of positive droplets were determined for each reaction. Because the input RNA concentration was different for each reaction, final results were normalized to the input total RNA concentration using the equation below. All the dilution factors were taken in to account in calculating the final result.

$$\frac{Number\ of\ copies}{RNA\ input} = \frac{\frac{Copies}{\mu L}\ x\ 20\ \mu L\ x\ dilution\ factor}{\frac{ng}{\mu L}\ x\ volume\ input\ for\ dd\ PCR} \qquad \text{(Eq.13)}$$

Here, 20 μL was considered since it was the volume used for the ddPCR reaction and the concentration of RNA in ng/μL was determined from the TapeStation as explained previously. Results obtained after normalization were directly used for generating heat maps for showing gene expression. For evaluating gene expression for diagnosing AIS, we selected gene cluster "4" identified by Adamski, *et. al*, which consisted of 5 genes: *FOS*, *VCAN*, *PLBD1*, *MMP9*, and *CA4*. This gene panel showed statistically significant difference ($p = 1.42 \times 10^{-5}$) between AIS patients and control samples. Upon stimulation with LPS, *PLBD1*, *FOS*, *MMP9*, *CA4* and *VCAN* genes will be upregulated because LPS has a strong stimulation effect on CD8+ T cells. All these genes respond to inflammation and brief explanation about each gene is given below.

Protein synthesized from *PLBD1* gene has a selective expression in alveolar macrophages, broad expression in bone marrow and in some of the immune cells in different tissues. Protein coded from this gene is considered to be an intracellular protein.[77-78] *FOS* gene encodes for a leucine zipper protein that can dimerize with proteins of the JUN family and form transcription factor complex AP-1. These FOS proteins are considered to be important as regulators of cell proliferation, differentiation and transformation. Moreover, expression of *FOS* gene has also been associated with apoptotic cell death.[79] Studies have also shown that *FOS* is induced by a variety of stimuli in various cell types and can suppress systematic inflammatory response to

endotoxin.[80] Proteins of the MMP family are involved in breakdown of the extracellular matrix in normal physiological processes like embryonic development, reproduction, tissue modelling as well as in disease processes. Most MMPs are inactive when they are secreted but are activated when cleaved by extracellular proteinases.[81] According to the literature, *MMP9* is considered to be another gene that shows inflammatory responses. Previous studies have shown that inflammatory macrophage migration requires *MMP9* activation.[82] CAs are a family of zinc metalloenzymes, which catalyzes the reversible hydration of carbon dioxide. These are involved in biological functions like respiration, calcification, and acid-base balance and it's also shown that CA4 regulates cell-mediated inflammation.[83-84] It is reported that VCAN interacts with myeloid and lymphoid cells promoting their adhesion and productions of inflammatory cytokines and VCAN shows significant increase in inflammation.[85]

Among the 5 genes profiled in CD8+ Molt-3 cells, 3 genes, *PLBD1*, *FOS*, and *VCAN* were upregulated upon LPS stimulation (p values of 0.0165, 0.0259, and 0.0401, respectively). In CD8+ EVs, two genes were upregulated, *PLBD1* and *FOS* with p values of 0.0469 and 0.0150, respectively (see Figure 2.28).

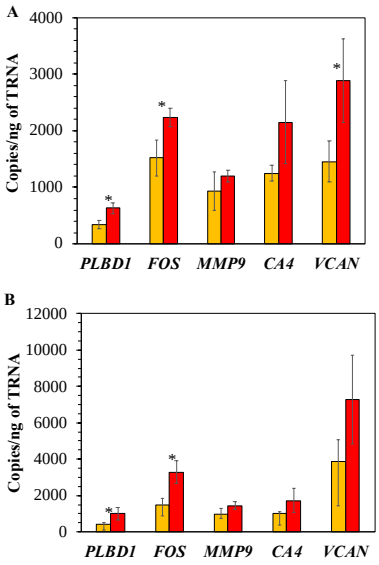

Figure 2 28: mRNA gene expression profiles of (A) CD8 T cells (B) CD 8 EVs ; Yellow : non-stimulated conditions (without LPS) , Red : Stimulated conditions (with LPS) conditions.

Heat maps generated for gene expression data showed that gene expression patterns of CD8+ T cells and CD8+ EVs were very similar (Figure 2.29). For non-stimulated conditions, there was no significant difference in gene expression observed between T cells and EVs for *PLBD1*, *FOS*, *MMP9* and *CA4* at the 95% confidence interval with p values of 0.509, 0.911, 0.943 and 0.094 respectively. For stimulated conditions, no significance difference in gene expression was observed between T cells and EVs for *PLBD1*, *MMP9* and *CA4* genes with p values of 0.132, 0.136 and 0.503 respectively. These results agree with the fact that, the gene expression of EVs are similar to those of cells which they originated from. Thus, EVs could potentially be used as a potential source of AIS biomarkers.

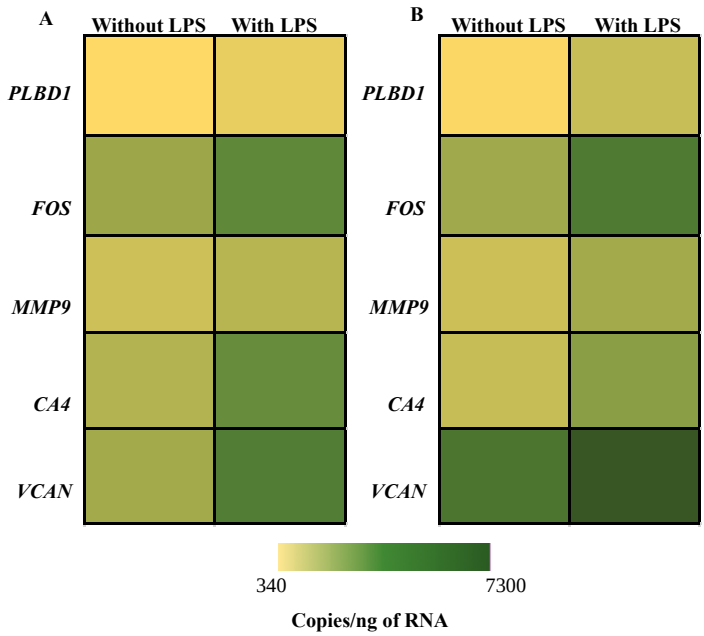

Figure 2.29: Heat maps illustrating the gene expression changes in (A) CD8 T cells (B) CD8 EVs isolated from Molt-3 cell line under stimulated and non-stimulated conditions.

2.18 TEM images of EVs isolated from stimulated and non-stimulated conditions

To analyze if there was any morphology change or size variation in stimulated versus non-stimulated EVs, TEM images were analyzed and are shown in Figure 2.30. Under these conditions, we did not see any change in size or morphology in EVs collected under LPS stimulated versus non-stimulated conditions.

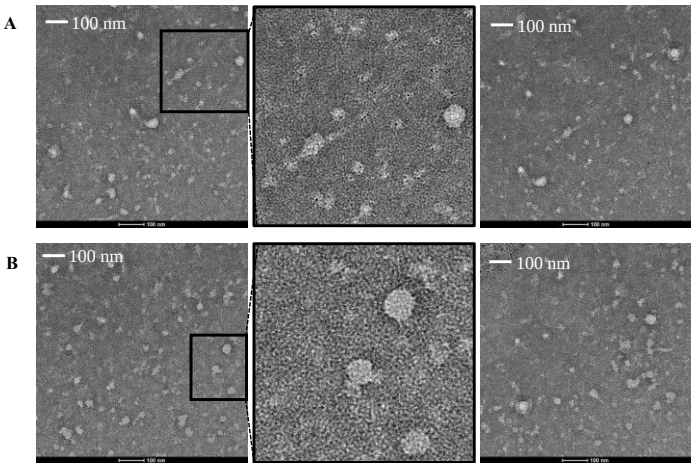

Figure 2.30: TEM images of (A) EVs released from non-stimulated cells. (B) EVs released from stimulated cells from Molt-3 cell line.

2.19 Poly ethylene glycol (PEG) precipitation to isolate EVs

The same samples used for EV isolation via microfluidic devices were also analyzed using PEG precipitation. Figure 2.31 briefly shows the steps involved in PEG precipitation. After adding PEG to the sample, we can see a cloudiness because the EVs start to coagulate. In Figure 2.31 B, we can see that EVs are pelleted by centrifugation. This pellet was resuspended in PBS.

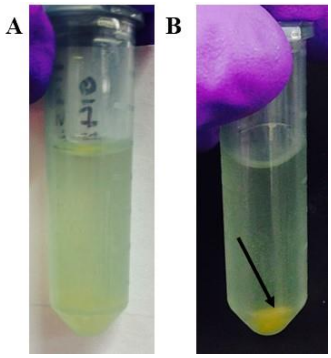

Figure 2.31: (A) After adding PEG to the cell media sample. (B) After keeping the sample over night at 4 ^{o}C and centrifuging the sample at 4000 g for 1 h (EV pellet is shown by the arrow).

2.19.1 TEM analysis of the EVs isolated by PEG precipitation

The TEM images shown in Figure 2.32 indicate that EVs of a wide size range have been precipitated by PEG. EVs released under non stimulated and stimulated conditions are shown in Figure 2.32 (A) and Figure 2.32 (B) respectively. We didn't observe any size difference EVs released under stimulated and non-stimulated conditions.

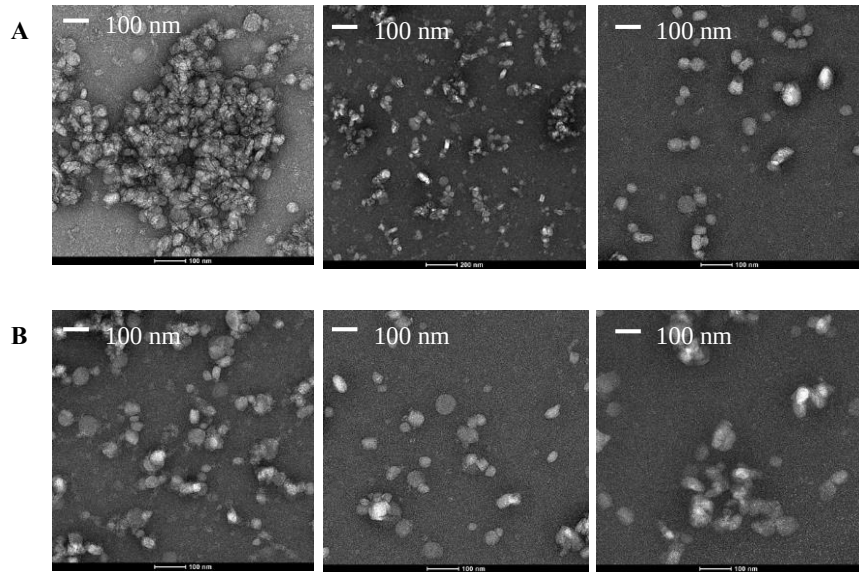

Figure 2.32: TEM images of EV isolated from PEG precipitation (A) EVs released from non-stimulated cells. (B) EVs released from LPS stimulated cells.

2.20 Droplet digital PCR for gene expression analysis of EV RNA isolated from PEG precipitation

After obtaining the EV pellet, it was dissolved in Trizol reagent and RNA was extracted, which was then used for cDNA synthesis and ddPCR. For the EVs' RNA isolated from PEG, ddPCR results, did not show a significant difference (based on the calculated p values at 95% confidence limit) between the stimulated and non-stimulated conditions (Figure 2.33). However, from gene expression results that we obtained from affinity selection using the microfluidic device we were able to see an expression difference in some of the genes between LPS stimulated and non-stimulated cells. It's clear that affinity selection was capable of differentiating between the stimulated and non-stimulated conditions with these conditions used to model stroke versus

non-stroke conditions. Thus, isolation of CD8+ expressing EVs instead of using a non-discriminate isolation method could provide more accurate results.

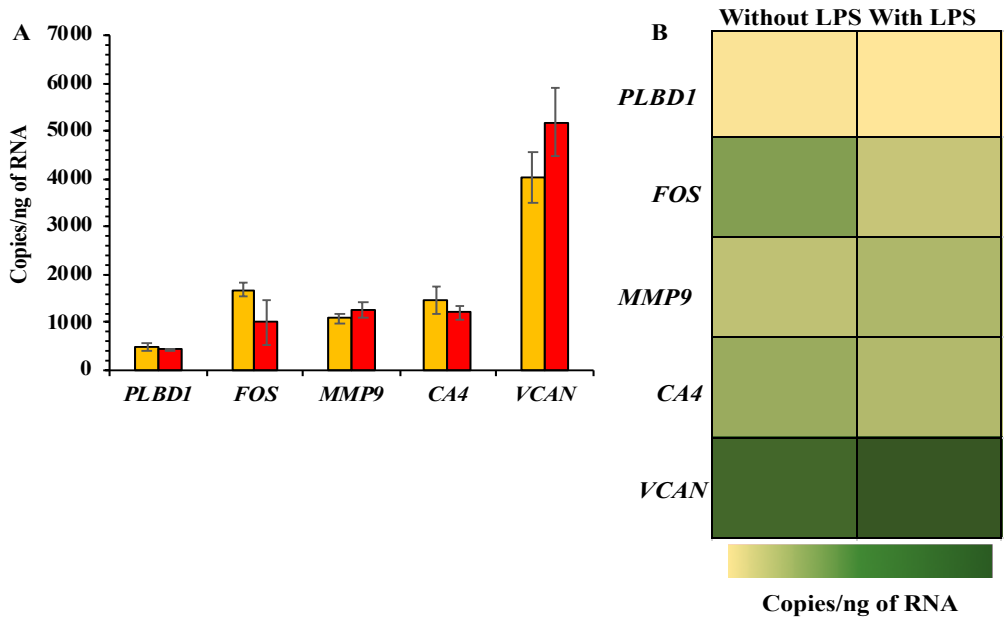

Figure 2.33: (A) Gene expression of stimulated and non-stimulated conditions for RNA extracted from PEG precipitated EVs. (B) Heat map comparing the gene expression of PEG EVs under stimulated and non-stimulated conditions.

2.21 Conclusions

With the aid of fluorescence microcopy, we demonstrated that the microfluidic fluidic device with arrays of micropillars can be used to affinity select CD8+ EVs from cell culture media with high specificity. EVs enriched on this device can be released from the capture surface via enzymatic cleavage with high efficiency >95% which can be used for downstream analysis. NTA analysis revealed that released particles have an average size of ~ 150 nm. LPS stimulation of T cells was used to model inflammatory responses taking place during an ischemic stroke event in order to analyze the gene expression of CD8 T cells and CD 8 EVs after an inflammatory response. Both stimulated and non-stimulated T cells and EVs were successfully isolated on microfluidic devices and TRNA was extracted from cells as well as from EVs. Following TRNA isolation, the RNA was reverse transcribed and via ddPCR, we demonstrated that gene expression of 5 genes we analyzed (*PLBD1*, *FOS*, *VCAN*, *CA4* and *MMP9*) of EV-RNA is similar to

that of T cells. Since PEG precipitation did not specifically isolate CD8 EVs, no difference was observed between gene expression between non-stimulated and stimulated conditions for EV RNA isolated from PEG precipitation.

2.21References

1. Schriger, D. L.; Kalafut, M.; Starkman, S.; Krueger, M.; Saver, J. L., Cranial computed tomography interpretation in acute stroke: physician accuracy in determining eligibility for thrombolytic therapy. *Jama* **1998,** *279* (16), 1293-1297.
2. Gibson, L.; Whiteley, W., The differential diagnosis of suspected stroke: a systematic review. 2013.
3. Ginde, A. A.; Foianini, A.; Renner, D. M.; Valley, M.; Camargo, J., Carlos A, Availability and quality of computed tomography and magnetic resonance imaging equipment in US emergency departments. *Academic emergency medicine* **2008,** *15* (8), 780-783.
4. Craig-Schapiro, R.; Fagan, A. M.; Holtzman, D. M., Biomarkers of Alzheimer's disease. *Neurobiology of disease* **2009,** *35* (2), 128-140.
5. Adamski, M. G.; Li, Y.; Wagner, E.; Seales-Bailey, C.; Bennett, N.; Yu, H.; Murphy, M.; Soper, S. A.; Baird, A. E., CD15+ granulocyte and CD8+ T lymphocyte based gene expression clusters for ischemic stroke detection. *Medical Research Archives* **2017,** *5* (11).
6. Tang, Y.; Xu, H.; Du, X. L.; Lit, L.; Walker, W.; Lu, A.; Ran, R.; Gregg, J. P.; Reilly, M.; Pancioli, A., Gene expression in blood changes rapidly in neutrophils and monocytes after ischemic stroke in humans: a microarray study. *Journal of Cerebral Blood Flow & Metabolism* **2006,** *26* (8), 1089-1102.
7. Tauro, B. J.; Greening, D. W.; Mathias, R. A.; Ji, H.; Mathivanan, S.; Scott, A. M.; Simpson, R. J., Comparison of ultracentrifugation, density gradient separation, and immunoaffinity capture methods for isolating human colon cancer cell line LIM1863-derived exosomes. *Methods* **2012,** *56* (2), 293-304.
8. Im, H.; Shao, H.; Park, Y. I.; Peterson, V. M.; Castro, C. M.; Weissleder, R.; Lee, H., Label-free detection and molecular profiling of exosomes with a nano-plasmonic sensor. *Nature biotechnology* **2014,** *32* (5), 490.
9. Chen, C.; Skog, J.; Hsu, C.-H.; Lessard, R. T.; Balaj, L.; Wurdinger, T.; Carter, B. S.; Breakefield, X. O.; Toner, M.; Irimia, D., Microfluidic isolation and transcriptome analysis of serum microvesicles. *Lab on a Chip* **2010,** *10* (4), 505-511.
10. Kanwar, S. S.; Dunlay, C. J.; Simeone, D. M.; Nagrath, S., Microfluidic device (ExoChip) for on-chip isolation, quantification and characterization of circulating exosomes. *Lab on a Chip* **2014,** *14* (11), 1891-1900.
11. Ashcroft, B.; De Sonneville, J.; Yuana, Y.; Osanto, S.; Bertina, R.; Kuil, M.; Oosterkamp, T., Determination of the size distribution of blood microparticles directly in plasma using atomic force microscopy and microfluidics. *Biomedical microdevices* **2012,** *14* (4), 641-649.
12. Zhang, P.; Zhou, X.; He, M.; Shang, Y.; Tetlow, A. L.; Godwin, A. K.; Zeng, Y., Ultrasensitive detection of circulating exosomes with a 3D-nanopatterned microfluidic chip. *Nature Biomedical Engineering* **2019**, 1.
13. Hupert, M. L.; Jackson, J. M.; Wang, H.; Witek, M. A.; Kamande, J.; Milowsky, M. I.; Whang, Y. E.; Soper, S. A., Arrays of high-aspect ratio microchannels for high-throughput isolation of circulating tumor cells (CTCs). *Microsystem technologies* **2014,** *20* (10-11), 1815-1825.
14. Nair, S. V.; Witek, M. A.; Jackson, J. M.; Lindell, M. A.; Hunsucker, S. A.; Sapp, T.; Perry, C. E.; Hupert, M. L.; Bae-Jump, V.; Gehrig, P. A., Enzymatic cleavage of uracil-containing single-stranded DNA linkers for the efficient release of affinity-selected circulating tumor cells. *Chemical communications* **2015,** *51* (15), 3266-3269.
15. Rider, M. A.; Hurwitz, S. N.; Meckes Jr, D. G., ExtraPEG: a polyethylene glycol-based method for enrichment of extracellular vesicles. *Scientific reports* **2016,** *6*, 23978.
16. Sargent, B. Cell Culture Basics. (accessed 03/16/2019).

17. Ozturk, S. S.; Palsson, B. O., Chemical decomposition of glutamine in cell culture media: effect of media type, pH, and serum concentration. *Biotechnology progress* **1990,** *6* (2), 121-128.
18. Bettger, W. J.; McKEEHAN, W. L., Mechanisms of cellular nutrition. *Physiological reviews* **1986,** *66* (1), 1-35.
19. Fang, C.-Y.; Wu, C.-C.; Fang, C.-L.; Chen, W.-Y.; Chen, C.-L., Long-term growth comparison studies of FBS and FBS alternatives in six head and neck cell lines. *PloS one* **2017,** *12* (6), e0178960.
20. Kornilov, R.; Puhka, M.; Mannerström, B.; Hiidenmaa, H.; Peltoniemi, H.; Siljander, P.; Seppänen-Kaijansinkko, R.; Kaur, S., Efficient ultrafiltration-based protocol to deplete extracellular vesicles from fetal bovine serum. *Journal of extracellular vesicles* **2018,** *7* (1), 1422674.
21. Lässer, C.; Alikhani, V. S.; Ekström, K.; Eldh, M.; Paredes, P. T.; Bossios, A.; Sjöstrand, M.; Gabrielsson, S.; Lötvall, J.; Valadi, H., Human saliva, plasma and breast milk exosomes contain RNA: uptake by macrophages. *Journal of translational medicine* **2011,** *9* (1), 9.
22. Jeppesen, D. K.; Hvam, M. L.; Primdahl-Bengtson, B.; Boysen, A. T.; Whitehead, B.; Dyrskjøt, L.; Ørntoft, T. F.; Howard, K. A.; Ostenfeld, M. S., Comparative analysis of discrete exosome fractions obtained by differential centrifugation. *Journal of extracellular vesicles* **2014,** *3* (1), 25011.
23. Lötvall, J.; Hill, A. F.; Hochberg, F.; Buzás, E. I.; Di Vizio, D.; Gardiner, C.; Gho, Y. S.; Kurochkin, I. V.; Mathivanan, S.; Quesenberry, P., Minimal experimental requirements for definition of extracellular vesicles and their functions: a position statement from the International Society for Extracellular Vesicles. Taylor & Francis: 2014.
24. Imbeaud, S.; Graudens, E.; Boulanger, V.; Barlet, X.; Zaborski, P.; Eveno, E.; Mueller, O.; Schroeder, A.; Auffray, C., Towards standardization of RNA quality assessment using user-independent classifiers of microcapillary electrophoresis traces. *Nucleic acids research* **2005,** *33* (6), e56-e56.
25. Greenberg, J. M.; Gonzalez-Sarmiento, R.; Arthur, D. C.; Wilkowski, C. W.; Streifel, B.; Kersey, J., Immunophenotypic and cytogenetic analysis of Molt-3 and Molt-4: human T-lymphoid cell lines with rearrangement of chromosome 7. *Blood* **1988,** *72* (5), 1755-1760.
26. Adams, A. A.; Okagbare, P. I.; Feng, J.; Hupert, M. L.; Patterson, D.; Göttert, J.; McCarley, R. L.; Nikitopoulos, D.; Murphy, M. C.; Soper, S. A., Highly efficient circulating tumor cell isolation from whole blood and label-free enumeration using polymer-based microfluidics with an integrated conductivity sensor. *Journal of the American Chemical Society* **2008,** *130* (27), 8633-8641.
27. Dharmasiri, U.; Balamurugan, S.; Adams, A. A.; Okagbare, P. I.; Obubuafo, A.; Soper, S. A., Highly efficient capture and enumeration of low abundance prostate cancer cells using prostate-specific membrane antigen aptamers immobilized to a polymeric microfluidic device. *Electrophoresis* **2009,** *30* (18), 3289-3300.
28. Chang, K.-C.; Hammer, D. A., The forward rate of binding of surface-tethered reactants: Effect of relative motion between two surfaces. *Biophys J* **1999,** *76* (3), 1280-1292.
29. Nagrath, S.; Sequist, L. V.; Maheswaran, S.; Bell, D. W.; Irimia, D.; Ulkus, L.; Smith, M. R.; Kwak, E. L.; Digumarthy, S.; Muzikansky, A., Isolation of rare circulating tumour cells in cancer patients by microchip technology. *Nature* **2007,** *450* (7173), 1235.
30. Becker, H.; Gärtner, C., Polymer microfabrication methods for microfluidic analytical applications. *ELECTROPHORESIS: An International Journal* **2000,** *21* (1), 12-26.
31. Soper, S. A.; Ford, S. M.; Qi, S.; McCarley, R. L.; Kelly, K.; Murphy, M. C., Peer Reviewed: Polymeric Microelectromechanical Systems. ACS Publications: 2000.

32. Lev, M. H.; Farkas, J.; Gemmete, J. J.; Hossain, S. T.; Hunter, G. J.; Koroshetz, W. J.; Gonzalez, R. G., Acute stroke: improved nonenhanced CT detection—benefits of soft-copy interpretation by using variable window width and center level settings. *Radiology* **1999,** *213* (1), 150-155.
33. Becker, H.; Locascio, L. E., Polymer microfluidic devices. *Talanta* **2002,** *56* (2), 267-287.
34. Hupert, M. L.; Guy, W. J.; Llopis, S. D.; Shadpour, H.; Rani, S.; Nikitopoulos, D. E.; Soper, S. A., Evaluation of micromilled metal mold masters for the replication of microchip electrophoresis devices. *Microfluidics and Nanofluidics* **2007,** *3* (1), 1-11.
35. Nunes, P. S.; Ohlsson, P. D.; Ordeig, O.; Kutter, J. P., Cyclic olefin polymers: emerging materials for lab-on-a-chip applications. *Microfluidics and nanofluidics* **2010,** *9* (2-3), 145-161.
36. Battle, K. N.; Jackson, J. M.; Witek, M. A.; Hupert, M. L.; Hunsucker, S. A.; Armistead, P. M.; Soper, S. A., Solid-phase extraction and purification of membrane proteins using a UV-modified PMMA microfluidic bioaffinity μSPE device. *Analyst* **2014,** *139* (6), 1355-1363.
37. Witek, M. A.; Aufforth, R. D.; Wang, H.; Kamande, J. W.; Jackson, J. M.; Pullagurla, S. R.; Hupert, M. L.; Usary, J.; Wysham, W. Z.; Hilliard, D.; Montgomery, S.; Bae-Jump, V.; Carey, L. A.; Gehrig, P. A.; Milowsky, M. I.; Perou, C. M.; Soper, J. T.; Whang, Y. E.; Yeh, J. J.; Martin, G.; Soper, S. A., Discrete microfluidics for the isolation of circulating tumor cell subpopulations targeting fibroblast activation protein alpha and epithelial cell adhesion molecule. *NPJ Precis Oncol* **2017,** *1*.
38. Jackson, J. M.; Witek, M. A.; Soper, S. A., In *Circulating Tumor Cells: Isolation and Analysis*, Fan, H., Ed. John Wiley & Sons: 2016; pp 85-119.
39. Battle, K. N.; Jackson, J. M.; Witek, M. A.; Hupert, M. L.; Hunsucker, S. A.; Armistead, P. M.; Soper, S. A., Solid-phase extraction and purification of membrane proteins using a UV-modified PMMA microfluidic bioaffinity microSPE device. *Analyst* **2014,** *139* (6), 1355-1363.
40. Rao, C. G.; Chianese, D.; Doyle, G. V.; Miller, M. C.; Russell, T.; Sanders, R. A., Jr.; Terstappen, L. W., Expression of epithelial cell adhesion molecule in carcinoma cells present in blood and primary and metastatic tumors. *Int J Oncol* **2005,** *27* (1), 49-57.
41. Gaster, R. S.; Xu, L.; Han, S. J.; Wilson, R. J.; Hall, D. A.; Osterfeld, S. J.; Yu, H.; Wang, S. X., Quantification of protein interactions and solution transport using high-density GMR sensor arrays. *Nat Nanotechnol* **2011,** *6* (5), 314-20.
42. Springer, T. A., Adhesion receptors of the immune system. *Nature* **1990,** *346* (6283), 425-34.
43. Lawton, E.; Miller, A.; Balwit, J., Effect of Chemical Structure of Vinyl Polymers on Crosslinking and Degradation by Radiation. *J. Polymer Sci* **1954,** *14*, 503-504.
44. Ranby, B. G.; Rabek, J. F., *Photodegradation, photo-oxidation, and photostabilization of polymers*. New York, Wiley: 1975.
45. Rivaton, A., Recent advances in bisphenol-A polycarbonate photodegradation. *Polymer Degradation and Stability* **1995,** *49* (1), 163-179.
46. Wei, S.; Vaidya, B.; Patel, A. B.; Soper, S. A.; McCarley, R. L., Photochemically patterned poly (methyl methacrylate) surfaces used in the fabrication of microanalytical devices. *The Journal of Physical Chemistry B* **2005,** *109* (35), 16988-16996.
47. Roy, S.; Yue, C.; Lam, Y.; Wang, Z.; Hu, H., Surface analysis, hydrophilic enhancement, ageing behavior and flow in plasma modified cyclic olefin copolymer (COC)-based microfluidic devices. *Sensors and Actuators B: Chemical* **2010,** *150* (2), 537-549.
48. Ishikawa, E.; Imagawa, M.; Hashida, S.; Yoshitake, S.; Hamaguchi, Y.; Ueno, T., Enzyme-labeling of antibodies and their fragments for enzyme immunoassay and

immunohistochemical staining. *Journal of Immunoassay and Immunochemistry* **1983,** *4* (3), 209-327.
49. Taylor, S. C.; Laperriere, G.; Germain, H., Droplet Digital PCR versus qPCR for gene expression analysis with low abundant targets: from variable nonsense to publication quality data. *Scientific reports* **2017,** *7* (1), 2409.
50. Akers, J. C.; Ramakrishnan, V.; Kim, R.; Phillips, S.; Kaimal, V.; Mao, Y.; Hua, W.; Yang, I.; Fu, C.-C.; Nolan, J., miRNA contents of cerebrospinal fluid extracellular vesicles in glioblastoma patients. *Journal of neuro-oncology* **2015,** *123* (2), 205-216.
51. Lobb, R. J.; Becker, M.; Wen Wen, S.; Wong, C. S.; Wiegmans, A. P.; Leimgruber, A.; Möller, A., Optimized exosome isolation protocol for cell culture supernatant and human plasma. *Journal of extracellular vesicles* **2015,** *4* (1), 27031.
52. Raposo, G.; Stoorvogel, W., Extracellular vesicles: exosomes, microvesicles, and friends. *J Cell Biol* **2013,** *200* (4), 373-383.
53. Conde-Vancells, J.; Rodriguez-Suarez, E.; Embade, N.; Gil, D.; Matthiesen, R.; Valle, M.; Elortza, F.; Lu, S. C.; Mato, J. M.; Falcon-Perez, J. M., Characterization and comprehensive proteome profiling of exosomes secreted by hepatocytes. *Journal of proteome research* **2008,** *7* (12), 5157-5166.
54. Guo, L.; He, B., Extracellular vesicles and their diagnostic and prognostic potential in cancer. *Translational Cancer Research* **2017,** *6* (3), 599-612.
55. Szatanek, R.; Baj-Krzyworzeka, M.; Zimoch, J.; Lekka, M.; Siedlar, M.; Baran, J., The methods of choice for extracellular vesicles (EVs) characterization. *International journal of molecular sciences* **2017,** *18* (6), 1153.
56. Bohren, C. F.; Huffman, D. R., *Absorption and scattering of light by small particles*. John Wiley & Sons: 2008.
57. Filipe, V.; Hawe, A.; Jiskoot, W., Critical evaluation of Nanoparticle Tracking Analysis (NTA) by NanoSight for the measurement of nanoparticles and protein aggregates. *Pharmaceutical research* **2010,** *27* (5), 796-810.
58. Jin, R.; Yang, G.; Li, G., Inflammatory mechanisms in ischemic stroke: role of inflammatory cells. *Journal of leukocyte biology* **2010,** *87* (5), 779-789.
59. Edwards, D. N.; Bix, G. J., The inflammatory response after ischemic stroke: Targeting B2 and B1 Integrins. *Frontiers in Neuroscience* **2019,** *13*, 540.
60. Selvaraj, U. M.; Stowe, A. M., Long-term T cell responses in the brain after an ischemic stroke. *Discovery medicine* **2017,** *24* (134), 323-333.
61. Tough, D. F.; Sun, S.; Sprent, J., T cell stimulation in vivo by lipopolysaccharide (LPS). *Journal of Experimental Medicine* **1997,** *185* (12), 2089-2094.
62. Rietschel, E. T.; Kirikae, T.; Schade, F. U.; Mamat, U.; Schmidt, G.; Loppnow, H.; Ulmer, A. J.; Zähringer, U.; Seydel, U.; Di Padova, F., Bacterial endotoxin: molecular relationships of structure to activity and function. *The FASEB Journal* **1994,** *8* (2), 217-225.
63. Xaus, J.; Comalada, M.; Valledor, A. F.; Lloberas, J.; López-Soriano, F.; Argilés, J. M.; Bogdan, C.; Celada, A., LPS induces apoptosis in macrophages mostly through the autocrine production of TNF-α. *Blood* **2000,** *95* (12), 3823-3831.
64. Zhao, G.; Yu, R.; Deng, J.; Zhao, Q.; Li, Y.; Joo, M.; van Breemen, R. B.; Christman, J. W.; Xiao, L., Pivotal role of reactive oxygen species in differential regulation of lipopolysaccharide-induced prostaglandins production in macrophages. *Molecular pharmacology* **2013,** *83* (1), 167-178.
65. Raza, H.; John, A.; Shafarin, J., Potentiation of LPS-induced apoptotic cell death in human hepatoma HepG2 cells by aspirin via ROS and mitochondrial dysfunction: protection by N-acetyl cysteine. *PloS one* **2016,** *11* (7), e0159750.
66. Kerr, J. F.; Wyllie, A. H.; Currie, A. R., Apoptosis: a basic biological phenomenon with wideranging implications in tissue kinetics. *British journal of cancer* **1972,** *26* (4), 239.

67. Elmore, S., Apoptosis: a review of programmed cell death. *Toxicologic pathology* **2007,** *35* (4), 495-516.
68. Rio, D. C.; Ares, M.; Hannon, G. J.; Nilsen, T. W., Purification of RNA using TRIzol (TRI reagent). *Cold Spring Harbor Protocols* **2010,** *2010* (6), pdb. prot5439.
69. Liao, J.; Gong, Z., Sequencing of 3′ cDNA clones using anchored oligo (dT) primers. *Biotechniques* **1997,** *23* (3), 368-370.
70. Hayden, R.; Gu, Z.; Ingersoll, J.; Abdul-Ali, D.; Shi, L.; Pounds, S.; Caliendo, A., Comparison of droplet digital PCR to real-time PCR for quantitative detection of cytomegalovirus. *Journal of clinical microbiology* **2013,** *51* (2), 540-546.
71. Bustin, S. A.; Benes, V.; Garson, J. A.; Hellemans, J.; Huggett, J.; Kubista, M.; Mueller, R.; Nolan, T.; Pfaffl, M. W.; Shipley, G. L., The MIQE guidelines: minimum information for publication of quantitative real-time PCR experiments. *Clinical chemistry* **2009,** *55* (4), 611-622.
72. Silver, N.; Best, S.; Jiang, J.; Thein, S. L., Selection of housekeeping genes for gene expression studies in human reticulocytes using real-time PCR. *BMC molecular biology* **2006,** *7* (1), 33.
73. Dheda, K.; Huggett, J. F.; Bustin, S. A.; Johnson, M. A.; Rook, G.; Zumla, A., Validation of housekeeping genes for normalizing RNA expression in real-time PCR. *Biotechniques* **2004,** *37* (1), 112-119.
74. Lin, J.; Redies, C., Histological evidence: housekeeping genes beta-actin and GAPDH are of limited value for normalization of gene expression. *Development genes and evolution* **2012,** *222* (6), 369-376.
75. Hindson, B. J.; Ness, K. D.; Masquelier, D. A.; Belgrader, P.; Heredia, N. J.; Makarewicz, A. J.; Bright, I. J.; Lucero, M. Y.; Hiddessen, A. L.; Legler, T. C., High-throughput droplet digital PCR system for absolute quantitation of DNA copy number. *Analytical chemistry* **2011,** *83* (22), 8604-8610.
76. Dube, S.; Qin, J.; Ramakrishnan, R., Mathematical analysis of copy number variation in a DNA sample using digital PCR on a nanofluidic device. *PloS one* **2008,** *3* (8), e2876.
77. PLBD1 phospholipase B domain containing 1 [Homo sapiens (human)]. https://www.ncbi.nlm.nih.gov/gene/79887#gene-expression (accessed 04/17).
78. Wunderlich, M. T.; Wallesch, C.-W.; Goertler, M., Release of neurobiochemical markers of brain damage is related to the neurovascular status on admission and the site of arterial occlusion in acute ischemic stroke. *Journal of the neurological sciences* **2004,** *227* (1), 49-53.
79. FOS gene (Protein coding). https://www.genecards.org/cgi-bin/carddisp.pl?gene=FOS (accessed 05/25/2019).
80. Ray, N.; Kuwahara, M.; Takada, Y.; Maruyama, K.; Kawaguchi, T.; Tsubone, H.; Ishikawa, H.; Matsuo, K., c-Fos suppresses systemic inflammatory response to endotoxin. *International immunology* **2006,** *18* (5), 671-677.
81. *MMP9 Gene (Protein coding).* https://www.genecards.org/cgi-bin/carddisp.pl?gene=MMP9 (accessed 05/25).
82. Gong, Y.; Hart, E.; Shchurin, A.; Hoover-Plow, J., Inflammatory macrophage migration requires MMP-9 activation by plasminogen in mice. *The Journal of clinical investigation* **2008,** *118* (9), 3012-3024.
83. *CA4* gene (Protein Coding). https://www.genecards.org/cgi-bin/carddisp.pl?gene=CA4 (accessed 05/25).
84. Henry, E. K.; Sy, C. B.; Inclan-Rico, J. M.; Espinosa, V.; Ghanny, S. S.; Dwyer, D. F.; Soteropoulos, P.; Rivera, A.; Siracusa, M. C., Carbonic anhydrase enzymes regulate mast cell–mediated inflammation. *Journal of Experimental Medicine* **2016,** *213* (9), 1663-1673.

85. Wight, T. N.; Kang, I.; Merrilees, M. J., Versican and the control of inflammation. *Matrix Biology* **2014,** *35*, 152-161.

Chapter 3: Microfluidic affinity selection of CD8+ EVs from plasma samples and CD8+ T-cells from blood samples for acute ischemic stroke diagnosis

3.1 Introduction

Liquid biopsies are generating a significant amount of interest in the medical and biological communities due to the minimally invasive nature of acquiring biomarkers and the fact that they can enable precision decisions on managing a variety of diseases, including oncology and non-oncology-related diseases.[1-2] Blood is the most widely used bodily fluid for liquid biopsy tests as it contains various molecules including EVs, proteins, circulating tumor cells, and cell free DNA that are good candidates as biomarkers for many diseases.[3-5]

EV isolation from plasma and gene expression analysis represents a novel idea for the development of a diagnostic test for AIS. EVs are present in high abundance in plasma (Healthy plasma contains ~10^7-10^8 EVs/ mL of plasma). Moreover, the number of EVs that are released by the cells can be increased during a stroke event.[6] Additionally, many disadvantages of current stroke diagnosis methods like long analysis time, complexity of the instruments, and use of high radiation dose could be overcome by developing a simple liquid biopsy assay for AIS.

Various microfluidic devices have been developed to selectively isolate EVs. Simplicity of these techniques make those well suited for point-of-care (POC) diagnostics. Recently, many microfluidic devices been developed and studied for isolating EVs from plasma. Many microfluidic methods, including paper microfluidic devices, immunomagnetic beads, photo sensitizer beads have been developed, based on immune affinity capturing using antibodies.[7-8] Some of those are briefly discussed below. In a previous study, magnetic beads (which are about 3 μm in diameter) were coated with anti-EGER to capture EVs from 100 μL of serum and has shown a capture efficiency of ~93%. This device is an integrated device that can perform EV isolation to RNA analysis by qPCR in a single chip.[9] In another study, after capturing EVs using anti-CD64-

magnetic beads, electric field-induced release and measurement was used for disrupting exosomes and monitoring RNA and protein biomarkers.[10] There are many devices that have been developed without using magnetic beads, where the surface of the device was modified with antibodies to capture EVs. In a previous study, an integrated nanostructured coating was used to reduce nonspecific interactions and this device was used to identify ovarian cancer patients from healthy controls.[11]

However, most of these methods use general affinity-enrichment of bulk EVs by targeting the tetraspanins such as CD9, CD63, and CD81.[12-14] By these methods we cannot isolate specific subpopulations of EVs. Thus, we have developed a method for affinity selection of a specific EVs subpopulation by targeting specific antigens that may be more related to disease onset, such as CD8 and CD15 antigens with AIS.[15]

In this chapter, the microfluidic devices that have been developed for isolating cells and EV (explained in chapter 1) will be used to analyze blood and plasma samples from healthy donors. Following T cell isolation, the selectivity of devices will be determined through immunephenotyping using fluorescently labeled (APC conjugated) CD 8 and CD 45 antibodies. The enriched CD8+ T cells and CD8+ EVs will be enumerated by releasing the enriched materials from the device surfaces via enzymatic cleavage. TEM analysis will be performed to inspect the morphology of the released EVs. After characterization, gene expression of CD8+ T cells and EVs will be analyzed using droplet digital PCR (ddPCR).

3.2 Material and Methods

3.2.1 Expression of CD8+ T cells in blood

The blood sample was placed on top of equal volume of Histopaque 1077 (Sigma-Aldrich, St.Louis, MO) without mixing. The solution was centrifuged at 400 g for 30 min. Then, the buffy coat, which is in between red blood cells and plasma layers, was separated carefully

using a pipette. Next, buffy coat was centrifuged at 300 g for 10 min and the pellet was resuspended in PBS and centrifuged again. The pellet was resuspended in 400 μL of 0.5% (w/v) bovine serum albumin in PBS with the sample divided into two aliquots. Twenty μL of APC conjugated mouse IgG2B anti hCD8∝ Ab (R & D systems, Minneapolis, MN) was added to one aliquot and 20 μL APC conjugated mouse IgG2B isotype control (R & D systems, Minneapolis, MN) was added to the other portion. The samples were then incubated at room temperature for 40 min and centrifuged at 300 g for 10 min. Finally, the pellet was resuspended in 1 mL of 0.5% (w/v) bovine serum albumin in PBS. A washing step was repeated for two more times before analyzing the sample with BD accuri C6 plus flow cytometer.

3.2.2 Blood processing for CD8+ T cell isolation

The initial studies were done using healthy donor blood samples. Healthy donor samples were obtained from the University of Kansas Medical Center, Kansas City. Blood samples were collected into EDTA tubes to prevent blood coagulation and analyzed on the same day the blood was collected. For CD8+ T cells isolation from blood, sinusoidal channel microfluidic devices modified with CD8 mAb was used. The devices were modified using the same protocol as explained in Chapter 2, section 2.2.5. Surface modified devices were then washed with 0.5% BSA/PBS solution at 55 μL/min. Next, 2 mL of blood was processed through the devices at 25 μL/min. Finally, the devices were washed with 0.5% BSA/PBS to remove non-specifically bound cells on the device surface. Captured cells were then imaged.

3.2.3 Release cells from the device, staining and counting the number of cells

The affinity selected cells using the microfluidic device possessing sinusoidal channels, twere released from the device's surface by infusing 2U/10 μL USER™ enzyme (New England Biolabs, Ipswich, MA) followed by incubation at 37°C. Immediately after incubation, released cells were washed from the microfluidic device and collected into a 96 well plate. For enumer-

ating, released cells were fixed with 2% paraformaldehyde (PFA) and stained with 4′,6-diamidino-2-phenylindole (DAPI) in triton. After staining the cells for 10 min, the plate was centrifuged at 300 g for 10 min. The plate was then visualized using a 200M inverted microscope (Zeiss) with a 40x objective (0.3 NA, Plan NeoFluar), XBO 75 Xe arc lamp, single band DAPI filter (Omega optical), Cascade:1K EM-CCD camera (Photometric), and MAC 5000 stage (Ludl Electronic Products), all of which were computer-controlled via Micro-Manager. Final images were background subtracted, analyzed using Image-J software using a custom macro (program) to calculate the number of cells.

3.2.4 Staining the cells with CD8 and CD45

Cells isolated using the sinusoidal microfluidic device were released with USER enzyme and collected into a 96 well plate. Then they were immunostained with Cy5-labeled anti-hCD8α mAb and FITC-labeled anti-CD45 mAb. The cells were centrifuged at 300 g for 10 min, and washed again before imaging with 200M inverted microscope (Zeiss) using a 10x objective (0.3 NA, Plan NeoFluar), XBO 75 Xe arc lamp, single band Cy5 and Cy3 filter set (Omega optical), Cascade 1K EM-CCD camera (Photometric), and MAC 5000 stage (Ludl Electronic Products), all of which were computer-controlled via Micro-Manager. Final images were background subtracted and analyzed using Image-J software.

3.2.5 Cell lysis, RNA extraction and cDNA synthesis

Cell lysis was performed inside a hood using a Zymo Research Science RNA kit (Zymo Research, Irvine, CA) according to manufacturer's protocol as explained in Chapter 2. Complementary DNA (cDNA) from purified RNA was synthesized via reverse transcription (RT). This was accomplished using a ProtoScript II First Strand cDNA Synthesis Kit (New England BioLabs, Ipswich, MA) according to the manufacturer's instructions and explained in Chapter 2 (section 2.2.9).

3.2.6 Separation of plasma from blood

For EV isolation, first plasma was separated from blood cells. Therefore, whole blood samples were first centrifuged at 300 g for 10 min to isolate the plasma followed by centrifuging at 1000 g for 10 min. The supernatant was used to isolate the CD8+ EVs.

3.2.7 Isolation of CD8+ EVs from plasma

Isolation of EVs from plasma was performed using the same protocol used for isolating EVs from Molt-3 cell line.

3.2.8 Release of enriched EVs from device surface

In order to release captured EVs from the device, the device was infused with 2U/10 μL USER^{TM} enzyme (New England Biolabs, Ipswich, MA) and incubated at 37°C. Immediately after incubation, released EVs were washed from the microfluidic device and collected into a pre-weighed centrifuge tube. TEM, NTA and ddPCR were performed using the same protocols as explained in Chapter 2 (Section 2.2.7.1 and 2.2.7.2).

3.3 Results and Discussion

3.3.1 Analyzing expression of CD8+ T cells in blood by flow cytometry

Blood is a suspension of elements. About 45% of total blood consists of erythrocytes and leukocytes, and platelets are <1% of total blood. About 55% of total blood is plasma. The formed elements of blood need to be separated from the plasma in order to enrich the leukocyte fraction from the whole blood. Therefore, we used density gradient centrifugation (Histopaque) to isolate leukocytes, which is also known as the buffy coat that contains most of white blood cells.

Histopaque 1077 is a sterile solution consisting of polysucrose (57 g/L) and sodium diatrizoate (90 g/L) adjusted to a density of 1.077 g/mL. It's important that the solution is at room temperature, because use of a cold solution can typically cause clumping of the cells. Red blood cell contamination can also result if cold histopaque is used.

Equal volume of anticoagulated blood was layered onto Histopaque 1077 carefully without mixing. During centrifugation erythrocytes are aggregated by polysucrose and sediment rapidly. Granulocytes become slightly hypertonic, increasing their sedimentation rate, that result in pelleting at the bottom of the tube as well. Under these conditions, lymphocytes and other mononuclear cells will remain at plasma/ histopaque interface as shown in Figure 3.1. Erythrocyte contamination is negligible under these conditions.

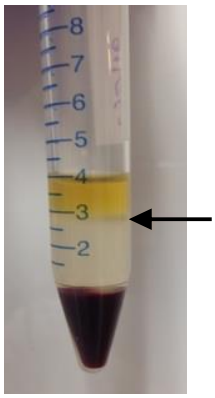

Figure 3.1: Buffy coat (shown by arrow) separated from healthy blood using histopaque density gradient.

The separated buffy coat was further centrifuged at 300 g to pellet the cells. Then, the same procedure delineated in Chapter 2 was followed to analyze the expression of CD8 antigen in T cells. Figure 3.2 shows the calibration plot and the data obtained for the buffy coat stained with anti-human mCD8 and IgG2B isotype control.

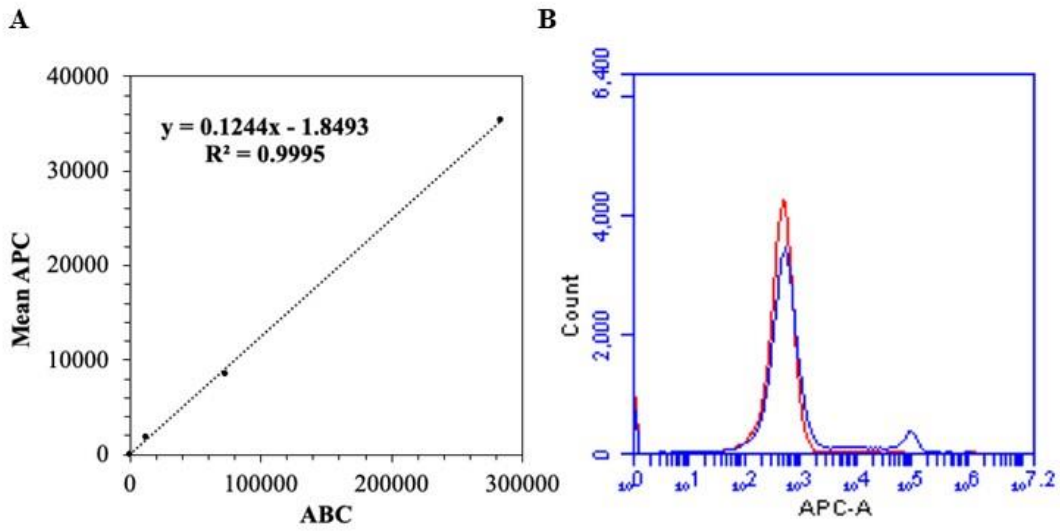

Figure 3.2: (A) Calibration curve generated with calibration beads. (B) Representative fluorescence histogram data for buffy coat isolated from blood stained with APC conjugated IgG2B isotype (red trace), APC conjugated CD8 Ab (blue trace).

In healthy blood 2-11% of leukocytes are CD8 T cells.[16] According to the flowcytometry results we obtained the percentage of CD8 T cell in leukocytes as 9.78%. Based on flow cytometry results, we obtained average of 6595.7 receptors for CD8 and the average value we obtained for isotype was 510.8.

3.3.2 Blood processing for CD8+ T cell enrichment

In order to analyze the gene expression of T cells, first T cells needed to be isolated from blood with high purity. Centrifugation methods like buffy coat separation, which was discussed previously will isolate all types of white blood cells. But affinity selection using CD8 mAb will allow to specifically isolate CD8 T cells from blood. For the initial studies healthy donor blood samples were used. For each sinusoidal channeled device ~ 2 mL of blood was used. Blood samples were processed at 25 µL/min flow rate. Figure 3.3 below illustrates the how blood is processed inside the sinusoidal channeled device, where blood enters the channels via inlet shown by an arrow in Figure 3.3 A. A zoomed in view of the inlet is shown in Figure 3.3 B.

Blood will move through the channels and then move out from the device through the capillary as shown in Figure 3.3A.

The architecture of the design is called the Z-configuration. Here, fluid will enter the selection bed through a single inlet channel composed perpendicular to an array of channels and exits also through a single outlet channel, which is also perpendicular to the channels. Previous studies have shown that, flow of the fluid throughout the device is also uniform in the Z-configuration and it has been shown that the flow through the inlet/outlet channels are higher than 2 mm/s which creates enough pressure to remove any air bubbles introduced during sample processing process.[17]

Blood flow closer to the exit channel is shown in Figure 3.3 D. These microfluidic devices are capable of processing blood samples quickly with 1 ml of blood processed in ~40 min.

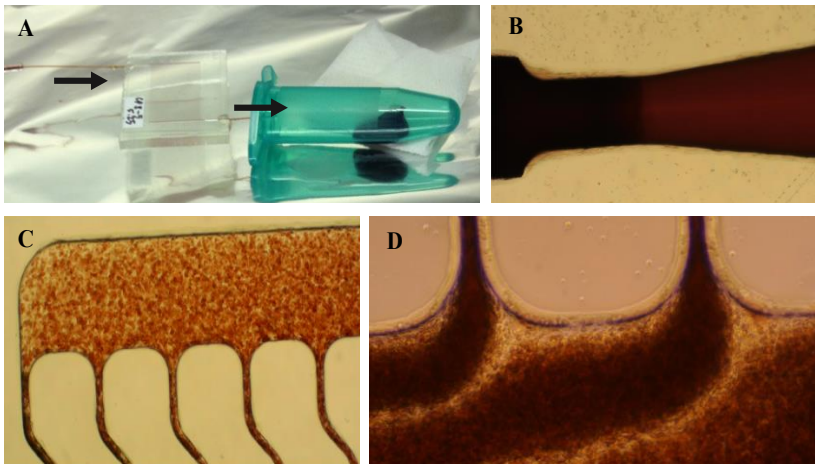

Figure 3.3: (A) Experimental setup for blood processing experiment, inlet and the out let are shown in arrows. (B) Zoomed in view of the blood inlet of the device. (C) Sample processing through the device (Close to the inlet). (D) Samples processing through the device close to the outlet.

Images of the captured cells in the microfluidic device is shown in Figure 3.4. Cells isolated on these devices could be used for cell enumeration and molecular analysis. Also, we stained the cells with Hoechst nucleic acid stain. Hoechst is a popular cell-permeant nuclear

counterstain that emits blue fluorescence when bound to dsDNA. Figure 3.4 (D)-(G) show images of stained cells that have been captured in the device.

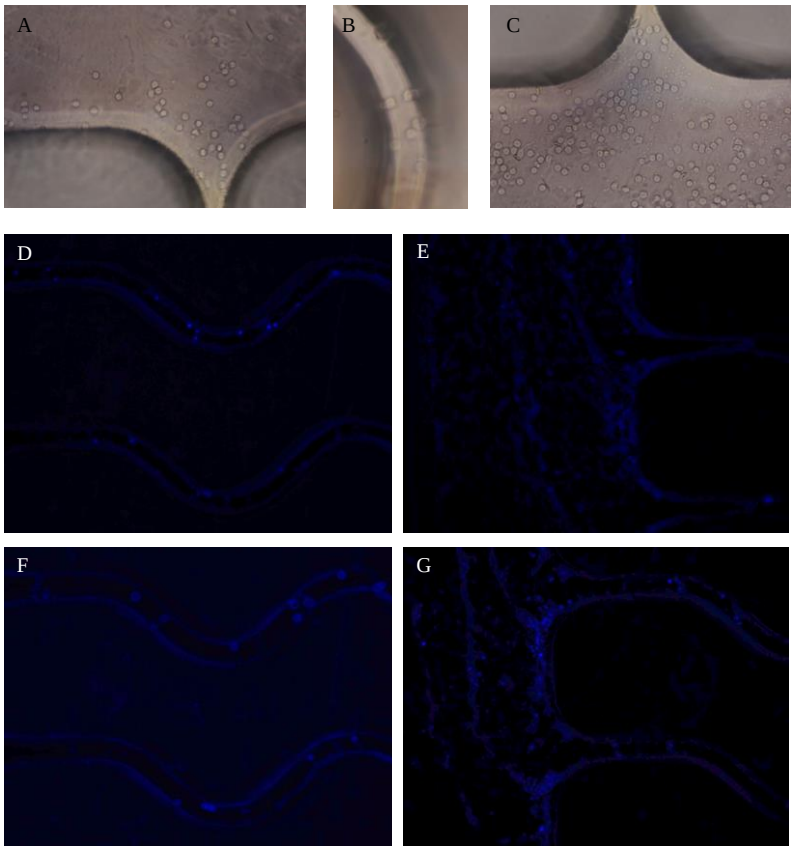

Figure 3.4: Brightfield images of CD8+ T cells captured in the microfluidic device (A). Closer to the inlet. (B) Inside the sinusoidal channels (C) Closer to the outlet channels. (D)-(G) Florescent images of the Hoechst stained cells in the device.

3.3.3 Cell enumeration and staining

Because Ab attachment was performed via the oligonucleotide with uridine residue, USER enzyme could be used to release cells from the device surface. The released cells were collected into a single well in a 96 well plate and the cells were stained with three different fluorescent markers. Due to high affinity of DAPI (4′,6-diamidino-2-phenylindole) for DNA, cells stained with DAPI was used for cell enumeration. DAPI is a highly specific DNA stain that preferentially binds to AT regions of the DNA molecules. It is a blue fluorescent DNA stain that exhibits ~20-fold enhancement of fluorescence upon binding to AT regions of dsDNA. After

staining, cells in the 96-well plate were imaged using fluorescence microscopy and finally the images were analyzed using ImageJ software with a custom written macro for cell enumeration. Many images are taken that covers all the areas of the well and later using a custom written macro in ImageJ (See Appendix 3) image of the complete well is created Figure 3.5 B). The cell enumeration was also performed using ImageJ software.

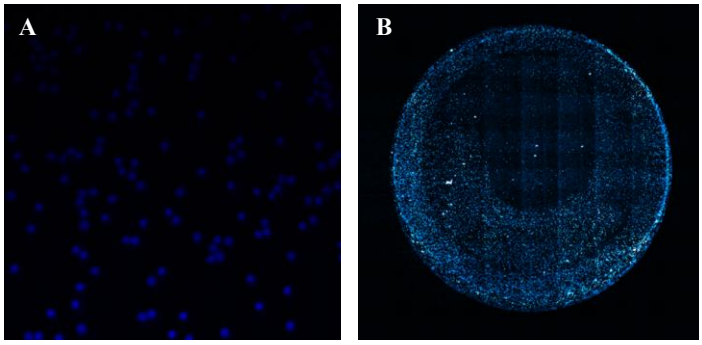

Figure 3 6: (A) DAPI stained cells imaged under (40x magnification). (B) DAPI stained cells in a well of a 96-well plate after processing all the images taken from ImageJ software for enumeration (All the cells were released to a single cell in the 96 well plate).

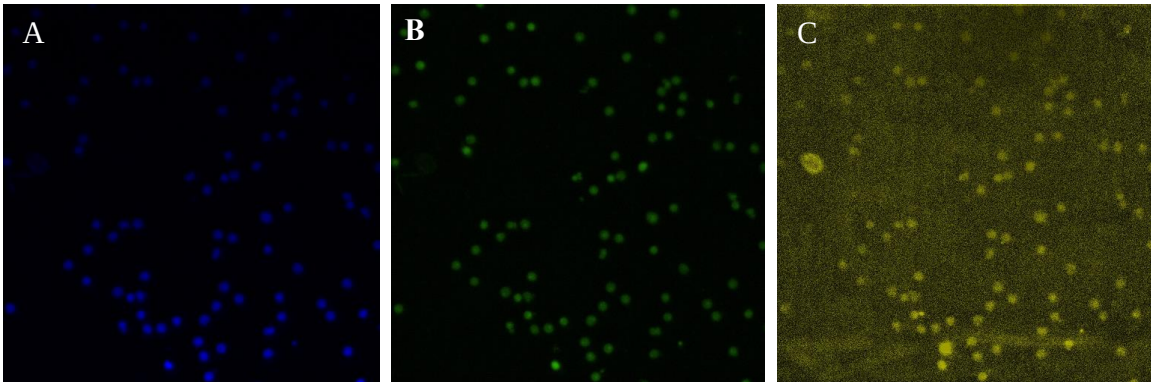

Figure 3.5: Cells released (and collected to a single well in a 96 well plate) from the microfluidic device after staining with (A) DAPI, (B) anti-human CD45 antibody, (C) anti-human CD8 antibody (40x magnification).

The average number of cells counted from the macro was ~24,000 from ~2 mL of blood. (Based on DAPI staining). Two more dyes CD45 and CD8, were used to stain the released cells. CD45 is a transmembrane glycoprotein that is expressed on most nucleated cells of hematopoietic origin. It has several isoforms, and hematopoietic cells express one or more of these

isoforms.[18] The presence of CD45 distinguishes leukocytes from non-hematopoietic cells. Figure 3.6 B shows the cells stained with CD45, which shows that leukocytes have been isolated on our microfluidic device.

To further demonstrate the selectivity of the device, we stained released cells with CD8 stain. Purity of cell isolation was calculated based on DAPI staining and CD8 staining. Calculated purity was 81.3 ±11.5%.

3.3.4 Extra cellular vesicle (EV) isolation from plasma

EVs are present in high abundance in body fluids, especially in plasma. Thus, plasma is a good source for isolating EVs. Use of plasma for the EV isolation has many advantages. Blood can be drawn via a minimally invasive liquid biopsy. Blood sample draws can be performed quickly, which is an important factor in a clinical situation especially in ischemic stroke diagnosis where time is the most critical factor.

3.3.5 Plasma separation from blood

First plasma was separated from blood by centrifugation. Blood was centrifuged at 300 g for 10 min to remove cells from the supernatant. Next, the plasma sample was centrifuged again for 10 min at 1000 g to remove any insoluble material present. Figure 3.7 below shows steps involved in separating plasma from the formed components of blood. The plasma can be directly injected into the microfluidic device without any additional sample processing steps.

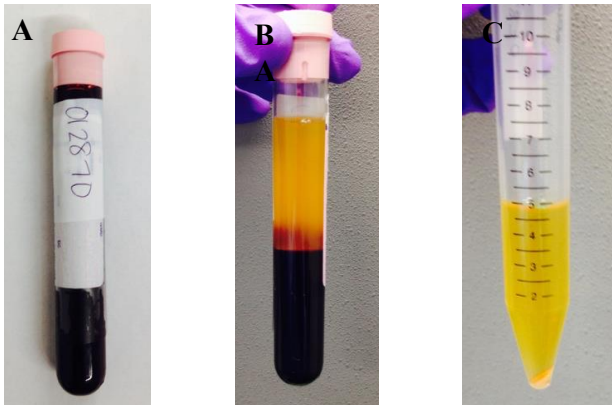

Figure 3.7: (A) Blood sample collected in a EDTA treated tube. (B) Plasma separation after centrfuging 300 g for 10 min. (C) After centrfuging the seperated plasma for 1000 g for 10 min.

3.3.6 Fluorescent imaging of the captured EVs from plasma

Because the size of EVs (30 nm – 1 μm) are smaller than that of cells (~10 μm), the dimensions of channels within the cell isolation device are not appropriate for EV isolation. It has been shown that for efficient isolation using these channels, at least one dimension of the microchannel must be close to average diameter of target that we are isolating (*i.e.*, cells, CTC, EVs) to help induce cell-wall interactons.[19] Even though the sinusoidal geometry can induce centrifugal forces to "push" cells toward the wall to induce cell-wall interactions, this would not occur for small particles, such as exosomes. Thus, only lateral diffusion would induce EV-wall interactions and to increase the number of potential wall interactions, the diffusional distance must be reduced.

Hence, for isolating EVs we designed a microfluidic device that consisted of pillar structures. This device consisted of 3-beds that are serially connected with capillary ports of 360 μm OD. Each bed was 2 mm wide and the length was 40.6 mm. Total length throughout the serially-connected beds was 122 mm. The entire device had 15,202 circular micropillars with each pillar being 92 μm in height, 117 μm in diameter and a spacing between pillars of 10 μm. Surface area and volume of this 3-bed device was 6.8 cm^2 and 6.5 μL respectively. Figure 3.8 shows the design of the microfluidic device we used for isolation of EVs from plasma.

The architecture of the device was carefully designed to maximize recovery of the EVs while providing high throughput sample processing. Sample infused into the device will enter the affinity bed and EVs will diffuse laterally to interact with the monoclonal antibodies immobilized on micropillar surfaces while at the same time driven hydrodynamically through the bed. Narrow inter-pillar spacing (~10 μm) and long bed lengths decrease diffusional distances and provide sufficient residence time, respectively, so that the EV recovery is favorable.

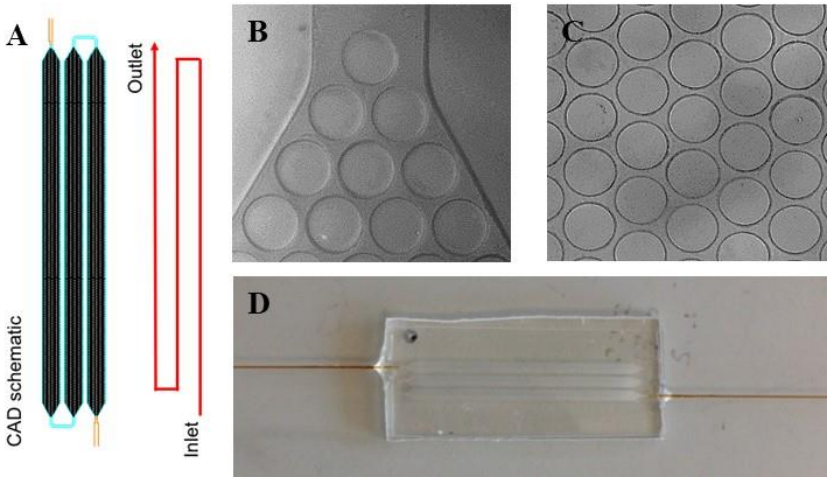

Figure 3.8: (A) Picture of CAD schematic showing the serial connection of three bed device with circular micro pillars. (B) Pillars of the device closer to the inlet – 10x magnification. (C) Pillars of device in the middle of bed 10x magnification. (D) Final device after assembly.

To check if the EVs can be actually captured on the modified devices, fluorescent microscopy was performed by staining EVs with Cy5 labeled CD8 Ab. Figure 3.9 below shows intensity scaled fluorescence images. Increase in fluorescence intensity was observed in the device modified with anti-CD8 mAb compared to the control, (device without anti-CD8 mAb), which reveals that CD8+ EVs have been captured on the microfluidic device.

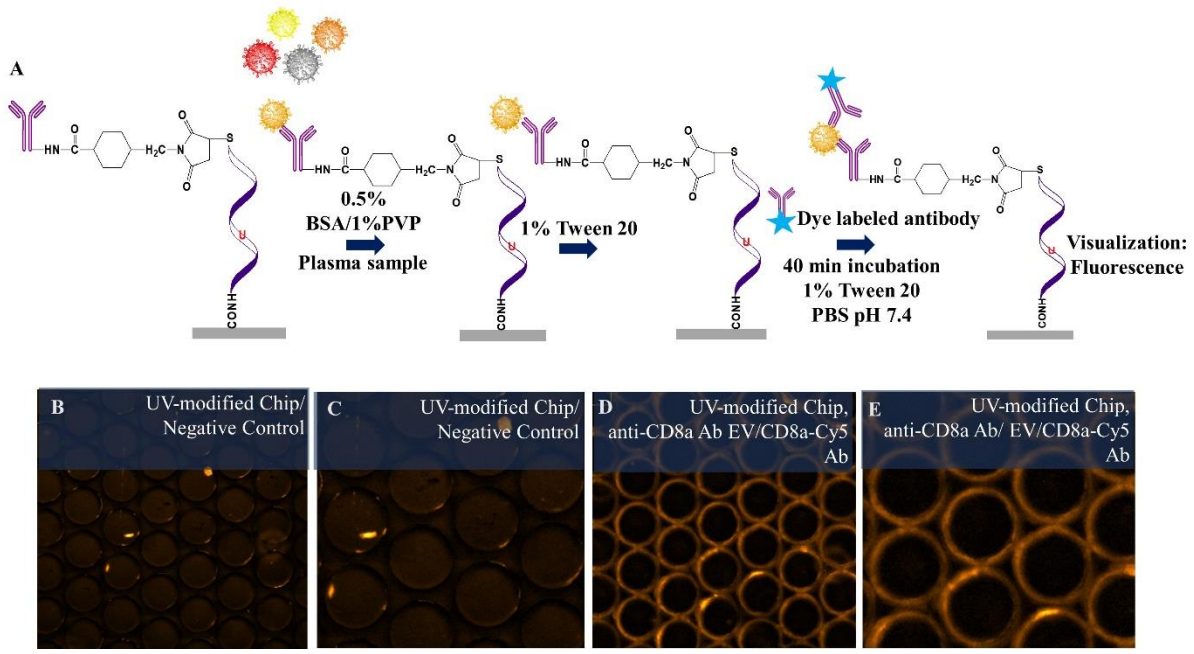

Figure 3.9: (A) Schematic diagram showing the steps involved in visualizing isolated EVs on the device. EVs isolated on a microfluidic device; EVs that has been affinity selected on the device stained with Cy5 labeled CD 8 secondary antibody. (B) Negative control (without CD8 mAb on the surface). (C) Zoomed view of negative control (without CD8 mAb on the surface). (D) CD8 EVs captured from cell media. (E) Zoomed view of CD8 EVs captured from plasma.

3.3.7 Releasing captured EVs from the device surface; TEM and NTA analysis

TEM images of plasma isolated EVs are shown in Figure 3.10. These images reveal that EVs from plasma can be isolated on our microfluidic device that we designed. The same samples used for TEM analysis were analyzed via NTA to obtain the size distribution of EVs. However, the refractive index of the particles and the medium can influence the NTA detection limit.[20] EVs typically have a refractive index of 1.37-1.39.[21] Depending on the refractive index of the material the lower detection limit of NTA might be ~10 nm for metal particles, around 30 nm for polymers and ~40 nm for EVs.

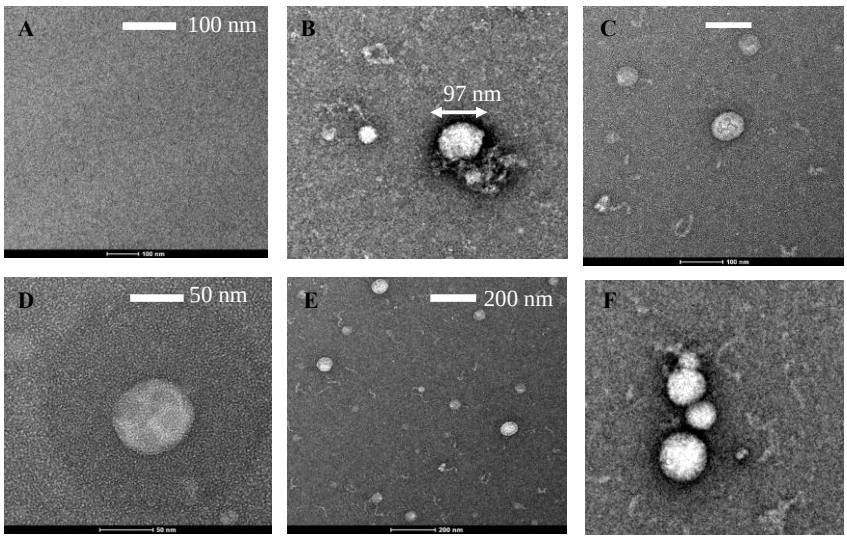

Figure 3.10: (A) TEM image of the USER enzyme and the buffer used for the release. (B)-(F) TEM images of the EVs captured (via CD8 mAb) and released from the healthy donor plasma samples.

3.3.8 NTA analysis of released EVs

Released EVs were diluted appropriately and analyzed using NTA. Average size of EVs calculated by NTA was (115.3 ±13.9). Based on NTA results the total number EVs released from the 3-bed microfluidic device was (7.36 ±0.86) x 10^9/mL. As explained in Chapter 2, the release efficiency of EVs determined by releasing the EVs twice from the device using the USER enzyme. Calculated release efficiency (Figure 3.11) of EVs was (96.5 ±1.4) % (n = 5 readings per sample). Figure 3.11 B and C shows the TEM images of the EVs that are released during first and second release by incubating with the USER enzyme.

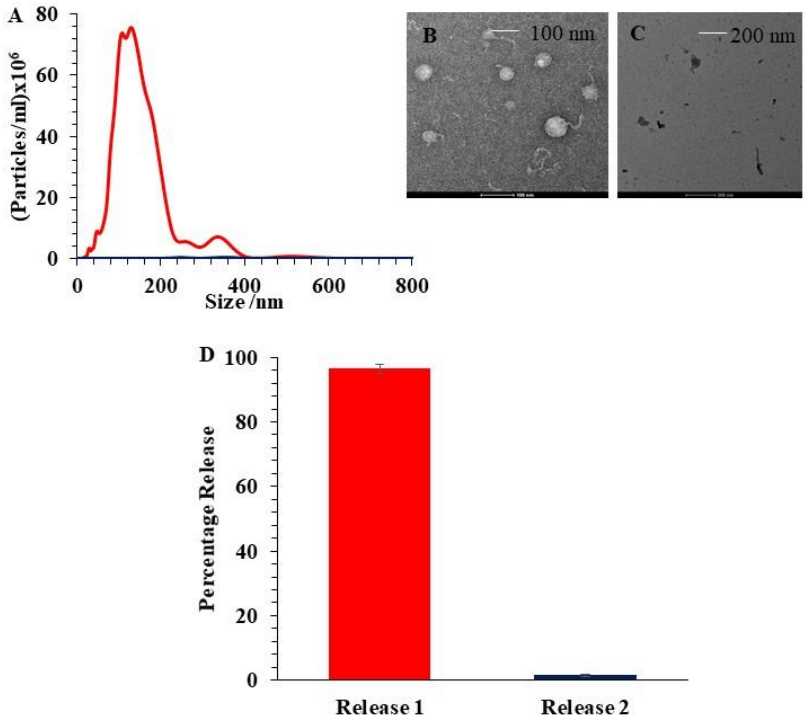

Figure 3.11: (A) NTA results showing the number of particles released during first and second release. (B) TEM image of a first released sample. (Affinity selected on CD8 mAb modified device and released with USER enzyme). (C) TEM image of a second released sample (Affinity selected on CD8 mAb modified device and released with USER enzyme). (D) Percentage of EVs released during the first and second release (n=3 and 5 readings per sample).

3.3.9 Sample processing and extraction of RNA

Healthy donor blood samples and the plasma samples were processed via sinusoidal channel device and pillar device (Both devices modified with CD 8 mAb) to isolated CD 8 T cells and CD8 EVs, respectively. Once the samples were processed, on-chip lysis was performed to extract the RNA from isolated T cells and EVs as explained in Chapter 2. (From both on-chip lysis method and USER release we can acquire same amount of RNA, On-chip lysis yielded 340 pg of RNA per chip and USER release yielded 317 pg) Figure 3.12 shows RNA profiles of total RNA (TRNA) isolated from cells and EVs. TRNA isolated from CD8+ T cells separated in gel electrophoresis showed typically observed TRNA profiles for eukaryotic cells with well pronounced ribosomal RNAs larger and smaller subunits. Because the ribosomal bands (28S and

18S) are clear and the 28S band was approximately twice as intense as the 18S band, it is clear that the TRNA isolated from cells isolated on the devices are intact.

Although the cellular mRNA has a size range of about 400 to 12,000 nucleotides, EV RNA show a size of <700 nucleotides.[22-23] The RNA profiles that we obtained for EV also show these specific characteristics as shown in Figure 3.12. On average we isolated 5.5 ng of TRNA from cells from 2mL of blood and 3.3 ng from EVs from ~400 µL plasma.

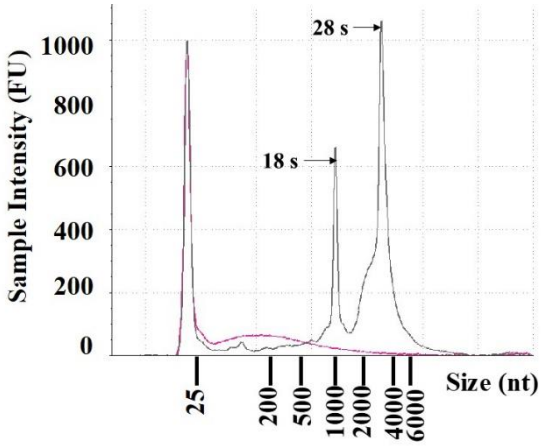

Figure 3.12: RNA profile of T cells (grey trace) isolated from blood and RNA profile (red) of EVs isolated from healthy donor plasma samples.

3.3.10 Droplet digital PCR (ddPCR)

For evaluating gene expression for diagnosing AIS, we selected gene cluster "4" identified by Adamski, *et. al*, which consisted of 5 genes: *FOS*, *VCAN*, *PLBD1*, *MMP9*, and *CA4*. This gene panel showed statistically significant difference ($p = 1.42 \times 10^{-5}$) between AIS patients and control samples. As shown in Figure 3.12 below, we can see that even within healthy donors, there are differences between the gene expression profiles between these 5 genes.

From healthy donor plasma the average RNA extracted was 3.3 ng. As stated in literature in EVs, 10% of RAN present in EVs are non-rRNA, and from this 25% of non-rRNA is long RNA which are > 100 nt. Approximately 10% of long RNA is coding RNA.[24] Considering

all these factors the amount of mRNA that could be isolated is ~8.25 pg. In the reverse transcription reaction (cDNA synthesis using Protoscript II kit from NEB), 2 ul of RNA will be taken from 10 ul which yield 1.65 pg of cDNA. (Assumption: cDNA synthesis is 100% efficient). This is ~6,022,000 mRNA molecules, assuming average length of mRNA in EV is 500 nt with a molar mass of 330 g/mol. In the final step, that is dd PCR, 2 ul of cDNA is taken from 20 ul of the reverse transcription reaction. Thus 602,200 mRNA molecules are used in the dd PCR reaction. Considering the 21,306 protein-coding genes in human genome[25] (assuming all genes are equally expressed) from the RNA we extracted from EV, we will obtain ~ 28 copies. (The detection level for dd PCR which is ~0.2 copies /µL)[26-27].

When designing the primes (Primer information are shown in Table 2.1) they were specifically designed close to poly-A tail and span the length of two exons, reducing the risk of amplifying genomic DNA through the intron.

Although there are no studies comparing the mRNA of T cells and EVs, recent studies have indicated that EVs enriched with specific RNAs compared to the originating cells suggestive of an active sorting mechanism.[28-29] To study the correlation between mRNA profiles of T cells and EVs, dd PCR was performed. Figure 3.13 below illustrates the changes in the gene expression between EV and T cells based on dd PCR results. When correlation between the gene expression in EVs and T cells was studied in separate individual healthy donors, two samples showed a moderate positive correlation with Pearson correlation coefficients of 0.62 and 0.56, another sample showed a poor correlation, while others showed a negative correlation. Although we can see a correlation between the mRNA profiles between T cells and EVs,

(by only considering the 5 genes, *PLBD1*, *FOS*, *MMP9*, *VCAN* and *CA4*) more samples needed to be analyzed to study the correlation between T cell mRNA and EV mRNA.

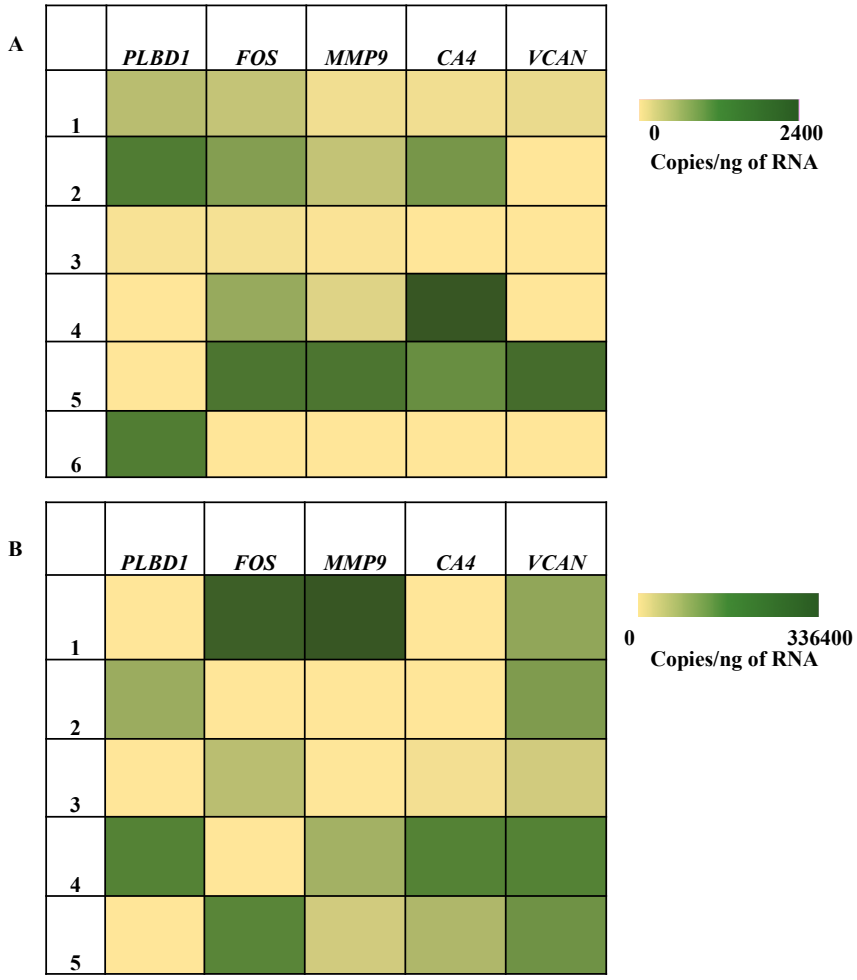

Figure 3.13: (A) Heat map of gene expression in EVs isolated from healthy donor plasma samples based on dd PCR (Number of copies obtained from dd PCR were normalized to total RNA values. All the dilution factors were considered for normalizing the data to generate heat maps) (B) Heat map of gene expression in T cells isolated from healthy donor blood samples.

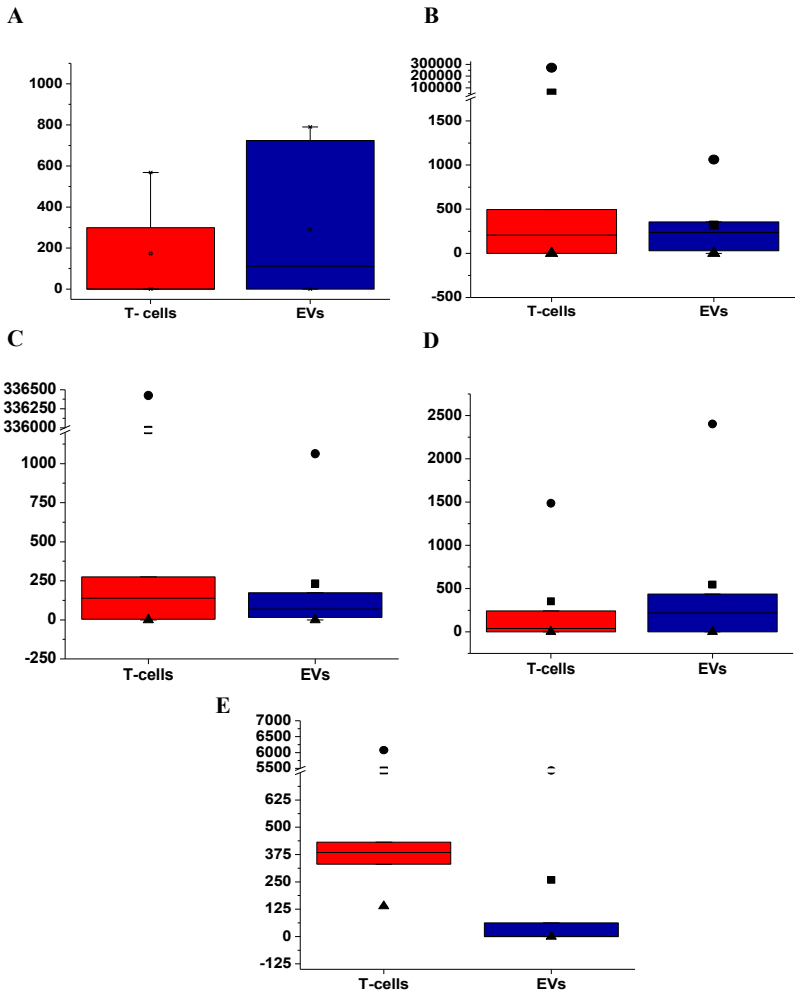

Figure 3.14: Box plots comparing the gene expression between T cells and EVs (A) *PLBD1* (B) *FOS* (C) *MMP9* (D) *CA4* (E) *VCAN*.

3.4 Conclusions

CD8+ T cells and their EVs were successfully isolated from healthy donor blood and plasma, respectively. Sinusoidal cell isolation device was used for cell isolation,[30] while pillared 3-bed device was used to affinity select EVs. The released cells stained with DAPI were enumerated and on average ~24,000 cells/mL of blood were isolated. Based on fluorescence images of CD45 and CD8+ stained cells (immunophenotyping), the purity of isolated cells was 81.3 ±11.5%. TRNA isolated from CD8 T cells separated in gel electrophoresis showed typically observed TRNA profiles for eukaryotic cells with well pronounced ribosomal RNAs larger and smaller subunits. Based on RNA size markers, we concluded the RNA isolated from EVs ranged in size between 50 nt and 2,000 nt. On average we isolated 5.5 ng of TRNA from cells from 2 mL of blood and 3.3 ng from EVs from ~500 µL plasma. We collected gene expression profiles for both CD8 T cells and EVs using ddPCR. Although we can see a correlation between the mRNA profiles between T cells and EVs, (by only considering the 5 genes, *PLBD1*, *FOS*, *MMP9*, *VCAN* and *CA4*) more samples needed to be analyzed to study the correlation between T cell mRNA and EV mRNA.

3.5 References

1. Macias, M.; Alegre, E.; Diaz-Lagares, A.; Patino, A.; Perez-Gracia, J. L.; Sanmamed, M.; Lopez-Lopez, R.; Varo, N.; Gonzalez, A., Liquid biopsy: from basic research to clinical practice. In *Advances in clinical chemistry*, Elsevier: 2018; Vol. 83, pp 73-119.
2. Jeffrey, S. S.; Toner, M., Liquid biopsy: a perspective for probing blood for cancer. *Lab on a Chip* **2019,** *19* (4), 548-549.
3. Marrugo-Ramírez, J.; Mir, M.; Samitier, J., Blood-based cancer biomarkers in liquid biopsy: A promising non-invasive alternative to tissue biopsy. *International journal of molecular sciences* **2018,** *19* (10), 2877.
4. Palmirotta, R.; Lovero, D.; Cafforio, P.; Felici, C.; Mannavola, F.; Pellè, E.; Quaresmini, D.; Tucci, M.; Silvestris, F., Liquid biopsy of cancer: a multimodal diagnostic tool in clinical oncology. *Therapeutic advances in medical oncology* **2018,** *10*, 1758835918794630.
5. Catarino, R.; Ferreira, M. M.; Rodrigues, H.; Coelho, A.; Nogal, A.; Sousa, A.; Medeiros, R., Quantification of free circulating tumor DNA as a diagnostic marker for breast cancer. *DNA and cell biology* **2008,** *27* (8), 415-421.
6. Couch, Y.; Akbar, N.; Davis, S.; Fischer, R.; Dickens, A. M.; Neuhaus, A. A.; Burgess, A. I.; Rothwell, P. M.; Buchan, A. M., Inflammatory stroke extracellular vesicles induce macrophage activation. *Stroke* **2017,** *48* (8), 2292-2296.
7. Tauro, B. J.; Greening, D. W.; Mathias, R. A.; Ji, H.; Mathivanan, S.; Scott, A. M.; Simpson, R. J., Comparison of ultracentrifugation, density gradient separation, and immunoaffinity capture methods for isolating human colon cancer cell line LIM1863-derived exosomes. *Methods* **2012,** *56* (2), 293-304.
8. Im, H.; Shao, H.; Park, Y. I.; Peterson, V. M.; Castro, C. M.; Weissleder, R.; Lee, H., Label-free detection and molecular profiling of exosomes with a nano-plasmonic sensor. *Nature biotechnology* **2014,** *32* (5), 490.
9. Shao, H.; Chung, J.; Lee, K.; Balaj, L.; Min, C.; Carter, B. S.; Hochberg, F. H.; Breakefield, X. O.; Lee, H.; Weissleder, R., Chip-based analysis of exosomal mRNA mediating drug resistance in glioblastoma. *Nature communications* **2015,** *6*, 6999.
10. Wei, F.; Yang, J.; Wong, D. T., Detection of exosomal biomarker by electric field-induced release and measurement (EFIRM). *Biosensors and Bioelectronics* **2013,** *44*, 115-121.
11. Zhang, P.; He, M.; Zeng, Y., Ultrasensitive microfluidic analysis of circulating exosomes using a nanostructured graphene oxide/polydopamine coating. *Lab on a Chip* **2016,** *16* (16), 3033-3042.
12. Chen, C.; Skog, J.; Hsu, C.-H.; Lessard, R. T.; Balaj, L.; Wurdinger, T.; Carter, B. S.; Breakefield, X. O.; Toner, M.; Irimia, D., Microfluidic isolation and transcriptome analysis of serum microvesicles. *Lab on a Chip* **2010,** *10* (4), 505-511.
13. Kanwar, S. S.; Dunlay, C. J.; Simeone, D. M.; Nagrath, S., Microfluidic device (ExoChip) for on-chip isolation, quantification and characterization of circulating exosomes. *Lab on a Chip* **2014,** *14* (11), 1891-1900.
14. Ashcroft, B.; De Sonneville, J.; Yuana, Y.; Osanto, S.; Bertina, R.; Kuil, M.; Oosterkamp, T., Determination of the size distribution of blood microparticles directly in plasma using atomic force microscopy and microfluidics. *Biomedical microdevices* **2012,** *14* (4), 641-649.
15. Adamski, M. G.; Li, Y.; Wagner, E.; Seales-Bailey, C.; Bennett, N.; Yu, H.; Murphy, M.; Soper, S. A.; Baird, A. E., CD15+ granulocyte and CD8+ T lymphocyte based gene expression clusters for ischemic stroke detection. *Medical Research Archives* **2017,** *5* (11).
16. Nau, K. C.; Crocco, T.; Biola, J.; Larrabee, H., Is it stroke, or something else? Rapid response to stroke is crucial, but the rush to treat can endanger patients with conditions that

mimic stroke. Here's how to more readily spot the difference. *Journal of family practice* **2010,** *59* (1), 26-32.
17. Hupert, M. L.; Jackson, J. M.; Wang, H.; Witek, M. A.; Kamande, J.; Milowsky, M. I.; Whang, Y. E.; Soper, S. A., Arrays of high-aspect ratio microchannels for high-throughput isolation of circulating tumor cells (CTCs). *Microsystem technologies* **2014,** *20* (10-11), 1815-1825.
18. Ngo, N.; Patel, K.; Isaacson, P. G.; Naresh, K. N., Leucocyte common antigen (CD45) and CD5 positivity in an "undifferentiated" carcinoma: a potential diagnostic pitfall. *Journal of clinical pathology* **2007,** *60* (8), 936-938.
19. Adams, A. A.; Okagbare, P. I.; Feng, J.; Hupert, M. L.; Patterson, D.; Göttert, J.; McCarley, R. L.; Nikitopoulos, D.; Murphy, M. C.; Soper, S. A., Highly efficient circulating tumor cell isolation from whole blood and label-free enumeration using polymer-based microfluidics with an integrated conductivity sensor. *Journal of the American Chemical Society* **2008,** *130* (27), 8633-8641.
20. Vestad, B.; Llorente, A.; Neurauter, A.; Phuyal, S.; Kierulf, B.; Kierulf, P.; Skotland, T.; Sandvig, K.; Haug, K. B. F.; Øvstebø, R., Size and concentration analyses of extracellular vesicles by nanoparticle tracking analysis: a variation study. *Journal of extracellular vesicles* **2017,** *6* (1), 1344087.
21. Gardiner, C.; Shaw, M.; Hole, P.; Smith, J.; Tannetta, D.; Redman, C. W.; Sargent, I. L., Measurement of refractive index by nanoparticle tracking analysis reveals heterogeneity in extracellular vesicles. *Journal of extracellular vesicles* **2014,** *3* (1), 25361.
22. Chen, T. S.; Lai, R. C.; Lee, M. M.; Choo, A. B. H.; Lee, C. N.; Lim, S. K., Mesenchymal stem cell secretes microparticles enriched in pre-microRNAs. *Nucleic acids research* **2009,** *38* (1), 215-224.
23. Batagov, A. O.; Kurochkin, I. V., Exosomes secreted by human cells transport largely mRNA fragments that are enriched in the 3′-untranslated regions. *Biology direct* **2013,** *8* (1), 12.
24. Wei, Z.; Batagov, A. O.; Schinelli, S.; Wang, J.; Wang, Y.; El Fatimy, R.; Rabinovsky, R.; Balaj, L.; Chen, C. C.; Hochberg, F., Coding and noncoding landscape of extracellular RNA released by human glioma stem cells. *Nature communications* **2017,** *8* (1), 1145.
25. Pertea, M.; Shumate, A.; Pertea, G.; Varabyou, A.; Chang, Y.-C.; Madugundu, A. K.; Pandey, A.; Salzberg, S., Thousands of large-scale RNA sequencing experiments yield a comprehensive new human gene list and reveal extensive transcriptional noise. *BioRxiv* **2018**, 332825.
26. Nour, M.; Liebeskind, D. S., Brain imaging in stroke: insight beyond diagnosis. *Neurotherapeutics* **2011,** *8* (3), 330-339.
27. Uchiyama, Y.; Nakashima, M.; Watanabe, S.; Miyajima, M.; Taguri, M.; Miyatake, S.; Miyake, N.; Saitsu, H.; Mishima, H.; Kinoshita, A., Ultra–sensitive droplet digital PCR for detecting a low–prevalence somatic GNAQ mutation in Sturge–Weber syndrome. *Scientific reports* **2016,** *6*, 22985.
28. Ragni, E.; Banfi, F.; Barilani, M.; Cherubini, A.; Parazzi, V.; Larghi, P.; Dolo, V.; Bollati, V.; Lazzari, L., Extracellular Vesicle-Shuttled mRNA in Mesenchymal Stem Cell Communication. *Stem cells* **2017,** *35* (4), 1093-1105.
29. Morhayim, J.; van de Peppel, J.; Dudakovic, A.; Chiba, H.; van Wijnen, A. J.; van Leeuwen, J. P., Molecular characterization of human osteoblast-derived extracellular vesicle mRNA using next-generation sequencing. *Biochimica et Biophysica Acta (BBA)-Molecular Cell Research* **2017,** *1864* (7), 1133-1141.
30. Jackson, J. M.; Witek, M. A.; Hupert, M. L.; Brady, C.; Pullagurla, S.; Kamande, J.; Aufforth, R. D.; Tignanelli, C. J.; Torphy, R. J.; Yeh, J. J., UV activation of polymeric high

aspect ratio microstructures: ramifications in antibody surface loading for circulating tumor cell selection. *Lab on a Chip* **2014,** *14* (1), 106-117.

Chapter 4: Clinical application of microfluidic devices for stroke diagnosis

4.1 Introduction

Thermoplastics such as COP, COC, PMMA and PC have been widely used to produce microfluidic devices due to their low cost. Microfluidic devices used in previous sections for isolating EVs and cells were fabricated on COC thermoplastic via hot embossing. Cyclic olefinic copolymer (COP) is another thermoplastic that is increasingly used as a substrate material for microfluidics. This is due to the promising properties of COP including high chemical resistance, low water absorption, and ease of fabrication. COPs are based on cyclic olefin monomers and ethene.[1]

The 3-bed microfluidic device, we used for previous studies, has a relatively narrow inter-pillar spacing (~20 μm) and long bed length (122 mm total) but relatively large micropillars (100 μm). At 5 μL/min, the 5.7 mm/s linear velocity results in a 41% simulated recovery. In order to process samples in a short time period with higher recovery, we used a 7-bed microfluidic device with high capacity. Short sample processing time will help to greatly reduce assay time, which is an important factor in developing ischemic stroke diagnosis assays.

The 7-bed device shortens the bed length (23 mm) but decreases pillar size to 10 μm, yielding a 97% EV recovery at the same volume flow rate. This enables higher throughput for processing clinical samples with the 7-bed chip (10 μL/min and ~90% recovery) and timely sample processing that is critical for meeting the time constraints placed on AIS diagnosis. The 7-bed chip provided an additional advantage that the surface area is ~6 times greater, enabling the capacity to enrich a high load of EVs (theoretical load of 2 $x10^{11}$ hexagonally packed EVs with 150 nm diameter).

Since high capacity device was fabricated on COP thermoplastic, properties of COC and COP were compared. For this purpose, 3-bed device was fabricated in COP and properties including contact angle, UV absorbance, carboxylic acid density and ability to modify surface for affinity selection were studied.

In order to check the applicability of developed method for detecting stroke patients, clinical samples (both healthy and ischemic stroke patient plasma samples) were analyzed using the 7-bed device and RNA was extracted for gene profiling. In addition to RNA profiling, TEM and NTA analysis were performed to determine any differences between EVs in ischemic stroke plasma samples and healthy controls. Finally, statistical analysis was performed to differentiate between the stroke patients and healthy controls from the analyzed clinical samples.

4.2 Experimental

4.2.1 3-bed device fabrication in COP thermoplastic

The molding master was fabricated in brass mold via high-precision micro milling (HPMM) using a commercial milling machine. Polymer replicas of the mold master were produced using hot embossing into cyclic olefin polymer (COP) (Zeonor 1060R) using a Precision Press model P3H-15-PLX (Wabash MPI, IN). Polymer plaques were dried in an oven at 65 ^{o}C overnight prior to hot embossing. The optimized hot embossing protocol used in this study is briefly described below. The embossing fixture was heated to 145 ^{o}C and top and bottom platens of the precision press model are heated to 145 ^{o}C and 120 ^{o}C respectively. Next a force of ~3000 lb is applied for 120 s before demolding the embossed device at 90 ^{o}C. COP cover plates which used for the devices were 1.2 mm in thickness.

4.2.2 Optimization of thermal fusion bonding protocol for COP devices

After hot embossing devices into COP thermoplastic, non-contact profilometry was performed to confirm the correct pillar dimensions of the microfluidic devices. Then, thermal fusion bonding protocol was optimized. Varying bonding temperatures and bonding times were tested

to find out the best conditions for an optimum bonding. After bonding, non-contact profilometry was performed to determine pillar dimensions. This was performed by using ImageJ software via a custom macro. Optimized bonding conditions were used for subsequent experiments.

4.2.3 Comparison of cyclic olefinic copolymer (COC) and cyclic olefinic polymer (COP) thermoplastics

4.2.3.1 Contact angle variation

Both COC and COP thermoplastics were used for the study. Small pieces of (2 cm x 2 cm) thermoplastic were cleaned by sonicating in 10% Micro-90 for 5 min and then rinsed with IPA and nano-pure water. These pieces of thermoplastics were dried at 65 °C overnight before measuring contact angle. Both pristine and UV-modified COC and COP were used for contact angle measurements which was performed using a VCA Optima instrument (AST products). A volume of 2 μL nanopore water (18.2 MΩ.cm at 25 °C) was dispensed onto thermoplastic surfaces and an image of each droplet was captured immediately. Then the images were analyzed using the software provided by the manufacturer. The measurements were repeated three times at different positions.

4.2.3.2 Carboxylic acid density measurements

Carboxylic acid density of COC and COP thermoplastics were measured as reported previously.[2] In brief, an *in-situ* incubation chamber (Bio Rad, Hercules, CA) was attached to substrate's surface and filled with 0.1% (w/v) Toluidene Blue O (TBO) in carbonate buffer (50 mM, pH =10.5). After 15 min, substrate was submerged in the same buffer for 15 min and then air dried. This step will remove any TBO molecules that are non-specifically attached to the substrate surface. To desorb TBO molecules that were attached through the carboxylic groups, 40% acetic acid (d= 1.0196 g mL^{-1}) was used. The volumes used for the desorption were collected to pre-weighed tubes and analyzed with a UV/vis spectrophotometer (Ultrospec 4000, Pharmacia Biotech) against a 40% acetic acid blank at TBO's absorption maximum, which is 630 nm. A

calibration curve was generated using TBO standards in 40% acetic acid. For calibration curve, known amounts of TBO were directly added to the buffer solution.

4.2.3.3 Optimization of UV activation protocol

3-bed microfluidic devices made out of COP were bonded using the optimized protocol. For some COP devices, the cover plate and the microfluidic devices were UV/O_3 modified before bonding. Other devices were first bonded and then UV/O_3 modified for 13 min (254 /185 nm, 22 mV/cm^2). To verify the effectiveness of carboxylic group formation for different UV modifying protocols used, (first UV-modifying and bonding and first bonding and then UV-modifying) a fluorescently tagged oligo nucleotide was used. A 5'-amino, 3'-Cy5 oligonucleotide linker (5'NH_2-C_{12}-T8CCCTTCCTCACTTCCCTTTUT9-Cy5, HPLC purified, 1 mM stock in nuclease free water; Integrated DNA Technologies) was used for this purpose. First, oligonucleotide was diluted to 10 μM in 20 mg/mL EDC in PBS and injected to microfluidic devices. Then the devices were kept 2 h at room temperature before rinsing with 1% Tween20 solution, which was then replaced with 500 μL PBS for imaging. The devices were then visualized using an inverted microscope (Zeiss 200 M) with a 10x objective (0.3 NA, Plan NeoFluar) equipped with XBO 75 Xe arc lamp, single band Cy5 filter set (Omega optical), Cascade:1K EM-CCD camera (Photometric), and an automated stage (MAC 5000 ,Ludl Electronic Products), all of which were computer-controlled via Micro-Manager. Final images were background subtracted and analyzed using Image-J software.

4.2.3.4 RNA extraction from COC and COP devices

To compare the amount of RNA extracted from both COP and COC thermoplastics, plasma samples were processed through both devices and the extracted RNA was quantified by Tape station.

4.2.4 7-bed device stimulation studies

A custom code for this model was programmed in Fortran 90, compiled with GFortran, and executed on a computer workstation. All the simulation studies explained in this chapter were performed by Dr. Matthew Jackson (Dr. Soper's Lab, The University of Kansas).

4.2.5 High capacity microfluidic device (7-bed microfluidic device)

The 7-bed microfluidic devices used in this study were provided by Biofluidica, Inc. (San Diego, CA). Devices were fabricated in cyclic olefin polymer (COP) via injection molding (Stratec, Austria). COP cover plates of 1.25 mm thickness were used for these devices and for inlet and outlets, peek tubing was used. These tubing were attached to devices using epoxy glue to prevent any leakages during sample processing.

4.2.6 7-bed device modification for affinity selection

For modification of device surface for affinity selection of EVs same protocol was used as for 3-ded devices. Since the surface area of the device is higher than that of 3-bed device higher mass of the CD8 mAb was used for 7-bed device (considering the loss of Ab during the purification step). Thus, starting Ab concentration for the 7-bed device was calculated as 2 mg/mL.

4.2.7 Analyzing clinical samples with the 7-bed device, RNA extraction and droplet digital PCR

Clinical samples (plasma samples) analyzed in this study was provided by Dr. Alison Baird at SUNY Downstate Medical Center. We obtained 10 clinical samples (5 samples were stroke patient samples and 5 were healthy controls). We performed a blinded study on these samples. These clinical samples were stored in the -80 °C after separating plasma from collected blood. The devices were treated in the same way as we did for the 3-bed devices. To release the captured EVs for TEM and NTA analysis USER enzyme was used as described in previous

chapters. As described in the previous sections, PEG precipitation was performed for some clinical samples.

4.2.8 Statistical analysis

We performed a statistical analysis using R-Studio software to find out the patient samples for this one-sided blinded study. Heat maps were generated and the Principle Component Analysis (PCA) was performed for the 10 clinical samples.

4.3 Results and Discussion

4.3.1 COP vs COP

Cyclic olefin copolymer (COC) and cyclic olefinic polymer (COP) are two main thermoplastics that have been widely used for developing microfluidic devices. COC is a polymer that consist of ethylene and norbornene. As shown in Figure 4.1 COCs are obtained via copolymerization of cycloolefin with ethylene or α-olefin.[3]

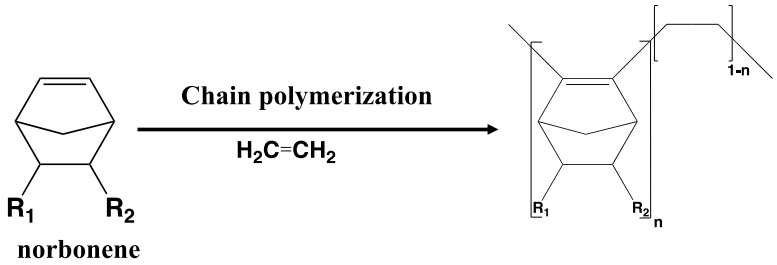

Figure 4.1: COC structure and synthesis pathway via copolymerization of cycloolefin with ethylene or α-olefin.

Through its characteristic molecular structure COC offers wide range of grade variations in terms of flow properties and heat resistance.[4] Thus, there are many COC thermoplastics available with different glass transition temperatures (Tg = 78 °C, 130 °C, 160 °C and 130 °C). Therefore, depending on the application, appropriate material can be selected. Most importantly, COC is easier to emboss. COC has a lower density compared to PMMA.[4] The water absorption of COC is <0.01% and that is 10 times lower than PMMA. Hence, the relative humidity changes in environment will not significantly affect devices that are embossed on COC.

Cyclic olefinic polymer (COP) is another thermoplastic that is increasingly used as a substrate material for microfluidics. This is due to the promising properties of COP including high chemical resistance, low water absorption, and ease of fabrication. COPs are based on cyclic olefin monomers and ethene.[1] Slightly different materials are obtained depending on the cyclic monomer and the polymerization process used.[5] Mechanism involved in synthesis of COP is called as ring-opening metathesis polymerization of cyclic monomers followed by hydrogenation which is shown in Figure 4.2.[5] Low water absorption of COP provides stability in changing environmental conditions.[6]

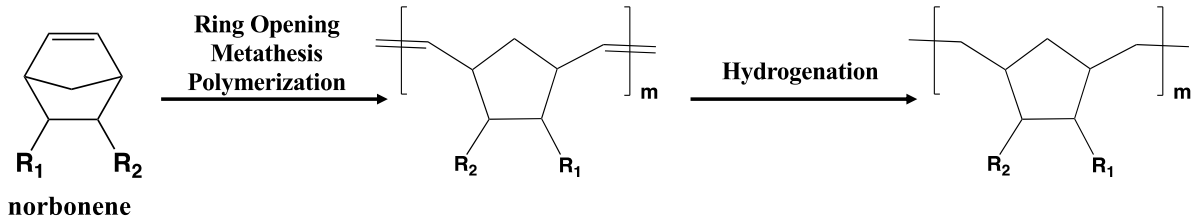

Figure 4.2: COP structure and synthesis pathway (ring-opening metathesis polymerization).

4.3.2 Optimization of annealing protocol for COP devices

As explained in Chapter 2, embossed devices and cover plates are bonded by thermally fusion bonding. Considering the Tg of 99 °C, we tried different protocols for bonding. Initially bonding was performed at 103 °C for 30 min using a high pressure (provided by the clips). Although perfect bonding was obtained by this protocol, there was no pillar spacing due to the high pressure as shown in Figure 4.3 A. Next, bonding was performed at 99 °C for 30 min, but there were many unbonded pillars under these conditions (shown by arrows in Figure 4.4 B). There were still some unbonded pillar regions, even the bonding was continued for another 30 min. (Figure 4.4 C). Next, bonding was performed at 103 °C for 30 min, but with lower pressure and these conditions yielded good bonding with good pillar spacing as shown in Figure 4.3 D. Thus, the optimum bonding conditions were concluded as annealing at 103 °C for 30 min with lower pressure.

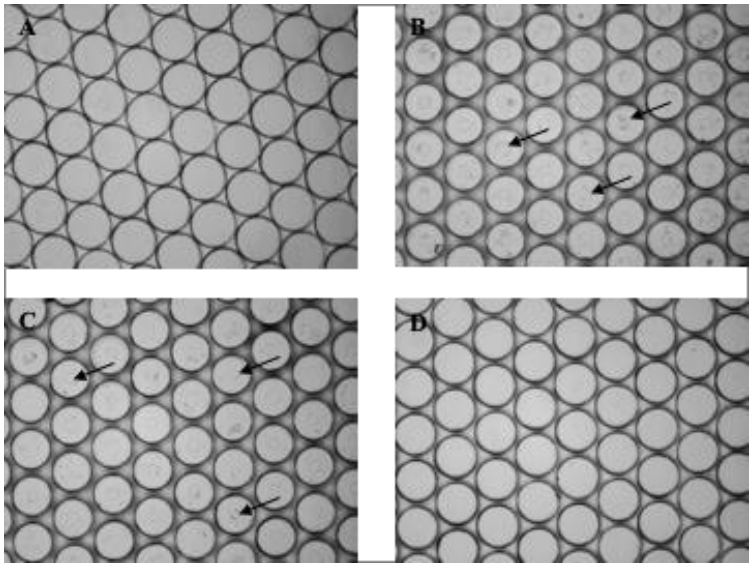

Figure 4.3: Microscope images of the devices bond at (A) 103 °C for 30 min with high pressure. (B) 99 °C for 30 min with high pressure – arrows show the non-bonded pillars. (C) 99 °C for additional 30 min with high pressure – arrows show the non-bonded pillars. (D) 103 °C for 30 min with less pressure.

4.3.3 Contact angle variation

Wettability of the thermoplastics is a measure of its hydrophobicity. The hydrophobicity of these thermoplastics can be problematic in microfluidic devices. To decrease surface hydrophobicity several techniques can be utilized. Low-pressure plasma[7], oxygen plasma, UV/O_3 and chemical treatment are some of those.[8-11] We used UV/O_3 treatment to increase the hydrophilicity of thermoplastics by creating carboxylic acid groups on the surface. In order to compare water contact angle of COC and COP, well cleaned thermoplastic pieces were used. Based on the contact angle measurements, pristine COC and COP were hydrophobic. Upon UV/O_3 treatment the contact angles decreased, indicating the increased hydrophilicity. Variation of contact angles of COC and COP before and after UV/O_3 treatment are shown in Figure 4.4 and Table 4.1.

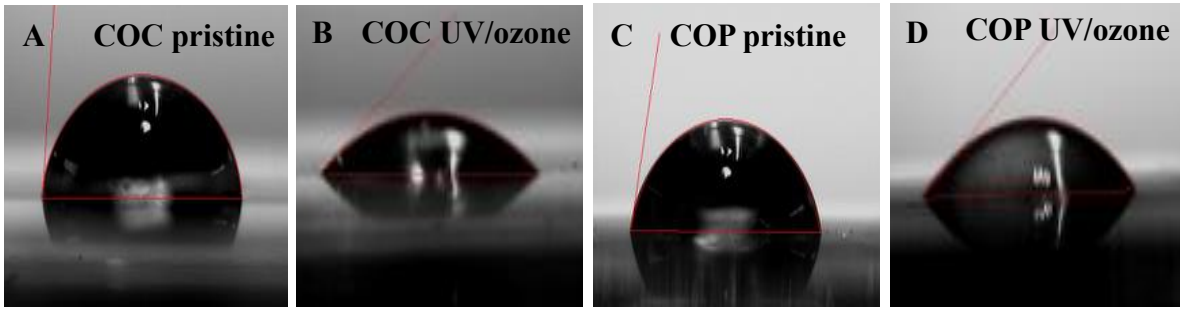

Figure 4.4: Contact angle variation of COC and COP thermoplastics; (A) COC pristine (B) COC UV/O_3 modified. (C)COP pristine. (D) COP UV/O_3 modified.

Table 4.1: Contact angle variation for COC and COP

Thermoplastic	Contact Angle (^{o})	
	Pristine (n=5)	UV/O_3 modified (22 mW/cm^2 for 13 min; n = 5)
COC	85.60 ± 2.52	33.68 ± 3.15
COP	79.73 ± 1.44	35.55 ± 3.89

4.3.4 Carboxylic acid density measurements

Since EDC/NHS coupling reaction was utilized to modify device surfaces, carboxylic acid density on the surface is an important factor that need to be tested. To determine carboxylic acid density on the COP and COC surface Toluidene Blue O (TBO) assay was performed. TBO is a dye that electrostatically binds to aliphatic or aromatic carboxylic acid due to the charge when deprotonated at high pH values like 10.5.[12-13]

The mechanism taking place during the TBO assay is shown in Figure 4.5. After incubation with TBO, polymer substrates were thoroughly rinsed in carbonate buffer to remove any excess dye molecules on the surfaces. TBO molecules that are attached to carboxylic groups on surface are released by 40% acetic acid. Here 40% acetic acid was selected since higher concentrations of acetic acid may cause dissolution of thermoplastics. However, 40% acetic acid can remove any photo-fragments generated by scissoring of the polymer backbone that can take place during UV/O3 treatment.[2, 14-15]

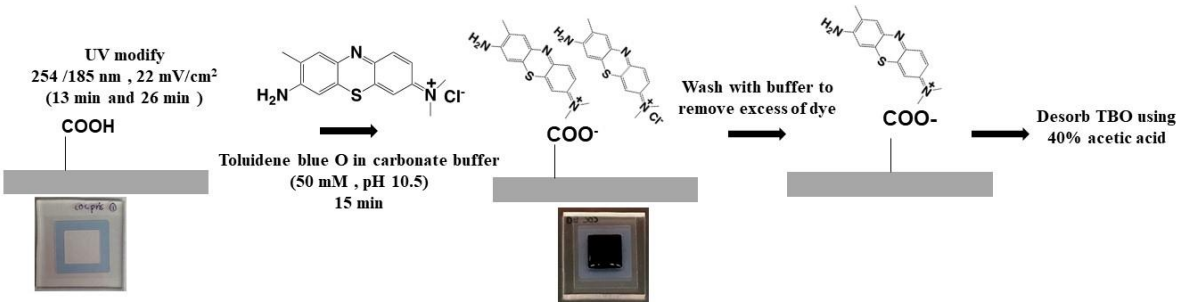

Figure 4.5: Schematic representation of steps involved in TBO assay for determination of carboxylic acid densities on COP and COC surfaces.

After releasing surface-bound TBO, UV-Vis spectroscopy was used to determine TBO molecules bound to surface using a calibration curve (considering factors including volume, surface area and densities of solutions used). For both pristine COC and COP, TBO assay background values showed 0.69 ± 0.06 nmol/cm^2 and 0.97 ± 0.17 nmol/cm^2, respectively. After 13 min of UV/O_3 modification, carboxylic acid densities were 34.88 ± 7.10 nmol/cm^2 and 34.39 ± 8.21 nmol/cm^2 for COC and COP, respectively. Repeated UV/O_3 modification of the COP thermoplastic for an additional 13 min showed no significant increase in COOH groups as shown in Figure 4.6. Based on the results we can see that the carboxylic acid densities of both COC and COP thermoplastics are same. Thus, same number of mAbs can be immobilized on both thermoplastics.

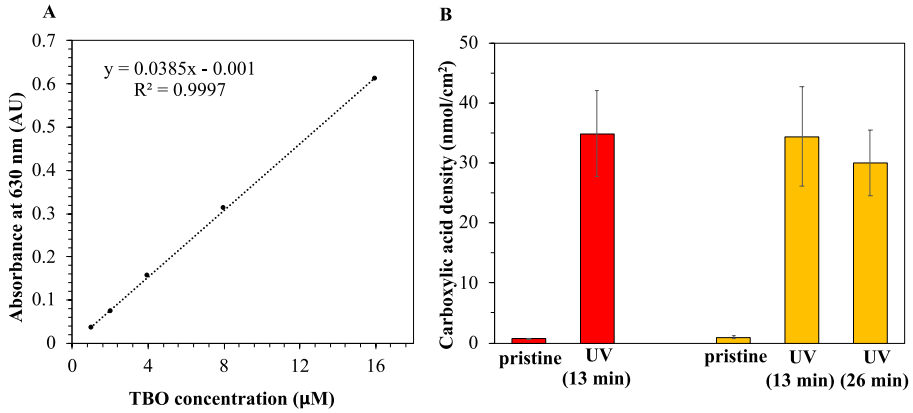

Figure 4.6: (A) Calibration curve for TBO in 40% acetic acid measured at TBO's absorption maximum, 630 nm. For the calibration curve, known amounts of TBO were directly added to the buffer solution (B). Carboxylic acid densities calculated from TBO for COC and COP thermoplastics; red- COC, yellow-COP.

4.3.5 Optimization of UV activation protocol

Since carboxylic group formation on the device surface is performed via UV/O_3 treatment it's important to compare the optical properties such as UV absorbance and transmittance in the 254 nm range (Since it is the wavelength that we use for UV/O_3 treatment). Moreover, COC (75 µm) and COP (1250 µm) cover plates we used in these studies are different in thicknesses which can also affect the UV absorbance and transparency. Thus, UV absorbance measurements were performed using two cover plates that we used in assembling the devices. Figure 4.7 shows the absorbance of COC and COP cover plates.

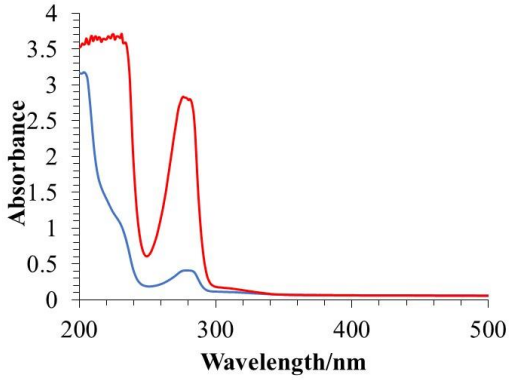

Figure 4.7: UV absorbance of COP and COC cover plates used for device assembly; red trace - COP, blue trace- COC.

The UV absorbance of COP cover plate is higher than that of COC cover plate which can be problematic in carboxylic acid group formation via UV/O_3 treatment. We used fluorescently tagged oligo nucleotide to check the UV modification efficiencies of both COC and COP devices. This 5'-amino, 3'-Cy5 oligonucleotide will attach to the carboxylic acid groups on the device surface via EDC coupling reaction, which is similar to what's taking place during mAb attachment. Thus, the fluorescent intensity will represent the efficiency of immobilization of the device surface.

First, COP devices were thermally bonded, and UV/O_3 modified, and efficiency was determined. Next, devices and cover plates were UV/O_3 treated separately and then thermally boned. Figure 4.8 shows the results obtained for COC and COP UV modification efficiencies. A negative control was performed without EDC coupling reagent.

Based on the results, for COC there is a significant difference between negative control and devices that were thermally bonded first and then UV/O_3 treated. However, for COP the devices, that were thermally bonded and then UV/O_3 treated showed a less intensity compared to devices that were UV modified first and then thermally bonded. Lower efficiency in thermally bonded and UV modified devices may be due to the high UV absorption of COP cover plates. Hence, for subsequent experiments COP cover plates and devices were first UV/O_3 treated and then thermally bonded. The devices were surface modified on the same day.

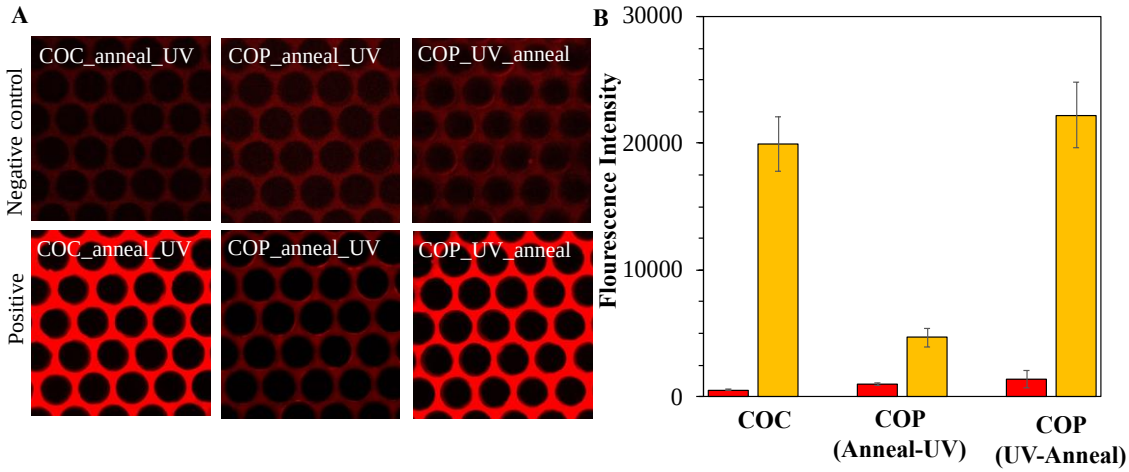

Figure 4.8: (A) Back ground corrected florescence images for COC and COP devices. (B) Calculated florescence intensities of the images (red - negative control without EDC, yellow with EDC, average of 2 devices, 9 measurements per device).

4.3.6 RNA extraction from COC and COP devices

Once the COC and COP 3-bed devices are assembled and modified using the CD8 mAb, plasma samples were processed through these devices separately and RNA was extracted via on-chip lysis to quantify the RNA isolated on these two types of thermoplastics. The quantity of isolated RNA from both thermoplastics did not show any statistical difference with a p-value of 0.84357 (at 95% confidence limit). This result is also supported by the fact that the carboxylic acid densities of both thermoplastics are similar to each other.

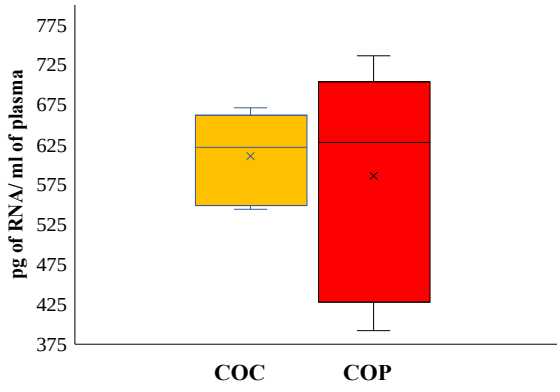

Figure 4.9: Quantification of RNA isolated on COC and COP devices (n=5).

4.3.7 7-bed device stimulation studies

One of the major drawbacks of microfluidic devices is the low sample processing speeds which takes long analysis time. This is a major disadvantage when developing assays in which time is a critical factor. For example, a recently EV affinity isolation microfluidic device was reported, which used 3-dimensional herringbone nanopatterns, operated at a volume flow rate of 0.5 µL min^{-1}, which would require 400 min (6.7 h) to process a volume of 200 µL of plasma.[16]

As discussed previously, since there is a short time window of ~4 h for ischemic stroke treatment sample processing has to be quick. The 3- bed device that was used in the initial evaluation of our method yield higher recoveries at low flow rates, (the recovery is ~80% at 2.1 µl/min) which means long time periods are required for sample processing. To overcome this problem and process the samples in a short time with higher recoveries we developed a high throughput microfluidic device. Once the device was designed simulation studies were performed to evaluate EV recovery as a function of flow rate.

Initial simulation analysis performed on this 7- bed device design is shown in Figure 4.10. Based on simulation studies, performed on 3-bed device at 5 µL/min the predicted EV recovery is 42%. But the new 7 bed device can process samples at 20 µL/min, which is 4 times faster than the flow rate of 3-bed device and still can give a recovery of ~65%. Figure 4.11 B below compares the calculated samples processing time for 3- bed and 7-bed device. As shown in Figure 4.11 B, compared to 3-bed device the sample processing time can be greatly reduced by using the new design with 7-bed device. Thus, in this study, 7-bed devices were used for stroke patient sample analysis.

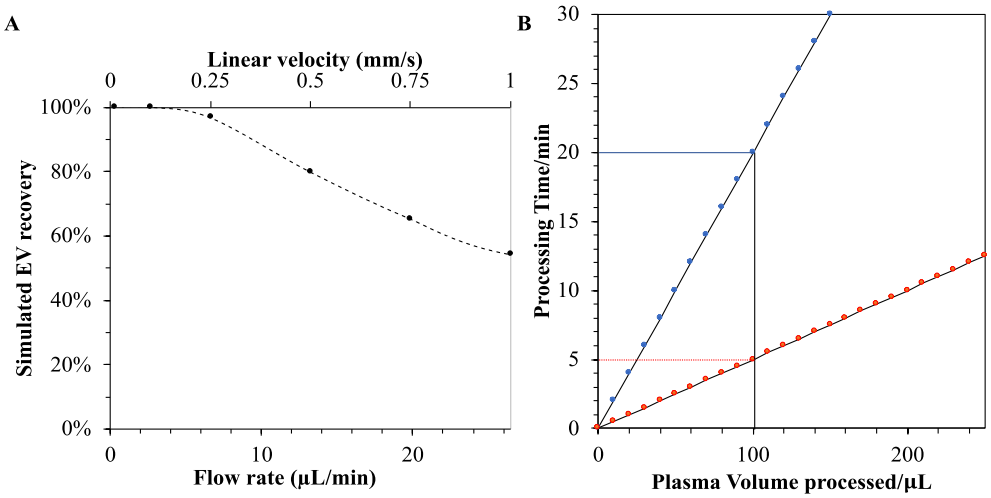

Figure 4.10: Stimulation studies on 7- bed device - EV recovery as a function of flow rate (A) Monte Carlo simulation results for the 7-bed device. Courtesy of Dr. Matt Jackson (B) Calculated sample processing time for 3 bed device – blue trace (5 µL/min) and 7 bed device- red trace (20 µL/min).

4.3.8 Device design of 7-bed device

The device contained 7 beds with diamond shaped pillars. Pillars are 50 µm in height and 50 µm in width. The spacing between the pillars is 10 µm. Each bed is 23.3 mm long and 3.6. mm in width, which is shorter compared to the bed length of 3-bed device (122 nm). The longer bed length but relatively larger micropillars (100 µm) and narrow inter-pillar spacing (10-20 µm) of 3-bed device results in relatively low EV recovery (~42%) at 5 µL/min (5.7 mm/s). But 7-bed device shortens the bed length (23 mm) but decreases pillar size to 10 µm, yielding only 0.19 mm/s at the same flow rate and 97% EV recovery. This enables higher throughput for processing clinical samples with the 7-bed chip (10 µL/min and ~90% recovery) and timely sample processing that is critical for AIS diagnosis. The 7-bed device provides an additional advantage that the surface area is ~6 times greater, enabling the capacity to enrich a high load EVs (theoretical load of 4.4 x 10^{11} hexagonally packed EVs with 100 nm diameter). High load of EVs in these 7-bed devices will help to increase the total EV mRNA that can be isolated from the devices. Table 4.2 below compares some parameters of 3-bed and 7-bed device.

Table 4.2: Comparison between 3-bed device and 7-bed device

Metric	**3-bed device**	**7-bed device**
Number of pillars	15,202	1,475,712
Surface area (bed with pillars) /cm^2	6.8	38.5
Internal volume / µL	6.5	22.4
EV capacity (Considering average size of 100 nm)	7.8×10^{10}	4.4×10^{11}

7-bed device design and SEM images of the pillars are shown in Figure 4.12. There are inlet and outlet ports where we connect the PEEK tubing to inject the samples. The inlet channel is further directed into 7 channels that are connected to each bed separately as shown in Figure 4.12 B. This device is made of COP and was purchased from BioFluidica Inc. which was already assembled.

An additional advantage of this device design is that it can be manufactured in a high production mode at low cost using injection molding. Injection molding is another commonly used fabrication technique which is popular due to its short fabrication cycle times.[17] In injection molding, pellets of COP are put into the hopper of the injection molding machine and are transported in the mold direction where they are simultaneously melted at a high temperature. The melted polymer is then injected with a high pressure against the mold that is maintained at de-molding temperature. After that a constant pressure is applied to COP and then sample is cooled down and de-moulded.[1] Figure 4.11 E shows the injected molded device after assembly.

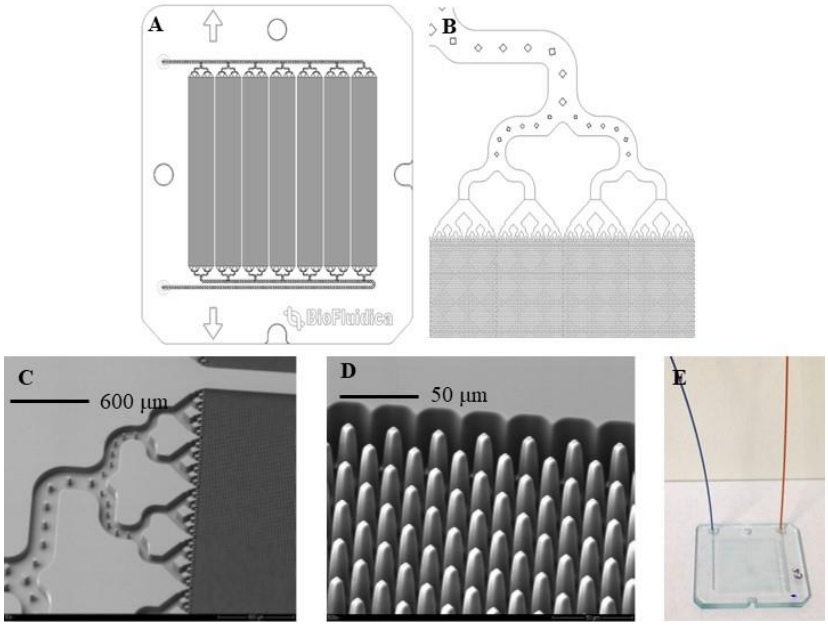

Figure 4.11: 7-bed microfluidic device design (A) Picture of 7-bed device showing the distribution channels and the diamond shaped micro pillars on the device surface. (B) Distribution channels to each bed. (C) SEM images of the mold: Distribution channels. (D) Micro pillars in the beds. (E) Final assembled device with PEEK tubing.

4.3.9 7-bed device surface modification

A fluorescently tagged oligo nucleotide was used to check the surface modification efficiency of the 7-bed device. This 5'-amino, 3'-Cy5 oligonucleotide will attach to the carboxylic acid groups on the device surface via EDC coupling reaction, which is similar to what's taking place during mAb attachment. Thus, the fluorescent intensity will represent the efficiency of immobilization of the device surface. As the negative control, a reaction was performed without EDC coupling reagent to compare the fluorescent intensities, the devices were imaged via fluorescence microscopy and then intensity scaled (based on the blank) using ImageJ software before comparing the fluorescent intensities.

Results obtained are shown in Figure 4.12. We observed an increase in the fluorescent intensity in the device with EDC coupling reagent compared to the negative control (Figure 4.12 A and Figure 4.12 B) which indicates that the EDC coupling reaction can be successfully performed on the 7-bed device surface.

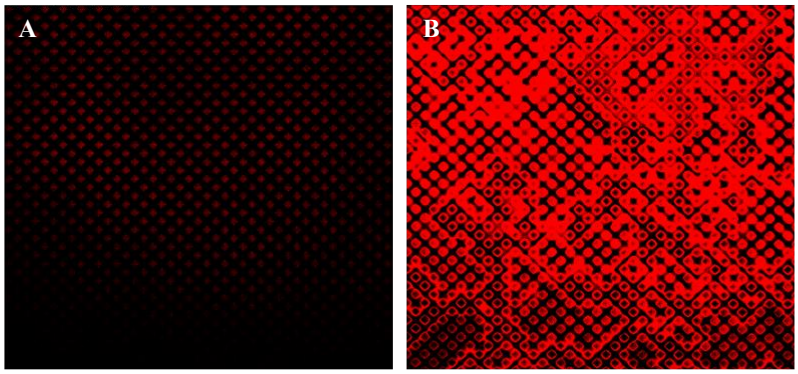

Figure 4.12: Surface modification test for 7-bed device with Fluorescently tagged oligo nucleotide; Background subtracted fluorescent images processed via ImageJ software (A) Negative control without EDC. (B) With EDC coupling reagents.

4.3.10 Analyzing clinical samples with the 7-bed device

For the initial studies we received 10 clinical samples (5 ischemic stroke patient samples and 5 healthy controls) from SUNY Downstate Medical center. (Information on the clinical samples are shown in Appendix 4). We performed a blinded study for these 10 samples. EVs were isolated using the 7-bed devices which were surface modified with CD8 mAb. After processing samples RNA was extracted from isolated EVs. For randomly selected 4 samples, NTA and TEM analysis were performed. Figure 4.13 below shows the TEM images of EVs isolated from clinical samples. Based on the TEM results no size difference in EVs was observed in these four samples.

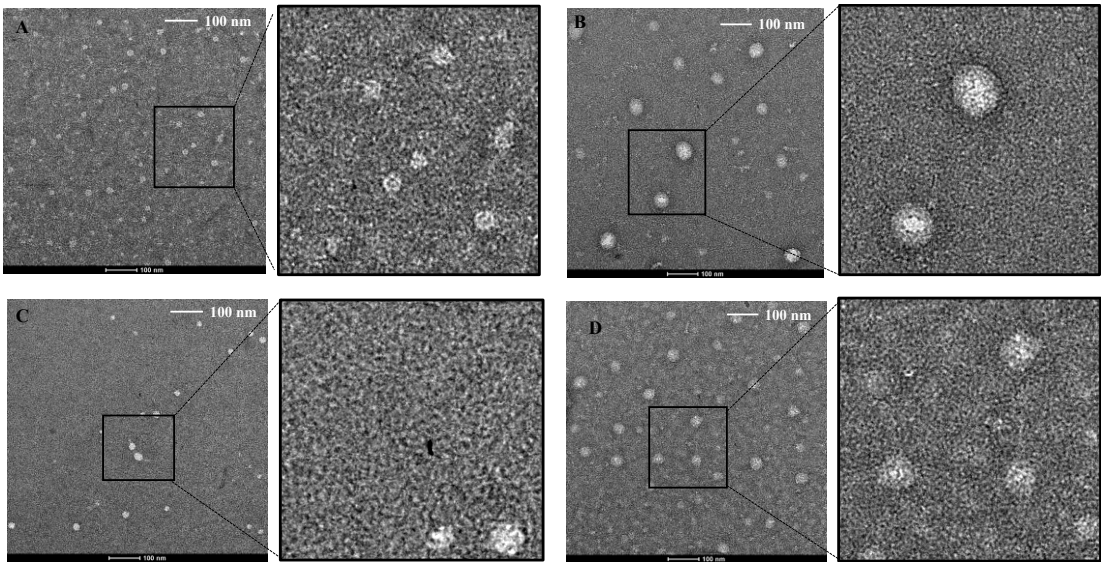

Figure 4.13: TEM images of clinical samples (A) Sample 1 (B) Sample 4 (C) Sample 6 (D) Sample 8.

4.3.11 NTA analysis of clinical samples

To quantify the number of EVs in each sample NTA was performed and the results obtained are shown in Figure 4.14. In a recent study performed by Yvonne Couch *et.al*, they showed that the EV number, but not size is significantly increased in acute stroke patients when compared to age-matched controls (n=38, $p<0.05$).[18] Figure 4.14 below shows the results they observed from NTA.

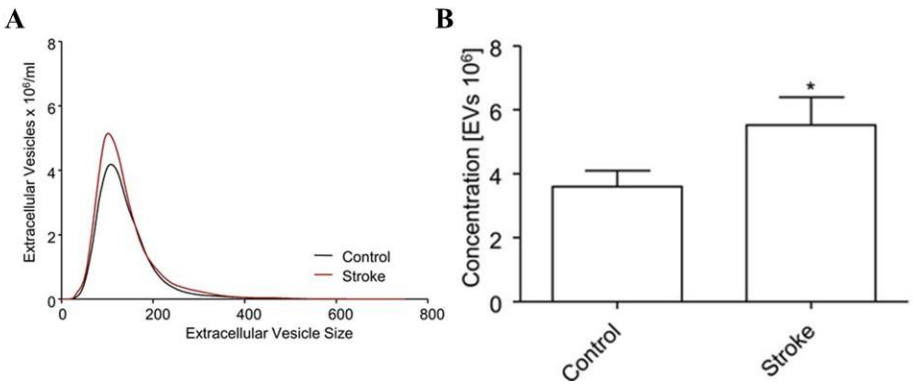

Figure 4.14: (A) Average distribution of vesicle size and number in the sera of stroke patients <24 h post stroke compared to age-matched controls (Detected by NTA). (B) NTA revealed an increase in number of vesicles per milliliter (Reproduced from reference 18).

According to NTA results, sample 4 and 6 showed higher number of particles compared to other two samples. EV numbers in sample 4 and 6 were 50.8 x 10^9 particles/mL and 17.1 x 10^9 particles/mL respectively and sample 1 and 8 contained 5.41 x 10^9 particles/mL and 4.35 x 10^9 particles/mL respectively (Figure 4.15). Thus, sample 4 and 6 may be stroke patient samples. The average sizes observed were 281.4 nm, 157.7 nm, 151.1 nm and 200.9 nm for samples 1,4,6 and 8 respectively. Moreover, if we consider the EV numbers we released from 3-bed device (2.94 ± 0.48) x10^9 particles/mL), more EVs can be isolated using the 7-bed device.

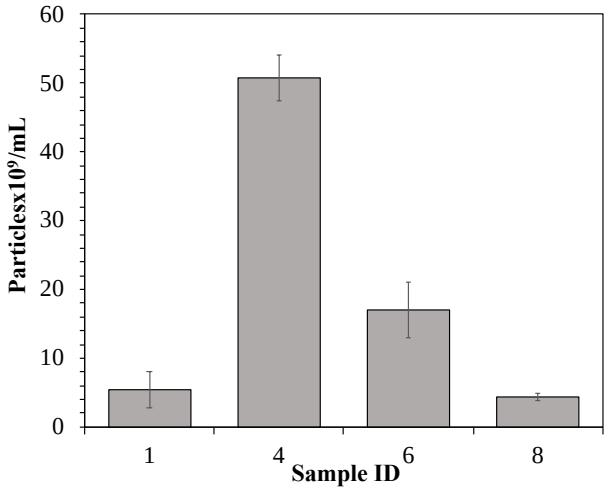

Figure 4.15: Number of EVs detected from NTA for clinical samples 1,4,6 and 8. (EVs were affinity selected by CD8 mAb and released with the USER enzyme).

4.3.12 PEG precipitation vs. affinity selection

PEG precipitation is a currently used method for EV isolation. However, inability to isolate specific type of EVs is a major disadvantage of PEG precipitation over affinity-based isolation of EVs using microfluidic devices. In order to compare EVs isolated by PEG and affinity based microfluidic device, sample 4 was selected and PEG precipitation and affinity selection were performed. Isolated EVs were analyzed via TEM and the results obtained are shown in Figure 4.16.

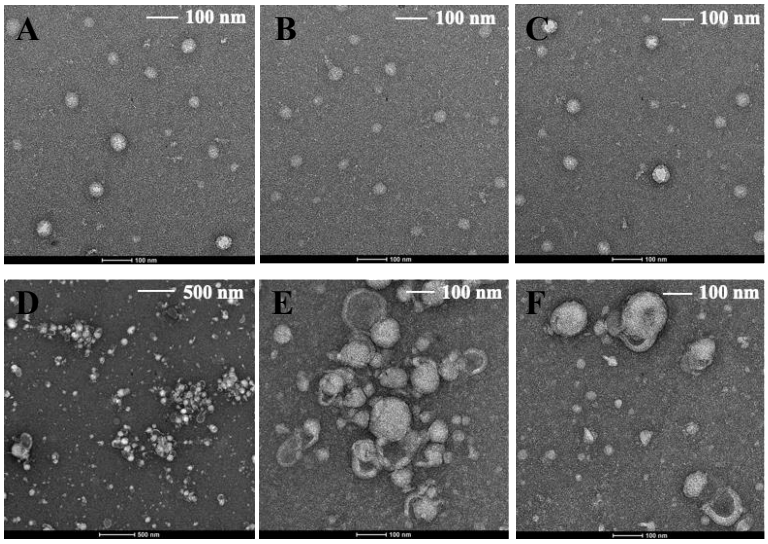

Figure 4.16: TEM images of EVs isolated from (A), (B) and (C) Microfluidic device via affinity selection; (D), (E) and (F) via PEG precipitation.

TEM results show the difference between the EVs that have been isolated from two methods. PEG precipitation showed a wide size range of EVs in the images. But EVs that isolated from affinity selection showed a narrow size range. NTA analysis of the EVs isolated from these two methods also supported this fact. As shown on Figure 4.16 A, for PEG EVs we can see a wide size distribution with an average EV size of 230.4 ± 109.8 nm, while for affinity selected EVs a homogeneous size distribution was observed with an average size of 157.8 ± 10.3 nm.

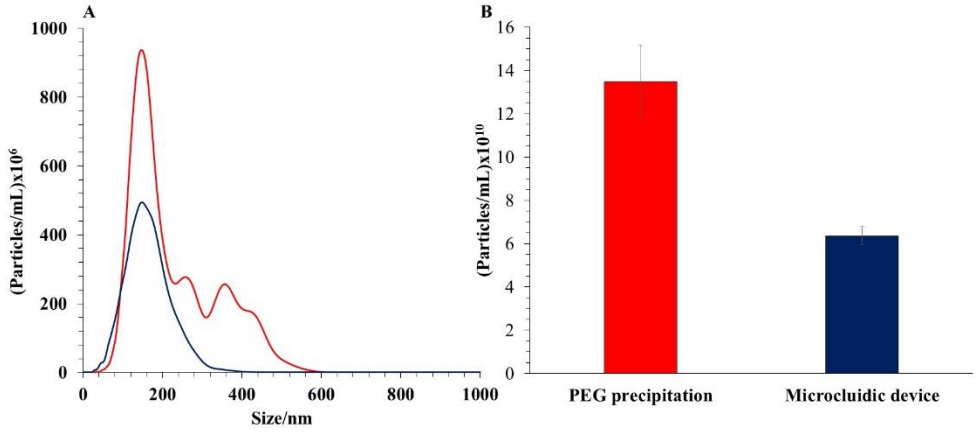

Figure 4.17: NTA results showing the different size distribution of EV isolated from: (A) Red trace- PEG precipitation, Blue trace- Affinity selection (B) Number of EVs isolated from Red trace- PEG precipitation, Blue trace- Affinity selection.

Total number of EVs isolated from PEG precipitation was (13.5 ± 1.7) x10^{10} particles/mL while from affinity selection (5.08 ± 0.4) x10^{10} as shown in Figure 4.16 B. Higher number of EVs isolated from PEG precipitation is due to non-specificity of PEG precipitation compared to the affinity-based isolation of EVs. PEG will precipitate all types of EVs present in plasma samples while affinity isolation only selects a sub population of EVs (In this study only CD8 EVs will be isolated). Furthermore, PEG precipitation yielded more TRNA than anti-CD8 microfluidic enrichment.

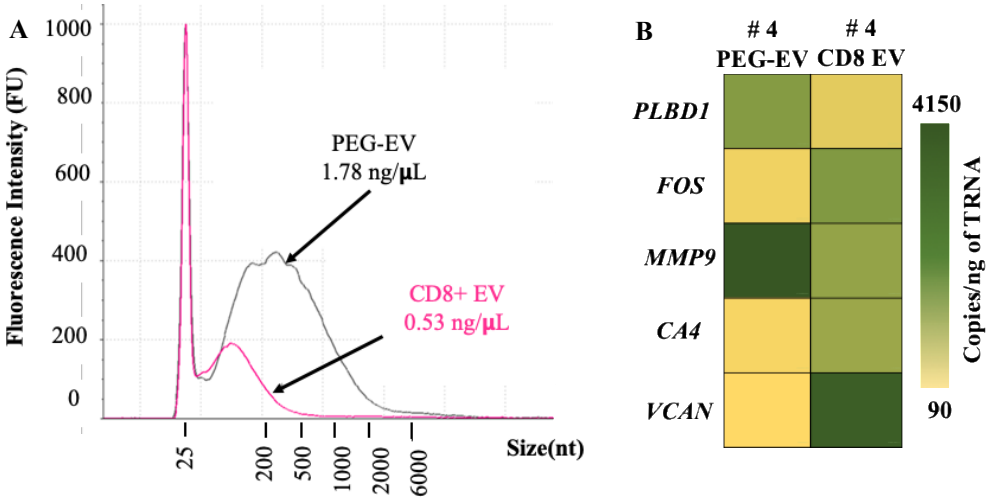

Figure 4.18: (A) RNA profiles of EV isolated from PEG precipitation and affinity selection. (B) Heat map showing the gene expression of EVs isolated from PEG precipitation and affinity selection.

RNA extracted from both methods were reverse transcribed and then analyzed via droplet digital PCR for gene expression analysis and the results are shown in Figure 4.17 B. Gene expression profiling of RNA extracted from these two methods were different from each other. The combination of wider EV size distributions, heterogenous EV morphology, and different mRNA profiles for PEG precipitation bolsters the premise of microfluidic affinity-enrichment, which targets a unique EV subpopulation rather than an ensemble average of all EVs in plasma. This is particularly critical for AIS diagnosis as the mRNA profiles outlined by Adamski, *et al.* are unique to specific leukocyte subpopulations (i.e., CD8 T-cells).[19]

4.3.13 Gene expression profiling of clinical samples

The foremost purpose of developing the affinity based microfluidic device for isolating CD8+ EVs from plasma is to analyze the EV mRNA as a biomarker for ischemic stroke diagnosis. Thus, the RNA extracted from 10 clinical samples were analyzed via droplet digital PCR after reverse transcription of RNA to cDNA.

For evaluating gene expression for diagnosing AIS, we selected gene cluster "4" identified by Adamski, *et. al*, which consisted of 5 genes: *FOS*, *VCAN*, *PLBD1*, *MMP9*, and *CA4*. This gene panel showed statistically significant difference ($p = 1.42 \times 10^{-5}$) between AIS patients and control samples. Figure 4.19 shows the heat map created for gene expression for the 10 clinical samples that we analyzed in this study.

But only based on this heat map, it's hard to identify the stroke patient samples. Statistical analysis was then performed to differentiate the stroke patient samples from healthy controls.

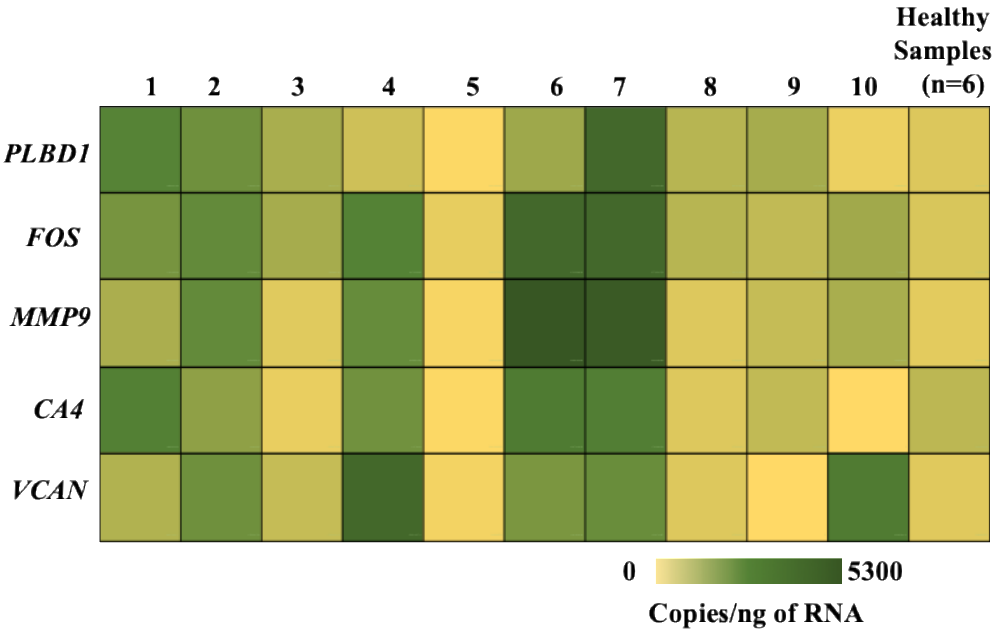

Figure 4.19: Heat map showing the gene expression of 10 clinical samples and average of the healthy donor plasma samples.

4.3.14 Statistical analysis

Principle Component Analysis (PCA) was used to differentiate the stroke patient samples from healthy controls. PCA is a statistical method that is used to summarize the information in a data set described by multiple variables. PCA is mainly performed to identify the hidden pattern in a data set, to reduce the dimensionality of the data set and to identify the correlated variables. PCA reduces the dimensionality of data with a large set of variations which is achieved by transforming the original data set into a new small set of variables without losing the most important information in the original data set and these new variables are called as principle components.[20] When PCA results is represented graphically, if there's correlation between the data sets those data points would be grouped together in the plot while the data points with less correlation will be grouped away. R studio software was used in this study for statistical data analysis. Figure 4.20 shows the results of the statistical analysis we performed on the clinical samples. All clinical samples together with 6 known healthy controls were analyzed together.

Based on the PCA results, samples grouped with known healthy donors were categorized as healthy controls, and samples grouped away from healthy samples were classified as AIS patient samples. Hence, samples 1, 3, 5, 8 and 9 identified as healthy, while 2, 4, 6, 7, and 10 were identified as AIS.

These results showed 80% success in correctly identifying patient status, where samples number 7 and 8 were misidentified. While these obtained results are promising, a larger pool of samples clearly must be analyzed to obtain clinical sensitivity and specificity for this assay. By analyzing more stroke patient samples and more gene panels based on CD 15 neutrophils more accurate results could be obtained from this assay. But as an initial study we were successful in developing a point-of-care test which only need few mililiters of blood to accurately identify ischemic stroke patients based on gene expression of EVs. Since, currently there is no molecular diagnostic test for ischemic stroke our method would be well suited to be utilized in clinical setup

that provide results quickly, within a short time window for effective treatment of ischemic stroke.

Sample size required in this diagnostic test was analyzed by Dr. Alision Baird at SUNY Downstate medical Center at New York. Based on their studies, the required sample size for the stroke and controls groups for detecting an effect of 0.07 with 95% confidence and 80% power for an AUC of 0.80 is 199 subjects.[21] Thus, by analyzing more samples we can increase the accuracy of this assay.

4.2.15 Assay modification

Analysis time for all the steps involved in the assay was ~3h, including plasma preparation, EV affinity-enrichment, mRNA extraction, RT, and preparation and execution of ddPCR. This timeline is shorter than the 4.5 h therapeutic window and could allow for rtPA administration to the patient and ultimately improving patient recovery after AIS. However, we started to look at modifications to reduce the total assay time. Modifications that we're suggesting for reducing the assay time will be discussed in detail the future directions section (Chapter 5).

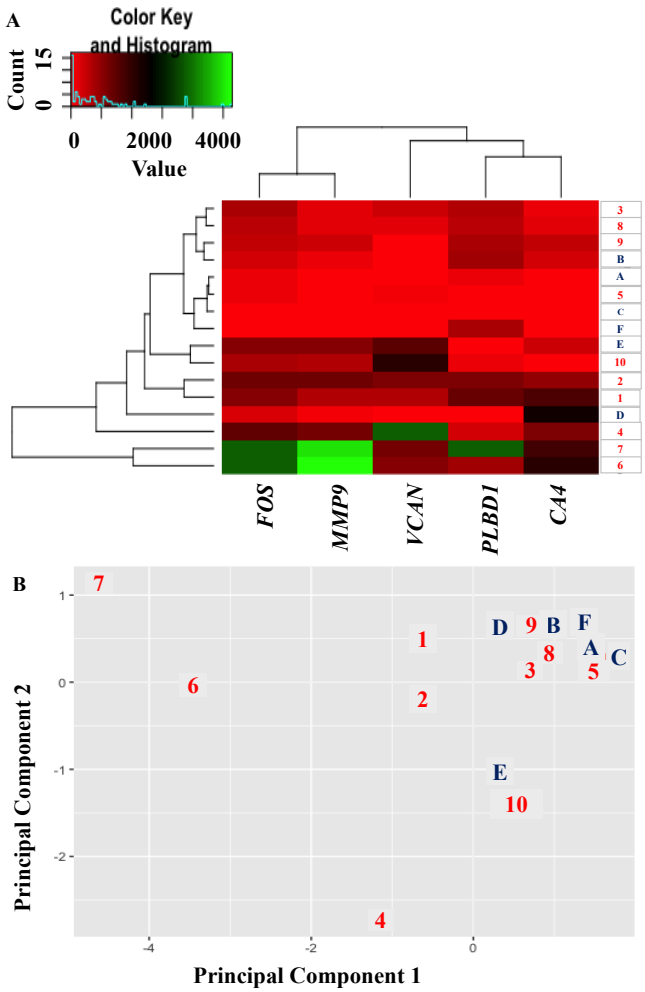

Figure 4.20: (A) Heat map analalysis of clinical samples (marked with numbers) and healthy donors (identified with letters). (B) principal component analysis for clinical samples (identified with numbers) and healthy donors (identified with letters).

4.4 Conclusions

EVs from clinical plasma samples were affinity isolated on an CD8 mAb modified surface of a 7-bed device owing to the high capacity of the bed and ability to provide high sample processing speed. The NTA results show much wider size range of PEG precipitated EVs when compared with affinity selected EVs. The amount of isolated TRNA was 4.5 ng and 15.1 ng for CD8 EV and PEG isolated EVs, respectively. The mRNA profiles obtained from CD8 EV

showed gene expression that is unique to the CD8 T-cell population, which according to Adamski, et al. is the subpopulation of leukocytes representing gene expression profile informative of AIS event.

The healthy samples previously analyzed were used as a control sample to differentiate between the stroke and healthy samples from clinical cohort. Normalized to ng RNA results from ddPCR were used to generate heat maps of gene copy number. Based on PCA, samples that are grouped together with the known healthy donor samples were categorized as healthy controls and the samples that are grouped away from the healthy samples were identified as ischemic stroke patient samples. Healthy controls were identified as sample# 1, 3, 5, 8 and 9 while sample # 2,4,6,7, and 10 were identified as coming from stroke patients. We were able to identify 80% samples correctly. Sample #7 and #8 were misidentified. It is clear that larger pool of samples must be analyzed; however, obtained results are very promising.

4.5 References

1. Nunes, P. S.; Ohlsson, P. D.; Ordeig, O.; Kutter, J. P., Cyclic olefin polymers: emerging materials for lab-on-a-chip applications. *Microfluidics and nanofluidics* **2010,** *9* (2-3), 145-161.
2. Jackson, J. M.; Witek, M. A.; Hupert, M. L.; Brady, C.; Pullagurla, S.; Kamande, J.; Aufforth, R. D.; Tignanelli, C. J.; Torphy, R. J.; Yeh, J. J., UV activation of polymeric high aspect ratio microstructures: ramifications in antibody surface loading for circulating tumor cell selection. *Lab on a Chip* **2014,** *14* (1), 106-117.
3. Cui, J.; Yang, J.-X.; Li, Y.-G.; Li, Y.-S., Synthesis of high performance cyclic olefin polymers (COPs) with ester group via ring-opening metathesis polymerization. *Polymers* **2015,** *7* (8), 1389-1409.
4. Jena, R. K.; Yue, C. Y., Cyclic olefin copolymer based microfluidic devices for biochip applications: Ultraviolet surface grafting using 2-methacryloyloxyethyl phosphorylcholine. *Biomicrofluidics* **2012,** *6* (1), 012822.
5. Shin, J. Y.; Park, J. Y.; Liu, C.; He, J.; Kim, S. C., Chemical structure and physical properties of cyclic olefin copolymers (IUPAC technical report). *Pure and Applied Chemistry* **2005,** *77* (5), 801-814.
6. Appasamy, S.; Li, W.; Lee, S. H.; Boyd, J. T.; Ahn, C. H., High-throughput plastic microlenses fabricated using microinjection molding techniques. *Optical Engineering* **2005,** *44* (12), 123401.
7. Stachowiak, T. B.; Mair, D. A.; Holden, T. G.; Lee, L. J.; Svec, F.; Fréchet, J. M., Hydrophilic surface modification of cyclic olefin copolymer microfluidic chips using sequential photografting. *Journal of separation science* **2007,** *30* (7), 1088-1093.
8. Nikolova, D.; Dayss, E.; Leps, G.; Wutzler, A., Surface modification of cycloolefinic copolymers for optimization of the adhesion to metals. *Surface and Interface Analysis: An International Journal devoted to the development and application of techniques for the analysis of surfaces, interfaces and thin films* **2004,** *36* (8), 689-693.
9. Hwang, S.-J.; Tseng, M.-C.; Shu, J.-R.; Yu, H. H., Surface modification of cyclic olefin copolymer substrate by oxygen plasma treatment. *Surface and Coatings Technology* **2008,** *202* (15), 3669-3674.
10. Tsao, C.; Hromada, L.; Liu, J.; Kumar, P.; DeVoe, D., Low temperature bonding of PMMA and COC microfluidic substrates using UV/ozone surface treatment. *Lab on a Chip* **2007,** *7* (4), 499-505.
11. Zhang, J.; Das, C.; Fan, Z. H., Dynamic coating for protein separation in cyclic olefin copolymer microfluidic devices. *Microfluidics and Nanofluidics* **2008,** *5* (3), 327-335.
12. Wang, Y.; Bachman, M.; Sims, C. E.; Li, G.; Allbritton, N. L., Simple photografting method to chemically modify and micropattern the surface of SU-8 photoresist. *Langmuir* **2006,** *22* (6), 2719-2725.
13. Uchida, E.; Uyama, Y.; Ikada, Y., Sorption of low-molecular-weight anions into thin polycation layers grafted onto a film. *Langmuir* **1993,** *9* (4), 1121-1124.
14. Wei, S.; Vaidya, B.; Patel, A. B.; Soper, S. A.; McCarley, R. L., Photochemically patterned poly (methyl methacrylate) surfaces used in the fabrication of microanalytical devices. *The Journal of Physical Chemistry B* **2005,** *109* (35), 16988-16996.
15. Wochnowski, C.; Eldin, M. S.; Metev, S., UV-laser-assisted degradation of poly (methyl methacrylate). *Polymer degradation and stability* **2005,** *89* (2), 252-264.
16. Zhang, P.; Zhou, X.; He, M.; Shang, Y.; Tetlow, A. L.; Godwin, A. K.; Zeng, Y., Ultrasensitive detection of circulating exosomes with a 3D-nanopatterned microfluidic chip. *Nature Biomedical Engineering* **2019**, 1.

17. Rötting, O.; Röpke, W.; Becker, H.; Gärtner, C., Polymer microfabrication technologies. *Microsystem Technologies* **2002,** *8* (1), 32-36.
18. Couch, Y.; Akbar, N.; Davis, S.; Fischer, R.; Dickens, A. M.; Neuhaus, A. A.; Burgess, A. I.; Rothwell, P. M.; Buchan, A. M., Inflammatory stroke extracellular vesicles induce macrophage activation. *Stroke* **2017,** *48* (8), 2292-2296.
19. Adamski, M. G.; Li, Y.; Wagner, E.; Seales-Bailey, C.; Bennett, N.; Yu, H.; Murphy, M.; Soper, S. A.; Baird, A. E., CD15+ granulocyte and CD8+ T lymphocyte based gene expression clusters for ischemic stroke detection. *Medical Research Archives* **2017,** *5* (11).
20. Shlens, J., A tutorial on principal component analysis. *arXiv preprint arXiv:1404.1100* **2014**.
21. Gardiner, C.; Shaw, M.; Hole, P.; Smith, J.; Tannetta, D.; Redman, C. W.; Sargent, I. L., Measurement of refractive index by nanoparticle tracking analysis reveals heterogeneity in extracellular vesicles. *Journal of extracellular vesicles* **2014,** *3* (1), 25361.

Chapter 5: Summary and future directions

5.1 Summary

Liquid biopsies are generating a significant amount of interest in the medical and biological communities due to the minimally invasive nature of acquiring these biomarkers and the fact that they can enable precision decisions on managing a variety of diseases, including the oncology and non-oncology-related diseases.[1-2] EV isolation from plasma and gene expression analysis represents a novel idea for the development of a diagnostic test for AIS. The microfluidic platform presented here could serve as an attractive tool to assist in developing such a diagnostic test for AIS in a point-of-care format due to the fact that it has the capacity to isolate the disease-associated EVs in a short time period to allow for subsequent expression profiling of their mRNA cargo. The assay based on mRNA expression profiling offers benefits of shorter latency time than for proteins. Therefore, AIS can be detected shortly after the stroke event allowing for more patients to receive therapy, including tissue plasminogen activator therapy.

We successfully developed a microfluidic device that is capable of affinity selecting CD8+ EVs and efficiently releasing the EVs for downstream applications. Our results indicated that there are similarities in expression profiles between cells and the EVs they produce. Compared to PEG precipitation isolation methods of EVs, our methodology is more advantageous because the affinity selected CD8+ EVs represent the population of interest and molecular data are not obscured by mRNA from background EVs. Isolation of all EVs using ultracentrifugation for applications where molecular analysis is a part of the diagnostic assay, (i.e., profiling of EVs mRNA) can be compromised as the abundance of background EVs in plasma can confound detection of the targets of interest.

The mRNA extracted from the isolated CD8+ EVs was successfully used in molecular profiling via ddPCR in which 5 genes were used aiding in the development of the diagnostic assay for AIS. In the future, we will introduce a larger gene panel in the testing as identified

by Adamski *et al.* Also, to improve test positivity (*i.e.*, clinical sensitivity) analysis of CD15+ EVs released by CD15+ neutrophils will be performed following gene expression as these granulocytes were also identified to be another major source of markers in response to AIS.[3] Presented data illustrate the advantages of affinity selection of the desired EVs by targeting specific antigens, such as CD8 on their surface as opposed to general affinity selection targeting the tetraspanin protein family such as CD9, CD63, CD81 markers.

Technologies, such as microfluidics, that can isolate EVs employing affinity-purification methods hold promise of being adaptable to clinically relevant applications. Microfluidics offer the potential for high EV recovery at high throughput for a wide range of sample volumes (a few µL to several mL of plasma) with the additional benefit of automation and system integration.

On average $1.94x10^{10}$ particles/mL were detected following EV isolation and release from the microchip from stroke patients' plasma samples. An average size of the CD8+ EVs isolated was 157.8 ±10.3 nm. Gene expression analysis performed via droplet digital PCR revealed that for the selected gene panel (*PLBD1*, *MMP9*, *VCAN*, *FOS*, *CA4*), there was no difference in mRNA expression profiles between cells and the EVs they generate when both were isolated either from cell culture and medium, respectively, or blood and plasma of healthy donors, respectively.

In a blinded study performed for healthy and AIS patient samples, we correctly identified 80% stroke patient samples and healthy samples. Processing 100 µL of the plasma sample took 20 min for the high capacity 7-bed device while achieving a ~97% recovery when operated at 5 µL/min, but a 20 µL/min flow rate, while reducing recovery to around 80%, will reduce the processing time to 5 min for the enrichment step. Analysis time for all the steps involved in the assay was ~3 h. The assay consisted of plasma preparation, EV affinity isolation and release, mRNA extraction, RT, and preparation and execution of ddPCR. The assay time was shorter

than the 4.5 h effective therapeutic time window for recombinant tissue plasminogen activator administration to the patient and ultimately providing high chance of recovery.

To further refine our assay, in the future we envision normalization of the gene expression data to the EV count. For that to be accomplished, EVs can be isolated and released from the surface using mAb that is immobilized to the surface via a coumarin-based photocleavable linker enabling release of EVs within 2 min by exposing to LED light[4] and counted in a label-free fashion using an in-plane nanopore sensor. The coumarin-based photocleavable linker yielded ~90 % of release efficiency of EVs from 2 min LED light exposure with minimal perturbation on the mRNA EV cargo.

5.2 Future directions

Although results reported here are very encouraging, more extensive studies are needed with a larger cohort of patients' samples and healthy donors to clearly determine receiver operating characteristics for the assay using EV derived mRNA expression. With larger sample numbers clinical sensitivity and specificity of the assay can be determined with higher confidence.

Determining the time of appearance of EV mRNA markers in plasma samples following the stroke event is another important factor that still needs to be analyzed as well. For this purpose, an animal model (pre-clinical model) could be used, which will be performed in collaboration with Dr. Frank C. Barone at SUNY Downstate Medical Center at New York. Using mice as an animal model, and following middle cerebral artery occlusion or photochemically induced stroke (Photo thrombosis model), blood from mice can be withdrawn at different time points following event onset.[5-7] EVs could be isolated via the microfluidic device we developed and mRNA analysis performed to determine kinetics of the EVs release to the blood in reference to stroke event. We will specifically look at the volume of plasma required at each time point and perform mRNA expression profiling to determine mass requirements for the gene

expression profiling and if there is a latency time for marker appearance that is gene dependent, respectively.

In addition to these 5 gene panel used in this study there are many other genes in the CD8 cells/EVs that could be used to increase assay accuracy in detecting stroke patients.[3] Furthermore, CD15 granulocytes have also been found to be a major source of expression changes in ischemic stroke. In a study performed by Adamski *et al.,* they showed that 14 genes in CD 15 granulocytes were upregulated and a CD15 + granulocyte-derived 3 gene cluster consisting of *CA4*, *MMP9*, and *NAIP* showed high accuracy for ischemic stroke detection with AUC of 0.813 and was 100% sensitive in a validation cohort. Thus, use of a CD15+ gene panel together with the CD8+ gene panel used in this study could yield a highly sensitive and accurate assay for ischemic stroke detection. Additionally, this assay can be utilized to differentiation ischemic stroke from hemorrhagic stroke if the gene expression changes taking place during a hemorrhagic stroke is known.

Initial studies have been performed on developing a heterobifunctional 7-aminocoumarin photocleavable (PC) linker for immobilizing Abs to surfaces that enables biomarker release using visible light (400-450 nm) with in 2 min (Figure 5.1). By immobilizing the mAb through this linker we can release the captured EV and then analyze the EV mRNA for gene profiling. This will further reduce processing time associated with the assay. Currently, we are using out hetero-bifunctional linker, which releases EVs via an enzymatic reaction. The reduction of release time from 1 h to 2 min will further reduce assay processing time. Release of intact EVs and enumerating them will provide a simple method to normalize our mRNA expression data.

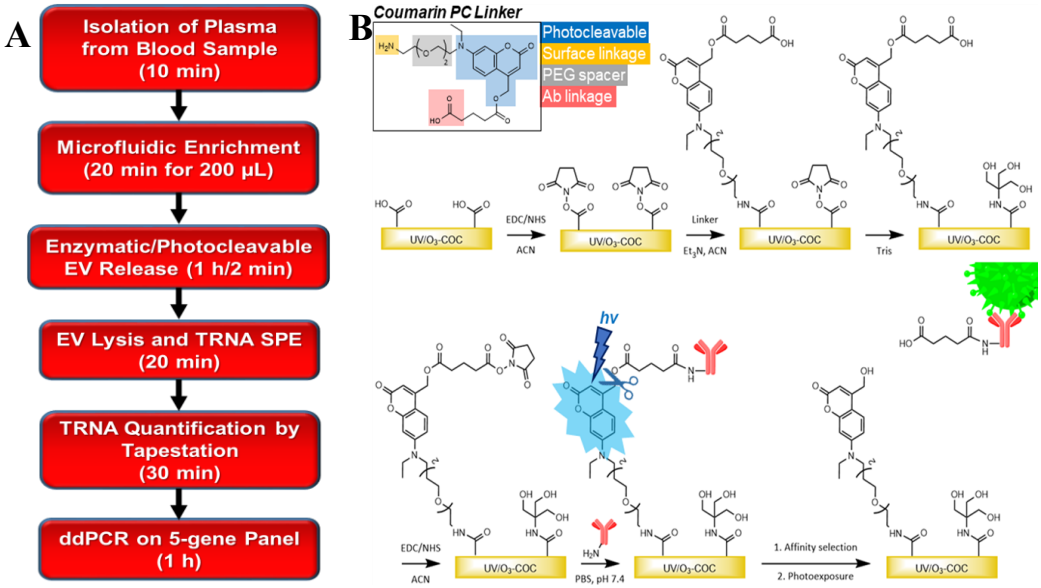

Figure 5.1: (a) Process flow chart showing the steps and time required for our EV mRNA expression profiling assay that uses a microfluidic for EV isolation and subsequent ddPCR quantification of the 5 genes used for AIS diagnostics. (b) Design and reaction scheme of the heterobifunctional, photocleavable (PC) linker. The linker's terminal primary amine attaches to COOH groups on UV/O3-activated COC devices via EDC/NHS coupling. Any remaining, free NHS esters are quenched with tris buffer. The PC linker's COOH group is then activated with EDC/NHS reagents for antibody coupling, yielding a covalent linkage of the affinity-selection Ab to the surface through the PC linker. After affinity selection, isolated biomarkers (EVs or CTCs) are released by exposing the linker to blue light (400-450 nm), thereby cleaving the coumarin derivative at the meta carbon via a carbocation intermediate. (Figure 5.1 B Courtesy of Thilanga Nandana)

Gene expression data normalized to the total EV count rather than normalizing to quantified TRNA would eliminate the need for the TRNA quantification step using gel electrophoresis performed by the Tapestation. The EV counting can be done online in conjunction with the EV release from the capture surface. For that to be accomplished, EVs must be released from the device with the EVs counted electrically with an integrated nanopore sensor,[8] which can also be mass produced at low cost in thermoplastic substrates and integrated directly to the

EV affinity enrichment microfluidic. This would reduce the total processing time by another 30 min, taking the estimated EV mRNA expression analysis to < 2 h.

Finally, we will also look to transitioning the ddPCR step to a fully integrated microfluidic-based assay (right now, only the droplets are generated using a microfluidic). Thus, all of the processing steps can be carried out on task-specific microfluidic chips that are integrated to a fluidic motherboard, which is shown in Figure 5.1. This will allow for fully automated sample preparation and measurement in a small form-factor instrument, potentially at the point-of-care as well.

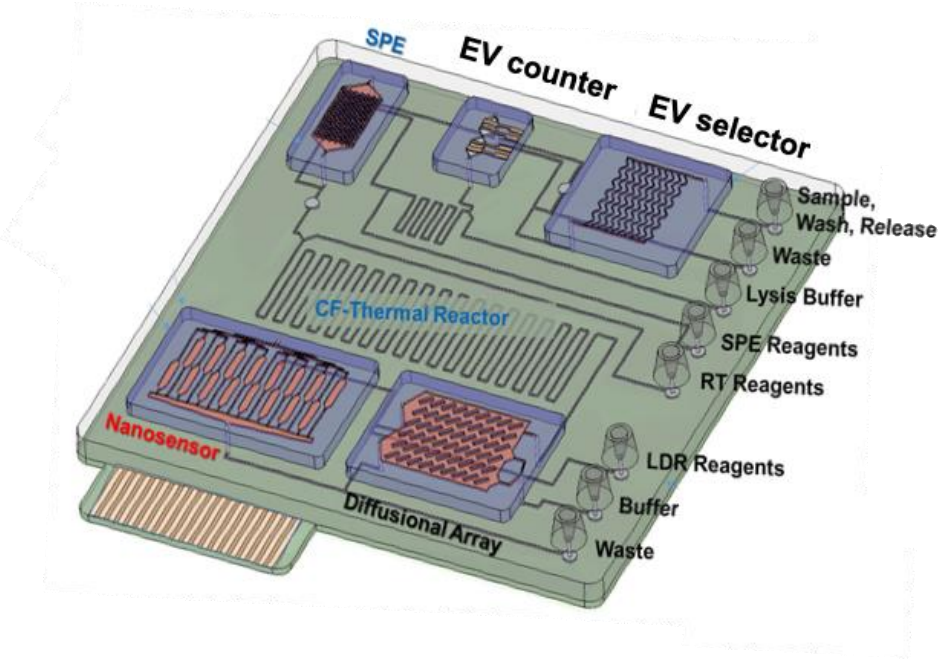

Figure 5.2: Integrated and modular microfluidic device developed for POCT.

5.3 References

1. Macias, M.; Alegre, E.; Diaz-Lagares, A.; Patino, A.; Perez-Gracia, J. L.; Sanmamed, M.; Lopez-Lopez, R.; Varo, N.; Gonzalez, A., Liquid biopsy: from basic research to clinical practice. In *Advances in clinical chemistry*, Elsevier: 2018; Vol. 83, pp 73-119.
2. Jeffrey, S. S.; Toner, M., Liquid biopsy: a perspective for probing blood for cancer. *Lab on a Chip* **2019,** *19* (4), 548-549.
3. Adamski, M. G.; Li, Y.; Wagner, E.; Seales-Bailey, C.; Bennett, N.; Yu, H.; Murphy, M.; Soper, S. A.; Baird, A. E., CD15+ granulocyte and CD8+ T lymphocyte based gene expression clusters for ischemic stroke detection. *Medical Research Archives* **2017,** *5* (11).

4. Thilanga N. Pahattuge, J. M. J., Digamber Rane,Harshani Wijerathne,Virginia Brown, Chamani Perera,Richard S. Givens,Blake R. Peterson,and Steven A. Soper, Photocleavable Linker for the Release of Rare Liquid Biopsy Biomarkers after Microfluidic Affinity Enrichment. *Angewandte Chemie (To be submitted)* **2019**, .
5. Chiang, T.; Messing, R. O.; Chou, W.-H., Mouse model of middle cerebral artery occlusion. *JoVE (Journal of Visualized Experiments)* **2011,** (48), e2761.
6. Ansari, S.; Azari, H.; McConnell, D. J.; Afzal, A.; Mocco, J., Intraluminal middle cerebral artery occlusion (MCAO) model for ischemic stroke with laser doppler flowmetry guidance in mice. *JoVE (Journal of Visualized Experiments)* **2011,** (51), e2879.
7. Labat-gest, V.; Tomasi, S., Photothrombotic ischemia: a minimally invasive and reproducible photochemical cortical lesion model for mouse stroke studies. *JoVE (Journal of Visualized Experiments)* **2013,** (76), e50370.
8. Vogel, R.; Coumans, F. A.; Maltesen, R. G.; Böing, A. N.; Bonnington, K. E.; Broekman, M. L.; Broom, M. F.; Buzás, E. I.; Christiansen, G.; Hajji, N., A standardized method to determine the concentration of extracellular vesicles using tunable resistive pulse sensing. *Journal of extracellular vesicles* **2016,** *5* (1), 31242.

Appendix 1: Bfd, a New Class of [2Fe-2S] Protein That Functions in Bacterial Iron Homeostasis, Requires a Structural Anion Binding Site

1.1 Introduction

Iron sulfur clusters are versatile prosthetic groups present in a wide range of proteins and enzymes ubiquitous in all kingdoms of life. These proteins support many important physiological functions including respiration, photosynthesis, DNA repair, and gene regulation.[1-2] The most common type of iron sulfur cluster are [2Fe-2S], [3Fe-4S] and [4Fe-4S], where Fe ions are coordinated to different protein ligands that are connected to one another by bridging sulfide ions.[3-4] Among these, [2Fe-2S] clusters consist of two iron atoms, which are coordinated in a distorted tetrahedral geometry by two inorganic sulfurs and four ligands from the protein. These ligands can be cysteine thiolates or a combination of cysteines and histidines.[5] The [2Fe-2S] cluster are further classified into four main groups as shown in Table 6.1 based on the amino acid sequences, structural alignments and position of the iron coordinating ligands in the protein sequence.[5-10] The four subgroups of [2Fe-2S] proteins are plant-, vertebrate-, and bacterial-ferredoxins, the [2Fe-2S] thioredoxin-like ferredoxins, the [2Fe-2S] Rieske proteins, and the more recently discovered [2Fe-2S] NEET proteins.

The main functions of plant-type ferredoxins are photosynthesis by shuttling electrons between photosystem I and several enzymes. The bacterial and vertebrate [2Fe-2S] clusters function by transferring electrons to hydroxylating enzymes.

Table 1.1: Classes of [2Fe-2S] Proteins

[2Fe-2S]-protein class	**Protein provided lig-**	**Ligand arrangement**
Plant/vertebrate ferredoxin	4Cys	C-X_{4-5}-C-X_2-C-X_{30-37}-C
Thioredoxin-like ferredoxin	4Cys	C-X_{10-12}-C-X_{29-34}-C-X_3-C
Rieske centers	2Cys and 2His	C-X-H-X_{15-17}-C-X_2-H
NEET proteins	3Cys and 1His	C-X-C-X_2-(S/T)-X_3-P-X-CDG-
Bfd	4 Cys	C-X_2-C-X_{31-32}-C-X_2-C

The thioredoxin-like [2Fe-2S] proteins have been observed mostly in nitrogen fixing bacteria, and they mainly are involved in nitrogen metabolism. The [2Fe-2S] Rieske proteins function as subunits of photosynthetic and respiratory electron transfer complexes, as well as subunits or domains in water soluble oxidases. The [2Fe-2S] NEET proteins function in cluster transfer to other proteins and as regulators of iron and ROS homeostasis.[10]

Figure 1.1 A shows a spinach ferredoxin (PDB 1A70). Plant and vertebrate [2Fe-2S] ferredoxins have a common β-grasp fold, where a four stranded β-sheet is covered by an α-helix. Here, the [2Fe-2S] cluster is located near the surface coordinated by 4 Cys ligands arranged in a conserved sequence motif (see Table 1.1).[6-7] In thioredoxin-like ferredoxins the [2Fe-2S] cluster located between two loop regions as shown in Figure 1.1 B where the cluster is coordinated by four Cys ligands arranged in a conserved motif.

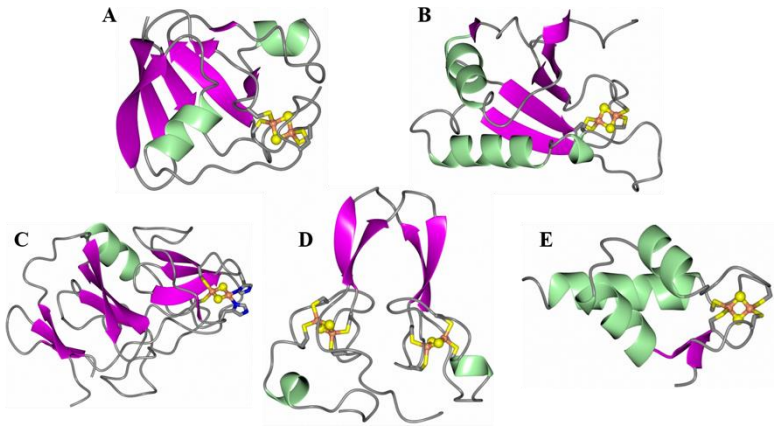

Figure 1.1: Crystal structures of **A**) spinach ferredoxin (PDB 1A70), **B**) thioredoxin-like ferredoxin from *Aquifex aeolicus* (PDB 1F37), **C**) Rieske protein from *Rhodobacter sphaeroides* (PDB 2NVE), **D**) Human mitochondrial inner NEET protein MiNT (PDB 6AVJ), and **E**) Bfd from the complex with BfrB (PDB 4E6K). The structures are colored by secondary structure showing the α-helices (green) and β-sheets (magenta). The 2Fe-2S atoms are rendered as spheres (Fe-coral and S-yellow) and coordinating residues are drawn as cylinders. (Reproduced with permission from reference Wijerathne et al)

The [2Fe-2S] Rieske proteins have a highly conserved fold as shown in Figure 1.1 C. In these proteins [2Fe-2S] cluster is held between two loops, which are coordinated by 2Cys and 2 His ligands arranged in a conserved sequence as shown in Table 1.1. In NEET proteins, there's a fold that consists of four-stranded β-cap residing above a structured loop and a turn of a helix. This helix harbors the [2Fe-2S] cluster and here the iron ions are coordinated by 3Cys and 1His ligands as shown in Figure 1.1D.

In 1989 Andrews *et al*. discovered the presence of a hypothetical 64-residue protein located upstream of *bfr* gene in *E. coli* K-12.[11] This small gene predicted a protein with four Cys residues arranged in a C-X-C-X_{32}-C-X_2-C motif, which is similar to the arrangement of Cys ligands in NifU in *Azinetobacter vinelandii* that binds the [2Fe-2S] cluster.[12]

This gene, which is called *bfd*, was cloned and then overexpressed. The resulted monomeric protein (Bfd) consisted of a [2Fe-2S] cluster that is capable of managing two oxidation states $[2Fe\text{-}2S]^{2+/+1}$.[12-13] Based on the results from affinity chromatography, it has been shown

that Bfd binds to bacterioferritin (Bfr). This result suggested that Bfd may function either as electron acceptor for the oxidation of Fe^{2+} and subsequent storage of Fe^{3+} in Bfr, or as electron donor to Fe^{3+} stored in Bfr for subsequent mobilization of Fe^{2+}.[12] Considering all these results a new function for [2Fe-2S] was appointed, namely electron transfer in bacterial iron metabolism.

We investigated this issue in the opportunistic pathogen *Pseudomonas aeruginosa* by capitalizing from the previously reported genetic response of *P. aeruginosa* to iron limiting conditions.[14] Although there are 118 genes that are upregulated during iron starvation only two of them code for electron transfer protein namely *bfd* and *fpr* (ferredoxin NADP reductase). We suggested that Bfd and Fpr function in the mobilization of Fe^{3+} stored in bacterioferritin B (BfrB) and proposed the model schematically illustrated in Figure 1.2, where electrons from Fpr are shuttled to the Fe^{3+} core in BfrB to promote the mobilization of Fe^{2+}.[15]

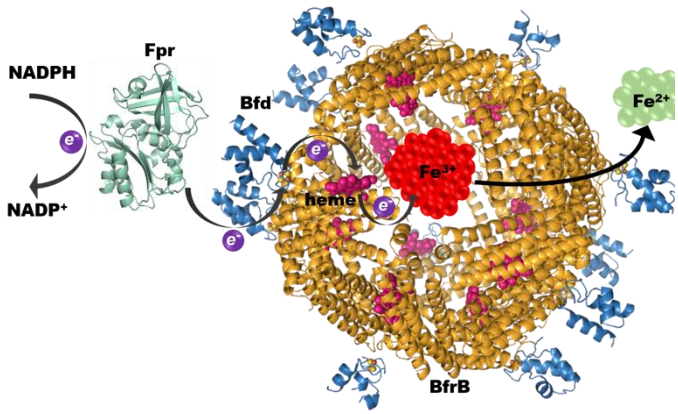

Figure 1.2: Schematic representation of the model for iron mobilization from BfrB, where electrons originating in NADPH are delivered to the Fe^{3+} mineral in the core of BfrB. (Reproduced with permission from Wijerathne et .al)

Furthermore, the *bfd*, *bfrB* and *fpr* genes from *P. aeruginosa* were cloned and the recombinant proteins characterized [16-17] and it was demonstrated that the [2Fe-2S] cluster of Bfd is required to deliver electrons to the heme in BfrB, which in turn relays the electrons to the Fe^{3+} mineral in the bacterioferritin core, as shown in Figure 1.2.[15, 18-19] Thus, this evidence corroborates the participation of a [2Fe-2S] Bfd protein in bacterial iron metabolism.

Due to the relatively small size of Bfd, which is approximately 40 residues shorter than other structurally characterized [2Fe-2S] proteins, and the unique arrangement of its Cys ligands as shown on Table 1.1, the Bfd structure may exhibit a fold distinct from those of known [2Fe-2S] proteins. In agreement with these expectations, the first example of a Bfd structure, which was obtained in complex with BfrB,[15] revealed a different helix-turn-helix fold which is shown in Figure 1.1E. In fact, the Bfd fold revealed in the structure of the Bfd:BfrB complex had not been previously observed in a single domain protein, although close matches had been observed in portions of domains incorporated into proteins and enzymes with diverse function belonging to the Fer2_Bfd Pfam family (PF04324).[19]

Based on the information obtained from the BfrB:Bfd complex interface, evidence showed that the key residues from each protein participating at the protein-protein interface are conserved in Bfd and Bfr proteins from a number of pathogenic bacteria. These observations suggested that the protein-protein interaction is likely conserved in many pathogenic bacteria.[18-19]

Additionally, the structural information at the protein-protein interface was also used to identify the hot spot residues responsible for the stability of the BfrB-Bfd protein complex. Using this information, we also demonstrated that a double mutation in BfrB (L68A/E81A) is sufficient to block the BfrB:Bfd interaction and inhibit iron mobilization from BfrB.[20]
Based on results from *in vitro* experiments, it was shown that BfrB to be the main iron storage protein in *P. aeruginosa* cells. It was also demonstrated that Bfd is essential for the mobilization of iron from BfrB in the bacterial cytosol.

Whenever Bfd is absent or when the BfrB:Bfd interaction is blocked, iron will be irreversibly accumulated in BfrB, resulting iron deficiency in the *P. aeruginosa* cytosol.[21] All these findings together strongly agreed with the fact that electron transfer from Bfd to be the only

mechanism in *P. aeruginosa* that enables mobilization of iron stored in BfrB. Thus, Bfd plays a major role for Bfd in bacterial iron homeostasis.

Although Bfd protein plays a key role in bacterial iron metabolism, the structural information of this novel protein is still not studied completely. For example, studies performed on the 3 Bfd molecules in the asymmetric unit of the BfrB:Bfd complex led to the hypothesis that the stability of the Bfd protein and associated [2Fe-2S] cluster is dependent on the coordination of a phosphate ion by three positively charged residues R26, R29 and K46.

Moreover, the studies performed on BfrB:Bfd structure revealed that small rearrangements are taking place in BfrB upon binding to Bfd. However, it is not known whether Bfd also undergoes any special structural changes upon binding, in order to enable the electron transfer between its [2Fe-2S] cluster and heme in BfrB.

In this study, we investigated the Bfd fold using site-directed mutagenesis, X-ray crystallography, and biochemistry in solution BfrB:Bfd complex, which will help to understand the important structural changes in Bfd that might help for the electron transfer between its [2Fe-2S] cluster and heme in BfrB.

1.2 Conclusions and future directions

We showed that the structure of Bfd is nearly identical to that in the BfrB:Bfd complex. These results revealed that Bfd does not undergo structural reorganization upon binding to BfrB.

We also showed that the stability of Bfd and it's [2Fe-2S] cluster is influenced by a conserved anion binding site. In the absence of an anion or at low ionic strengths Bfd loses its [2Fe-2S] cluster and starts to unfold. Site-directed mutagenesis and X-ray crystallography were also utilized to show the influence of the anion binding site on the structural stability of Bfd.

These mutant proteins are structurally nearly identical to Bfd, but where the stabilizing interactions conferred by anion binding are replaced by intramolecular hydrogen bonding and packing interactions.

In this study we showed that the stability of *P. aeruginosa* Bfd and the integrity of its [2Fe-2S] cluster depends on an anion binding site composed of the side chains of Arg26, Arg29, and Lys46, whose function is most likely to stabilize the two-turn helix α-2.

When a suitable anion is not present helix α-2 probably experiences folding and unfolding excursions, which will also affect the stability of loop L3. This loop L3 harbors the Fe ligands Cys38 and Cys41. Here we suggest that the anion binding site on Bfd recognizes and offer the following observations in support. Amino acid sequence alignments show that the anion binding site in *P. aeruginosa* Bfd is conserved in many Bfd structures from different organisms which is shown in Figure 6.3. Residues at positions 29 and 46 are invariably Lys or Arg and residue 26 is either Lys, Arg or Gln.

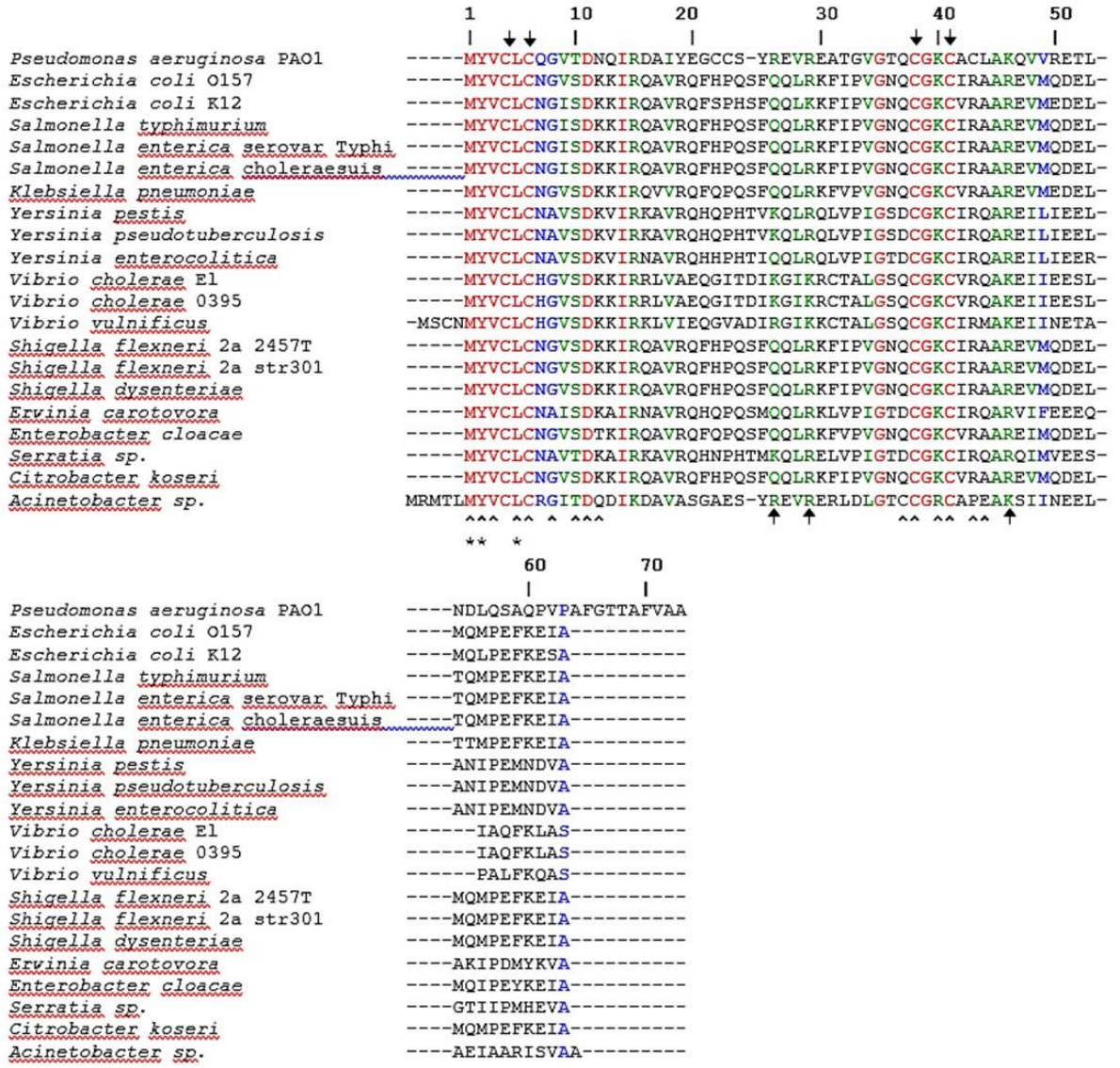

Figure 1.3: Sequence alignment of Bfd with Bfd-like molecules from different organisms. Conserved cysteine residues coordinating iron in the [2Fe-2S] cluster are highlighted by an arrow (↓), residues buried at the BfrB:Bfd interface are denoted by (^), hot spot residues at the BfrB:Bfd interface are denoted by (*), and residues in the phosphate binding site are indicated by an up arrow (↑). Conserved residues across the alignment are in red, conservative substitutions in green and semi-conservative substitutions in blue, sequence numbering according to Bfd (Reproduced with permission from Wijerathne, Yao et al. 2018)

Previous studies performed to investigate the phosphate recognition by protein show that phosphate binding site residues are more conserved than other residues in the alignment, with Arg and Lys having the largest occurrence when the site recognizes phosphate via side

chains.[22-23] Hence, these characteristics of phosphate binding sites are consistent with the exclusive presence of Arg, Lys, or Asn at positions 26, 29, and 40 in the sequence alignment of Bfd proteins.

Moreover, other important facts to note are: the core iron mineral of bacterioferritins isolated from natural sources contain high levels of phosphate (Fe:P ~ 1:1); [24] and iron uptake and mobilization from bacterioferritin is accompanied by a corresponding flux of phosphate across the Bfr shell.[18, 25]

1.3 References

1. Beinert, H.; Holm, R. H.; Münck, E., Iron-sulfur clusters: nature's modular, multipurpose structures. *Science* **1997,** *277* (5326), 653-659.
2. Crack, J. C.; Green, J.; Thomson, A. J.; Brun, N. E. L., Iron–sulfur clusters as biological sensors: the chemistry of reactions with molecular oxygen and nitric oxide. *Accounts of chemical research* **2014,** *47* (10), 3196-3205.
3. Fontecave, M., Iron-sulfur clusters: ever-expanding roles. *Nature chemical biology* **2006,** *2* (4), 171.
4. Beinert, H., Iron-sulfur proteins: ancient structures, still full of surprises. *Journal of Biological Inorganic Chemistry* **2000,** *5* (1), 2-15.
5. Atkinson, J. T.; Campbell, I.; Bennett, G. N.; Silberg, J. J., Cellular assays for ferredoxins: a strategy for understanding electron flow through protein carriers that link metabolic pathways. *Biochemistry* **2016,** *55* (51), 7047-7064.
6. Liu, J.; Chakraborty, S.; Hosseinzadeh, P.; Yu, Y.; Tian, S.; Petrik, I.; Bhagi, A.; Lu, Y., Metalloproteins containing cytochrome, iron–sulfur, or copper redox centers. *Chemical reviews* **2014,** *114* (8), 4366-4469.
7. Meyer, J., Iron–sulfur protein folds, iron–sulfur chemistry, and evolution. *JBIC Journal of Biological Inorganic Chemistry* **2008,** *13* (2), 157-170.
8. Paddock, M. L.; Wiley, S. E.; Axelrod, H. L.; Cohen, A. E.; Roy, M.; Abresch, E. C.; Capraro, D.; Murphy, A. N.; Nechushtai, R.; Dixon, J. E., MitoNEET is a uniquely folded 2Fe–2S outer mitochondrial membrane protein stabilized by pioglitazone. *Proceedings of the National Academy of Sciences* **2007,** *104* (36), 14342-14347.
9. Lipper, C. H.; Karmi, O.; Sohn, Y. S.; Darash-Yahana, M.; Lammert, H.; Song, L.; Liu, A.; Mittler, R.; Nechushtai, R.; Onuchic, J. N., Structure of the human monomeric NEET protein MiNT and its role in regulating iron and reactive oxygen species in cancer cells. *Proceedings of the National Academy of Sciences* **2018,** *115* (2), 272-277.
10. Tamir, S.; Paddock, M. L.; Darash-Yahana-Baram, M.; Holt, S. H.; Sohn, Y. S.; Agranat, L.; Michaeli, D.; Stofleth, J. T.; Lipper, C. H.; Morcos, F., Structure–function analysis of NEET proteins uncovers their role as key regulators of iron and ROS homeostasis in health and disease. *Biochimica et Biophysica Acta (BBA)-Molecular Cell Research* **2015,** *1853* (6), 1294-1315.

11. Andrews, S. C.; Harrison, P. M.; Guest, J. R., Cloning, sequencing, and mapping of the bacterioferritin gene (bfr) of Escherichia coli K-12. *Journal of bacteriology* **1989,** *171* (7), 3940-3947.
12. Garg, R. P.; Vargo, C. J.; Cui, X.; Kurtz, D. M., A [2Fe-2S] protein encoded by an open reading frame upstream of the Escherichia coli bacterioferritin gene. *Biochemistry* **1996,** *35* (20), 6297-6301.
13. Quail, M. A.; Jordan, P.; Grogan, J. M.; Butt, J. N.; Lutz, M.; Thomson, A. J.; Andrews, S. C.; Guest, J. R., Spectroscopic and Voltammetric Characterisation of the Bacterioferritin-Associated Ferredoxin ofEscherichia coli. *Biochemical and biophysical research communications* **1996,** *229* (2), 635-642.
14. Ochsner, U. A.; Wilderman, P. J.; Vasil, A. I.; Vasil, M. L., GeneChip® expression analysis of the iron starvation response in Pseudomonas aeruginosa: identification of novel pyoverdine biosynthesis genes. *Molecular microbiology* **2002,** *45* (5), 1277-1287.
15. Weeratunga, S. K.; Gee, C. E.; Lovell, S.; Zeng, Y.; Woodin, C. L.; Rivera, M., Binding of Pseudomonas aeruginosa apobacterioferritin-associated ferredoxin to bacterioferritin B promotes heme mediation of electron delivery and mobilization of core mineral iron. *Biochemistry* **2009,** *48* (31), 7420-7431.
16. Wang, A.; Zeng, Y.; Han, H.; Weeratunga, S.; Morgan, B. N.; Moënne-Loccoz, P.; Schönbrunn, E.; Rivera, M., Biochemical and structural characterization of Pseudomonas aeruginosa Bfd and FPR: ferredoxin NADP+ reductase and not ferredoxin is the redox partner of heme oxygenase under iron-starvation conditions. *Biochemistry* **2007,** *46* (43), 12198-12211.
17. Wang, A.; Rodríguez, J. C.; Han, H.; Schönbrunn, E.; Rivera, M., X-ray crystallographic and solution state nuclear magnetic resonance spectroscopic investigations of NADP+ binding to ferredoxin NADP reductase from Pseudomonas aeruginosa. *Biochemistry* **2008,** *47* (31), 8080-8093.
18. Rivera, M., Bacterioferritin: structure, dynamics, and protein–protein interactions at play in iron storage and mobilization. *Accounts of chemical research* **2017,** *50* (2), 331-340.
19. Yao, H.; Wang, Y.; Lovell, S.; Kumar, R.; Ruvinsky, A. M.; Battaile, K. P.; Vakser, I. A.; Rivera, M., The structure of the BfrB–Bfd complex reveals protein–protein interactions enabling iron release from bacterioferritin. *Journal of the American Chemical Society* **2012,** *134* (32), 13470-13481.
20. Wang, Y.; Yao, H.; Cheng, Y.; Lovell, S.; Battaile, K. P.; Midaugh, C. R.; Rivera, M., Characterization of the bacterioferritin/bacterioferritin associated ferredoxin protein–protein interaction in solution and determination of binding energy hot spots. *Biochemistry* **2015,** *54* (40), 6162-6175.
21. Eshelman, K.; Yao, H.; Hewage, A. N. P.; Deay, J. J.; Chandler, J. R.; Rivera, M., Inhibiting the BfrB: Bfd interaction in Pseudomonas aeruginosa causes irreversible iron accumulation in bacterioferritin and iron deficiency in the bacterial cytosol. *Metallomics* **2017,** *9* (6), 646-659.
22. Copley, R. R.; Barton, G. J., A structural analysis of phosphate and sulphate binding sites in proteins: estimation of propensities for binding and conservation of phosphate binding sites. Elsevier: 1994.
23. Gruber, M.; Greisen Jr, P.; Junker, C. M.; Hélix-Nielsen, C., Phosphorus binding sites in proteins: Structural preorganization and coordination. *The Journal of Physical Chemistry B* **2014,** *118* (5), 1207-1215.
24. Bradley, J. M.; Moore, G. R.; Le Brun, N. E., Mechanisms of iron mineralization in ferritins: one size does not fit all. *JBIC Journal of Biological Inorganic Chemistry* **2014,** *19* (6), 775-785.

25. Yao, H.; Rui, H.; Kumar, R.; Eshelman, K.; Lovell, S.; Battaile, K. P.; Im, W.; Rivera, M., Concerted motions networking pores and distant ferroxidase centers enable bacterioferritin function and iron traffic. *Biochemistry* **2015,** *54* (8), 1611-1627.

1.3 Macro used for measuring the pillar dimensions

```
macro "PillarAnalysis_10X [s]" {

dir = getDirectory("Choose a Directory ");
list = getFileList(dir);

setBatchMode(true);

Roi_AverageFeret = newArray(list.length);
Roi_StDevFeret = newArray(list.length);
Roi_AverageInterpillar = newArray(list.length);
Roi_StDevInterpillar = newArray(list.length);

for (k = 0; k < list.length; k++) {
	open(list[k]);
	selectWindow(list[k]);

scale = 0.351; //um/pixel, 10XImage

if(roiManager("count") != 0){
roiManager("deselect");
roiManager("delete");
}

if (isOpen("Mask") == true) {
	close("Mask");
}

run("Duplicate...", "title=Mask");

setAutoThreshold("Default dark");
run("Convert to Mask");
//run("Dilate"); //Dilation included to match Keyence measurements
run("Analyze Particles...", "size=30000-Infinity circularity=0.10-1.00 exclude add");
RoiN = roiManager("count");

Roi_X = newArray(RoiN);
Roi_Y = newArray(RoiN);
Roi_Feret = newArray(RoiN);
Roi_Interpillar_Ave = newArray(RoiN);

for (i=0; i<RoiN; i++){
```

```
	roiManager("select",i);
	List.setMeasurements;
	Roi_X[i]=List.getValue("X");

	roiManager("select",i);
	List.setMeasurements;
	Roi_Y[i]=List.getValue("Y");

	roiManager("select",i);
	List.setMeasurements;
	Roi_Feret[i]=List.getValue("Feret");
}

//For each ROI:
//Find nearest ROI and distance -- Output: Roi_Nearest[i], Roi_NearestDistance[i]
for (i = 0; i < RoiN; i++) {
	interpillar_count = 0;
	interpillar_sum = 0;

	for (j = 0; j < RoiN; j++) {
		distance = sqrt((Roi_X[i]-Roi_X[j])*(Roi_X[i]-Roi_X[j])+(Roi_Y[i]-
Roi_Y[j])*(Roi_Y[i]-Roi_Y[j]));

		if (distance != 0) {
			if (distance < Roi_Feret[i]*1.75) {
				interpillar = distance - Roi_Feret[i]/2 - Roi_Feret[j]/2;
				interpillar_count = interpillar_count + 1;
				interpillar_sum = interpillar_sum + interpillar;
			}
		}
	}
	Roi_Interpillar_Ave[i] = interpillar_sum/interpillar_count;
}

//print("Roi Feret Interpillar_Average");
print(list[k]);
for (i=0; i<RoiN; i++){
	print(i, Roi_Feret[i]*scale, Roi_Interpillar_Ave[i]*scale);
}
print("");

Roi_AverageFeret[k] = 0;
Roi_AverageInterpillar[k] = 0;
for (i=0; i < RoiN; i++){
```

```
	Roi_AverageFeret[k] = Roi_AverageFeret[k] + Roi_Feret[i];
	Roi_AverageInterpillar[k] = Roi_AverageInterpillar[k] + Roi_Interpillar_Ave[i];
}
Roi_AverageFeret[k] = Roi_AverageFeret[k]/RoiN;
Roi_AverageInterpillar[k] = Roi_AverageInterpillar[k]/RoiN;

Roi_StDevFeret[k] = 0;
Roi_StDevInterpillar[k] = 0;
for (i=0; i < RoiN; i++){
	Roi_StDevFeret[k] = Roi_StDevFeret[k] + (Roi_Feret[i]-Roi_AverageFeret[k])*(Roi_Feret[i]-Roi_AverageFeret[k]);
	Roi_StDevInterpillar[k] = Roi_StDevInterpillar[k] + (Roi_Interpillar_Ave[i]-Roi_AverageInterpillar[k])*(Roi_Interpillar_Ave[i]-Roi_AverageInterpillar[k]);
}
Roi_StDevFeret[k] = sqrt(Roi_StDevFeret[k]/(RoiN-1));
Roi_StDevInterpillar[k] = sqrt(Roi_StDevInterpillar[k]/(RoiN-1));


close(list[k]);
}

for (k=0; k < list.length; k++) {
	print(list[k], Roi_AverageFeret[k]*scale, Roi_StDevFeret[k]*scale, Roi_AverageInterpillar[k]*scale, Roi_StDevInterpillar[k]*scale);
}

setBatchMode(false);

}
```

1.4 Macro used for determining the fluorescence intensity

```
macro "ChannelIntensity [s]" {

roiManager("reset");

Name=getTitle;
NameDup = "Duplicate";

selectWindow(Name);
```

```
run("Subtract Background...", "rolling=50");
run("Duplicate...", "title="+NameDup);

selectWindow(NameDup);
getStatistics(area, mean, min, max, std);

setAutoThreshold("Default dark");
//setThreshold(250, max);
setThreshold(400, max);
setOption("BlackBackground", false);
run("Convert to Mask");
run("Create Selection");
roiManager("Add");

roiManager("Select", 0);
selectWindow(Name);
roiManager("Measure");

selectWindow(NameDup);
close ();
}
```

1.5 Stitching Macro used for enumerating cells

```
macro StitcherAnalyzer
{

Overlap = 36; //Percent

//Open the directory for processing
dir = getDirectory("Choose a Directory ");
list = getFileList(dir);

print("Processing nuclear channel: Rotating, flipping, and saving individual images...");

//Reorient images in preparation for stitching
dirout = dir + "Processed\\";
File.makeDirectory(dirout);

setBatchMode(true);
```

```
open(list[0]);
getDimensions(dummy, dummy, channels, dummy, frames);
close();

setBatchMode(false);

if (channels > 1){
	Dialog.create("Choose nuclear channel");
	Dialog.addMessage("On which channel are nuclei labeled?");

	if (channels == 2){
		dialoglabels = newArray("Channel 1","Channel 2");
	}
	if (channels == 3){
		dialoglabels = newArray("Channel 1","Channel 2","Channel 3");
	}
	if (channels == 4){
		dialoglabels = newArray("Channel 1","Channel 2","Channel 3","Channel 4");
	}
	if (channels == 5){
		dialoglabels = newArray("Channel 1","Channel 2","Channel 3","Channel 4","Channel 5");
	}

	Dialog.addRadioButtonGroup("Nuclear Channel",dialoglabels,channels,1,"Channel 1");
	Dialog.show;
	nuclear = Dialog.getRadioButton();

	if(nuclear == "Channel 1"){
		NuclearChannel = 0;
	}
	if(nuclear == "Channel 2"){
		NuclearChannel = 1;
	}
	if(nuclear == "Channel 3"){
		NuclearChannel = 2;
	}
	if(nuclear == "Channel 4"){
		NuclearChannel = 3;
	}
	if(nuclear == "Channel 5"){
		NuclearChannel = 4;
	}
```

```
} else {
	NuclearChannel = 0;
}

setBatchMode(true);

j=NuclearChannel;
for (i=0; i < list.length; i++) {
	open(list[i]);
	run("Duplicate...", "  channels="+j+" title=Channel.tif");

	selectWindow(list[i]);
	close();

	File.rename("Channel.tif",list[i]);
	pathout = dirout+list[i];

	run("Rotate 90 Degrees Right");
	run("Flip Vertically","stack");

	run("Subtract Background...", "rolling=50");
	run("Gaussian Blur...", "sigma=2");

	pathout = dirout+list[i];
	saveAs("tiff",pathout);
	close();
}

print("Parameterizing and running the stitching program for nuclear channel...");

//Parameterize file naming system for stitching
XYtemplate = replace(list[0],"000_000","{xxx}_{yyy}");

//Parameterize number of X images and Y images for stitching
indX = indexOf(XYtemplate,"{xxx}");
indY = indexOf(XYtemplate,"{yyy}");
Xmax = 0;
Ymax = 0;
for (i = 0; i < list.length; i++) {
	Xcurr = substring(list[i],indX,indX+3);
	Ycurr = substring(list[i],indY-2,indY+1);
	Xcurrint = parseInt(Xcurr);
	Ycurrint = parseInt(Ycurr);
```

```
		if (Xcurrint > Xmax) {
			Xmax = Xcurrint;
		}
		if (Ycurrint > Ymax) {
			Ymax = Ycurrint;
		}
}
Xmax = Xmax+1;
Ymax = Ymax+1;

setBatchMode(false);

//Stitch the nuclear image, computing overlap
run("Grid/Collection stitching", "type=[Filename defined position] order=[Defined by file-
name ] grid_size_x="+Xmax+" grid_size_y="+Ymax+" tile_overlap="+Overlap+"
first_file_index_x=000 first_file_index_y=000 directory="+dirout+" file_names="+XYtem-
plate+" output_textfile_name=TileConfiguration.txt fusion_method=[Linear Blending] re-
gression_threshold=0.05 max/avg_displacement_threshold=2.50 absolute_displace-
ment_threshold=3.50 compute_overlap subpixel_accuracy display_fusion computation_pa-
rameters=[Save computation time (but use more RAM)] image_output=[Fuse and display]");

if (channels == 1){
		selectWindow("Fused");
		run("Cyan Hot");
		AutoContrast();
		pathout = dirout + "Stitched";
		saveAs("tiff",pathout);

		//Delete the unstitched images in the processed folder
		for (i = 0; i < list.length; i++) {
			File.delete(dirout + list[i]);
		}

} else {
		selectWindow("Fused");
		close();

		setBatchMode(true);

		//Modify tile configuration file for multi-dimensional stitching
		Tile = "TileConfiguration.registered.txt";
		TileMod = "TileConfiguration.modified.txt";
		string=File.openAsString(dirout+Tile);
		string = replace(string,"dim = 2","dim = 3");
```

```
	string = replace(string,"\\)",", 0.0\\)");
	File.saveString(string,dirout+TileMod);

	//Delete single channel processed images
	for (i = 0; i < list.length; i++) {
		File.delete(dirout+list[i]);
	}

	//Prepare multi-channel images for stitching
	for (i = 0; i < list.length; i++) {
		open(list[i]);
		getDimensions(dummy, dummy, channels, dummy, frames);
		if (channels > frames) {
			run("Re-order Hyperstack ...", "channels=[Frames (t)] slices=[Slices (z)] frames=[Channels (c)]");
		}

		//Split up stack, adjust each frame, reassemble in stack
		selectWindow(list[i]);
		run("Stack to Images");

		ROOT = replace(list[i],".tif","-");
		for (j = 0; j<channels; j++){
			if (j==0){
				DAPI = replace(list[i],".tif","-0001");
			}
			if (j==1){
				FITC = replace(list[i],".tif","-0002");
			}
			if (j==2){
				CY3 = replace(list[i],".tif","-0003");
			}
			if (j==3){
				CY5 = replace(list[i],".tif","-0004");
			}
			if (j==4){
				CY7 = replace(list[i],".tif","-0005");
			}
		}
		run("Images to Stack", "name="+list[i]+" title="+ROOT+" use");

	//Rotate and flip the images in prep for stitching, save to the processed folder
		run("Rotate 90 Degrees Right");
		run("Flip Vertically","stack");
```

```
		run("Subtract Background...", "rolling=50 stack");
		run("Gaussian Blur...", "sigma=2 stack");

		pathout = dirout+list[i];
		saveAs("tiff",pathout);
		close();
}

setBatchMode(false);

print("Stitching multidimensional images...");

//Parameterize file naming system for stitching
XYtemplate = replace(list[0],"000_000","{xxx}_{yyy}");

//Parameterize number of X images and Y images for stitching
indX = indexOf(XYtemplate,"{xxx}");
indY = indexOf(XYtemplate,"{yyy}");
Xmax = 0;
Ymax = 0;
for (i = 0; i < list.length; i++) {
		Xcurr = substring(list[i],indX,indX+3);
		Ycurr = substring(list[i],indY-2,indY+1);
		Xcurrint = parseInt(Xcurr);
		Ycurrint = parseInt(Ycurr);
		if (Xcurrint > Xmax) {
			Xmax = Xcurrint;
		}
		if (Ycurrint > Ymax) {
			Ymax = Ycurrint;
		}
}
Xmax = Xmax+1;
Ymax = Ymax+1;

	run("Grid/Collection stitching", "type=[Positions from file] order=[Defined by Tile-Configuration] directory="+dirout+" layout_file="+TileMod+" fusion_method=[Linear Blending] regression_threshold=0.05 max/avg_displacement_threshold=2.50 absolute_displacement_threshold=3.50 subpixel_accuracy display_fusion computation_parameters=[Save computation time (but use more RAM)] image_output=[Fuse and display]");

		//Save stitched image
		pathout = dirout + "Stitched";
```

```
saveAs("tiff",pathout);

//Delete the unstitched images in the processed folder
for (i = 0; i < list.length; i++) {
	File.delete(dirout + list[i]);
}

//Split up the stitched stack. Apply LUT, autocontrast and save all channels.
selectWindow("Stitched.tif");
run("Stack to Images");

print("Applying LUTs and saving stitched images...");

//Delete the extra image from stitching
selectWindow("Stitched-000"+channels+1);
close();

selectWindow("Stitched-0001");
run("Cyan Hot");
AutoContrast();
pathout = dirout + "Stitched_DAPI";
saveAs("tiff",pathout);
run("Tile");

if(isOpen("Stitched-0002")){
selectWindow("Stitched-0002");
run("Green");
AutoContrast();
pathout = dirout + "Stitched_FITC";
saveAs("tiff",pathout);
run("Tile");
}

if(isOpen("Stitched-0003")){
selectWindow("Stitched-0003");
run("Orange Hot");
AutoContrast();
pathout = dirout + "Stitched_Cy3";
saveAs("tiff",pathout);
run("Tile");
}

if(isOpen("Stitched-0004")){
selectWindow("Stitched-0004");
```

```
            run("Red");
            AutoContrast();
            pathout = dirout + "Stitched_Cy5";
            saveAs("tiff",pathout);
            run("Tile");
            }

            if(isOpen("Stitched-0005")){
            selectWindow("Stitched-0005");
            run("Magenta Hot");
            AutoContrast();
            pathout = dirout + "Stitched_BF";
            saveAs("tiff",pathout);
            run("Tile");
            }

}
}


function AutoContrast() {
AUTO_THRESHOLD = 5000;
 getRawStatistics(pixcount);
 limit = pixcount/10;
 threshold = pixcount/AUTO_THRESHOLD;
 nBins = 256;
 getHistogram(values, histA, nBins);
 i = -1;
 found = false;
 do {
        counts = histA[++i];
        if (counts > limit) counts = 0;
        found = counts > threshold;
 }while ((!found) && (i < histA.length-1))
 hmin = values[i];

 i = histA.length;
 do {
        counts = histA[--i];
        if (counts > limit) counts = 0;
        found = counts > threshold;
 } while ((!found) && (i > 0))
 hmax = values[i];
```

```
 setMinAndMax(hmin, hmax);
 //print(hmin, hmax);
}
```

1.6 Stroke clinical data (Stroke patients and healthy controls)

Patient ID	Patient age/gender	Diagnosis	Single blinded patient code #	Blood draw date
HCS 006	59/F	Control	1	3/10/2011
HCS 007	61/F	Control	3	6/3/2011
HCS 008	83/F	Control	5	5/27/2011
HCS 009	61/M	Control	7	6/15/2011
HCS 010	53/M	Control	9	7/19/2011
sp036	66/M	AIS patient	2	7/22/2011
sp039	72/M	AIS patient	4	8/4/2011
sp041	67/M	AIS patient	6	8/18/2011
sp045	95/F	AIS patient	8	11/7/2011
sp052	85/F	AIS patient	10	12/12/2011